Electronic Theses and Dissertations, 2004-2019

2012

Evaporation, Precipitation Dynamics And Instability Of Acoustically Levitated Functional Droplets

Abhishek Saha
University of Central Florida

EVAPORATION, PRECIPITATION DYNAMICS AND INSTABILITY OF ACOUSTICALLY
LEVITATED FUNCTIONAL DROPLETS

by

ABHISHEK SAHA
B.S., Mechanical Engineering, Jadavpur University, India, 2006
M.S., Mechanical Engineering, University of Central Florida, 2010

A dissertation submitted in partial fulfillment of the requirements
for the degree of Doctor of Philosophy in Mechanical Engineering
in the department of Mechanical, Materials and Aerospace Engineering
in the College of Engineering and Computer Science
at the University of Central Florida
Orlando, Florida

Summer Term
2012

Major Professors: Ranganathan Kumar & Saptarshi Basu

ABSTRACT

Evaporation of pure and binary liquid droplets is of interest in thermal sprays and spray drying of food, ceramics and pharmaceutical products. Understanding the rate of heat and mass transfer in any drying process is important not only to enhance evaporation rate or vapor-gas mixing, but also to predict and control the final morphology and microstructure of the precipitates. Acoustic levitation is an alternative method to study micron-sized droplets without wall effects, which eliminates chemical and thermal contamination with surfaces. This work uses an ultrasonic levitation technique to investigate the vaporization dynamics under radiative heating, with focus on evaporation characteristics, precipitation kinetics, particle agglomeration, structure formation and droplet stability. Timescale and temperature scales are developed to compare convective heating in actual sprays and radiative heating in the current experiments. These relationships show that simple experiments can be conducted in a levitator to extrapolate information in realistic convective environments in spray drying.

The effect of acoustic streaming, droplet size and liquid properties on internal flow is important to understand as the heat and mass transfer and particle motion within the droplet is significantly controlled by internal motion. Therefore, the droplet internal flow is characterized by Particle Image Velocimetry for different dropsize and viscosity. Nanosuspension droplets suspended under levitation show preferential accumulation and agglomeration kinetics. Under certain conditions, they form bowl shaped structures upon complete evaporation. At higher concentrations, this initial bowl shaped structure morphs into a ring structure. Nanoparticle

migration due to internal recirculation forms a density stratification, the location of which depends on initial particle concentration. The time scale of density stratification is similar to that of perikinetic-driven agglomeration of particle flocculation. The density stratification ultimately leads to force imbalance leading to a unique bowl-shaped structure.

Chemically active precursor droplet under acoustic levitation shows events such as vaporization, precipitation and chemical reaction leading to nanoceria formation with a porous morphology. The cerium nitrate droplet undergoes phase and shape changes throughout the vaporization process followed by formation of precipitate. Ex-situ analyses using TEM and SEM reveal highly porous morphology with trapped gas pockets and nanoceria crystalline structures at 70°C.

Inhomogeneity in acoustic pressure around the heated droplet can induce thermal instability. Short wavelength (Kelvin-Helmholtz) instability for diesel and bio-diesel droplets triggers this secondary atomization, which occurs due to relative velocity between liquid and gas phase at the droplet equator. On the other hand, liquids such as Kerosene and FC43 show uncontrollable stretching followed by a catastrophic break-up due to reduction in surface tension and viscosity coupled with inhomogeneity of pressure around the droplet.

Finally, a scaling analysis has been established between vaporizing droplets in a convective and radiative environment. The transient temperature normalized by the respective scales exhibits a unified profile for both modes of heating. The analysis allows for the prediction of required laser flux in the levitator experiments to show its equivalence in a corresponding heated gas stream. The theoretical equivalence shows good agreement with experiments for a range of droplet sizes.

ACKNOWLEDGEMENTS

TABLE OF CONTENTS

LIST OF FIGURES

yttrium. The precursors are mixed according to the final composition of 7 wt.% yttria-stabilized zirconia (7YSZ). The coating these single scan correspond to is reasonably dense (88%) and hard (1023 Hv). Same morphology has been observed in single pass for dense Al_2O_3–40 wt.% 7YSZ coatings, TiO_2 coatings and in 7YSZ coatings for porous TBCs. Cracked shells as well as molten solid mass are visible. 183

xx

LIST OF TABLES

CHAPTER ONE: INTRODUCTION

1.1 Droplet evaporation and morphology

Droplet vaporization is a widely observed phenomenon that occurs both in industrial applications and natural processes. Power generation units that run on liquid fuels, such as IC engines, gas turbines for aero-engines utilize poly-dispersed fuel sprays as a technique to inject fuel in pre-vaporizers or combustor chambers. Dynamics of fuel droplet evaporation controls homogeneity of fuel-air mixing which is required for lean and low emission combustions. Some of these power generation units also use droplet combustion to initiate the combustion process and a precursor to gas phase (mixture of fuel vapor and air) combustion.

Spray drying is another important industrial application where droplet evaporation is used. In general, a spray of water-based solution or colloidal suspension is injected into a hot gas which vaporizes the solvent part precipitating the solute or the particles of different morphologies. An upscaled version of the same process is used for powder production. Particle size and area-to-volume ratio are two important parameters that need to be controlled in the powder industry. Both food and pharmaceutical industries use spray drying to generate powders containing particles of different shapes and sizes. Other than powder generation, the spray pyrolysis is used to generate thermal coating. In processes such as SPPS (Solution Precursor Plasma Spray), HVOF (High Velocity Oxy-Flame) generally precursor solution of colloidal suspension is sprayed into a high temperature plasma (SPPS) or into a flame environment. The high temperature of the gaseous environment not only vaporizes the solvent but also thermally decomposes the salt or in other words, it pyrolizes. The droplet which eventually transforms into

a molten pyrolized particle is transported by the high velocity gas onto the substrate where it gets deposited as a splat. The process ultimately generates the thermal coating. The coating quality and microstructure depends on in-flight vaporization and precipitation kinetics of the precursor droplets. SPPS and HVOF processes are widely used to generate Thermal Barrier Coating (TBC), oxygen resistive coating, optical coatings and other similar applications.

Other than these applications, vaporization of liquid droplets is also used in ink-jet printing, spray cooling, drug delivery, and surface patterning. Owing to its widespread application in various industries, vaporization of liquid droplets has been both experimentally and numerically studied in the literature. Besides global vaporization pattern for some of these applications, understanding of droplet level physics is very important and central to the development of new innovative techniques and system designs. These droplet level studies cover a wide range of spectrum including migration and agglomeration of particles in vaporizing droplet, pure droplet evaporation, chemical kinetics of pyrolization etc. Many of the experimental studies on droplets involve wall-droplet or droplet-droplet interactions. It has been proven that binary droplet (containing solute) shows a preferential solute-migration pattern during drying process. Park and Moon (2006) discussed the roll of competing effects of natural convection and Marangoni flow in creating different structures due to solute migration. A well- known "coffee ring" phenomena has been studied by Deegan et al. (1997, 2000). They analyzed the ring formation around the edge of a vaporizing liquid pool (droplet) on a solid surface. They reported that the effects of surface tension gradient, solute diffusion and gravity are negligible for this ring formation. They showed that outer edge gets pinned to the solid surface. This results in an outward fluid flow due

to the squeezing of the free surface in order to compensate the evaporation loss. They also experimentally supported their theory of this contact line deposition of particles.

On the other hand, applications which involve liquid spray do not have surface effects. A detailed study on vaporizing droplet and spray has been reported by Sirignano (1999). He modeled a single vaporizing droplet under convective heating. He used an Eulerian/ Lagrangian model to simulate the gas phase and liquid phase separately. He used semi-empirical correlations to calculate Nusselt number and Sherwood number. For a single vaporizing droplet, he argued that the droplet does not have much effect on the ambient gas phase. Thus, he used a one-way coupled model, which he later extended for liquid sprays. Law [Law (1973, 1976a, 1976b, 1977, 1982), Botros et al. (1980), Fernandez-Pello and Law (1982a, 1982b)] extended this modeling work for droplet combustion with multicomponent droplets and oil/water emulsions. They proposed modification of the basic model for correct prediction of droplet drying rate and surface temperatures in different environments. Recently, Castanet and co-workers [Castanet et al. (2002, 2005), Maqua et al. (2008) and Depredurand et al. (2010)] experimentally studied monodisperse droplet evaporation both in flame and without flame. They employed optical techniques such as laser induced fluorescence and particle dynamic analyzer (PDA) to measure the temperature and diameter of the droplets.

In the field of thermal spray, Pawlowski (1995) discussed the need for studying inflight thermophysical and morphological changes in droplets as final microstructure and spray quality depends on these changes. Both HVOF and SPPS processes are used for generating thermal coating employed for the production of protective coatings on hardware components such as

thermal barrier coatings on gas turbine blades, among other numerous examples. SPPS, being comparatively a newer method using plasma, has been studied extensively over the last decade. The effect of droplet size, injection method and plasma condition on the spray pyrolysis and thickness of the coating has been studied by Sampath et al. (1999), Padture et al. (2001, 2002), Jordan et al. (2004), Bhatia et al. (2002) and others. The fluctuating and turbulent nature of the plasma flow makes it very difficult to perform experimental analysis of the thermo-physical processes inside the droplets injected into plasma. Modeling of the process of vaporization in a convective high temperature field of DC arc plasma or oxy-fuels has been described by Ozturk and Cetegen (2004, 2005a, 2005b, 2006). Castillo and Munz (2007) provided detailed modeling of droplets injected in a low temperature RF plasma. A collective analysis of the various stages in the SPPS process is portrayed in the work of Basu et al. (2008b). These works detailed the inflight droplet behavior and stages of droplet heating in plasma sprays. Chandra and his group [Pershin et al. (2003), Dhiman et al. (2007), McDonald et al. (2008, 2010)] modeled the splat formation and coating generation mechanism on the substrate in plasma sprays. They showed that the coating quality and porosity not only depends on the in-flight changes in the droplet, but also on the velocity, viscosity and surface tension of the droplets when it reaches the substrate. He showed experimentally the effects of temperature and surface quality of the substrate on the splat dimension, which governs the quality of the coating.

1.2 Radiative heating

Radiative heating in droplet evaporation has been studied widely due to its importance in flames and in plasmas. Although radiation heat transfer can be neglected for droplet evaporation in low temperature environment, it becomes important for applications involving time, temperature,

plasma or high temperature combustion. Radiative sources are sometimes used to study single droplet evaporation in separate-effects experiments. Mild to high intensity of laser heating can mimic similar thermo-physical transformations observed in droplets under convection heating.

Laser heating of liquid droplets has been studied by many authors in different contexts. Park and Armstrong (1989) and Lage and Rangel (1993) studied in detail the heat transfer and hydrodynamics of irradiated water droplets. Drombosky and Sazhin (2003) and Lage and Rangel (1993) studied droplets heated by radiation, though their work was concentrated on the effects of blackbody radiation on diesel fuel droplets. Sazhin et al. (2004) found the absorption efficiency of diesel fuel droplets irradiated by blackbody radiation and proposed a correlation linking various parameters and droplet size. Their results however did not include any effect of composition of the droplet on the absorption efficiency. Abramzon and Sazhin (2005) modeled heat and mass transport phenomena within a droplet under blackbody radiation assuming homogeneous absorption. Park and Armstrong (1989) proposed a model for two dimensional directional heating of a water droplet using CO_2 laser. They also reported that over a threshold power level, the droplet undergoes explosive boiling. They also showed the effect of non-uniform source function on thermodynamic processes within the droplet. Works of Park and Armstrong (1989) indicated that for directional and spherically symmetric laser irradiation, the variation of temperature is practically negligible inside a moderately sized droplet. However, their work did not consider effects of concentration of components within a binary mixture as the main focus was on pure water droplet. Basu and Cetegen (2008a) was the first to model the heat and mass transfer within a binary solution droplet under laser irradiation. Their work was focused on the effects of laser power intensity, time of irradiation and droplet size on the thermal

and mass transport within the droplet and the formation dynamics of the final residue. Their work, though based on homonuclear precipitation theory, showed the equivalence of plasma and laser heating rates and served as the starting point for experiments described here to study the chemical kinetics and morphology within the precursor droplets when heated by infrared laser irradiation.

Most of these studies are theoretical or computational in nature. Experimental work on hydrodynamics and heat transfer of an irradiated binary droplet exhibiting solute agglomeration has not been studied before.

1.3 Experimental studies with levitator

In addition to sprays, containerless processing of materials also deals with liquid droplet evaporation without any interactions with surface or other droplets. Levitation is one of the adopted techniques to study vaporizing droplets in the absence of any surface effects. Studies on different levitation processes using magnetic, non-magnetic material and live animals have been performed extensively by several research groups [Brandt (2001), Xie and Wei (2007)]. In an acoustic levitator, small objects can be suspended with the help of a standing acoustic wave. The pressure difference between two poles of the objects counteracts the gravity. Yarin et al. (1998) showed through a detailed analytical work that acoustic streaming has a strong effect on the aspect ratio and vaporization characteristics of a suspended droplet. In addition to this work, Tian and Apfel (1996) experimentally studied the effect of acoustic streaming on the evaporation process which showed good agreement with the analytical work. However, these studies involved only pure liquid droplets.

Later Yarin et al. (2002) also studied natural drying process of liquid droplets containing glass beads. They delineated two distinct stages of evaporation: the first stage is due to pure vaporization of the solvent where the droplet diameter reduces with time, whereas in the later stage it becomes constant due to the formation of a porous solid shell of glass beads at the droplet surface. However, they noted that evaporation process still continues after the pure evaporation phase through the porous structure. They experimented with different concentrations of glass beads and observed shorter pure evaporation phase for higher concentration levels. They were able to obtain a correlation between porosity of the final precipitate, drying temperature, initial mass fraction and initial droplet size. Their work did not involve external heating.

1.4 Outline of the dissertation

In this thesis, the author study single and multicomponent under radiative heating to understand the effect of heating rate, perikinetics and external pressure field on droplet evaporation and structure formation. The novelty of this work is in connecting the flow structure within levitated droplet with the agglomeration and precipitation within a levitated droplet system. This work also brings out a novel way of using acoustic levitator and laser heating to study droplets in spray system by revealing time and temperature scales which can connect these two different heating conditions.

The experimental studies are conducted on a setup using an acoustic levitator and infrared laser irradiation as a heat source. Chapter 2 details the experimental setup used for this work along with the optical techniques and related uncertainties. Through Particle Image Velocimetry (PIV) the flow field inside a levitated droplet is mapped and furthermore, the dependence of the

velocity scale on parameters such as levitator frequency, acoustic pressure intensity, droplet size and viscosity on the internal flow field is established through a correlation. A correlation on maximum velocity scale has been established in Chapter 3.

This work reports the formation of a bowl and ring type structures from agglomeration of nanoparticles during evaporation of nanosuspension. In Chapter 4, through the experimental evidence and theoretical analysis of nanosilica suspension the effect of the acoustic streaming induced flow on particle migration and agglomeration has been delineated. In Chapter 5, this work also reports the precipitation kinetics of cerium nitrate solution droplets under laser irradiation. Besides delineating four stages of heating, the experimental study also shows formation of nanoceria with grain size of 10 nm at low temperature of $70^{\circ}C$.

The dissertation reports the effects of viscosity and surface tension on droplet stability under acoustic levitation. In Chapter 6, thermally induced instability in levitated droplets is discussed. The inhomogeneity of acoustic pressure around the droplet tries to stretch it increasing the aspect ratio, while droplet surface tension and viscosity provides the restoring force by. The study shows that when the droplet is heated by the laser, its temperature increases sharply reducing the surface tension and viscosity. The study shows that when certain criteria are met, the droplet undergoes Kelvin Helmholtz instability and possible catastrophic breakups.

In Chapter 7, the work also establishes a numerical model of droplet evaporation in a plasma environment as it happens in Solution Precursor Plasma Spray (SPPS) process. It shows depending on injection type (axial or transverse), either smaller or larger droplets have better chances of getting pyrolized before reaching substrate.

Finally, a scaling argument is introduced in Chapter 8 to show the connection between actual convective environment of droplet heating and separate effect experiments with levitated droplet under laser irradiation. It is shown that wetbulb temperature achieved by droplet during both of these environments can be estimated through a simple scaling analysis. Using this scaling analysis, one can establish a relationship between gas temperatures in convective heating with the effective laser flux required in levitator experiment to achieve the same wet bulb temperature.

.

CHAPTER TWO: INSTRUMENTATION AND EXPERIMENTAL SETUP

2.1 Global experimental setup

The basic experimental setup used for most of the experiments described in subsequent chapters employs an ultrasonic levitator (Tec5 ultrasonic levitator, 100 kHz) to levitate droplets. Majority of the experiments was done with an initial dropsize of 500 (+/-10) μm in diameter. Experiments were also conducted with dropsize ranging from 125 μm to 1000 μm. A 30W (tunable) CO_2 laser (beam diameter 2mm) which irradiates at wavelength of 10.6 μm was used to heat the droplet. As shown in Figure 1, a high speed camera (Phantom V12 and Fastec TSHRMM with maximum frame rate of 16000) was placed at an angle of 30^0 with the axis of the laser to image the heating event. To achieve a moderate resolution, the framing rate was kept limited at 5000 fps. A zoom lens assembly (Navitar 6000) was used to achieve high spatial resolution. A goose neck probe light or a high intensity LED white light was used to backlight the droplet.
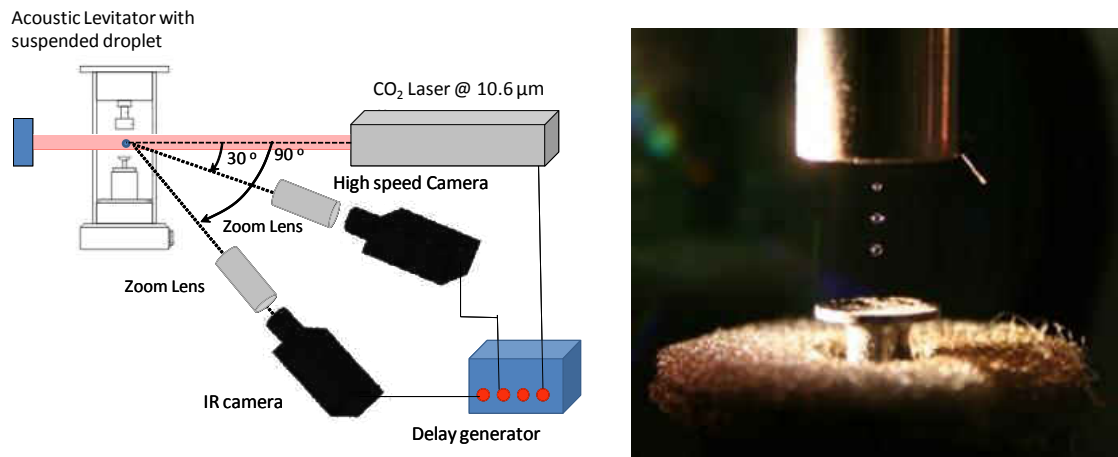
Figure 1: Experimental setup

The temperature of the droplet was measured using an IR camera sitting perpendicular to the laser axis as shown in Figure 1. The IR Camera (FLIR Silver: calibrated for a temperature range of -5 to 200°C) was attached to a special zoom lens to achieve 3X magnification at a working distance of 40mm. A working temperature range use for current experiment was 25-80°C and this uses an integration time of 1.173 msec. The IR camera was operated between 100-300 fps.

To facilitate minute spatial adjustments, the levitator and the high speed camera were placed on two separate X-Y-Z stages. The IR camera was stationed on an X-Y platform. The cameras and the laser were synchronized using an external delay generator.

The PIV experiments were done for a dropsize of 700 μm in diameter. Commercially available 15% volume concentrated nanosilica dispersion in water has been used as source. Different concentrations of nanosilica suspended solution were prepared by adding precise amount of DI water in the concentrated solution. This was followed by 15 minutes of sonication to ensure homogenous mixing. In our current work, various concentrations of nanosilica solution were used while maintaining the laser intensity at 0.85 MW/m^2.

The high speed images were analyzed using a custom-developed Matlab code. The code uses an intensity threshold based edge detection method to calculate an equivalent volume of the droplet which results in an instantaneous equivalent diameter. From these high speed images, the diameter change with time was determined. High speed images were also used to identify morphological changes and reorientation of the structures formed by agglomerates or precipitates.

The IR camera captures surface temperature of the droplet depending on the intensity of thermal radiation recorded by the infrared sensor within the camera. The emissivity of the surface can be input in the ALTAIR software which is used for data processing. The emissivity for DI water was found to be 0.95-0.98 in Bremson (1968) and Wolfe and Zissis (1978). For these values of emissivity, temperature changes by $0.3^{o}C$. For the current study, the emissivity of water was kept at 0.98. Also, through Fourier Transform Infrared Spectroscopy (FTIR) it was confirmed that the absorption coefficient does not change by more than 1% for 10.6 μm (laser wavelength) for different concentrations of nanosilica solutions. To obtain the temperature data from individual frames, a zone of interest was defined around the droplet edge and the maximum and average temperature were recorded using the ALTAIR software. It is important to note that due to oscillation, the droplet went in and out of focus of the IR camera, which has a small depth of field. For data analysis, only the in-focus images were considered. The IR camera is capable of recording temperature with an accuracy of $+/-0.1^{o}C$. Considering the effect of emissivity, the total uncertainty lies within $+/-0.4^{o}C$.

Referring to Figure 1, the experimental set up included an ultrasonic levitator (Tec5 ultrasonic levitator, 100 kHz) to suspend the droplet. The suspended cerium nitrate droplet was heated by a CO_2 laser irradiating at 10.6 μm with a beam diameter of 2 mm. The power of the laser can be tuned from 0 W (no heating) to 30 W ($\sim$10MW/m^2) using a controller coupled with a power supply. An IR camera was placed perpendicular to the laser beam to measure the temperature of the droplet. The IR camera (FLIR Silver: calibrated for a range of -5 to $200^{o}C$ with an accuracy of $\pm 1^{o}C$) was attached to a microscopic zoom (FLIR G3-F/2) lens to facilitate 3X magnification with a working distance of 40 mm. The IR camera was operated at 100 frames per second (fps)

and the recorded images were processed by 'ALTAIR' software to extract the temperature data of the droplet during the heating process. The integration time of the IR camera depends on the temperature range. Most of the experiments were performed in the temperature range of 20 to 80°C which required an integration time of 1.63 msec. The camera is pre-calibrated for a standard emissivity of 1. However, the emissivity can be changed using the ALTAIR software.

A high speed camera (Fastec TSHRMM, with maximum speed of 16000 frames per second) along with a zoom lens assembly (Navitar 6000) was used to capture the physical processes occurring within the droplet during laser irradiation. This camera was placed at an angle of 30° to the laser axis as shown in Figure 1. The vaporization process was recorded at 1000 fps, the maximum that could be achieved without loss of spatial resolution. The images from the high speed camera were used to determine the instantaneous diameter of the droplet. To facilitate fine adjustment of the relative position, the IR camera was placed on an X-Y stage while the levitator was attached to an X-Y-Z stage. The high speed camera was also positioned on a unidirectional stage (X-stage). The laser and the cameras were synchronized using an external delay generator as shown in Figure 1.

2.2 Acoustic levitator

Acoustic levitation uses standing sound waves to suspend objects heavier than air. An acoustic levitator consists of a transducer and a reflector which are co-axially located as shown in Figure 2. The transducer is attached to a piezoelectric crystal which vibrates at a fixed frequency generating a continuous sound wave and the reflector which reflects the sound wave. The reflector can be moved closer or farther from the transducer using a micrometer. If the reflector

and the transducers are kept at a certain distance which is multiple of half wavelength of the sound wave, then it generates a standing wave and at this condition levitation is possible. In a standing wave the point of maximum pressure is called pressure node, while the points of minimum pressure is called pressure antinode. The intensity of the sound wave can be controlled using an external power source. It is important to note that the sound intensity or SPL needed to hold a small substance against gravity is substantially higher than normal sound waves. A typical range of SPL used in acoustic levitators is 150-170dB, which is significantly higher than sounds we hear in normal life (Busy traffic ~70dB, Jet Engine ~140dB).
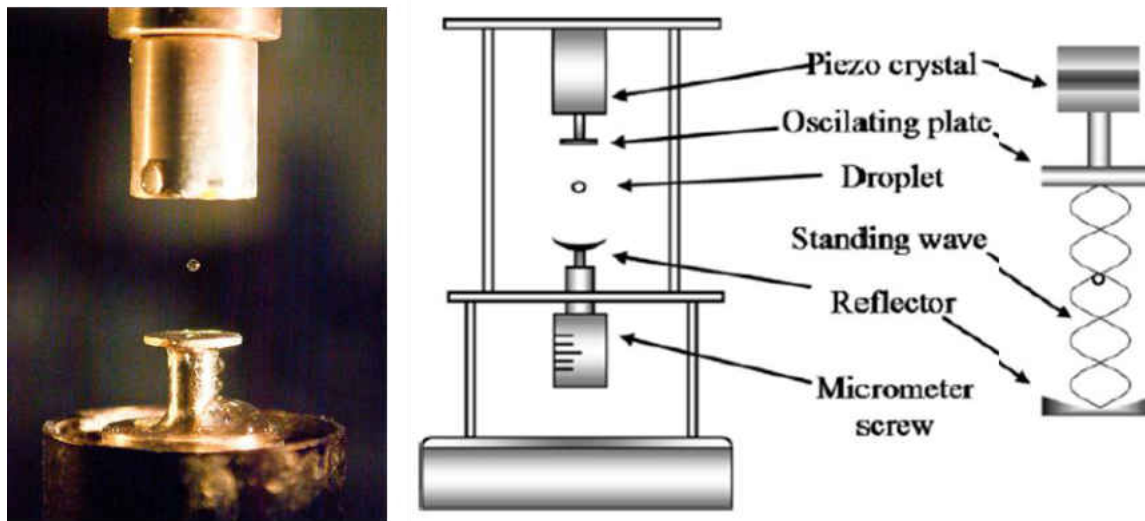
Figure 2: Actual image and schematic of an acoustic levitator

2.3 Thermography by IR camera

The working principle of an infrared camera depends on thermal radiation. Based on the surface temperature, an object radiates in a wide range of wavelengths. Planck's law and Wien's displacement relate the wavelength of the maximum intensity and intensity of this radiation at

14

this wavelength. According to Wien's Displacement Law, the wavelength of the maximum intensity can be calculated by [Incropera et al (2007)],

$$\lambda_{max}.T = 2897.6\,\mu\text{m.K}$$

(2.1)

An Infrared camera captures the radiation from the surface of the object and using the principle of thermal radiation determines the temperature of the surface. Current experimental setup uses an IR camera calibrated for -5 to 200°C, which corresponds to mid-IR range (3 to 6μm). From the intensity of radiation in this range, the camera uses Planck's law to convert the intensity to temperature reading using a complex calculation.

An IR camera looking at the surface receives radiation not only from the surface but also from the surrounding. The total radiation power received by the sensor can be written as $W_{tot} = \varepsilon\tau W_{obj} + (1-\varepsilon)\tau W_{refl} + (1-\tau)W_{atm}$. The emission from the object is calculated as $\varepsilon\tau W_{obj}$, where ε is the emissivity of the object and τ is the transmittance of the atmosphere. The reflected emission from ambient sources is captured by the term $(1-\varepsilon)\tau W_{refl}$, where $(1-\varepsilon)$ is the reflectance of the object. The ambient sources have the temperature T_{refl}. The emission from the atmosphere is calculated by $(1-\tau)\tau W_{atm}$, where $(1-\tau)$ is the emissivity of the atmosphere. W_{obj}, W_{refl} and W_{atm} are radiation received by the camera sensor from blackbody surfaces at temperatures T_{obj} (object temperature), T_{refl} (temperature of the object surrounding) and T_{atm} (temperature of the ambient) respectively. The output voltage of the sensor changes linearly with the received radiation. In most measurements through air medium transmittance is considered to be 1. Depending on the emissivity of the surface and temperature of the object surrounding (T_{refl}), the calibration of the camera determines the T_{obj} from the output voltage. This process is

repeated for every active pixel in the camera. Another important aspect of IR thermography is the integration time of the camera which depends on the temperature range interested. The integration time is equivalent to exposure time in normal CCD cameras. The sensor remains active during this time to receive radiation from the object. The factory calibration of the camera is performed for a fixed level of output voltage. To make sure that the output voltage remains within that range, the integration time needs to be changed for different ranges of temperature. Most of the experiments reported in this work were performed in the temperature range of 20 to 80°C which required an integration time of 1.63 msec. The camera is pre-calibrated for a standard emissivity of 1. Thus an emissivity correction needs to be performed while measuring the surface temperature of objects with different emissivity. This correction can be performed through the ALTAIR software which is also used for data processing and controlling the camera.

2.4 PIV setup and uncertainties

Particle image velocimetry has been performed on levitated droplets to understand the effect of viscosity on the flow field inside the droplet. In this work, PIV was restricted to non-heating conditions using three different liquids of different viscosities. The experimental setup described in the previous section was modified for PIV as shown in Figure 3. A dual pulsed Nd-YAG laser with 70mJ/pulse energy has been used as the light source. The 532 nm output (green) of the laser of 4 mm diameter was converted into an approximately 65 μm thick light sheet using a series of plano-convex lens (focal length 25.4mm) as shown in Figure 3. The levitator was placed at the focal length of the lens, so that the laser sheet was formed right at the location where the droplet was suspended. After finalizing the location, a photographic was used to record laser burn marks which were imaged under optical microscope to confirm the thickness of the light sheet.

16

a)

b)
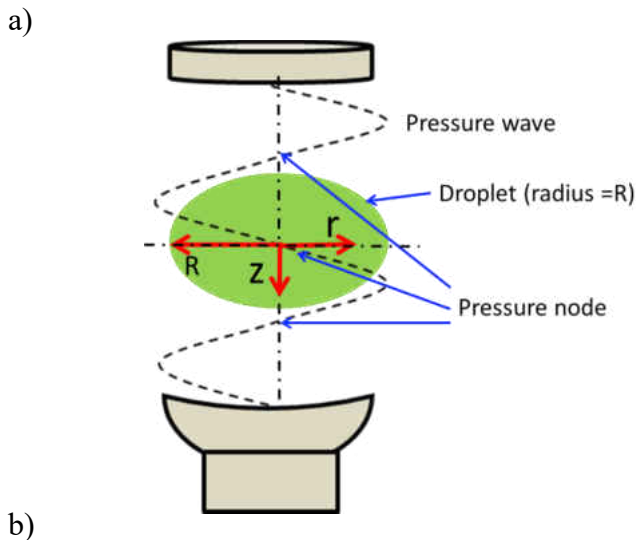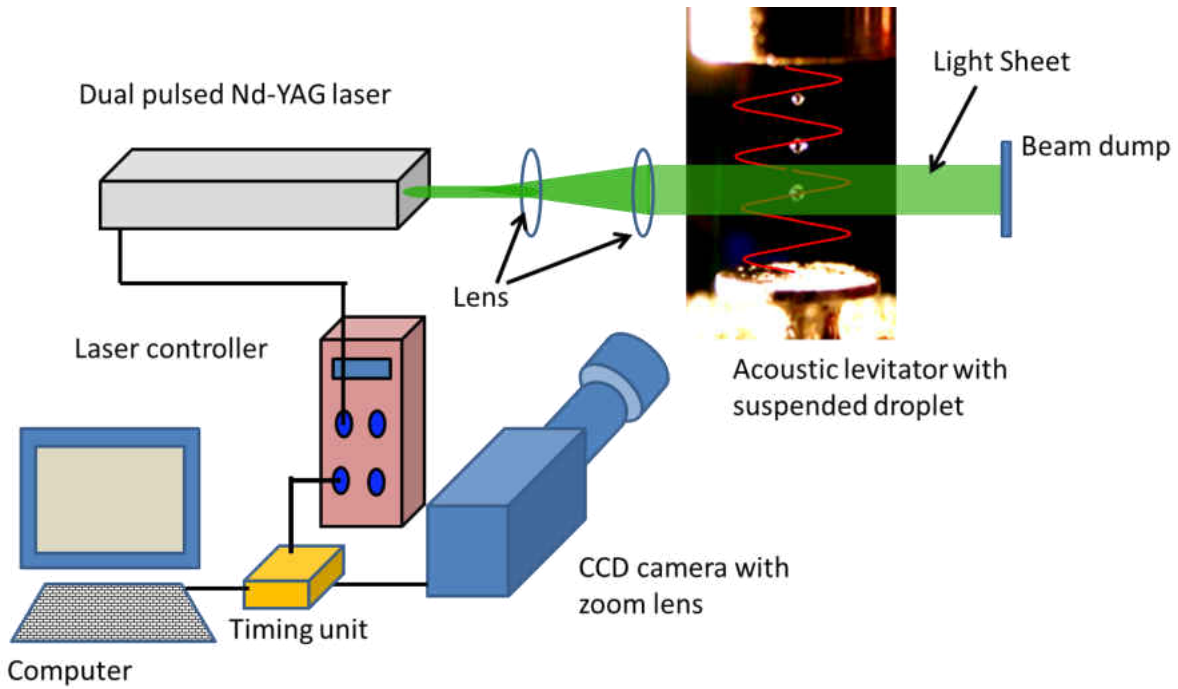
Figure 3: Experimental setup with PIV

A CCD camera (LaVision Imager Intense, 1376 x 1040 resolution) was used for imaging the

droplet. The camera was attached to the Navitar zoom lens assembly to enhance the spatial

resolution. The CCD camera, operated at dual frame mode, was synchronized with the laser using a Portable Timing Unit. The maximum frame rate of the PIV system was 5 fps. The droplets were seeded using polystyrene fluorescent spheres (1μm average diameter). The laser and the acoustic levitator were placed such that the laser sheet intersected the droplet at the central plane. This was achieved by slowly moving the levitator with respect to the laser using the x-y-z stage. A set of 100 image-pairs were recorded for each case. The images were processed using DaVis software. Background subtraction was used to get rid of any scattered intensity from ambient. The vectors were generated using 32 x 32 pixel interrogation windows.

The correlation function at a certain interrogation spot is generally given by:

$$R_{II}(x, y) = \sum_{i=-K}^{K} \sum_{j=-L}^{L} I(i, j).I^{'}(i+x, j+y) \tag{2.2}$$

Where I and I' are intensity values in 1st and 2nd exposures respectively. The interrogation window size is (2M+1)x(2N+1). In this work, a frequency domain method has been adopted to calculate the correlation peaks.

$$R_{II} \Leftrightarrow (x, y) = \hat{I}.\hat{I}^{'*} \tag{2.3}$$

where $\hat{I}$ and $\hat{I}$' are Fourier Transform of I and I' and the * indicates the conjugate. The highest peak of the aforementioned correlation function corresponds to the particle displacement. To screen out unreliable vectors, a threshold value for displacement to noise peak ratio was set to be 1.5, below which the displacement peak was discarded.

The random error associated with this statistical method in determining the displacement vectors decreases with the ratio of maximum displacement and linear size of interrogation window. Scarano and Reithmuller (1999) reported that for displacements more than 2 pixel, this random error is limited to 1% in case of 32x32 window size. However, an increase in the displacement of particles within interrogation windows also results in loss of correlation peak [Raffel et al. (1998)]. Here, the maximum displacement was kept limited to 15 pixels using the PIV processing software. The flow field within the droplet being steady, the correlation peak is supposed to occur at the same location, which justifies the usage of ensemble correlation,

$$R_{ensemble}(x, y) = \frac{1}{N} \sum_{k=1}^{N} (R_{II}(x, y))_k$$

(2.4)

N = number of image pairs

The uncertainty leading from inherent grid generation, correlation, peak validation becomes insignificant with increase in number of image pairs. As mentioned earlier, N=100 was used to achieve good quality vectors with less uncertainty.

The uncertainty in the measured velocity is also dependent of particle size. If the particle images are smaller than the pixel size, then it would increase the bias error in correlation function owing to finite numerical resolution. On the other hand, if the particle size is too large then the random error due to irregularities in the image will be significant [Prasad et al. (1992)]. Santiago et al. (1998) showed that for particle diameters around 3-4 pixel, the resultant uncertainty in determining particle displacement can be limited within $1/10^{th}$ of the particle image diameter. In our PIV measurements within suspended droplets, the camera records digital images with

resolution of 1376x1040 pixel and each image corresponds to an area of 1650x1300µm, i.e., the area of each pixel is ~1.5 µm². The seeding particles with maximum diameter of 2 µm, occupies approximately 4 pixels. Thus, the uncertainty involved within displacement of each particle is around 0.2µm. Current study involves 200µsec pulse separation time on an average, which leads to a velocity uncertainty of 1 mm/sec.

The other aspect of the seeding particle which needs to be considered is its ability to flow with the fluid. The response time of the particles is an important parameter to understand whether they can react fast enough in a sharply accelerating flow. The first order response of these spherical particles in constant flow acceleration can be characterized by the response time, $\tau = \dfrac{d_p{}^2 \rho_p}{\mu_l}$, where d_p is diameter of particles, ρ_p is density of the particle and μ_l is viscosity of the fluid. In the current experiment with polystyrene spheres of d_p=1µm and ρ_p =1.03 gm/cc, the response time is $\tau \sim 10^{-7}$sec. The separation used between two pulses is 200 µsec, which is 3 orders higher than the response time. Therefore, the particles have enough time to follow the flow.

The corrections due to droplet curvature were carried out using algorithms prescribed by Kang et al. (2004) and Minor et al. (2007). They used ray tracing method to calculate the optical distortion and proposed an algorithm for its correction. This algorithm has been used in this work to correct for the velocity vectors inside the levitated droplet.

CHAPTER THREE: FLOW VISUALIZATION WITHIN LEVITATED DROPLET: EFFECT OF VISCOSITY AND DIAMETER

3.1 Introduction

Evaporation of pure and binary liquid droplets is of interest in thermal sprays and spray drying of food, ceramics and pharmaceutical products. Understanding the rate of heat and mass transfer in any drying process is important not only to enhance evaporation rate or -gas mixing, but also to predict and control the final morphology and microstructure of the precipitates. In drying research, liquid precursor droplets are converted into fine particles or powders [Yarin et al. (1999), Saha et al. (2010b), (2012a), Kumar et al. (2010)] of unique agglomeration morphologies and microstructures in an acoustic single-axis levitator. In nanoparticle suspension based precursor solutions, viscosity increases with nanoparticle concentration and changes the morphology. Various techniques have been adopted to study droplet drying such as crosswire, glass filament, micro needle etc. [Ranz and Marshall (1952), Chen and Lim (2004)]. These techniques, however, are not free from surface contamination. Moreover, the solid-liquid contact does not allow the droplet to rotate. For droplets with suspension, the problems become severe as particles start to deposit along the solid surface. One of the alternative ways of conducting drying research is use an acoustic levitator to suspend sub-millimeter size droplet [Saha et al. (2010b), Kumar et al. (2010), Al-Zaitone and Tropea (2011)]. We can gain understanding of the fundamental mechanisms by examining the vaporization characteristics of isolated levitated droplets in an acoustic field. Studies at the level of individual droplets can reveal precipitation mechanisms and important physics related to thermophysical transformations that lead to unique morphological structures.

Several of our recent studies have been in droplets containing pure fluids and nanosuspensions [Saha et al. (2010b), (2012a), (2012b), Kumar et al. (2010), Basu et al. (2012)]. In suspensions, we delineated different stages of evaporation and agglomeration/precipitation. A levitated Cerium Nitrate [$Ce(NO_3)_3$, $6H_2O$] droplet under external heating shows initial faster evaporation leading to precipitation, followed by a thermal decomposition of cerium nitrate forming nanoceria [Saha et al. (2009b), (2010b)]. The final precipitate is porous in nature as the gas liberated during thermal decomposition left vents on the surface. On the other hand, droplets with nanosilica form a bowl-shaped structure after the initial evaporation stage. The bowl-shaped structure is the outcome of preferential migration of the nanoparticles to the bottom of the droplet, followed by agglomeration. At high particle concentrations, the bowl-shaped structure further transforms into a horizontal ring shaped morphology, which again reorients itself to a vertical ring. The initial bowl formation is dependent on the flow structure within the droplet in addition to the pressure imbalance due to density stratification [Saha et al. (2012b)]. Levitation also facilitates a lab-on-a-drop type of studies on evaporation characteristics of new biofuels. Our previous work with biofuels [Saha et al. (2010a)] showed that the study of a single droplet of bio-derived fuels in a levitator could be used to predict vaporization rate and evaporation constants.

Droplet drying in a levitator is controlled by the acoustic streaming-induced motion in the droplet. In order to understand the heat and mass transfer inside a levitated droplet undergoing drying, it is important to determine the velocity field inside the droplet triggered by the flow field in the ambient as a result of acoustic streaming. However, maximum velocity in the droplet can change due to the relative strength of the acoustic streaming and pressure amplitude in addition

to the size and thermo-physical properties of the droplet. Therefore, the measured velocity profiles inside the droplets in different levitators should be scaled using appropriate parameters to obtain a generalized correlation in terms of normalized size and viscosity. This chapter addresses these issues by measuring the velocity in levitated droplets of size 300 μm to 1 mm. In order to mimic the viscosity of nanofluids at different concentrations, solvents such as water, cerium nitrate solution and glycerol have been used. The specific objectives of this chapter are to understand the fundamental effects of internal circulation inside a droplet for different viscosity fluids using Particle Image Velocimetry (PIV) and provide a correlation for maximum velocity and rotation for levitators of different acoustic frequency and amplitude in terms of non-dimensional parameters.

There have been several studies on different levitation processes using magnetic, non-magnetic material and live animals [Brandt (2001), Xie et al. (2006)]. The pressure difference between two poles of a levitated droplet counteracts gravity. Acoustic streaming affects aspect ratio and vaporization characteristics of a levitated droplet [Yarin et al. (1998), (1999), Tian and Apfel (1996)]. The properties of a levitator are such that as the levitator frequency increases, the droplet diameter that can be levitated will go down. Hasegawa et al. (2009) and Yan et al. (2011) used frequencies ~20kHz to levitate 4mm size droplets. Yarin et al. (1999) and Saha et al. (2012a) levitated 1.6mm and 500 μm drops at 56 kHz and 100 kHz respectively. While Yarin et al.'s (1998) work showed two toroidal cells, Hasegawa et al. (2009), Yan et al. (2011) and Saha et al. (2012a) showed the presence of a strong single recirculation cell. This chapter discusses the single cell versus the double cell pattern and will make a case that for high SPL (Sound Pressure Level) needed in single axis levitators, a complete control of droplet rotation is

unavoidable, however, it is predictable. This droplet rotation lends its way toward various morphological changes such as bowl and ring shapes, which would not be possible in the absence of rotation. This work will utilize the data from the literature and the data generated in this chapter to develop a generalized correlation for velocity and rotation in a single vortex that can be applied to any levitator. The correlation can be used for modeling where liquid phase velocity needs to be specified in order to compute vaporization rate, precipitation kinetics and particle agglomeration.

3.2 Experimental setup

The experimental setup involves a 100 kHz acoustic levitator operated at a sound pressure level (SPL) of ~164+/-1 dB. The droplet is held in position as a result of multiple reflections between an ultrasonic radiator and a solid, flat or concave reflector, which is adjusted concentrically so that a standing wave with equally spaced nodes and antinodes is generated. Solid or liquid samples with effective diameters of 300μm to 1 mm can be levitated without contact below the pressure nodes as a result of the axial radiation pressure and radial Bernoulli stress. More details of the experimental setup have been reported by Saha et al. (2012a).

A dual-pulsed 532nm Nd-YAG laser with beam diameter of 4 mm was used for PIV. Using a set of cylindrical and spherical lenses, the circular beam was converted into a ~65μm thick laser sheet with a height of 4mm (Figure 4a). The laser was placed in such a way that the vertical light sheet passes through the center of the droplet. The levitator was stationed on X-Y-Z table in order to achieve minute control over the light sheet location with respect to the suspended droplet. A CCD camera (pixel resolution of 1376x1040) along with a zoom lens was placed

perpendicular to the light sheet. The liquid was seeded by adding polystyrene microspheres (diameter ~ 1μm) with a concentration of less than 2% of volume. The images were analyzed using an edge detection method to calculate an equivalent volume of the droplet from which the diameters of the droplets were measured [Saha et al. (2012a)].
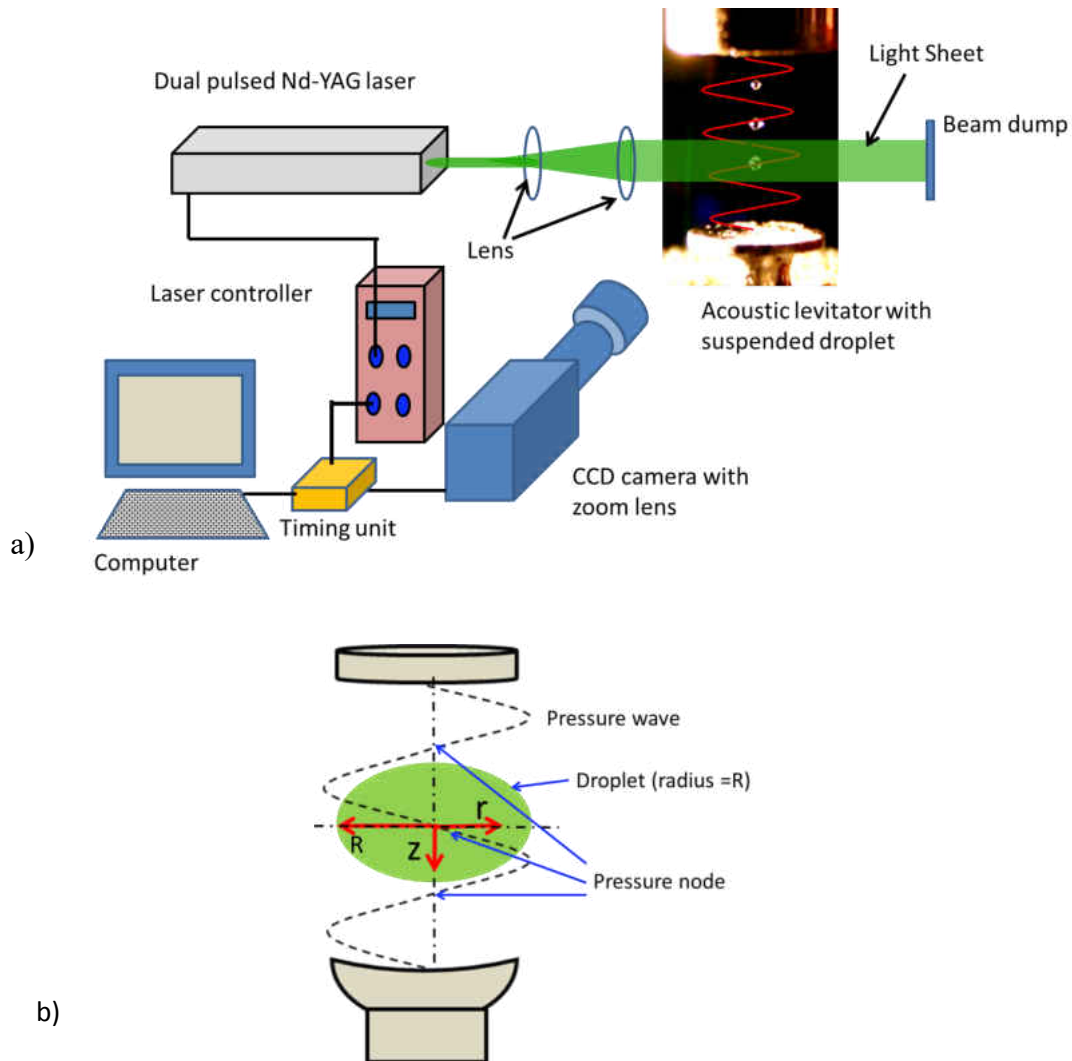
Figure 4: (a) Experimental setup used for PIV, (b) Acoustic levitator with suspended droplet

The laser pulses and the camera frames were synchronized using an external timing unit. The pulse duration of the laser is on the order of 10nsec. The whole setup was operated at 5fps. The

time lag between two pulses (Δt) was varied to see the effect on the velocity field. After a few iterations it was determined that 200 μsec is optimum for the flow field. A set of 100 image-pairs was averaged to get the PIV vectors [Saha et al. (2012a)]. This number was determined to be sufficient to minimize the uncertainty from grid generation, correlation and peak validation.

The random error associated with this statistical method of cross-correlation peak in PIV to determine displacement vectors decreases with the ratio of maximum displacement to linear size of interrogation window [Saha et al. (2012a)]. In our 32x32 window size, this random error is limited to 1% .The maximum displacement was kept limited to 15 pixels [Saha et al. (2012a)]. The uncertainty from inherent grid generation, correlation, peak validation becomes insignificant with increase in number of image pairs. A hundred image pairs were used to achieve good quality vectors. In our PIV measurements, the camera records digital images of a droplet with a resolution of 1376x1040 pixel and each image corresponds to an area of 1650x1300μm, i.e., the area of each pixel is ~1.5 μm^2. The seeding particles with maximum diameter of 1 μm, occupies approximately 4 pixels. Thus, the uncertainty involved within displacement of each particle is around 0.1μm. Current study involves 200 μsec pulse separation time on average, which leads to a velocity uncertainty of 0.5 mm/sec [Saha et al. (2012a)]. The response time is estimated to be 10^{-7}sec [Saha et al. (2012a)]. The separation used between two pulses is 200 μsec, which is 3 orders higher than the response time. Therefore, the particles have enough time to follow the flow. The corrections due to droplet curvature were carried out using algorithms prescribed by Minor et al. (2007). They used ray tracing method to calculate the optical distortion and proposed an algorithm for its correction. This algorithm is used to correct for the velocity vectors

inside the levitated droplet. More details about the experimental setup have been provided in Chapter 2.

3.3 Results

In a levitator, a droplet is suspended by acoustic forces. The pressure distribution between the transducer and the reflector is shown in Figure 4(b). The acoustic pressure is symmetric around the pressure nodes as shown in Figure 4(b). For a stable levitation, the pressure (acoustic) force around the droplet balances the weight and surface tension forces of the droplet. Levitated droplets in a zero gravity environment would remain at the pressure node as shown in Figure 4(b). However, under gravity the droplet shifts downwards so that the pressure distribution around the droplet can balance the weight of the droplet. When a droplet is levitated, it tends to take an ellipsoidal shape due to the asymmetric pressure distribution around the droplet. Our previous works [Saha et al. (2012a), (2012b)] have shown that the shape and location of the droplet depend on the droplet size, density, viscosity and sound pressure level (SPL).

3.3.1 Single cell vs. Toroidal cell

In a perfectly controlled experiment, the flow structure inside a levitated, non-rotating droplet will have two toroidal cells. This was observed by Yarin et al. (1999) in a single axis levitator. Trinh and Wang (1982) ultrasonically levitated a droplet in an immiscible liquid and observed shape oscillations that resembled a two toroidal cell mode (quadruple). However, Trinh and Wang (1982) also reported that when the shape oscillations reached a threshold amplitude, a rotational instability would set in and possibly break the symmetry of these toroidal cells. In most single axis levitators, small misalignments are inevitable which leads to droplet rotation

about the horizontal axis and hence break the symmetry of the toroidal cells leading to a single cell forced vortex type structure. In addition to our current and previous work, many articles have reported this single cell flow structure within the droplets [Hasegawa et al. (2009), Yan et al. (2011)]. Saha et al. (2012a) reported that the droplet rotates about the vertical axis of the levitator as well. These multiaxial droplet rotations contribute towards the destruction of the symmetry of the internal flow field. These rotations are consistent and repeatable for the same levitator and flow conditions.

Thus, the droplets in single axis levitator exhibit rotations about both horizontal and vertical axes mainly due to the acoustic torque arising out of small misalignments/perturbations, compositional inhomogeneity and non-spherically symmetric external heating (like directional laser irradiation in the current work). Smaller droplet size, as in the current experiment, also augments this rotational rate. The rotation, in essence, merges the two toroidal cells normally expected into a single cell structure. For any single axis levitator involving a multi-component droplet, this behavior can be expected, unless the environment is completely controlled with low sound pressure level and partial vacuum. As shown in our previous papers [Saha et al. (2012a), (2012b)], when droplets with nanosuspensions are levitated in an acoustic field, it may be in our best interest to allow such rotations in droplets in order to obtain desired morphology of the final dried particle. Therefore, a single vortex as found by us and others is inevitable and later in section 3.5, we provide correlations for the maximum velocity and rotation that can be expected in any levitator operated at any frequency.

3.3.2. Nanosuspensions in droplets

We have observed multicomponent levitated droplets like nanosilica [Saha et al. (2012a), (2012b), Kumar et al. (2010)] and cerium nitrate solution [Saha et al. (2010b)], exhibit two modes of rotations, one about the horizontal axis and another about the vertical axis of the levitator. The pure liquid droplets primarily rotate about a horizontal axis as shown in Figure 5. When the liquid content of the droplet with nanosilica or precursor solution is significantly higher compared to the solid particles (or precipitate), the droplets primarily rotate about the horizontal axis, while the motion about the vertical axis is very slow (less than one hundredth of a revolution per second). However, when the droplet is heated, it evaporates and undergoes heterogeneous precipitation or agglomeration between the top and bottom halves (compositional inhomogeneity), leading to stronger rotation about the vertical axis and correspondingly weaker motion about the horizontal axis. Upon complete precipitation of salts (cerium nitrate) or agglomeration of nanoparticles (nanosilica), the droplet generally takes a heterogeneous bowl-shaped structure [Saha et al. (2010b), (2012a), Kumar et al. (2010)] which rotates only about the vertical axis. With external heating, the droplets with high concentration of nanosilica can form a ring shaped structure which rotates about the vertical axis at an even faster rate. Further heating results in the reorientation of the ring in the vertical axis when the ring rotates about both horizontal and vertical axes; however the rotation about vertical axis still dominates [Saha et al. (2010b), (2012a), Kumar et al. (2010)]. It is clear that the internal circulation in the liquid phase of the droplet causes such structural and morphological changes. Therefore it is important to determine the flow patterns and rotational speeds prior to such morphological changes.

3.3.3 Qualitative visualization of rotation
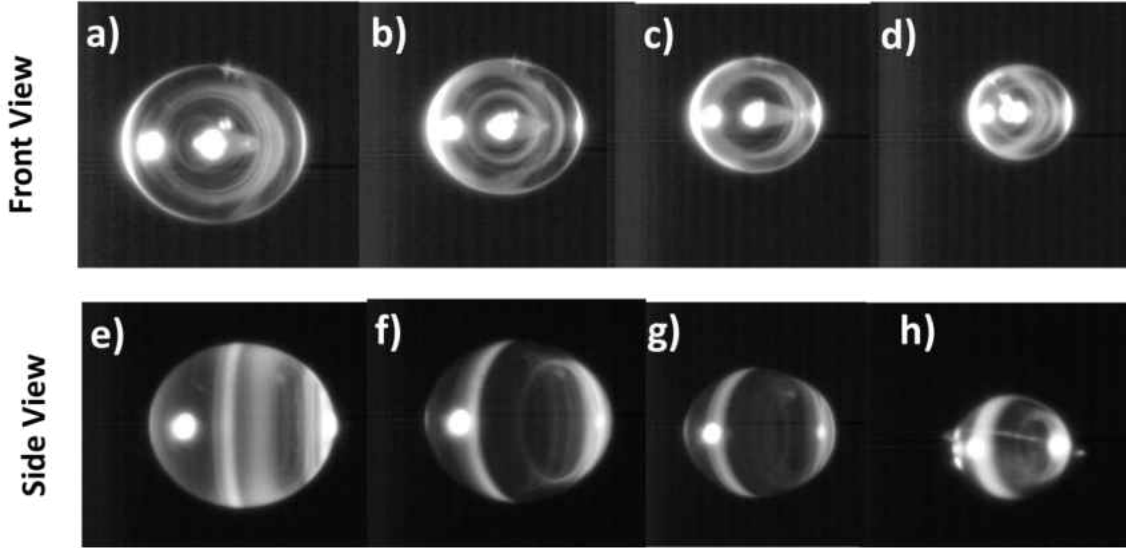
Figure 5: Streak images of rotating droplet, (a-d): Frontal view, (e-h): Side view

Initially for qualitative understanding, we used long exposure imaging technique to capture the flow structure inside liquid droplets. Droplets were seeded with 8-10 μm glass beads and an LED light source was used to illuminate the droplet at an angle of 30° with the camera. The light scattered from the glass beads was captured using the Phantom V12 camera in conjunction with Navitar zoom lens. Streaklines are imaged when the camera sensor is exposed for 0.02 seconds. The long exposure time limits the camera framing rate to 50 fps. Hence, external heating was absent for this set of experiments. The droplet vaporized naturally over 25 minutes and the evaporation process was captured to observe the evolution of the flow structure with time. Figure 5 shows a set of the streak images. As the acoustically levitated droplet shows small oscillations about the axis of the levitator, the long exposed images look slightly blurry. However a qualitative understanding of the flow pattern can still be obtained. From Figure 5a-d, a single vortex cell rotating about a horizontal axis can be observed. When the camera is set parallel to

the horizontal plane (Figure 5a-d), concentric circles are first seen. In time, when the droplet rotates about 90° (Figure 5e-h), the camera sees parallel lines, showing the trajectories of the particles on the surface. The rotational speed about the vertical axis is weak and is measured to be around 0.0167 rpm (Figure 5e-h).

Longer exposed high resolution images with glass beads (streak images) in Figure 5, clearly show that the predominant liquid motion is in the vertical plane. If there was any strong motion in the horizontal plane (i.e., if the droplet was rotating about a vertical axis), then the streak images (Figs 3.2e-h) would not show parallel rings in vertical plane. These parallel rings in vertical plane confirm that the predominant rotation is about the horizontal axis only. However, as stated before, the rotation about the vertical axis increases significantly for nanosilica around the structure formation time. The rotational speed depends on the concentration of nanosilica in water. For example, for 3% concentration, the rotation speed about the vertical axis is 900 rpm (15 rps) after the bowl formation. For higher concentrations of nanosilica, further heating results in a horizontal ring formation and the speed increases to 4200 rpm (70 rps). Later, when the horizontal ring reorients to become a vertical ring, the speed further increases to 7200 rpm (120 rps). This change of the rotational speed about the vertical axis is shown using real images schematically in Figure 6. To investigate the rotational speed about the horizontal axis, Particle Image Velocimetry (PIV) has been performed.
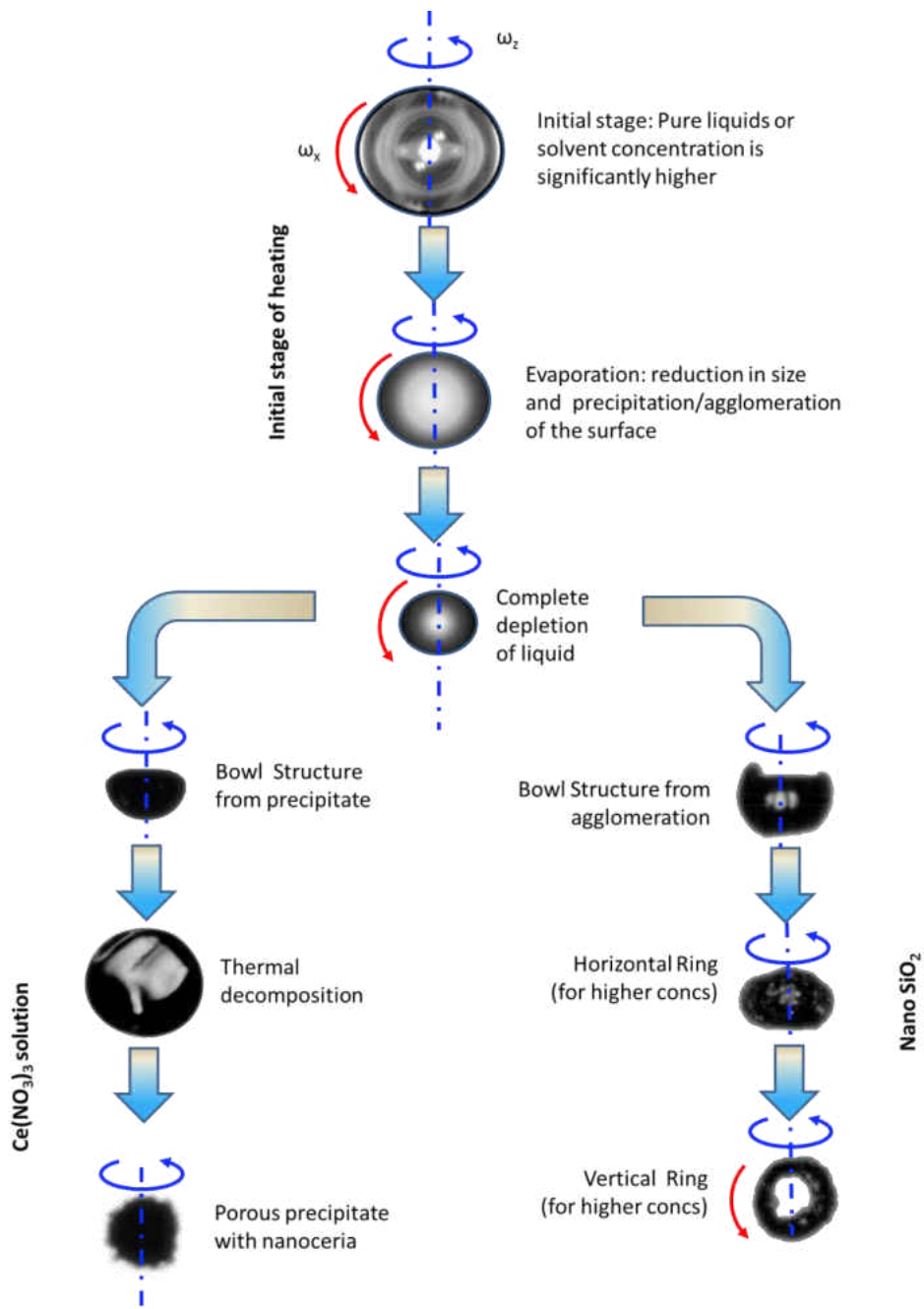
Figure 6: Different stages of evaporation of nanosilica and cerium nitrate droplets

PIV studies were conducted on droplets with three different liquids and three different droplet diameters. The properties of these liquids are given in Table 1. These liquids are chosen such that they mimic the viscosity levels of nanosuspensions at different concentrations [Saha et al. (2012a), Milanova and Kumar (2005), (2008), Vassallo (2004)].

Liquid	Density (kg/m^3)	Dynamic viscosity (Pa-s)
Water	998	0.73×10^{-3}
Cerium Nitrate-water solution (0.5M)	1090	1.33×10^{-3}
Glycerol-water solution (3:2 v/v)	1120	11.10×10^{-3}

Table 1: Properties of the liquids

3.3.4 Quantitative flow structure using PIV

In this section, two-dimensional velocity measurements using PIV are shown in a vertical plane passing through the origin. Only the flow field in the vertical plane (parallel to levitator axis) has been resolved. PIV vectors on levitated droplets with different diameter and viscosity show a similar flow structure as observed during streak imaging. This structure resembles a forced vortex flow around the center of the droplet. At any point inside the droplet, the flow is tangential, and velocity is maximum at the outer radius and minimum (zero) at the center. The strength of the flow decreases with increase in viscosity and diameter. Figure 7 shows the vectors for all three liquids at three different diameters. Preliminary velocity vectors in a levitated droplet were earlier reported by Saha et al. (2012a).

It is interesting to understand how the velocity inside the droplets changes radially. Figure 8 shows the velocity profile along the radius for different fluids. Vector fields from PIV also show that the primary velocity field is tangential in nature. Moreover, from Figure 8, it can be inferred that the velocity changes linearly along the radius. This confirms that the velocity field inside the droplet resembles a forced vortex or rotating droplet, where the slope of each curve in Figure 8 represents the rotational speed.
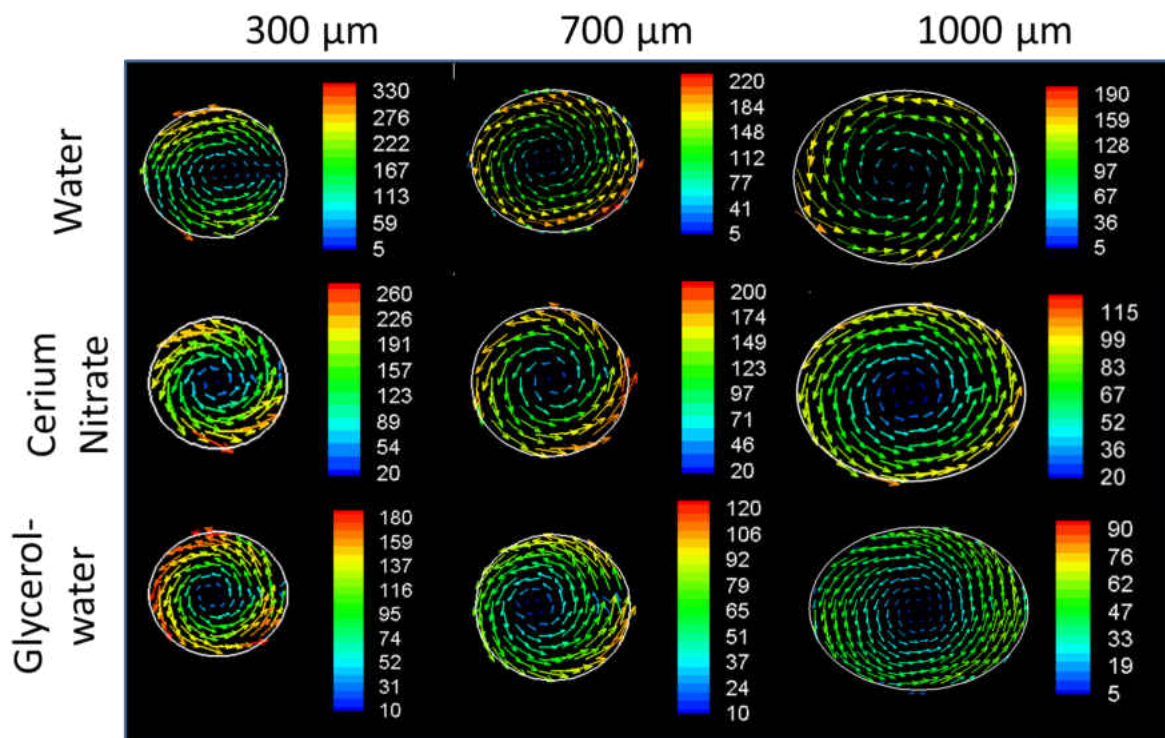
Figure 7: Velocity vectors in a vertical plane passing through droplet center

The important inference can be drawn by combining the streak images and the PIV vectors that the pure liquid droplet essentially contains rotation about a horizontal axis. As discussed earlier, PIV measurements in the center plane (on a vertical plane which intersects the droplet center)

34

show single cell structures. From the streak images it is now clear that the single vortex about the

horizontal axis is maintained, as the droplet slowly rotates about the vertical axis. The rotational

speed about the vertical axis is so small that it does not have any significant effect on the single

cell structure. These streak images also show that even after the droplet size reduces significantly

due to natural evaporation, the flow structure remains unaltered. However, if the droplet contains

a secondary species which may precipitate or agglomerate during evaporation, this flow structure

will be disturbed and will decay rapidly.
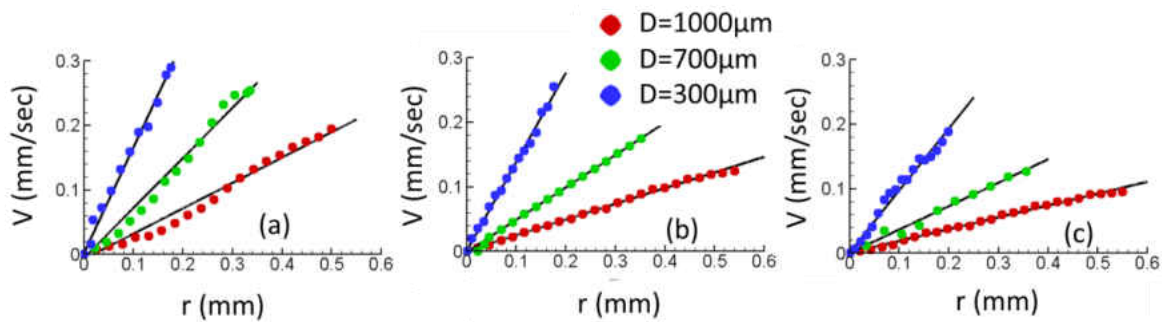
Figure 8: Velocity distribution along horizontal radius of the droplet (a) Water, (b) Cerium Nitrate-water solution (0.5M), (c) Glycerol-water solution (3:2 v/v)

3.3.5 Correlation of maximum velocity and rotation

The velocity vectors show that the maximum velocity (V_{max}) occurs at the equator or at the

radius of the droplet. Also, we have seen that this V_{max} varies with droplet radius and viscosity of

the liquid. Figure 9 shows how V_{max} changes with droplet radius at three different viscosities,

namely for water, cerium nitrate and diluted glycerol. The properties of these liquids are

provided in Table 1.
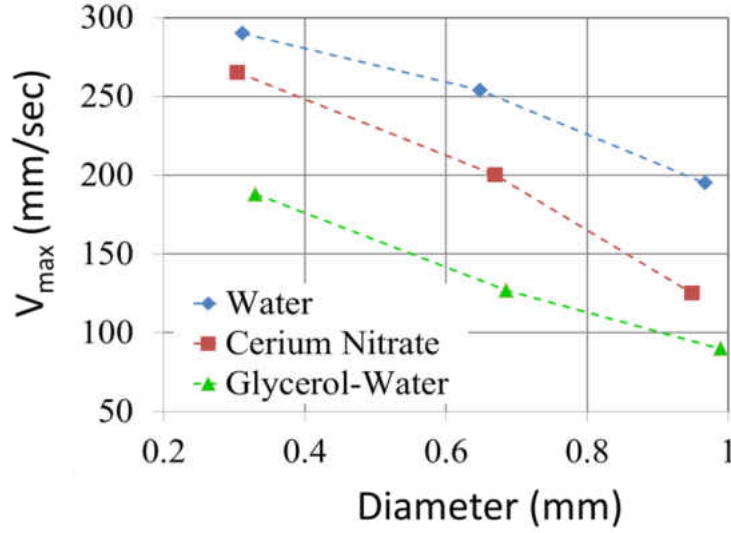
Figure 9: Change in maximum velocity (V_{max}) with droplet diameter

Although there is some scatter in the V_{max} data for different diameter and viscosity, they follow a trend. We see that V_{max} reduces with both size and viscosity of the droplet. In order to understand the dependence of V_{max} on the droplet diameter and viscosity of the liquid, we first performed a dimensional analysis. Three non-dimensional parameters are introduced in the analysis namely D^* (normalized diameter), μ^* (normalized dynamic viscosity), V_{max}^* (normalized maximum velocity inside the droplet). The diameter of the droplet is normalized by the wave number (k_0), and the liquid viscosity and V_{max} are normalized by the surrounding fluid (air) viscosity and velocity scale of the surrounding medium in the absence of a droplet.

$$D^* = k_0 D \tag{3.1}$$

$$\mu^* = \mu_l / \mu_g \tag{3.2}$$

$$V_{max}^{*} = V_{max} / U_{scale}(D) \tag{3.3}$$

where μ_l is the dynamic viscosity of the liquid and μ_g is the dynamic viscosity of the gas phase surrounding the droplet. U_{scale} is the velocity scale which depends on the levitator and the surrounding medium in the absence of a liquid droplet and is derived from the theory of standing waves. According to acoustic theory [Lierke (2002)], this gas velocity is

$$U(r,z) = U_{max} \cos(k_z z) J_0(k_r r) \tag{3.4}$$

where r and z are measured in radial and vertical coordinates respectively with respect to the pressure node. The wavenumbers in the radial and axial directions, k_r, k_z (wavenumbers in the radial and axial directions respectively) and k_0 are related by $k_0 = \sqrt{k_r^2 + k_z^2}$ and $q = k_r / k_z$. Using these relations, we can rewrite,

$$U(r,z) = U_{max} \cos(\frac{k_0 z}{\sqrt{1+q^2}}) J_0(\frac{q k_0 r}{\sqrt{1+q^2}}) \tag{3.5}$$

Here, $U_{max} = Ma.c_0$ and $SPL[dB] = 197 + 20\log(Ma)$ [Lierke (2002)]. Ma is acoustic Mach number, c_0 is speed of sound and SPL is sound pressure level of the levitator in dB. This equation for SPL is valid for unperturbed acoustic wave without any levitated droplet. The gas phase velocity scales are generally computed based on the maximum velocity attained in unperturbed standing wave [Yarin et al. (1998), (1999), Lierke (2002)], and are related to SPL through this equation. Yarin et al. [(1998), (1999)] showed that the presence of levitated droplet alters the SPL due to its ellipsoidal shape. As the use of SPL in the current study is limited only to determine the velocity scale of the unperturbed field, this variation is not considered. Thus, the

velocity scale $U(r,z)$ is valid only when there is no liquid droplet present in the levitator. This velocity scale will be substantially altered in the presence of a liquid droplet.

Since the gas velocity at the location of droplet radius defines a limit for the maximum velocity (V_{max}) within the liquid droplet, U_{scale}= U(r=R, z=0) was used where R= radius of the droplet (=D/2). Thus,

$$U_{scale}(D) = U_{max} J_0 \left(\frac{qD^*}{2\sqrt{1+q^2}} \right)$$ (3.6)

V_{max}^*, D^*, μ^* contain information about the levitator frequency, SPL and properties of the liquid and the external gas field. Note that V_{max}^* is a quantity that is not equal to 1 since the velocity scale $U_{scale}(D)$ is only defined when no liquid droplet is present. In essence, $U_{scale}(D)$ is the most generic velocity scale that is only dependent on the frequency and amplitude of the levitator in the absence of any droplet. Clearly it is prudent to develop a relation such as $V_{max}^* = f(D^*, \mu^*)$. By definition, V_{max}^* can achieve a value between 0 and 1. On the other hand, μ^* has a limiting value of 1. μ^*=1 implies that the inner and outer fluids are the same (air bubble in the levitator), and for this limiting case, V_{max} should be U_{scale}, or V_{max}^*=1. Thus, we develop a correlation using D* and (μ*-1) as follows:

$$V_{max}^* = f[(D^*)^n (\mu^* - 1)^m]$$ (3.7)

Having rationalized the form of Equation 3.7, the data shows best fit with n=1 and m=1/4. Figure 10 shows the plot of V^*_{max} vs $[(D^*).(\mu^*-1)^{0.25}]$. The blue symbols represent the current experiments, which are fitted using an exponential fit of the form,

$$V^*_{max} = \exp(-0.4D^*(\mu^*-1)^{\frac{1}{4}}) \qquad (3.8)$$

Although a value of 0.25 has been used for coefficient 'm' in Equation 3.7, scatter in the data was minimal when values of 0.23-0.27 were used for 'm'.

This equation has the following physical attributes. (1) When the liquid viscosity approaches the surrounding gas viscosity ($\mu^* \to 1$), the droplet becomes indistinguishable from the surrounding (an air bubble), implying that the velocity scale within the droplet should also approach the velocity scale in the gas phase (outside the droplet), or $V_{max}^* \to 1$. (2) In the limit when the droplet approaches a solid body ($\mu^* \to \infty$), the flow within the droplet should approach zero, ($V_{max}^* \to 0$). (3) In the limit $D^* \to 0$, the droplet becomes a massless point on the levitator axis, and the velocity scale approaches the velocity at the pressure node where (acoustic pressure is minimum and velocity is maximum). From the correlation, it can be seen that as $D^* \to 0$, $V_{max}^* \to 1$. (4) For large diameters ($D^* \to \infty$), the outside gas phase velocity is weak, therefore, the flow field within the droplet will be weak as well ($V_{max}^* \to 0$).

Yarin et al. (1999) derived the liquid velocity scale on the droplet surface, $\sqrt{\dfrac{\mu_0 \rho_0}{\mu_l \rho_l}} U_{max}$, where U_{max} is the maximum gas phase velocity in the unperturbed standing wave and μ_0, ρ_0, μ_l, ρ_l are dynamic viscosities and densities of gas phase and liquid phase respectively. In this , we use a

velocity scale, U_{scale} which is the gas phase velocity at the droplet equator (where maximum liquid velocity occurs) and directly related to U_{max} as shown in Equations 3.4 to 3.6. Thus, the velocity scale is independent of liquid properties.

Equation 3.8 has $V_{max}*$ as a function of $\mu*^{0.25}$ (when the higher order terms are neglected) while Yarin et al. (1999) obtained a $\mu*^{0.5}$ dependence from shear balance at the interface. The differences in the velocity scale may be attributed to the fact that the droplet rotates about both vertical and horizontal axes, with the latter being stronger than the former. Yarin's model assumes axi-symmetry and predicts 2 toroidal vortices, whereas the flow field observed in the current experiment is a single cell forced vortex structure. The rotation about a horizontal motion can significantly alter the outside flow field, which makes the velocity scale different.

The data points from Yan *et al.* (2011) and Hasegawa *et al.* (2009) for different levitator settings are normalized and plotted with the current data. Yan *et al.* (2011) studied a water droplet of 3.72 mm diameter suspended using a levitator with 22kHz frequency and reported a maximum velocity of 70mm/sec. Hasegawa et al. (2009) worked with 4 mm diameter water and glycerol droplets in a levitator with 19.4kHz frequency. For a glycerol droplet, they reported that they did not observe any velocity in vertical plane. Thus, the correlation developed appears to predict the data from other levitators as well as for much larger droplets with different viscosities.

As seen in Figures 7 and 8, the flow inside the droplet resembles a forced vortex, therefore, $V_{max} = \omega_x(D/2)$, where ω is rotational speed. If we define non-dimensional rotational speed as $\omega_x^* = V_{max}^*/(D^*/2)$, then, $\omega_x^* = \omega/(k_0 U_{scale})$. Applying these relations in Equation 3.8, an expression for non-dimensional rotational speed can be obtained,

$$\omega_x^* = \frac{2}{D^*} \exp(-0.4D^*(\mu^*-1)^{1/4}) \qquad\qquad (3.9)$$

Using Equation 3.9, a non-dimensional rotation speed can be calculated for a given droplet diameter for different viscosities. Converting this non-dimensional rotation speed to dimensional rotational speed, one can now plot the rotational speed (ω_x) in rpm with respect to dynamic viscosity as shown in Figure 11. In this figure, dotted lines represent the change in rotational speed with viscosity for three diameters of droplets, 300, 700 and 1000 μm. Now if we compare the experimental data of rotational speed for these three diameters at three viscosities, we see the values to lie very closely with the values predicted by the correlation (Figure 11). The small variations can be attributed to the uncertainty in droplet diameter during the experiments. The variation in droplet diameter was found to be ±5% which yields a maximum ±10% variation in rotational speed within the viscosity range of these droplets (0.5-5 cP).
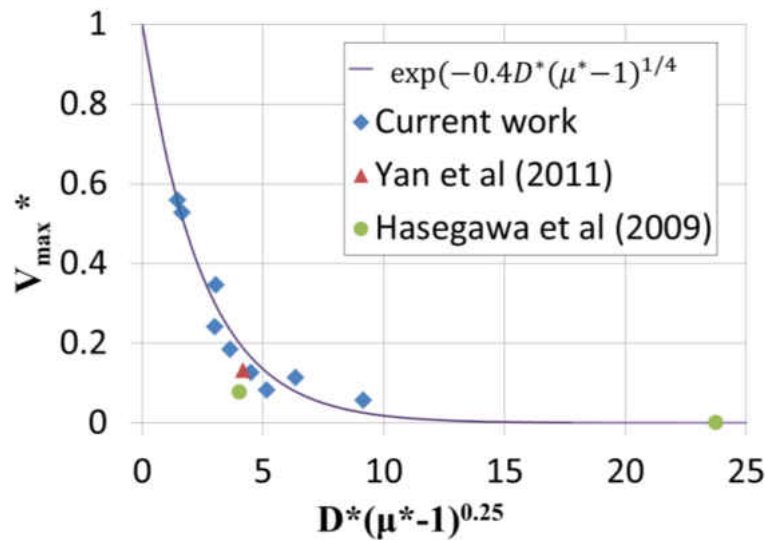
Figure 10: Proposed correlation closely matches with the experimental data from and data from Hasegawa et al. (2009)and Yan et al. (2011)

Our previous work [Saha et al. (2012a)] showed rotation of droplet containing nanosilica suspensions captured through high speed images. Figure 12(a) shows viscosity profiles in terms of particle concentration for nanosilica (10 nm) and nanoalumina (50 nm). From Figure 12(a) we can see that for the same concentration of 3%, nanosilica and nanoalumina have different viscosities of 1.55 and 1.85 cP respectively. In this work, the nanosuspensions are considered to be Newtonian while calculating the viscosity. Any possible non-Newtonian effect was not considered in this correlation. However, it is to be noted that the proposed correlation applies equally to single component fluids (without nanosuspensions). The PIV measurements were principally carried out in pure liquids with analogous viscosity behavior as nanosuspensions. Thus, from the proposed correlation, it can be seen that at this concentration for the same diameter, nanosilica droplet would rotate faster than the nanoalumina droplet. Based on the correlation (Equation 3.9), rotational speed is plotted versus viscosity for a droplet of 450 μm in Figure 12(b). From this figure, we can confirm that for 3% concentration of nanoparticles, the nanosilica droplet rotates at ~9000rpm and nanoalumina rotates at ~6000rpm. The external heating vaporizes the droplet faster and it goes through a structure formation stage. The rotation captured through high speed images shown in Figure 12(c) is for a nanosilica structure when most of the solvent is depleted. The rotation speed is calculated through careful frame by frame investigation of high speed images. As shown in Figure 12(c), the angular displacement of a natural marker on the droplet surface such as surface irregularity, is measured between few frames. In Figure 12(c) this displacement is shown as $(\theta_2-\theta_1)$. Knowing the time interval between those two frames $(t_2 - t_1)$, we can calculate the rotational speed (ω_x) as $(\theta_2-\theta_1)/(t_2 - t_1)$.
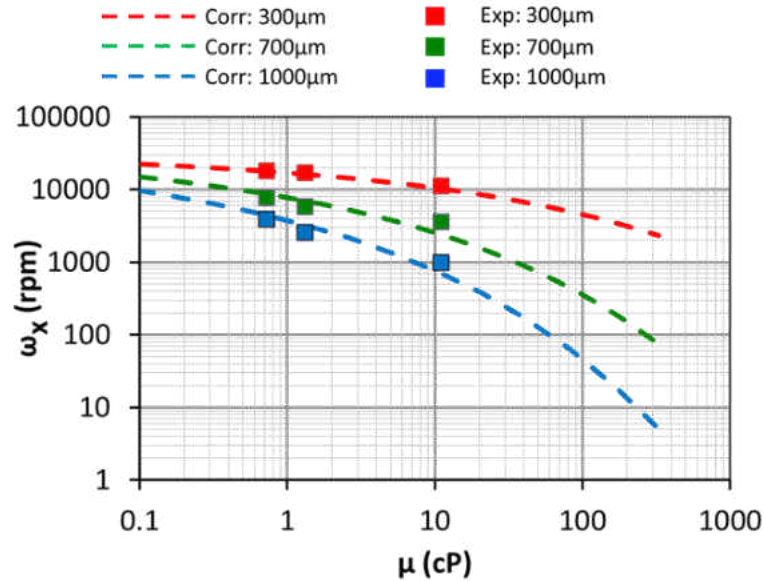
Figure 11: Comparison of rotational speeds (ω_x) from experimental data and from the correlation (Equation 3.9) for three different droplet diameters

This would mean that the nanosilica concentration would have become very high, although there is no other way of measuring viscosity at this stage. Image analysis shows that the measured rotation for this condition for nanosilica is 400-600 rpm. Based on the correlation (Equation 3.9), for the measured range of rotation (400-600 rpm), the viscosity of the colloidal suspension is expected to be very high, and is estimated from Figure 12(b) to be in the range 800-1500 cP. This shows that after structure formation, the droplet is almost devoid of liquid.
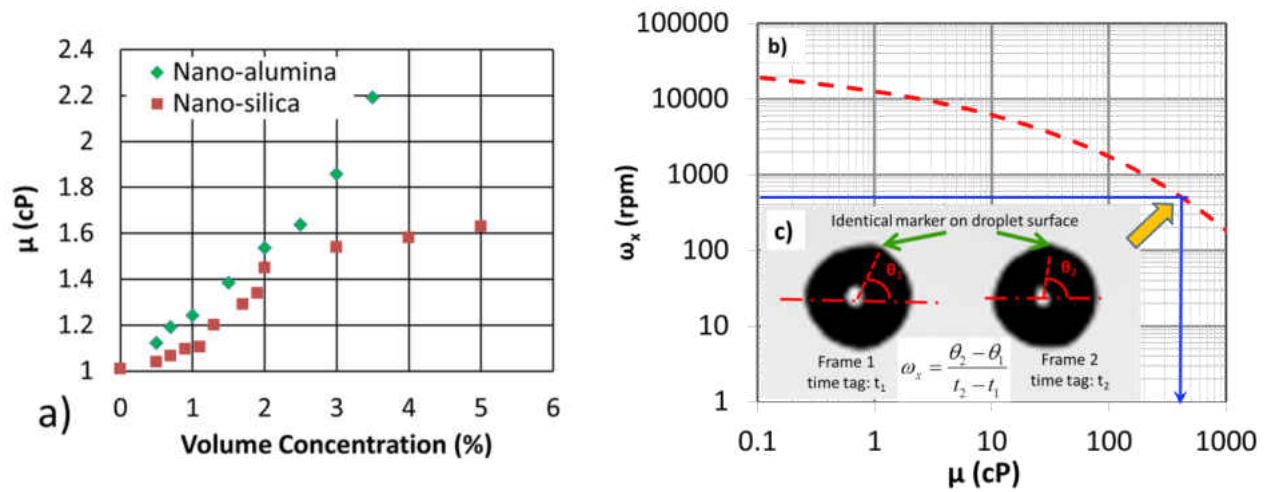
Figure 12: (a) Viscosity of nanosuspensions (nanosilica 10nm and nanoalumina 50nm) at different nanoparticle concentration, (b) Rotational speed (ω_x) for a 450µm droplet as a function of viscosity, (c) High speed images of 3% nanosilica droplet under laser irradiation: snapshots near the liquid depletion point.

3.4 Summary

Internal flow structures in micron-sized droplets are difficult to measure, but are important for the understanding of drying processes of nanoparticle suspensions. Viscosities of nanosuspensions are significantly higher than that of the base fluid, and increase further during vaporization. In this work, using Particle Imaging Velocimetry (PIV), detailed velocity measurements have been made in a levitated droplet of different diameters and viscosity. Different viscosities were so chosen to mimic the fluid motion inside a precursor droplet with suspended nanoparticles. The motion inside the droplet is that of a forced vortex which has also been reported in different levitators in two other papers. Physically based, non-dimensional correlations for maximum velocity and rotation have been obtained which follow not only the current data but also from two other papers which used levitators of different amplitudes and

44

frequencies, and larger drop sizes. The rotational speed of nanosilica droplets at an advanced stage of vaporization observed through high speed images compares well with that predicted by the correlation. These correlations can now be used to predict velocity and rotation *a priori* before performing droplet experiments in a new levitator. These correlations will also be very effective for modeling droplet drying in levitator environment.

CHAPTER FOUR: DROPLET WITH NANOPARTICLES (NANOSILICA)

4.1 Introduction

In this chapter a detailed experimental study on laser heated nanosilica suspended water droplets is presented. This study shows preferential accumulation and agglomeration of suspended nanoparticles during heating process, which eventually forms ring or bowl shaped structures. These suspended nanosilica particles in the droplet do not undergo chemical reaction and phase transition like, cerium nitrate droplet which will be reported later in this dissertation (Chapter 5). In this chapter, the effects of acoustic streaming and internal recirculation on solute migration and agglomeration are delineated through high speed imaging, IR thermography and particle image velocimetry. The details of the phase transitions of the nanosilica droplets (based on morphological and thermo-physical changes) as a function of concentration has also been reported here.

Optical diagnostics in levitated droplet have been reported by very few researchers. Omrane et al. (2004) studied naturally vaporizing droplet in the absence of external heating. They used 3rd and 4th harmonics of an Nd-YAG laser to perform optical measurements on the levitated droplet. They measured the temperature of the vaporizing droplet using Laser Induced Phosphorescence, and measured species concentration simultaneously using Laser Induced Fluorescence. However, owing to longer lifetime of phosphorescence they saw interference with the fluorescence signal. Yarin et al. (1997) used flow visualization technique to map the flow field outside of a droplet suspended in an acoustic levitator. They showed existence of vortex structures enclosing the levitated droplet due to acoustic streaming. Recently, Abe et al. (2007) reported stereo PIV

measurements in a levitated droplet of water and glycerol. They used droplet sizes of around 4 mm. Their study showed the presence of a strong single recirculation cell within the droplet.

Agglomeration of suspended particles is an important field of study in colloid science. Two important phenomena in this field are perikinetics and orthokinetics [Mason (1977)]. Perikinetics is a process of agglomeration of suspended particles due to Brownian rotation and diffusion. On the other hand, orthokinetics is an agglomeration process arising due to shear/velocity gradient within the liquid layers. Mason studied orthokinetics phenomena in a dispersed flow field. He used numerical and experimental approach to understand different orthokinetics effects in rotational and irrotational flow. Bremer et al. (1995) worked on the aggregation time scale of orthokinetics. They estimated time scale of macroscopic aggregation or the time scale when precipitation becomes visible. They also showed that the number of bond formed is as important as aggregation rate for the aggregation process. This led them to define a physical time scale based on orthokinetic sedimentation which does not include arbitrary parameters like visibility of precipitation.

This is an experimental analysis of an acoustically levitated droplet containing nanosilica solutions at different concentrations heated by a CO_2 laser. Laser irradiation of the droplet shows agglomeration of suspended nanoparticles resulting in solid structures. The chapter will analyze the effect of concentration on the shape of final structure using high speed imaging, IR thermography and particle image velocimetry.

4.2 Experimental setup

The basic experimental setup employs an ultrasonic levitator (Tec5 ultrasonic levitator, 100 kHz) to levitate nanosilica suspended water droplets. A 30W tunable CO_2 laser which irradiates at wavelength of 10.6 μm was used to heat the droplet. As shown in Figure 13, a high speed camera (Phantom V12) was placed at an angle of 30^0 with the axis of the laser to image the heating event. To achieve a moderate resolution of 512x512 pixels, the framing rate was kept limited at 5000 fps. A zoom lens assembly (Navitar 6000) was used to achieve high spatial resolution. A goose neck probe light was used to backlight the droplet. The temperature of the droplet was measured using an IR camera sitting perpendicular to the laser axis as shown in Figure 13. The IR camera was operated at 100 fps. An external delay generator was used to synchronize all the cameras with the CO_2 laser. Further details of the experimental setup along with the uncertainties of the techniques are provided in Chapter 2.
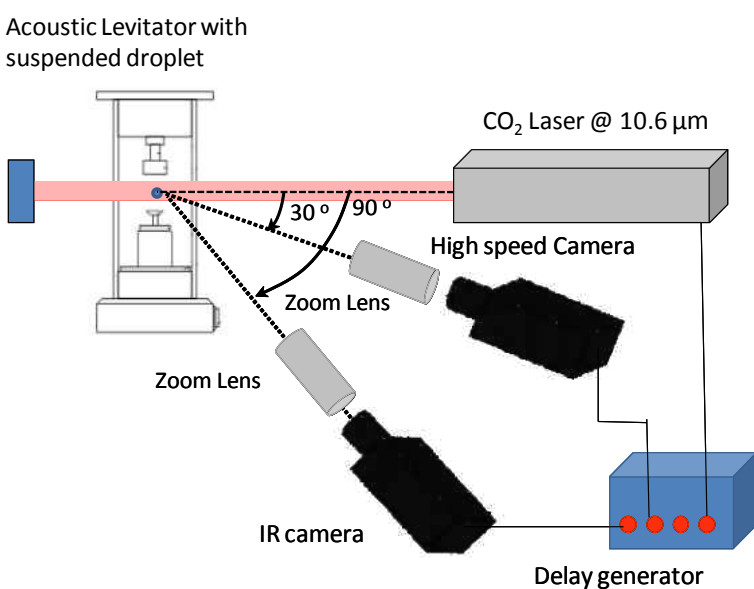
Figure 13: Experimental setup with levitated droplet

The high speed images were analyzed using edge detection technique in Matlab. The edge detection method was employed to calculate an equivalent volume of the droplet which results in an instantaneous equivalent diameter. From these high speed images, the diameter change with time was determined. High speed images were also used to identify morphological changes and reorientation of the structures formed by nanosilica agglomerates.

Most of the diameter and temperature profiles were done with an initial dropsize of 500 (+/-10) μm in diameter. The PIV experiments were done for a dropsize of 700 μm in diameter. Commercially available 15% vol concentrated nanosilica dispersion in water has been used as source. Different concentrations of nanosilica suspended solution were prepared by adding precise amount of DI water in the concentrated solution. This was followed by 15 minutes of sonication to ensure homogenous mixing. In our current work, various concentrations of nanosilica solution were used while maintaining the laser intensity at 0.85 MW/m^2.

4.3 Results and discussions

This section is broadly divided into two parts. The first part of the section discusses the behavior of nanosilica droplets under laser irradiation. Vaporization of the droplet and subsequent formation of bowl and ring time structures is reported here. These phenomena observed during the heating process have been explained in detail using PIV results in last chapter (Chapter 3). The second part of this section presents a mathematical model to predict the bowl formation event in nanosilica droplets. The model connects phenomena like, agglomeration and perikinetics to a density gradient in a vaporizing nanosilica droplet, which results in bowl formation.

4.3.1 Heated droplets

Different concentrations of nanosilica have been used to delineate the effects of nanosilica concentration on the vaporization and agglomeration process. As the nanosilica suspended droplets were heated by the laser and this heating process was recorded by high speed and infrared cameras. It will be shown in this section that depending on concentration, the agglomerated nanoparticles may form two different structures, namely bowl and ring. Analysis of high speed images clearly shows the presence of two distinct stages during vaporization. During the first stage of pure evaporation, solvent (water) vaporizes resulting in a sharp decay in diameter. On the other hand, after initial sharp reduction in diameter, the droplet takes the shape of a bowl with no further change is size. This point is considered to be the initiation of the second stage of structure formation.
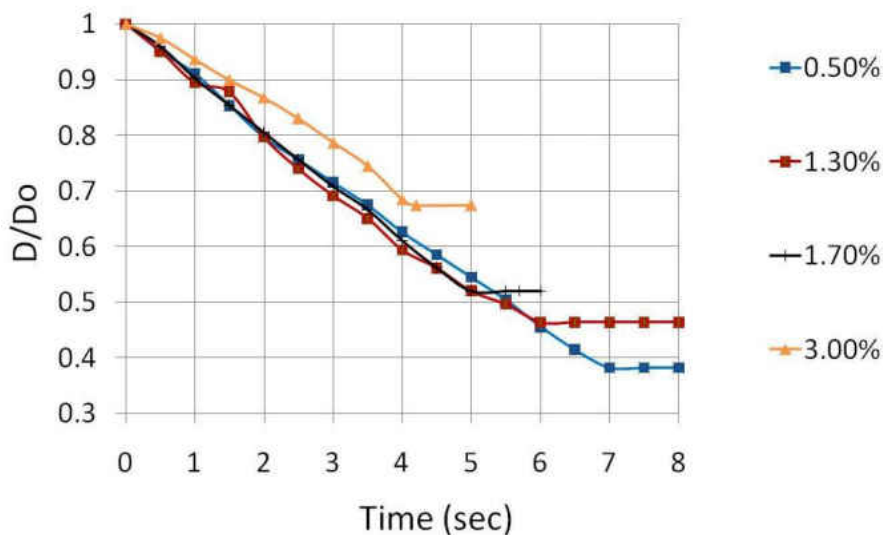
a)
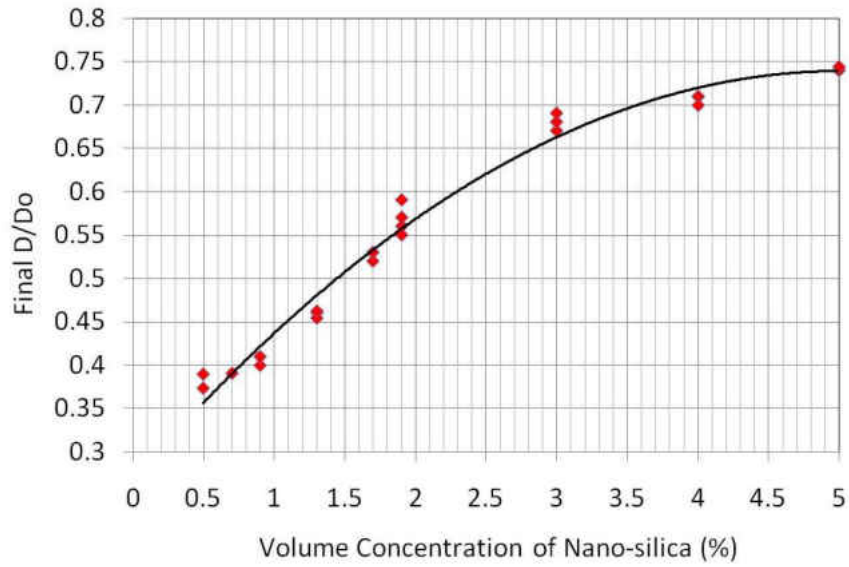
b)

Figure 14: (a) Non-dimensional diameter reduction with time. (D_0=initial diameter 500µm); (b) Non-dimensional diameter at the end of pure evaporation stage
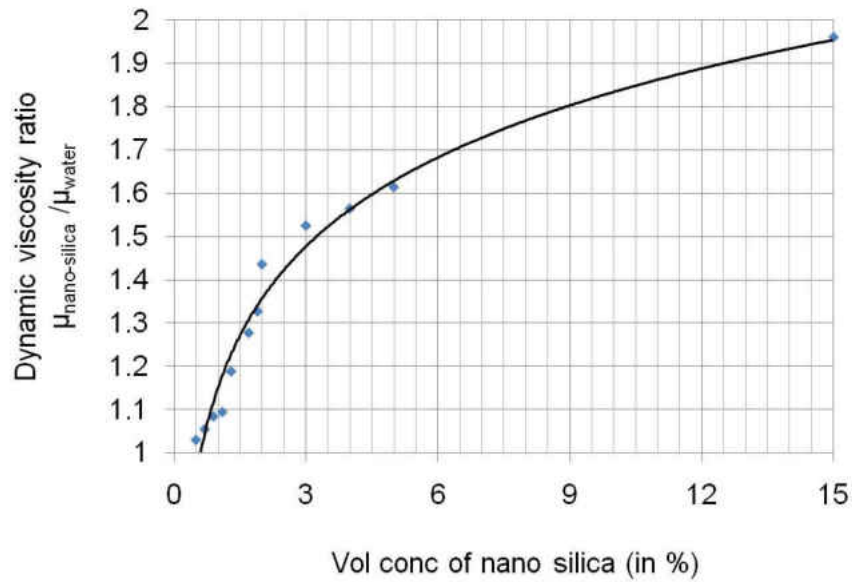
Figure 15: Viscosity of nanosilica suspensions at different concentrations.

Figure 14a shows diameter reduction plot for four different concentrations. It is clear that the time duration of pure evaporation stage gets shorter with increase in concentration. Higher concentration of nanosilica reduces the amount of solvent to be vaporized leading to reduction in vaporization time. Higher solute concentration also results in suppression of vapor pressure according to Raoults' law. This slows down the vaporization rate, reducing the slope with increase in concentration as shown in Figure 14a. As mentioned earlier, an increase in nanosilica concentration increases the viscosity of the solution as seen in Figure 15. As shown in the previous section, the velocity scale of the flow field within the droplet gets reduced with increase in viscosity. Sirignano (1999) showed that mass vaporization rate from a vaporizing droplet depends on Sherwood number and Spalding mass transfer number.

$$\dot{m} = 2\pi\rho_g D_{g\infty} r_s Sh^* \ln(1 + B_M) \tag{4.1}$$

Where, $\dot{m}$ is mass vaporization rate, ρ_g is density of vapor phase, $D_{g\alpha}$ is diffusivity of vapor phase into ambient, r_s is instantaneous radius of the droplet, Sh* is modified Sherwood number and B_M is Spalding mass transfer number. Sh* is a function of Reynolds number (Re) while B_M is a function of solute concentration at the droplet surface. Reynolds number is defined based on the relative velocity of droplet and ambient. Since the acoustic frequency of the levitator remains constant, the flow induced by acoustic streaming around the droplet will remain the same for each concentration of nanosilica. So, the effect of Sherwood number will be negligible as Reynolds number is found be of the order of ~1 for current experimental setup. On the other hand, the scale for B_M is around 10^{-3}. Through semi-empirical correlations prescribed by

Sirignano 1999, it can be seen that if Reynolds number changes by 10%, Sh* will change by 0.1%.

However, B_M is strongly dependent on solute concentration. Sirignano (1999) showed with increase in surface concentration of solute, the value of B_M decreases due to decrease in vapor pressure. Here, it is found that the value of B_M changes from 1.63×10^{-3} to 1.51×10^{-3} if the silica concentration changes from 0.5% to 3%. Due to this, mass vaporization rate also reduces by 7%. This calculation is based on the initial concentration level of nanosilica in the droplet. However with heating, the surface concentration difference between the 0.5 % and 3 % droplet becomes much greater than the initial concentration difference of 2.5 % by volume, leading to further reduction in B_M and mass vaporization rate. So, it can be inferred that the slower vaporization rate for higher concentration of nanosilica is primarily due to decrease in vapor pressure. The increase in viscosity and corresponding reduction in strength of recirculation do not have such a significant effect on vaporization rate.

Figure 14b shows the final diameter at the end of pure evaporation stage. It shows that it increases with concentration owing to less amount of solvent available for vaporization. In addition, the solute concentration buildup near the surface is significantly augmented for high concentration nanosilica droplets. This solute layer near the droplet surface coupled with low mass diffusivity effectively halts any further regression of the droplet. However the solvent continues to vaporize through the porous solute crust.

4.3.1.2 Structure formation stage

At the onset of the stage of structure formation, it is observed that the top half of the droplet collapses to form a bowl structure. Until this point of heating, all the concentrations behave similarly. But further heating shows different phenomena for different concentrations. It was observed that for concentrations less than 1.3%, the droplets form a bowl structure and remains in that form for the rest of the heating cycle. However, for concentrations more than 1.9 %, initial bowl structure goes through a morphological change to form a horizontal ring (axis of the ring vertical). The horizontal ring keeps oscillating about the axis of the levitator (like a pendulum) and at one point of time it reorients itself to form a vertical ring (axis of the ring horizontal). For concentrations between 1.3% and 1.9%, formation of both bowl and ring structures are possible. This range of concentrations is termed as the transition zone. Figure 16 represents this transition phase diagram. This diagram has been prepared based on repeated experiments at different concentrations. The thick solid line (red triangle) represents the time at which pure evaporation ends for different concentrations. The other information captured in Figure 16 is the ring formation time and the reorientation time. The dotted line (solid circle) shows the ring formation time, while the thin solid line (green square) represents the time when the ring reorients to form a vertical ring. It can be observed from the figure that for the same concentration, the reorientation time varies to some extent. This has been explained in the next section. Although the ring formation time has been shown as a line in the figure, but in reality it is a very fuzzy boundary between transformations of the bowl into a horizontal ring. High speed images show that this shape transformation occurs gradually over a period of time. On the other

hand, in cases of evaporation time and ring reorientation time, the boundaries are much less fuzzy as evident from high speed images.
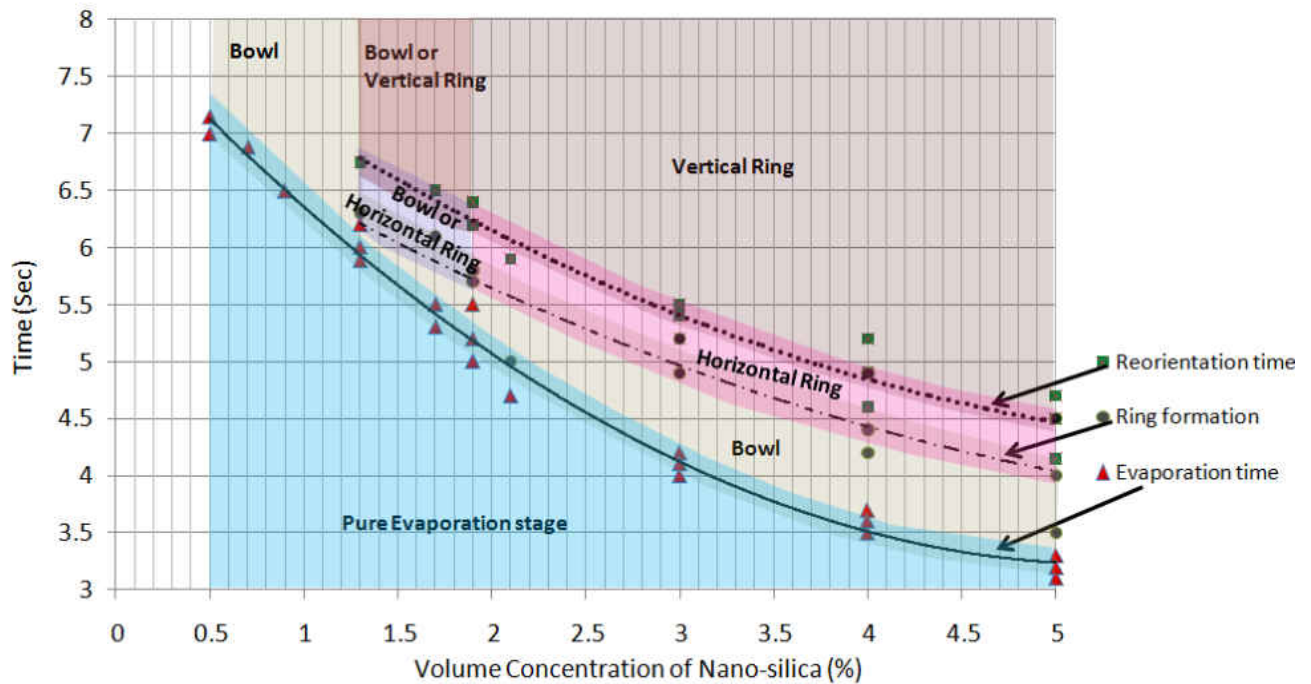
Figure 16: Structural changes in the droplet over time at different solute concentration

Based on the aforementioned observation of ring and bowl formation, Figure 16 has been divided into a number of zones. These zones are indicated with different colors which represents different structures. For a given concentration at a given time instant during the heating cycle, the most probable structure can be predicted using this phase diagram.

4.3.1.2.1 Formation mechanisms of ring and bowl shaped structures
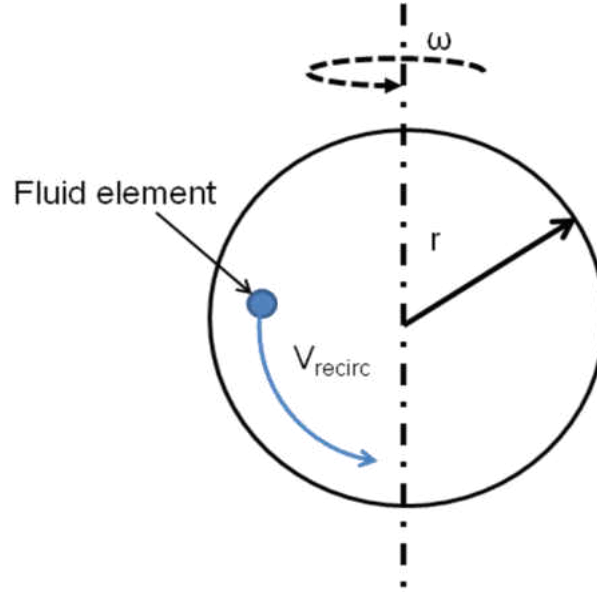
Figure 17: Rotation of the droplet about levitator axis and recirculation velocity acting on a fluid element

Acoustic streaming within the droplet promotes preferential solute migration during the evaporation phase resulting in initial bowl formation. The velocity scale due to Marangoni convection inside the droplet is given by

$$u_M \sim \frac{\alpha}{r} Ma \sim \frac{d\sigma}{dT}(\frac{\Delta T}{\mu_{drop}}).$$

(4.2)

u_M=velocity due to Marangoni flow; a=thermal diffusivity; Ma=Marangoni number; $d\sigma/dT$ is measured in our experiment as -0.2N/m°C. Saha et al. 2010b, Kumar et al. (2010) showed by order of magnitude analysis that Marangoni convection inside the droplets is negligible compared to acoustic streaming velocities. In this work, the author also used PIV results to show the presence of a single cell recirculation zone centered around the droplet center with negligible

Marangoni convection. Although the PIV has been performed in the absence of external heating, the flow pattern will remain similar as Marangoni effects are negligible.

To understand the bowl and ring formation mechanisms, a time scale τ_{recirc} can be defined, which is the time needed for a fluid element to reach the bottom of the droplet from the equator as shown in Figure 17. If one defines the recirculation velocity to be V_{recirc}, the time scale is

$$\tau_{recirc} \approx \frac{r}{V_{recirc}} \tag{4.3}$$

On the other hand, due to rotation about the vertical axis of the droplet, there would be a dominant centrifugal force which would try to carry the fluid element towards the outer periphery of the droplet near the equator. If one defines the rotation speed to be ω, then the time scale for carrying the droplet towards the periphery of the droplet, $\tau_{centrifugal}$ can be defined as,

$$\tau_{centrifugal} \approx \frac{1}{\omega} \tag{4.4}$$

It can be argued that whether a bowl or ring structure is formed depends on which time scale is dominant. To form a bowl structure, the τ_{recirc} has to be smaller than $\tau_{centrifugal}$ resulting in faster accumulation of particles at the bottom of the droplet. On the other hand if τ_{recirc} is higher than $\tau_{centrifugal}$ then the particles would accumulate around the periphery of the droplet near the equatorial plane creating a horizontal ring. Thus, the criterion for bowl and ring formation may be written as follows,

$$\frac{r}{V_{recirc}} < \frac{1}{\omega} \ (bowl)$$

$$\frac{r}{V_{recirc}} > \frac{1}{\omega} \ (ring) \tag{4.5}$$

High speed images confirm that the rotational speed ω is similar for initial stages of the heating when the solvent content is substantial. PIV results show that V_{recirc} decreases with increase in viscosity. Figure 15 confirms that the initial viscosity of the solution increases with increase in nanosilica concentration.

As a first order estimate, the decrease in recirculation velocity (from 236 mm/sec to 189 mm/sec) is about 50 mm/sec for a 1.8 times increase in viscosity. Viscosity ratio of 1.8 corresponds to that when solute concentration of nanosilica is increased from 0.5 to 5 %volume. The corresponding increase in τ_{recirc} can be calculated as $\tau_{recirc, \ 5 \%}/ \ \tau_{recirc, \ 0.5\%} = 1.25$, which implies a 25 % increase in the timescale for recirculation. Assuming that the centrifugal timescale governed by the rotation of the droplet about the levitator axis is constant across all concentrations, the implication is that the propensity of droplets to form ring shaped structures increases with concentration. However, the exact cross-over from bowl to ring shaped is very hard to pinpoint as there exists a fuzzy boundary between 1.3 % and 1.9 % concentration droplets. However, concentrations more than 1.9% always results in ring formation and concentrations less than 1.3% shows repeated bowl formations. It should be noted that the initial structure in all droplets is a bowl, and a ring only forms for the higher concentration values. The phase diagram also confirms this observation. It is also possible that the recirculation which is initially strong gets diminished (as the solvent vaporizes thus increasing the concentration with time) due to increase in viscosity and onset of

perikinetic or orthokinetic aggregation. It may also be argued that during the initial formative stages, the strong recirculation present for all concentrations (0.5 to 5 %) lead to a generic bowl shaped structure. It is only later that weakening of recirculation (due to combined viscosity increase and solute aggregation) especially at higher concentrations leads to a ring formation as per Equation 4.5. Interestingly, high speed images suggest that rotational speed remains almost a constant during the entire cycle of bowl formation and bowl to ring transition. This confirms that an increase in τ_{recirc} makes the centrifugal effect relatively more dominant leading to solute migration in the equatorial plane forming ring shaped structures.

4.3.1.2.2 Reorientation of ring shaped structure

It is important to mention here that the rotation around the axis of the levitator still persists even after the formation of ring. The non-uniform accumulation of solute around the periphery of the ring leads to an imbalance in the pressure force around the ring circumference causing the ring to oscillate back and forth in the vertical plane. As shown in stage 1 of Figure 18, F_z, the acoustic force in z direction balances W, the weight of the ring. The radial forces cause the oscillation about the axis of the levitator. It was shown by Lierke and Holitzner (2008) that the radial direction acoustic force,

$$F_r(r,z) \approx -\frac{k_r}{2}\sin(k_r r)\cos(2k_z z)$$ (4.6)

where r and z are distances from the levitator axis and antinode respectively. Parameters k_r and k_z depend on acoustic frequency and are constant. The sinusoidal nature of the force at a fixed 'z' explains the oscillatory motion of the levitator about the levitator axis.
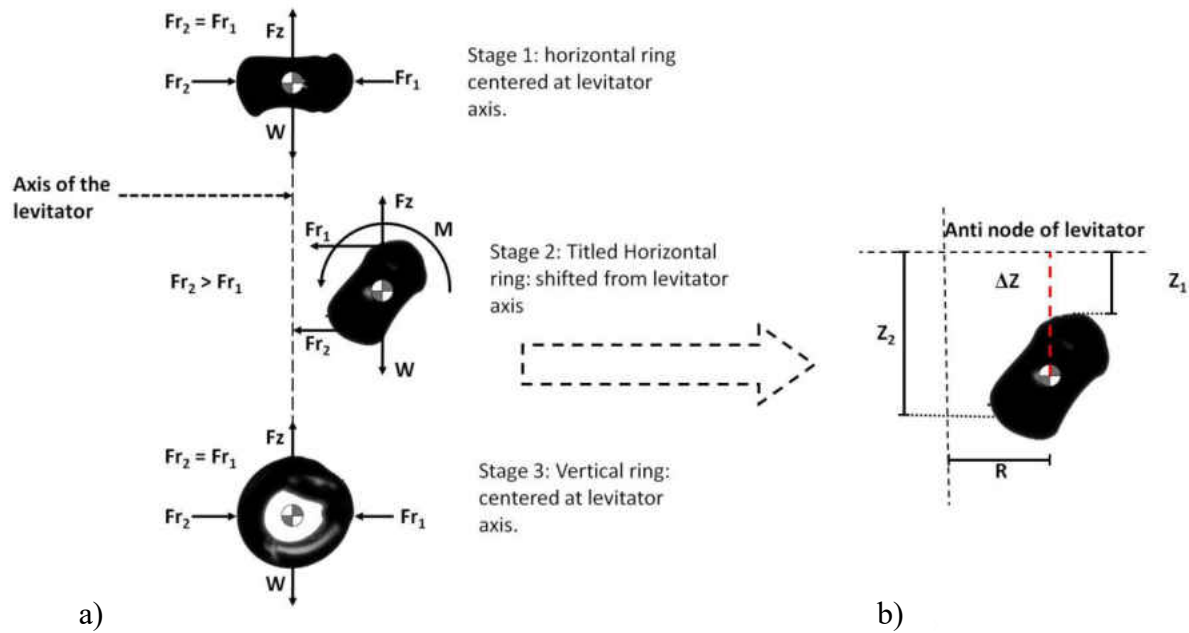
Figure 18: Different stages of ring reorientation for 3% nanosilica concentration

However it so happens that the ring reaches a point far enough from the levitator axis where the acoustic field imposes an unbalanced turning moment causing it to reorient from a horizontal position to a vertical position. Different stages of this reorientation are shown in Figure 18. Just before the reorientation, the oscillating ring becomes tilted. This is shown as stage 2 in Figure 18. This inclination results from the combined effect of oscillation about the levitator axis and rotation about its own axis. Once the ring is tilted the forces are highly imbalanced. The free body diagram at this instant has been shown in Figure 18. The vertical force F_z still balances the weight of the ring, W. The two radial forces, F_{r1} and F_{r2} act at the outer and inner edge of the ring respectively. At this point it is worth mentioning that the levitated object under gravity shows a finite amount of shift from the antinode. This has been reported by Rednikov 2006 and Lierke and Holitzner 2008. Assuming Δz is the shift of the center of gravity of the ring from the antinode, at the inclined position two extremes of the ring will be at different 'z' location as

60

shown in Figure 18b. Considering Z_1 and Z_2 as the distances of outer and inner extreme distances of the ring from the plane of antinode, one can see $Z_1 < Z_2$.

From equation 4.6, one can write

$$F_{r1} \approx -\frac{k_r}{2}\sin(k_r r)\cos(2k_z Z_1)$$
$$F_{r2} \approx -\frac{k_r}{2}\sin(k_r r)\cos(2k_z Z_2)$$

(4.7)

Now $Z_1 < Z_2$ implies that $Fr_1 > Fr_2$. This creates a moment M around the center of gravity of the ring resulting in reorientation. Once reoriented in the vertical plane, the ring returns to the axis of the levitator as shown as stage 3 in Figure 18. The vertical ring now starts rotating due to acoustic streaming about the axis of the levitator.

Bowl shaped structures do not experience this reorientation. Figure 16 shows the ring re-orientation time for different concentrations. It is worth noting that the reorientation has been observed for all the cases of ring formation. However, the reorientation phenomenon being a result of instability caused by asymmetry of the ring structure, time instant for this orientation does not follow a particular trend. That is the reason wide variations of reorientation time can be observed between different experiments at the same concentration.
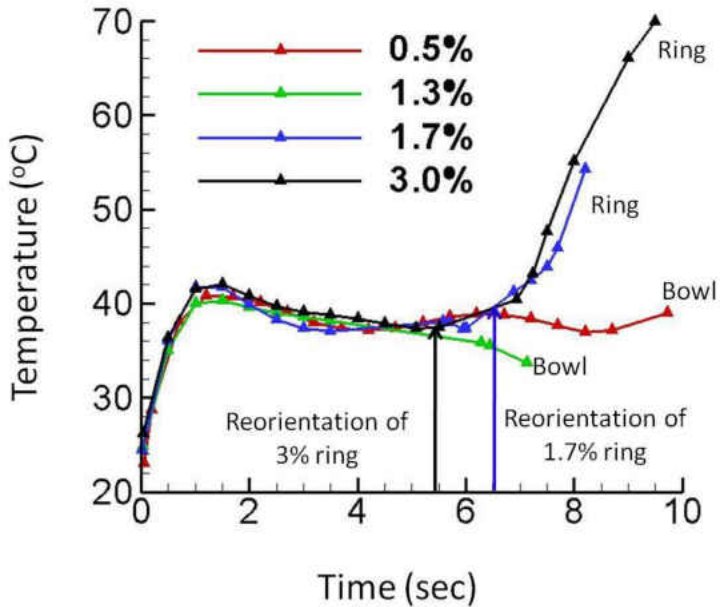
Figure 19: Average temperature during the heating cycle for various nanosilica concentrations

Analysis of IR images shows a very similar trend for temperature history for all concentrations. Figure 19 shows temperature profile for four different concentrations of nanosilica. At the onset of heating the average temperature of droplet surface sharply rises from room temperature and attains a maximum value around 40-42°C. Afterwards the average surface temperature starts decreasing at a very slow rate until most of the solvent vaporizes. This behavior can be explained by comparing the latent heat and sensible heat budgets. At the beginning of the heating process, the droplet surface temperature is low resulting in slower vaporization rate. Thus the droplet needs a small amount of latent heat. The sensible heat being higher, the temperature rises very fast. However, with increase in temperature, vaporization rate also increases, thus the latent heat requirement increases. At some point, all the heat absorbed through laser irradiation is used for

latent heat in vaporizing the droplet. From this point onwards, latent heat dominates sensible heat resulting in a slight decrease of droplet average temperature.

In cases of ring formation, it was observed that the temperature again rises very sharply after the reorientation of the ring as shown in Figure 19. It can be explained from the point of view of area exposed to laser irradiation. As long the ring remains horizontal the surface area which is being irradiated remains constant. However, after reorientation, the surface area absorbing the laser increases. This, in turn, increases the amount of heat transfer into the ring structure. At this point the structure does not contain any solvent to vaporize, thus the entire amount of absorbed heat helps to increase the temperature of the structure resulting in a sharp rise in surface temperature.

After ring reorientation, the structure keeps rotating about the levitator axis. However, it is observed that the rotational speed initially stays slow immediately after reorientation and gradually increases. This change in speed also has an effect on temperature rise. It can be argued that the rotational speed dictates average duration of exposure of any point on the surface to laser irradiation. Faster the rotation, longer is the average exposure duration and hence faster is the temperature rise.
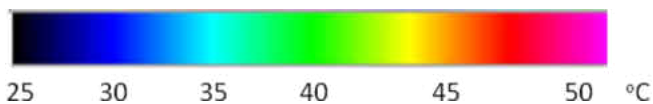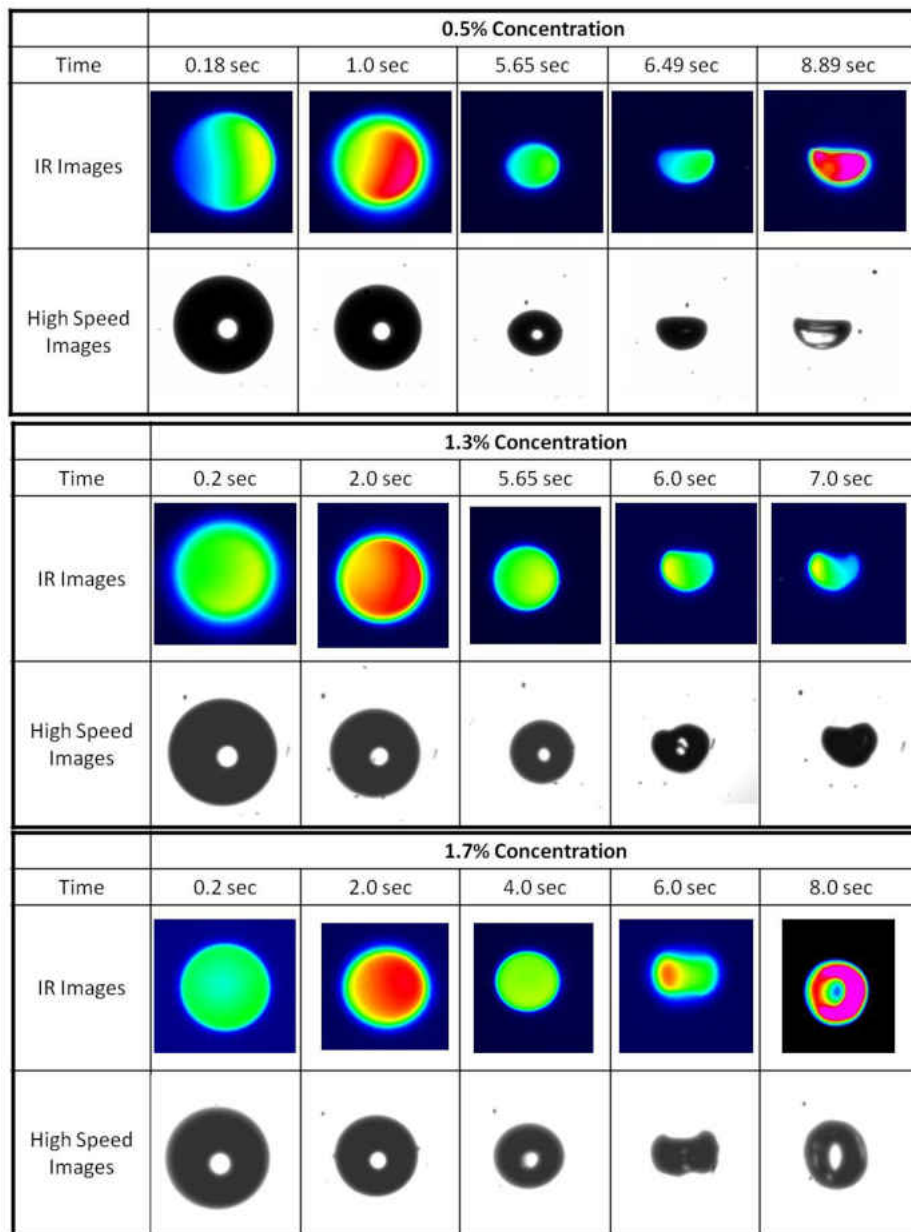
Figure 20: Infrared camera and high speed camera images at different time instants of the heating cycle for various nanosilica concentrations.

For the 3% concentration reported in Figure 19, the reorientation occurs after 5.5 sec as shown also in Figure 16. The average temperature of the droplet at this instant is 38°C. From high speed images it was evident that immediately after reorientation, the rotation about the levitator axis is slower. For this particular case, the average rotational speed immediately after reorientation was found to be 1.2 rps. However, high speed images show that after 7.1 sec the vertical ring starts rotating faster with an average speed of 9 rps. The temperature plots show a sharp change in slope at 7.2 sec. The temperature after 7.2 secs with slow rotation is 41.5°C. With increase in rotation speed to 9 rps, the temperature rises to 70°C in approximately 2 secs. It shows that the rate of temperature rise is 1.67°C/sec during slow rotation, and 15.83°C/sec during faster rotation. So, it shows that a 7.5 times increase in rotational speed causes a 9.5 times increase in the rate of temperature rise, suggesting that the rate in temperature increase is probably proportional to the rotational speed about the levitator axis.

$$\frac{dT}{dt} \sim \omega \qquad (4.8)$$

Figure 20 shows sample IR and high speed images at different time instants during the heating phase for different concentration levels. The initial stage of pure evaporation is marked by a sharp decrease in diameter before reaching a constant value. This stage is dominated by internal recirculation rising from acoustic streaming. At this stage, the droplet takes the shape of a bowl with collapsed top half. The next stage of structure formation is dominated by orthokinetic aggregation or agglomeration of particles. Due to increase in viscosity coupled with weaker recirculation, higher concentration of nanosilica (more than 1.9%) solution shows morphological transformation to form a horizontal ring, which eventually reorients itself to become a spinning

vertical ring. However, lower concentrations (less than 1.3%) do not show such a transformation and remains in bowl shape for rest of the heating cycle.

4.3.2 Theoretical analysis to connect bowl formation with perikinetics

After an initial pure vaporization regime, the droplet transforms into a bowl-shaped structure which is a generic morphology for levitated droplets, and is common regardless of the chemical composition and properties of the binary liquid system. It was observed that $Ce(NO_3)_3$ and NaCl solutions also form bowl-shaped structures as shown in Figure 21a. The only difference between these different binary liquid systems is the time scale at which the structure turns into a bowl. The physics governing the bowl formation is specific to the type of binary liquid system but the precursor events which facilitate bowl formation by creating density stratification (such as the recirculation velocity induced by acoustic streaming inside the droplets) are universal for any binary liquid system. This density stratification leads to bowl formation by collapsing the top sector of the droplet due to an imbalance in force between the top and bottom sectors of the droplet. In short, the local force imbalance is due to density stratification, caused by preferential migration of nanoparticles. The high-speed images were analyzed using an edge detection method to calculate an equivalent volume of the droplet, to obtain the instantaneous diameter. The flow was mapped inside the droplet using particle image velocimetry (PIV) with a 65 μm thick laser sheet as reported in Chapter 3. It has been shown that nanoparticle concentration increases the viscosity of the solution [Vassallo et al (2004); Milanova and Kumar (2005), (2008); Saha et al. (2012a)]. Saha et al. (2012a) showed that the viscosity normalized by the viscosity of water increases by 60% for a 5% increase in nanosilica concentration. However, the surface tension remains almost constant. To examine the effect of the increase in concentration

(which results in change in viscosity) on the recirculation strength within the droplet, PIV was performed on droplets of different liquids having a wide variation in viscosity. The author used pure water, cerium nitrate and glycerol–water solution (all without nanoparticles) with corresponding normalized viscosities of 1, 1.8 and 15 (normalized by viscosity of water). These images that recirculation resembles a forced vortex, with velocity diminishing with increase in viscosity (Figure 21b). Similar results are expected for nanosilica droplets as well at increasing concentrations. It is important to mention here that a thin layer of nanosilica forms in the droplet periphery while the droplet is heated, and will significantly alter this single-cell recirculation. So the PIV measurements are in essence the initial flow vectors when the droplet is placed in the levitator. As time progresses with laser heating, the flow pattern is altered and there occurs a preferential accumulation of particles at the bottom to create the density gradient. Saha et al. (2012a) reported the temperature history of the nanofluid droplet drying. The surface temperature of the nanosilica droplets increases from room temperature to 40–45°C for the laser heat flux of 0:85 MW/m^2. Within this temperature range, the viscosity of water (also the nanosilica suspension) changes by 10–20%, compared with other liquids (especially oils) where this change can be of the order of 60–70%. It was also observed that the surface temperature for all nanosilica concentrations follows a similar trend.
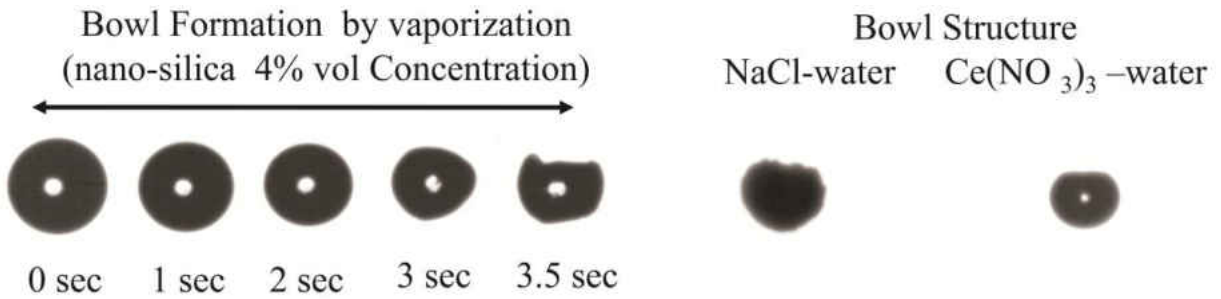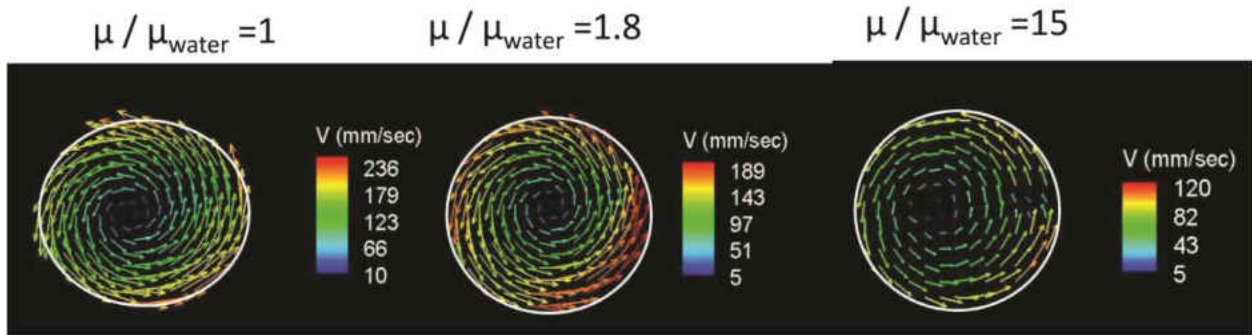
Figure 21: (a) High speed images showing bowl formation in nanosilica, NaCl and Ce(NO₃)₃. (b) Velocity vectors illustrating internal recirculation inside levitated droplets at different viscosities.

In the following sections, the droplet location within the pressure field and the actual pressure distribution around the droplet will be calculated. From the force differential between two sectors of the droplet at different particle concentration, a criterion for bowl formation will be established. Finally, a theoretical calculation will be done with experimental validation to show that the bowl formation time scale is actually connected to perikinetics of the colloidal solution.

4.3.2.1 Global displacement of the droplet due to vaporization

Globally, the droplet weight is balanced by the acoustic forces around the surface of the droplet. However, accumulation of particles at the bottom of the droplet will create an inhomogeneity in weight distribution resulting in unbalanced local forces. To calculate this force imbalance, the droplet location within the pressure field is determined. As the pressure field is perfectly symmetrical around the pressure nodes of the levitator under microgravity, the droplet resides at one of the pressure nodes in the standing wave of the levitator. However, under gravity, the acoustic force needs to balance the weight of the droplet in order to achieve successful levitation, and the droplet shifts downward from the pressure node. This shift in droplet location, Z_{cg}, can be calculated at different time instants for a vaporizing levitated droplet (under laser irradiation) by incorporating the effect of droplet deformation, acoustic scattering into the calculation of displacement of the droplet from the pressure node [Lierke (2002)]:

$$Z_{cg} = \frac{\lambda_z}{8} \frac{\arctan(1/\eta_s)}{\pi/2}$$

(4.9)

where η_s is the levitator safety factor and λ_z is the wavelength of the levitator. One can also write:

$$Ba.\eta_s \approx 8.7 \frac{f_2(A,c,q)}{A(1+1.4A^2)} \frac{c-1}{2c+1}$$

(4.10)

where $Ba = \frac{\rho_s}{\sigma_s} \frac{g_0}{k_0{}^2}$ is the acoustic Bond number, ρ_s and μ_s are the density and surface tension of the liquid sample, g_0 is gravitational acceleration, k_0 is the wavenumber of the acoustic wave and

q= k_r/k_z. Here, A=k_0r_0, c is the aspect ratio and r_0 is the radius of the droplet. Here, the effect of the aspect ratio on the sound pressure level (SPL) has not been accounted for in this and is assumed to be constant. It has been observed through high-speed video that the change in the aspect ratio until bowl formation time is not very significant (1.1<c<1.4). Results reported by Yarin et al. (1998) also show that the aforementioned variation in aspect ratio will result in a change in SPL by less than 1 dB for a droplet 1 mm in diameter. So, for the current experiments involving 500 μm droplets, this change would be even smaller. Thus, the assumption of constant SPL is valid. According to Maidanik (1957), the secondary force generated from scattering of the acoustic waves can be calculated by multiplying the acoustic power density with differences between forward and backward scattering cross-sections of the droplet. Lierke (2002) incorporated the effect of shape and scattering in defining the factor f_2 (A, c, q). Experimental droplet diameter (D=$2r_0$) and aspect ratio (c) were calculated at each time instant from the high-speed images. For a droplet that is ellipsoidal in shape, the volume is calculated using the formula, volume $= (4/3)\pi(a^2b)$, where 2a is the length of the horizontal axis and 2b is the length of the vertical axis of the ellipsoid. Instantaneous density of the droplet was determined based on the assumption that the size reduction of the droplet was solely due to vaporization of solvent (water). These calculations and image processing also assume that the droplet is always axisymmetric. The author has cross-checked this assumption by viewing the droplet at an angle of ~30° with the horizontal axis.

Instantaneous diameter, density and aspect ratio were used to calculate Z_{cg} from equations (4.9) and (4.10). This shift from the pressure node for four concentrations of nanosilica is calculated until the bowl formation time (Figure 22a). Frame-by-frame analysis provides the time range at

which the top half of the droplet collapses and takes the shape of a bowl. This is termed as the bowl formation time. The top half collapses through 300–400 frames approximately, which are recorded at a rate of 3000 frames per sec. Thus, the uncertainty of this bowl formation time is roughly +/-0.05 sec.

a)

b)

c)
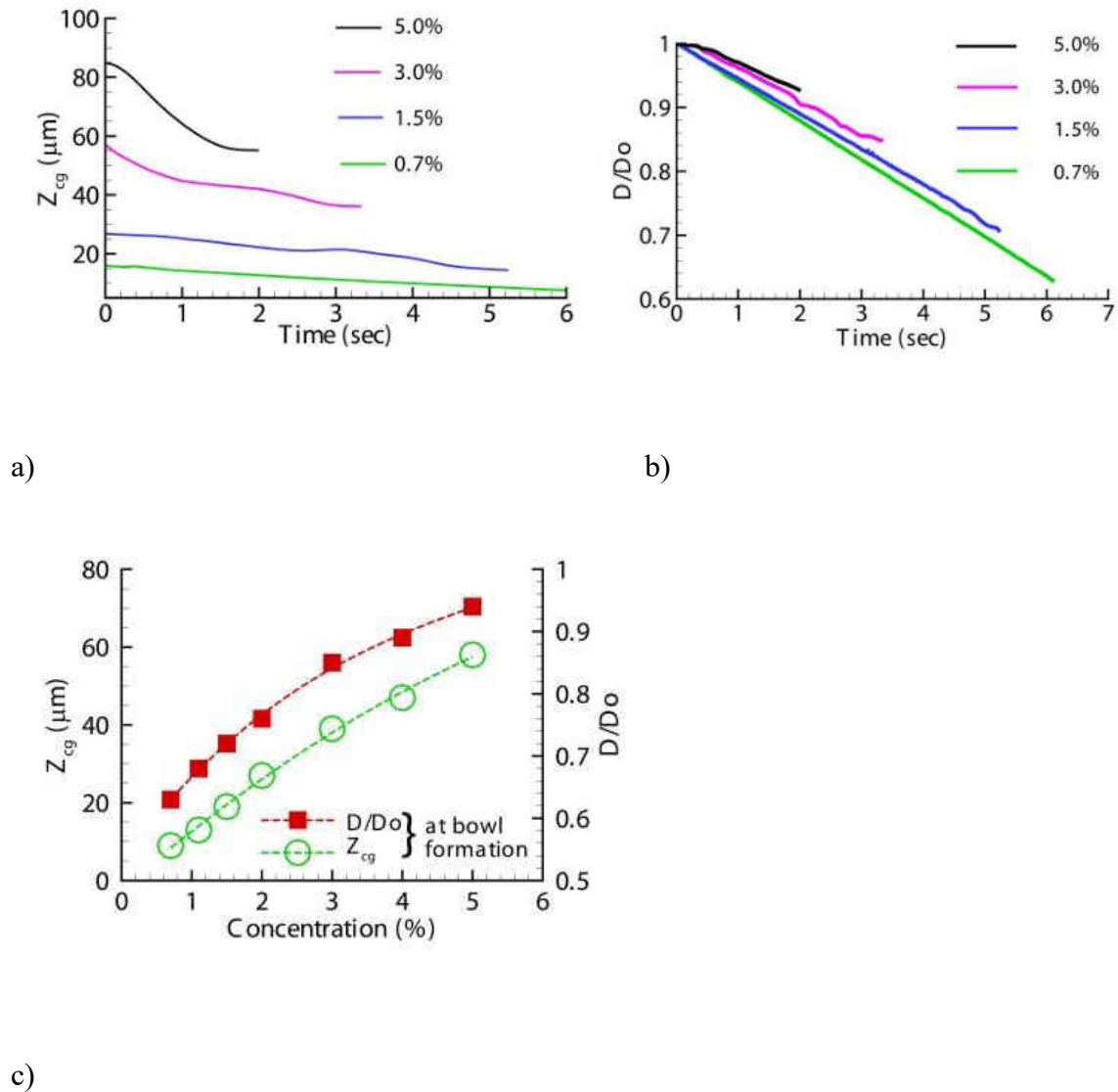
Figure 22: Change in (a) Location (Z_{cg}) and (b) Diameter during heating of 500 µm nanosilica droplet at different concentrations. (c) Final Diameter and droplet location at the bowl formation instances for different concentrations.

The acoustic force increases away from the pressure node. Therefore, with increase in initial concentration, the droplet becomes heavier, resulting in increased downward shift to counteract higher gravitational force. The change in Z_{cg} with time is dependent on the vaporization rate and aspect ratio. Our measurement shows that surface tension remains almost constant, and the droplet aspect ratio does not change drastically during the vaporization process. With the increase in solute concentration near the surface (as well as due to thin porous flake formation), a combination of Raoult's law and formation of porous crust makes the vaporization rate decrease significantly (Figure 22b). Yarin et al. (2002) also reported similar effects with micrometer-sized glass beads. The droplet with lower initial concentration takes longer to form a bowl. The droplet with higher initial concentration exhibits lower reduction in size resulting in a comparatively heavier droplet during bowl formation. Consequently, the shift in the center of gravity, Z_{cg}, is higher towards the end of the vaporization process (Figure 22a). Experiments were performed for a wider range of concentrations yielding similar results in center of gravity shift which are plotted in Figure 22(c) along with diameter at bowl formation.

4.3.2.2 Flow-induced density stratification

As seen in Figure 21(b), vortex strength decreases with the increase in nanosilica concentration. This flow structure is different than the toroidal vortices reported in the analytical results of Rednikov et al. (2006). The droplet in the levitator was observed to oscillate in the directions parallel and perpendicular to the levitator axis. Trinh & Wang (1982) also reported this kind of oscillation which led to the rotation of the droplet about the horizontal axis. PIV results in Figure 21(b) also display a single-cell vortex structure resembling a solid body rotation. Saha et al. (2012a) argued that this oscillation occurs due to possible misalignment or perturbations of

droplet axis with the levitator axis, inhomogeneity in the droplet composition and asymmetric heating. When the droplet oscillation reaches a critical value, the droplet starts rotating about its horizontal axis. This leads to a solid body rotation of the droplet, which can be observed as a single-cell circulation in the center plane. However, when the thin layer forms due to perikinetic agglomeration, the droplet is shielded from acoustic streaming and the velocity field or recirculation inside the droplet starts decaying rapidly. The velocity field now is no longer symmetric and becomes weaker in magnitude. This asymmetric velocity field enables the particles to settle to the bottom and increases agglomeration. The migration of particles due to this convective flow results in a density gradient within a very small time instant inside the droplet. To analyze this gradient, the author defines an interface inside the droplet which will be considered as the boundary between the low and high concentration zones within the droplet. Although local density will continuously vary azimuthally from the north to the south pole of the droplet, for simplified analytical description, the authors assume a discrete jump in density across a fixed chord within the droplet. This is a reasonable assumption since for a particular initial concentration, the top sector of the droplet always collapses along a fixed chord yielding a bowl structure (Figure 23a). Location of this chord/interface is a function of the initial concentration and is constant across all experimental runs. Therefore, one may consider this location as a line demarcating the boundary between high and low concentration (density) zones within the droplet. An angle, ϕ, can be defined to denote the location of this chord with respect to the horizontal diameter/axis as shown in Figure 23(a). It is assumed that the migration of particles due to recirculation (Figure 21b) from the top sector to the bottom sector of the droplet results in a density stratification across the chord located at ϕ from the horizontal diameter

73

(Figure 23a). The density in the upper sector is less as it contains fewer nanoparticles. The density ratio ($\rho*$) between these two sectors starts from unity and reduces with time as more particles migrate towards the bottom sector due to recirculation.

a)   b)
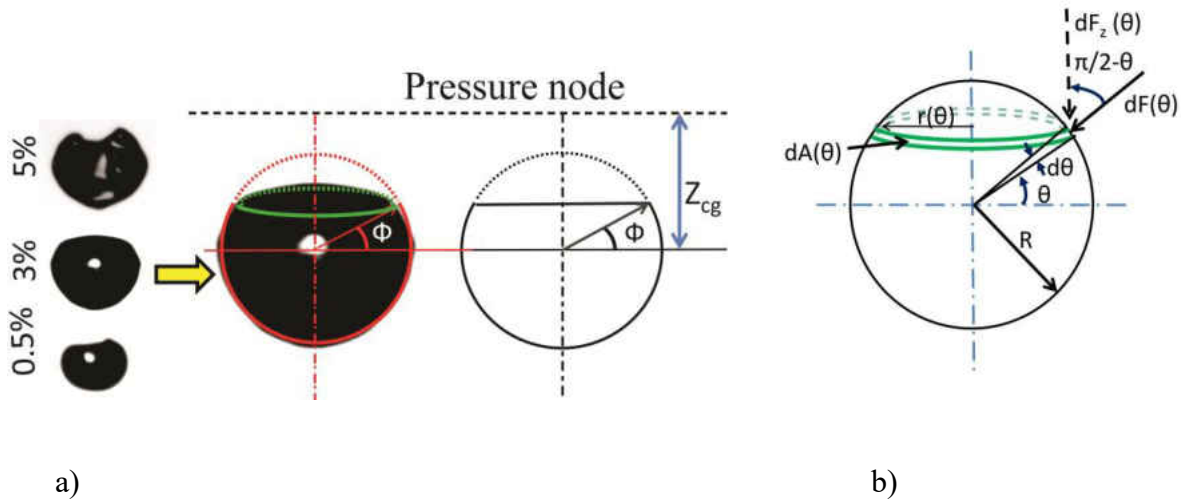
Figure 23: (a) Sample bowls for different concentrations with the definition of angle ϕ to locate density stratification. (b) Schematic of a levitated droplet showing the direction and orientation of acoustic forces.

4.3.2.3 Force distribution due to density stratification

The total force on a levitated droplet can be expressed as $F_{total} = F_a + W + F_s$, where W is the weight, F_a is the total acoustic force and F_s is the force due to surface tension at the interface. The force due to surface tension at the interface will be equal and opposite for the two sectors.

The forces acting on the top and bottom sectors, $F_{total-t}$ and $F_{total-b}$ are calculated using the following procedure. Weight of the droplet sectors (W) will be different for each sector, as vaporization progresses with time. The total acoustic forces can be calculated by integrating the acoustic pressure around the surface for each sector. Time-averaged pressure distribution in the acoustic levitator is [Barmatz & Collas (1985), Lierke (2002)]

74

$$p_a = \frac{p_{in}^{\;2}}{2\rho_0 c_0^{\;2}} - \frac{\rho_0}{2} v_{in}^{\;2}$$

(4.11)

where p_{in} and v_{in} are the acoustic pressure and velocity and ρ_0 and c_0 are gas phase density and sonic velocity. The acoustic radiation pressure and velocity can be written as [Lierke (2002)],

$p_{in} = P_{max}\left[\sin(k_z.z).J_0(k_r.r)\right]$, $v_{in} = V_{max}\left[\cos(k_z.z).J_0(k_r.r)\right]$ and $P_{max} = \rho_o c_o^{\;2}\frac{V_{max}}{c_o} = P_0\gamma_0 Ma$. From these expressions,

$$p_a = -\frac{P_0\gamma_0 Ma}{2\rho_0 c_0^{\;2}}\left[\cos(2k_z.z).J_0(k_r.r)^2\right]$$

(4.12)

where J_0 is the zeroth-order Bessel function of the first kind, Ma is acoustic Mach number (Ma= v_{max}/c_0), P_0 is ambient pressure, γ_0 is the ratio of the specific heats, r and z are the radial and axial distances measured from the pressure node and k_r and k_z are radial and axial wavenumbers, respectively. They are related to total wavenumber (k_0) by $k_0^2 = k_r^2 + k_z^2$. Considering a droplet suspended by acoustic levitation, Equation (4.12) gives the pressure distribution around the droplet. The net acoustic force acting on the droplet can be evaluated by integrating over the surface. Figure 23(b) shows a schematic of a droplet with the acoustic force acting around the surface. For a droplet of radius R, the acoustic force on the elementary area dA, can be calculated as $dF(\theta) = p_a dA$, where $dA = 2\pi r(\theta)Rd\theta$. From Equation (4.12), the pressure term, p_a, is a function of r and z measured from the levitator pressure node. If the droplet shifts by Z_{cg}, then $z(\theta) = Z_{cg} - R\sin\theta$. Since the z-component of this acoustic force is of interest, the force acting on the surface is

$$dF_z(\theta) = -\frac{P_0\gamma_0 Ma}{2\rho_0 c_0^2}\left[\cos(2k_z.z).J_0(k_r.r)^2\right]\pi.R^2.\sin 2\theta.d\theta$$

(4.13)

To calculate the acoustic forces, $F_{total-t}$ and $F_{total-b}$ around the droplet surface for the top and bottom sectors, Equation (4.13) is integrated and following Figure 23(a), the complete expressions for the acoustic forces for the two sectors are $dF_{a-t}(\phi) = \int_\phi^{\pi/2} dF_z(\theta)$ and

$dF_{a-b}(\phi) = \int_{-\pi/2}^\phi dF_z(\theta)$. The weights of the top and bottom sectors are,

$$W_t(\phi) = \frac{2\pi\rho_t R^3}{3}(1-\sin\phi)g \quad W_b(\phi) = \frac{2\pi\rho_b R^3}{3}(1+\sin\phi)g$$
and

(4.14)

Here,

$$\rho_b(\phi) = \frac{2\rho_{total}}{[(1-\rho^*)\sin\phi + (1+\rho^*)]} \quad \text{and} \quad \rho^* = \rho_t/\rho_b$$

(4.15)

and ρ_{total}, ρ_t, ρ_b are densities of the total droplet, top and bottom sectors, respectively. The z component of the surface tension at the interface is F_s. Here F_s will be equal and opposite in direction at the interface of the top and bottom sector of the droplet. The total downward forces in the top sector of the droplet, $F_{total-t}$, and the total upward force in the bottom sector, $F_{total-b}$, are thus calculated.

It is evident that these forces are dependent on the total density of the droplet (ρ_{total}), density ratio (ρ^*) and location of the chord (ϕ) across which the density stratification occurs. The time at which bowl is formed and the corresponding diameter of the droplet and the downward shift of the droplet (Z_{cg}) can be obtained for different concentrations from the high-speed images. The

diameter of the droplet at this time instant gives the total density of the droplet. Thus, $F_{total-t}$ and $F_{total-b}$ are functions of ρ^* and ϕ. Density ratio (ρ^*) at the beginning of the heating process is one and subsequently will decrease with time. The functions $F_{total-t}$ and $F_{total-b}$ at any value of density stratification (ρ^*) exhibit a monotonically decreasing trend with (ϕ) for a given concentration (Figure 24a). At any ϕ, the net downward force on the top sector of the droplet is higher than the net upward force at the bottom sector of the droplet.

4.3.2.4 Collapse of a droplet into a bowl

The bottom sector never collapses due to the net upward force as quantified in the preceding section and as seen in the experiments. Thus, the maximum force on the bottom sector can be considered as a threshold value for force on the upper sector below which deformation or collapse is not possible. Hence, a critical angle (ϕ_{crit}) can be defined for each density ratio (ρ^*), at which the net downward force on the upper sector is the same as the maximum upward force on the bottom sector. The actual bowl formation angle, ϕ, has to be less than a critical angle, ϕ_{crit}, for different density ratios (ρ^*) at different concentrations of nanosilica (Figure 24b). Since the weight of the droplet is less than the acoustic force, only a small variation of ϕ_{crit} is seen for a large density ratio change from 0.9 to 0.3. This variation in ϕ_{crit} increases at higher concentrations as the quantity (W_t - W_b) becomes slightly larger. Physically, this shift in ϕ_{crit} indicates that the chord location along which the top sector collapses is higher towards the north pole of the droplet (Figure 24b). As a consequence, with increase in nanosilica concentration, droplets show increasingly asymmetric bowl formation when the horizontal axis passing through the droplet center (horizontal diameter) is considered to be the line of symmetry. Our

experimental data for ϕ_{crit} also suggests that it monotonically increases with concentration (Figure 24c).
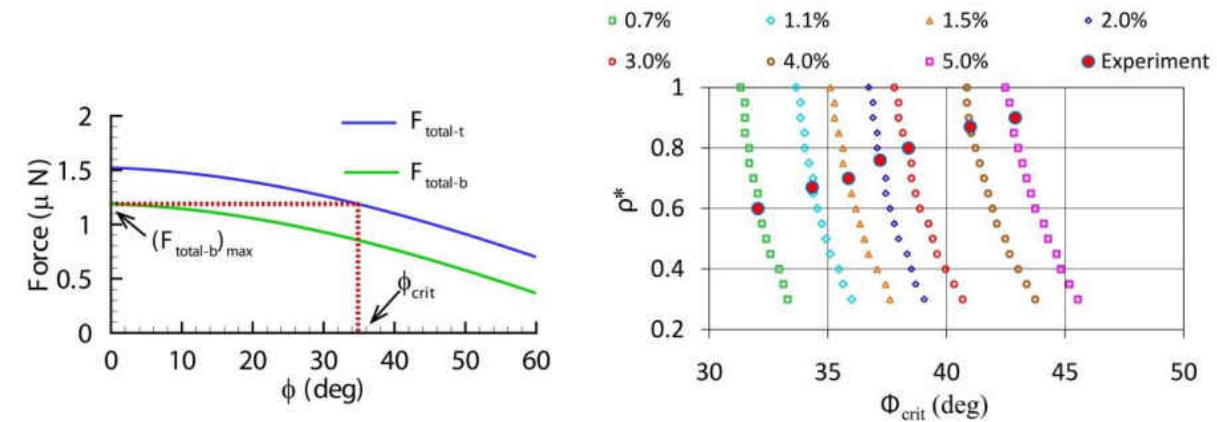
a)

b)
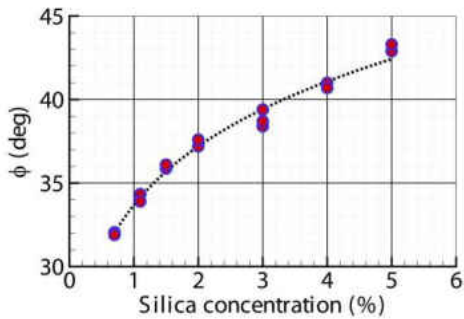
c)

Figure 24: (a) $F_{total-t}$ and $F_{total-b}$ vs. ϕ for a fixed ρ^*. (b) Changes in ρ^* with ϕ_{crit} for different concentration with experimentally observed ϕ. (c) Experimentally observed ϕ at different concentrations.

These experimental points in Figure 24(c) can now be plotted in Figure 24(b) to obtain the correct ρ^* for each concentration of nanosilica. These experimental points are shown using large filled circles in Figure 24(b). The density ratio at which bowl formation is triggered, increases

78

monotonically with ϕ_{crit}. This also illustrates that for lower concentration, large density stratification, i.e. lower ρ^*, is needed to create the necessary force imbalance for the top sector to collapse. For higher concentrations, the density stratification required to trigger the collapse is small, i.e. $\rho^* \to 1$, and the top sector collapses closer to the pole. The experimental high-speed images show that the time scale for bowl formation becomes smaller as concentration increases (Figure 22b). Hence, it can be argued that for smaller time scales, recirculation-induced density stratification will not only be lower but also more confined towards the poles. The density stratification front only moves towards the equator for longer time scales. These inferences are consistent with both theoretical and experimental trends in Figures 23 and 24.

4.3.2.5 Theoretical estimation of the density ratio

The density ratio, ρ^*, can also be estimated from theoretical calculations based on recirculation-driven particle movement within the droplet. Recirculation becomes weaker with increase in viscosity. The particles from the top sector of the droplet are advected towards the bottom sector increasing local nanosilica concentration. This, in turn, will create a concentration gradient across the droplet triggering particle diffusion towards the top sector of the droplet. If $C_u(t)$ is the nanosilica concentration at the top sector of the droplet, then the volume flow rate of particles migrating to the bottom sector of the droplet can be expressed as, $\dot{V}_{adv}(t) = v_{circ}.C_u(t).A_c$, where v_{circ} is recirculation velocity; A_c is the cross-sectional area at the interface. As described earlier v_{circ} will decay over time. However, for initial time instances before agglomeration occurs, it can be considered to be constant. The diffusion flow rate away from bottom sector of the droplet is

$\dot{V}_{diff}(t) = -D_{ij}.\frac{\partial C(s,t)}{\partial s}.A_c$.

Here C(s, t) is nanoparticle concentration within the droplet and 's' is the space coordinate. Considering the diffusion between top and bottom sectors of the droplet, the concentration gradient can be simplified to

$$\frac{\partial C(s,t)}{\partial s} \approx \frac{C_l(t) - C_u(t)}{R} \quad \text{with} \quad \frac{C_u(t)}{2} + \frac{C_l(t)}{2} = c_{in} \tag{4.16}$$

Hence,

$$\frac{\partial C(s,t)}{\partial s} \approx \frac{2.C_{in}}{R} \left(1 - \frac{C_u(t)}{C_{in}}\right) \tag{4.17}$$

Here, $C_l(t)$ is the nanoparticle concentration in the lower sector of the droplet, C_{in} is initial concentration and R is droplet radius. Combining the above expressions and equation (4.17),

$$\frac{\dot{V}_{adv}(t)}{\dot{V}_{diff}(t)} \approx \frac{R.v_{circ}}{D_{ij}} \frac{C_u(t)}{2(C_{in} - C_u(t))} \tag{4.18}$$

and R ~ 2.5x10^{-4} m, v$_{circ}$ ~ 10^{-1} m/sec, D$_{ij}$ ~ 10^{-7}–10^{-12} m^2/sec and $\frac{C_u(t)}{2(C_{in} - C_u(t))} \approx 1$.

Therefore, $\frac{\dot{V}_{adv}(t)}{\dot{V}_{diff}(t)} \gg 1$. A wide range of values for the diffusion coefficients of nanoparticles has been reported in the literature. They vary from 10^{-7} to 10^{-12} m^2/sec. An order of magnitude analysis shows that advection is very strong compared with the opposing diffusion phenomenon and, therefore, diffusion can be neglected. Considering recirculation to be the dominant transport mechanism, the total particle volume transported towards the bottom sector of the droplet over time 't' can be written as

$$\Delta V_p(t) = \int_0^t \dot{V}_{adv}(t).dt = A_c.v_{circ}.\int_0^t C_u(t).dt$$

(4.19)

From equation (4.19) the change in nanosilica concentration at the top and bottom sector of the droplet, i.e. $\Delta C_u(t)$ and $\Delta C_l(t)$, can be obtained. In a colloidal suspension, the density can be defined as $\rho_{global} = \rho_{water}(1 - C_{particle}) + \rho_{particle}.C_{particle}$. This can be extended for the two sectors of the droplet, and the density ratio, ρ^*, is written as a measure of density stratification,

$$\rho^*(t) = \frac{\rho_u(t)}{\rho_b(t)} = \frac{\rho_{water}[1 - C_{in} + \Delta C_u(t)] + \rho_{particle}[C_{in} - \Delta C_u(t)]}{\rho_{water}[1 - C_{in} - \Delta C_u(t)] + \rho_{particle}[C_{in} + \Delta C_u(t)]}$$

(4.20)

With $\rho_{in} = \rho_{water}(1 - C_{in}) + \rho_{particle}.C_{in}$, Equation (4.20) can be simplified as

$$\rho^*(t) = \frac{\rho_{in} - \Delta\rho.\dfrac{A_c}{V_u}.v_{circ}.\int_0^t C_u(t).dt}{\rho_{in} + \Delta\rho.\dfrac{A_c}{V_l}.v_{circ}.\int_0^t C_u(t).dt}$$

(4.21)

where $\Delta\rho = \rho_{particle} - \rho_{water}$. Equation (4.21) provides an expression, linking density ratio between the top and bottom sectors of the droplet as a function of concentration and recirculation velocity. It is seen that ρ^* will start from unity and will decrease with time. From geometry, $A_c = \pi R^2 \sin^2\phi$, $V_u = (2\pi R^3/3)(1 - \sin\phi)$ and $V_l = (2\pi R^3/3)(1 + \sin\phi)$. For small values of 't'

integral term in Equation 3.18 can be simplified as $\int_0^t C_u(t).dt \approx C_{init}.t$. Let us define a time scale t_s at which the density stratification or ρ^* attains its final value:

81

$$t_s = \frac{\rho_{in} \cdot \rho^*}{C_{init} \cdot \Delta\rho \cdot A_c \cdot v_{circ} \cdot \left[\dfrac{1}{V_u} - \dfrac{1}{V_l} \right]}$$

(3.22)

Then, using the ρ^* and ϕ calculated for different concentration, the time scale (t_s) can be calculated for different concentrations (Figure 25a). Particle-suspended systems show two different mechanisms in general for aggregation namely perikinetics and orthokinetics [Bremer et al. (1995)]. It is well understood that for high-concentration systems (concentration > 0.1 %), Brownian motion of particles (perikinetics) dominates the aggregation compared with shear driven motion (orthokinetics). Acoustic streaming driven particle motion plays a major role in levitation. For nanosilica suspended water droplets under levitation, the perikinetic time scale (t_c), and the time scale for particle migration from top to bottom sector are approximately the same. The perikinetic time scale can be calculated by [Bremer et al. (1995)]

$$t_c = \left(\mu \pi r_p^{\ 3} \middle/ kT \right) \cdot C_{init}^{\ 3/(D-3)}$$

(4.22)

where μ is liquid viscosity, r_p is particle size, k is Boltzmann constant, T is temperature and D_f is fractal dimension. It is observed that for nanosilica suspension at different concentrations, t_c is very close to t_s as shown in Figure 25(a). This similarity in two time scales shows that aggregation of particles due to perikinetics results in the formation of clusters or flocculation. This flocculation starts around perikinetic time scale (t_c). One can infer that flocculation triggers the formation of a thin porous crust around the droplet periphery. With the evolution of this semi-solid/porous surface, acoustic streaming induced internal recirculation decays very rapidly just beyond the perikinetic time. This allows for the establishment of a balance between diffusion

82

and recirculation-induced particle transport leading to a pseudo-steady state of the density stratification levels that exist between the top and bottom sectors of the droplet. Hence, this ensures that there is no significant variation of ρ^* beyond the perikinetic time scale. Note that flocculation does not imply immediate bowl formation. Bowl formation occurs at a much later time when the flocculation induced crust formation attains a certain level of thickness. In addition, flocculation starts while the droplet is in the evaporation stage. The vaporization rate is reduced with the formation of this porous thin crust and flocculation. However, sufficient porosity does exist [Yarin et al. (2002); Kumar et al. (2010)] to allow for substantial vaporization to occur until the bowl formation event. Pure droplets with no particles never show any structure formation. It is also observed that droplets with micrometer-sized particles exhibit longer bowl formation time, which is in agreement with the fact that the perikinetic time scale increases exponentially with particle size [Bremer et al. (1995)]. Alternatively, it can also be shown that if one uses the perikinetic time scale (t_c) in equation (4.21), to calculate final ρ^* for different concentration of nanosilica, it compares well with experimental ρ^*. Thus, the perikinetic time scale (t_c) is an important parameter to determine whether a droplet would transform into a specific structure. For micrometer-sized particles, the aggregation time scale is larger than the droplet lifetime. For such cases, the particles just clump together when the liquid content completely vaporizes.
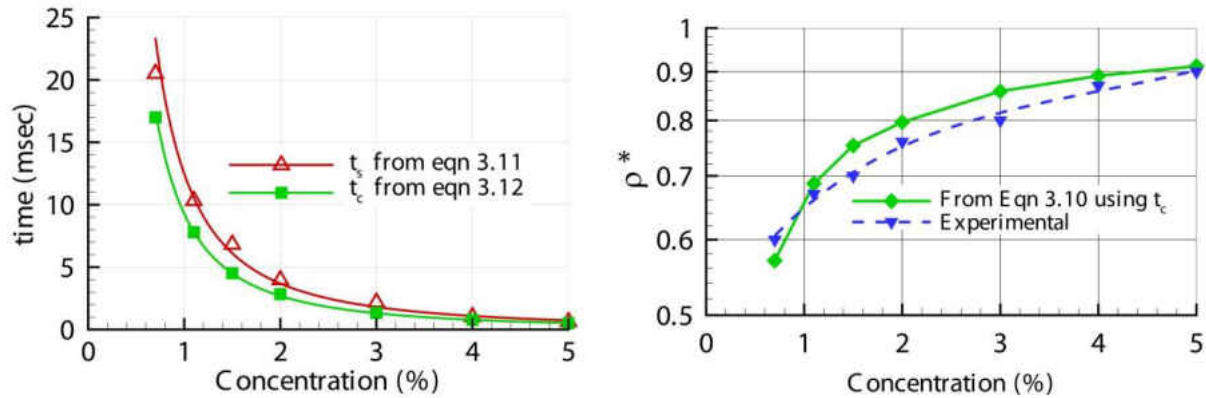
a)   b)

Figure 25: (a) Comparison of theoretical time scale (t$_s$) and perikinetic time scale (t$_c$) (b) Comparison of ρ* obtained from Equation 3.10 using perikinetic time scale (t$_c$) and experimental ρ*

4.4 Summary

Heating of nanosilica suspended solutions with different initial concentration shows a fascinating agglomeration and structure formation. In the initial stages of heating when significant evaporation has not taken place, the hydrodynamic effects caused by acoustic streaming is stronger compared to other effects such as orthokinetic aggregation. Soon, the evaporate rate becomes stronger resulting in a sharp diameter reduction. At the end of this stage, accumulation of nanosilica sets in as the droplet takes the shape of a bowl due to acoustic pressure difference, and the dropsize stops reducing further. As the solvent is depleted, the hydrodynamic effect becomes weaker. This marks the onset of the structure formation stage which is dominated by aggregation or agglomeration of nanosilica particles. The current results show two different structures depending on the initial solute concentration. For nanosilica concentration of less than 1.3%, the droplet maintains the bowl structure. On the other hand, for concentration greater than

1.9%, the initial bowl transforms into a horizontal ring. For the concentrations between 1.3 and 1.9, the droplet either forms a ring or a bowl. The formation of ring can be explained as follows. Further increase in viscosity with concentration decreases the strength of recirculation. The centrifugal effect due to droplet rotation about levitator axis becomes stronger than recirculation resulting in the accumulation of particles around the droplet equatorial plane. Thus a horizontal ring is formed due to asymmetries in mass distribution. The horizontal ring first starts oscillating within the acoustic field and eventually reorients itself to form a vertical ring due to an imbalance of forces.

A theoretical analysis shows that an acoustically levitated droplet with particle suspension transforms into a generic bowl-shaped structure upon heating, due to force imbalance caused by density stratification. The collapsing top sector becomes smaller with the increase in the initial concentration. The force and time scale analysis shows the conditions at which a bowl may or may not form. A significant finding is that the type of nanoparticle is irrelevant to the occurrence of bowl formation, as droplets with both soluble (cerium nitrate) and insoluble (nanosilica) impurities either through direct introduction or though phase transformation may undergo structural transformation. However, nanoparticle size is important since it can change the fractal dimensions and change the time scale. Pure droplets with no particles never exhibit any structural changes, while microsuspensions exhibit longer bowl formation time compared with nanosuspensions, which is in agreement with the fact that perikinetic time scale increases exponentially with particle size [Bremer et al. (1995)]. Likewise, concentration and density stratification due to recirculation affect flocculation which forms a porous crust on the droplet surface, changes the solvent viscosity, impedes the flow recirculation and vaporization rate and

triggers a top sector collapse. The time scale of final density stratification matches the perikinetic time scale which governs the flocculation event of the nanoparticles. These findings have significance in nanofluid drying, droplet combustion and crystal growth.

CHAPTER FIVE: DROPLET WITH PRECURSOR SOLUTION (CERIUM NITRATE)

5.1 Introduction

In surface coating industry, processing of liquid droplet containing salts of the ceramic precursors in high temperature environments like plasma or combustion flames has been used to produce nanostructured powder [Masters (1985)] and [Pawloski (1995)] as well as functional coating [Padture et el (2001)], [Jordan et al. (2004)] and [Bhatia et al. (2002)]. One of the most popular methodologies used for generating functional coating is Solution Precursor Plasma Spray (SPPS), where liquid precursor droplets are injected as spray into a high temperature dc-arc plasma field. In SPPS, the injected droplets undergo a series of thermo-physical transitions and chemical transformations. These in-flight stages are solvent vaporization, surface precipitation, shell rupture, volumetric precipitation and heating and melting of solid particles. Modeling of these processes has been reported by Ozturk and Cetegen (2004) and Basu and Cetegen (2007). In these works, the mass and heat transfer phenomena involved at the droplet scale for each of the above mentioned stages have been modeled. These results were used to predict the precipitate formation and final state of the droplet before reaching the substrate.

However all the models assume homonuclear precipitation to model the precipitation dynamics in the precursor droplets. In this theory, the droplet is considered to precipitate instantaneously when the surface concentration of the solute reaches a certain preset supersaturation limit and the precipitation front engulfs all parts of the droplet wherever the equilibrium concentration is exceeded. These classical nucleation theories were not sufficient to make good predictions regarding the nucleation within the droplets even at low heating rates [Cohen et al. (1987),

Leong (1987), Borra (2006), Oxtoby (1992) and Palermo (1968)]. For high heating rates, as in plasma, this problem is even more critical and the homonuclear precipitation theory comes under serious scrutiny. Though attempts have been made to improve the model by including density function approach, these models ignored the effect of heating rate on the homonucleation process. These models are much more applicable for low heating rate and temperature rise like, 10^2–10^3 K/s. But for high heating rates (10^5–10^6 K/s) as within dc plasma field or oxy fuel flames, these models are limited in predicting the exact phenomena. Additionally, the hostile nature of environment of the plasma field makes it very difficult to perform any kind of in-situ process analysis. It is imperative to perform better characterization of the droplet level thermo-physical processes using simpler complimentary experimental and computational analyses. Basu and Cetegen (2008a) showed that it is possible to heat a single stream of precursor droplet with infrared irradiation and replicate similar heating rates as encountered in the plasma or oxy-fuel flame environments. Although radiative heating of droplets are expected to have fundamental differences compared to convective heating within plasma field but comparable heating rates with plasma would imply similar precipitation mechanisms and thermophysical transformations. Basu and Cetegen (2008a) have also shown that radiative and convective heating are quite comparable in terms of heating rate and temperature profiles within the droplet. Later in Chapter 8 this analogy has also been established.

In this chapter, as a proof of concept, at first a pendant precursor droplet is heated by an infrared heating source like a CO_2 laser and the morphological transformations of the droplet is photographed by a high speed video camera during the entire heating phase. In addition, ex-situ analyses have been done on precipitates generated by heating the precursor droplet with CO_2

laser. These involve Scanning Electron Microscope (SEM) images and chemical analyses by XPS. The effect of heating rate and concentration of precursor solution on the final microstructure has also been studied in this chapter.

In the second part of this chapter acoustic levitation has been used to study the thermophysical phenomena in more details. The author reports four distinct stages of evaporation, precipitation and chemical transformation. Ex-situ analyses show the phase transformation to nanoceria occurs at very low droplet temperature. The final precipitate is porous in nature due to the presence of trapped gases and the porosity increases with increase in laser flux.

5.2 Pendant droplet

5.2.1 Experimental procedure

In this part of work, the primary endeavor was to set up a simple experiment where in-situ process kinetics analysis of radiatively droplets can be achieved. The setup shown in Figure 26a uses a power tunable, externally triggerable, continuous emission CO_2 laser as the radiative heating source for a single pendant precursor droplet. Though the process environment for this experiment is completely different from highly turbulent and luminous plasma in actual SPPS, the heating rate for these two scenarios are comparable. For the proposed experimental setup, the continuous CO_2 laser used has a beam spot size of 2 mm diameter with maximum power of 30 W, which results in a maximum heating rate of 10 MW/m^2, which is within and higher than the magnitude of the thermal heating rate of the plasma. A micro needle attached with a micro syringe has been used to create and anchor a pendant droplet at the tip of the needle. The blunt needle tip has an outer diameter of 210 μm and inner diameter of 115 μm, capable of creating a

droplet of 600 μm in diameter. During the plasma spray process an atomizer is generally used to generate droplets of sizes ranging between 10 and 500 μm. It is reported in the literature that smaller droplets usually result in good quality coating while the larger droplets lead to unpyrolization. Hence droplet dynamics and precipitation characteristics of the larger droplets are more interesting and needs to be analyzed in details. Also for in-situ analysis (as in the current experiment) it was realized that the larger droplets would be easier to generate consistently. They can also be visualized with high spatial resolution with a CCD camera. The droplet created at the tip of the needle is placed exactly in the center of beam path of the CO_2 laser. To record the morphological changes inside the droplet, a high speed video camera (Olympus i-speed2) was coupled to a long distance microscope (Quester-1000D) and placed perpendicular to the laser beam. The long distance microscope (Quester-1000D) is used to magnify the small droplet substantially. Though the camera has a maximum recording speed up to 33,000 frames per second (fps), only 4000 fps recording speed was used in the current experiment to prevent degradation in spatial resolution of the images with increase in recording speed. A strobe light was used to back illuminate the droplet for providing sufficient intensity for high speed video imaging. The laser, camera and strobe light were synchronized with each other using a delay generator (BNC model 565 pulse/delay generator), which triggered the connected instruments. The camera has frame duration of 0.25 msec. However, within this frame duration the sensor is activated only for 0.245 msec and the rest 5 μsec is the response time. The strobe had a flash rate aligned with the camera providing enough light during the imaging duration. The synchronization pattern has been shown graphically in Figure 26b. After the droplet was generated and anchored, a TTL pulse from the delay generator triggered the laser for specific

time duration. The same delay generator also triggered the video camera and strobe light in synchronization with the laser emission. In the experiment the laser heating time was controlled. The high speed camera used a chip memory (3 GB) to store the video images for each experimental run. Subsequently the stored images were copied in a compact flash card (Sandisk Ultra® II CompactFlash® 1 GB) and processed in a computer using LaVision imaging software.
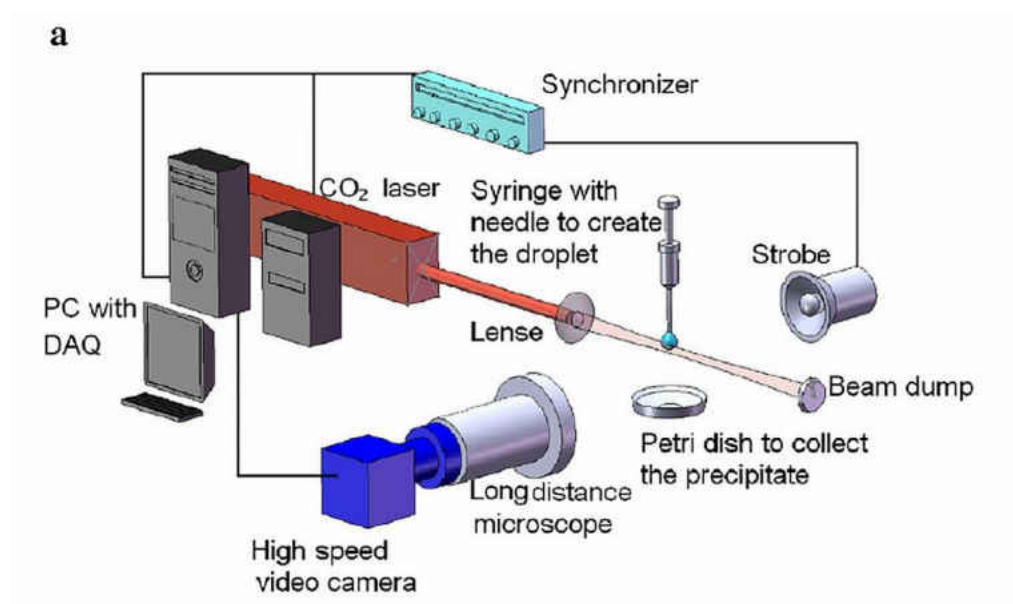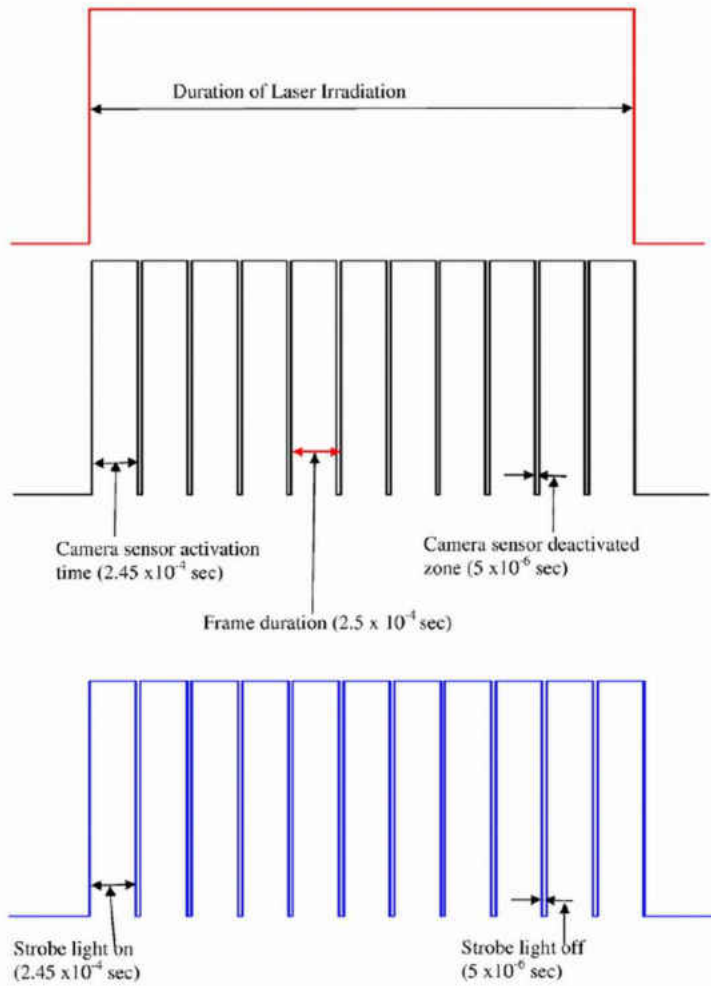
Figure 26: (a) Experimental setup for laser heating of pendant droplet, and (b) Synchronization of the laser, camera and strobe light.

After the laser heating process, the formed precipitates were collected in a Petri-dish kept under the needle. After collecting sufficient samples for identical conditions, ex-situ chemical analyses, like SEM and XPS, were performed on them. SEM images detailed the microstructure and morphology of the precipitates, while XPS results predicted the chemical constituents of the precipitates.

For this part of the work, water based cerium nitrate precursor has been used. Parametric variations of power level of the laser (resulting in variation of heating rates) and initial solute loading of the precursor droplets were performed. The initial solution loading and laser power used for the current work are tabulated in Table 2. In the current work, the precursor droplets were heated by laser irradiation till the droplet gets completely pyrolized. The time required for complete pyrolization was determined by trial and error method using ex-situ analyses like SEM. The analysis and variations of heating time durations and droplet sizes have been deferred for future work.

Solute concentration	Laser power
High concentration, 0.576 M	High laser power, 27 W
	Medium laser power, 21 W
	Low laser power, 15 W
Medium concentration, 0.23 M	High laser power, 27 W
	Medium laser power, 21 W
	Low laser power, 15 W
Low concentration, 0.115 M	High laser power, 27 W
	Medium laser power, 21 W
	Low laser power, 15 W

Table 2: Initial loading of cerium nitrate solution and laser power used

5.2.2 Results with high speed imaging of pendant droplet

In this work, water based cerium nitrate precursor with three different concentrations have been used in conjunction with three different power levels of the CO_2 laser. It has been noticed that for each case the heating process within the droplet is dominated by formation of bubbles as

predicted by Basu and Cetegen (2008a), which leads to explosive breakup and significant instabilities in the droplets. Also expected phenomena like shrinkage of droplet due to surface evaporation, shell formation by surface and volumetric precipitations have been observed. The high speed video images also clearly depict the relative time scales for these phenomena.

5.2.2.1 High concentration precursor (0.576 M)

5.2.2.1.1 High laser power (27 W)

The initial stages of the laser heating process is marked by rapid shrinkage in the size of the droplet due to surface evaporation followed by rapid bubble formation as shown in Figure 27. The droplet al.so exhibits severe deformations in shape leading to explosive breakup. Figure 27 also shows the precipitation dynamics of the heated droplets. It is seen that initially surface precipitation occurs followed by the advancement of the precipitation zone to engulf the entire volume of the droplet. It is also observed that following initial precipitation there occurs observable phase and morphological changes in the precipitate upon further heating.
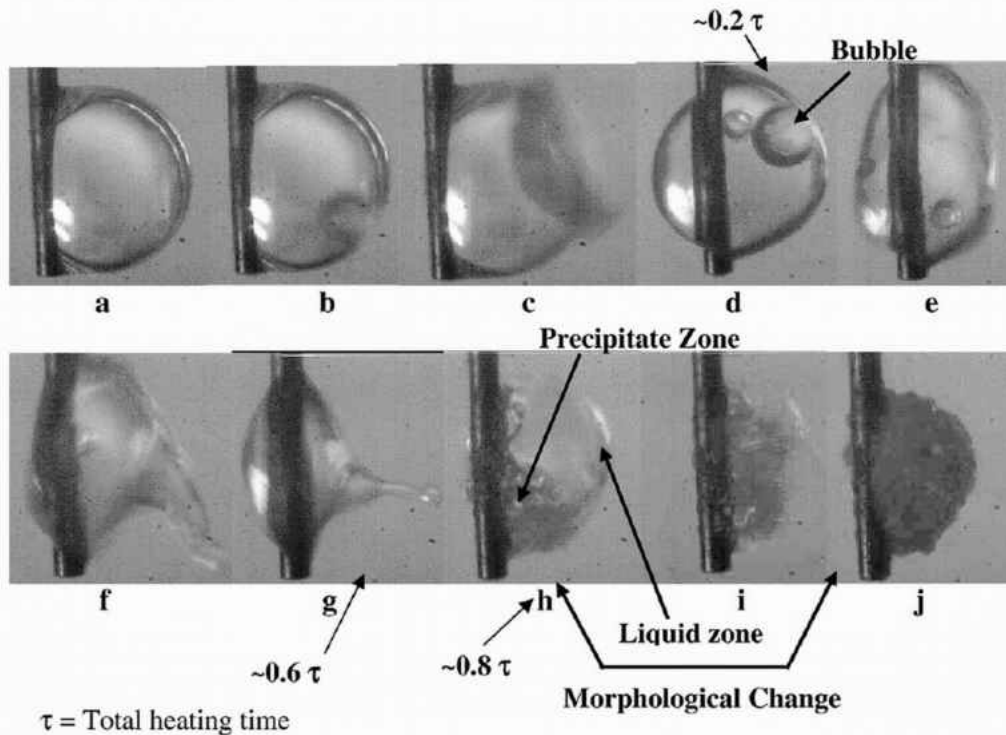
Figure 27: The high speed images (taken at 4000 fps) show the bubble formation and precipitation mechanism within a 600 μm diameter droplet of high concentration (0.576 M) precursor solution heated with high laser power (27 W).

The initial size shrinkage is coupled with erratic bubble formation leading to explosive breakup, making it very hard to exactly identify the transition from predominantly volumetric shrinkage to surface precipitation mode. Analysis of the high speed images reveals that the volumetric shrinkage is dominant for the first 65% of total heating time resulting in 60% reduction in hydraulic diameter. Around this point of time, surface precipitation is triggered. During this precipitation stage two distinct phases (liquid and solid) could be identified as shown in the high speed images in Figure 27. It was also observed that the precipitate transitions through a series of chemical transformations from the initial gelatinous phase into the final solid agglomerate. This morphological change was witnessed during last 5–10% of total heating time as depicted in the

last 3 images of Figure 27 (frames h–j). Figure 27 summarizes the different instances of the heating process for high concentration precursor solution irradiated with high laser power. The total heating time for this condition was 581 msec.

The formation of bubbles in radiative or convective heating especially under rapid heating rates has been also reported by Park and Armstrong (1989). They predicted that hot spots can form inside a droplet under rapid heating where the temperature exceeds the superheat limit, creating vapor pockets. These vapor zones will manifest as bubbles which will eventually grow and explode the droplets. This makes the heating process erratic and unstable, as was noticed in Figure 27 (frames d–g). The directional heating method applied in current experiment results in non-uniform heating rates leading to asymmetric surface vaporization. This lack of fore aft symmetry also aids in bubble formation and droplet deformations.

In this instance of high laser power and high precursor concentration, the bubble formation and corresponding deformation of the droplet starts at the onset of heating. However, as the process approaches the first observable precipitation, the intensity and frequency of deformation is drastically reduced. This can be attributed to the fact that the droplet size is significantly lower than the initial diameter. Smaller droplets have lower Weber number leading to better shear stability. After the occurrence of first surface precipitate the droplet deformation is drastically reduced. At this stage, the outer crust shields the inner trapped liquid from direct radiation. As a result, heating process of the trapped liquid in between the islands of the formed precipitates is significantly lower. However, this trapped liquid does get heated and form gaseous pockets that vent through the precipitate mass [Basu and Cetegen (2008b)]. Towards the end of the entire

heating process, especially the morphological transformation stage of the residue is devoid of any size deformation due to the absence of any solvent.

5.2.2.1.2 Medium laser power (21 W)

The images shown in Figure 28 depict that the heating process for medium laser power qualitatively is similar to the high laser power described in previous section. The total heating time under this condition was 856 msec. The bubble formation was noticed almost at the onset of heating, making it very difficult to separate the evaporation stage from precipitation stage. The comparative study reveals that volumetric shrinkage due to surface evaporation was predominant for 60% of heating time reducing the hydraulic diameter by 60%. At this point, the first evidence of surface precipitation was observed and the precipitation continued throughout the remainder of the heating time. During the last 5–7% of the heating time, the residue undergoes series of morphological changes. Figure 28 depicts different instances of heating for high concentration precursor with medium heating rate. It was noticed that the rate of bubble formation was lower in this case compared to the high laser power. This can be attributed to the lower heating rate (due to lower laser power), which causes less number of hot spots within the droplet which are responsible for bubble formation. It is observed that the bubble formation coupled with asymmetric vaporization and instability leads to explosion of the mother droplet significantly reducing its size. As the rate of bubble formation is low in case of medium laser power, the deformation rate and explosive breakup of the parent droplet is suppressed to an extent; hence more time is required to achieve similar volumetric shrinkage compared to the high laser power case. Also, as the heating rate is low, the absolute time required for the precipitation process to

initiate and complete also increases. The last three snapshots in Figure 28 (frames f–h) reveal the morphological changes of the residue.
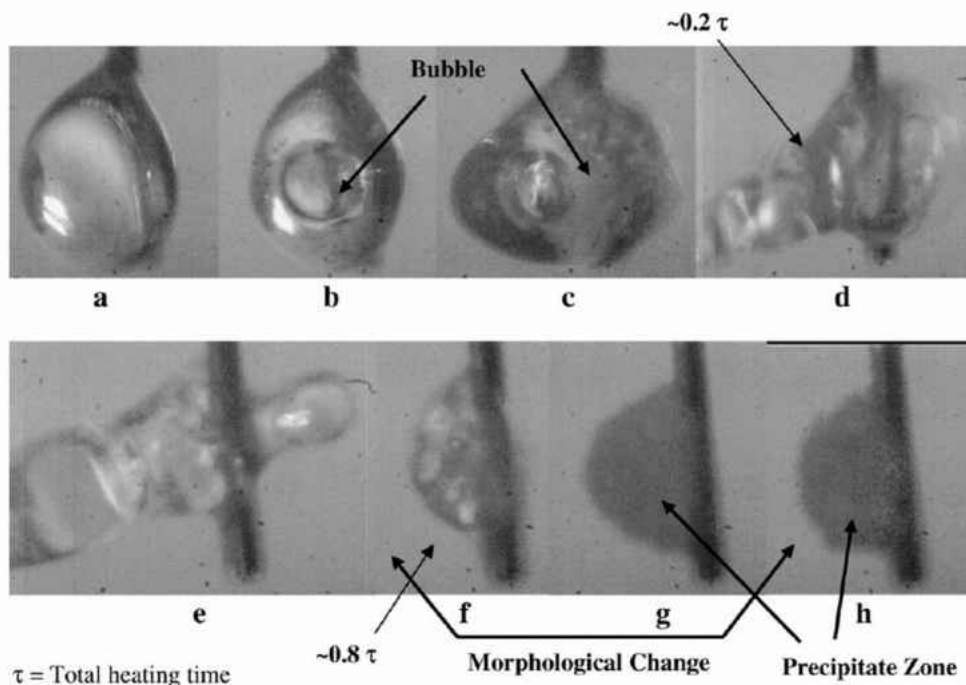
Figure 28: The high speed images (taken at 4000 fps) show the bubble formations are less rapid and erratic within a droplet of high concentration (0.576 M) precursor solution heated with medium laser power (22 W).

5.2.2.1.3 Low laser power (15 W)

In this instance as well, the images show that the process is qualitatively similar to the previous two cases. The total heating time for this case was 1187 msec. The images at different time instances of the heating process have been shown in Figure 29. The rate of bubble formation was reduced further compared to the previous cases. The droplet underwent volumetric shrinkage resulting in a reduction of 55% of the initial diameter in 55% of the total heating time before undergoing precipitation. The percentage of time consumed for surface evaporation process slightly decreases which is agreeable to the trend which was observed in previous two cases. It

should be noted that the total absolute time for a predominantly vaporization driven process is still much higher for the lower laser powers. In Figure 29, frames f–h exhibit the morphological changes in the precursor droplet.
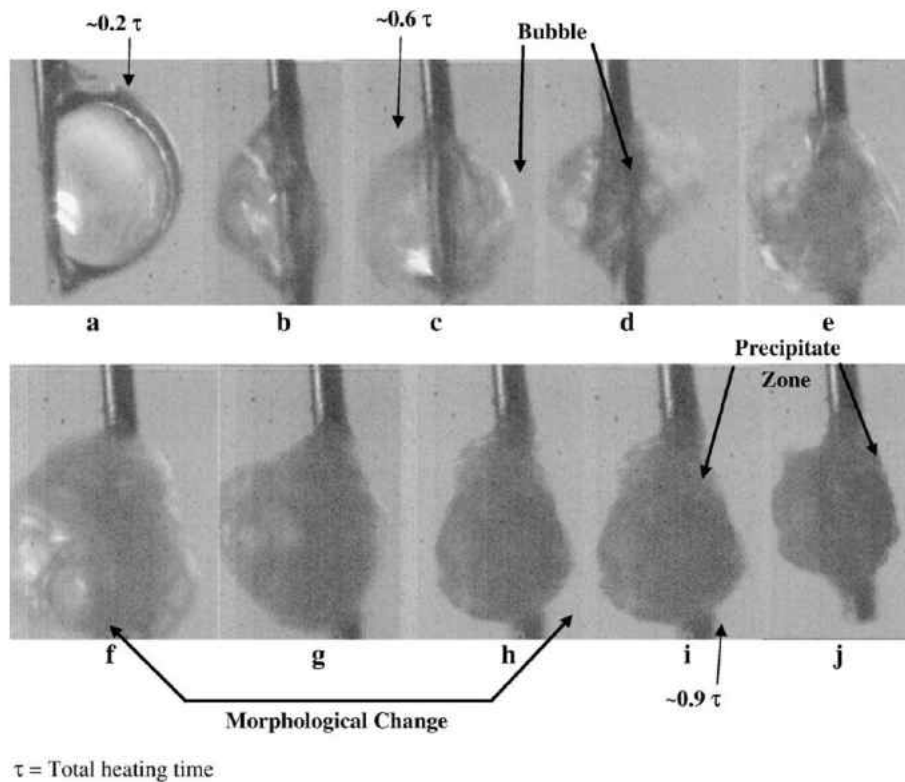
Figure 29: The high speed images (taken at 4000 fps) show the bubble formations are less erratic within a droplet of high concentration (0.576 M) precursor solution heated with low laser power (15 W).

In the case of high concentration solution irrespective of the laser power, it has been observed that the bubble formation starts from the onset of heating creating the surface evaporation process very erratic. The percent reduction in diameter due to surface evaporation is almost same for different power of heating. However, the percentage time taken for this surface evaporation process before precipitation reduces marginally with decrease in power, which can be attributed

to combined effect of lesser bubble formation and higher time requirement for the precipitation process to complete.

5.2.2.2 Medium concentration precursor (0.23 M)

5.2.2.2.1 High laser power (27 W)

In case of medium concentration solution, the initial surface evaporation and shrinkage stages were clearly visible, unlike the cases of higher concentration. The bubble formation starts after some time into the heating process, when the size of the droplet has already reduced by a substantial amount. The precipitation process also starts at this point. For higher laser power it was observed that it took almost 63% of total heating time (996 msec) to reduce the droplet diameter by 72% before precipitation started. The images from different time instances have been shown in Figure 30, where the stages of size reduction due to surface evaporation and precipitation are clearly visible. Though the initial vaporization process is free from any kind of bubble formation, the latter half of the heating process is accompanied by explosive bubble growth. The deformation observed in this case during the bubble formation phase is much higher than the high concentration counterpart. During the final 5% of the heating time, the precipitate went through series of morphological changes which can be seen in Figure 30 (frame h–i).

It can be noted that the deformation of droplet is dependent on Ohnesorge Number. Droplet deformation is usually damped by the viscous force. If the droplet has high viscosity it is more stable against the deformation. In the case of precursors, the viscosity decreases with the decrease in solute concentration making the droplet more prone to deformation. With medium concentration (0.23 M) precursor solution, the viscosity at room temperature decreases almost by

17% compared to the viscosity of the high concentration (0.576 M) precursor solution [Ouerfelli and Bouanz (1996)]. This explains the higher rate of deformation during bubble formation.
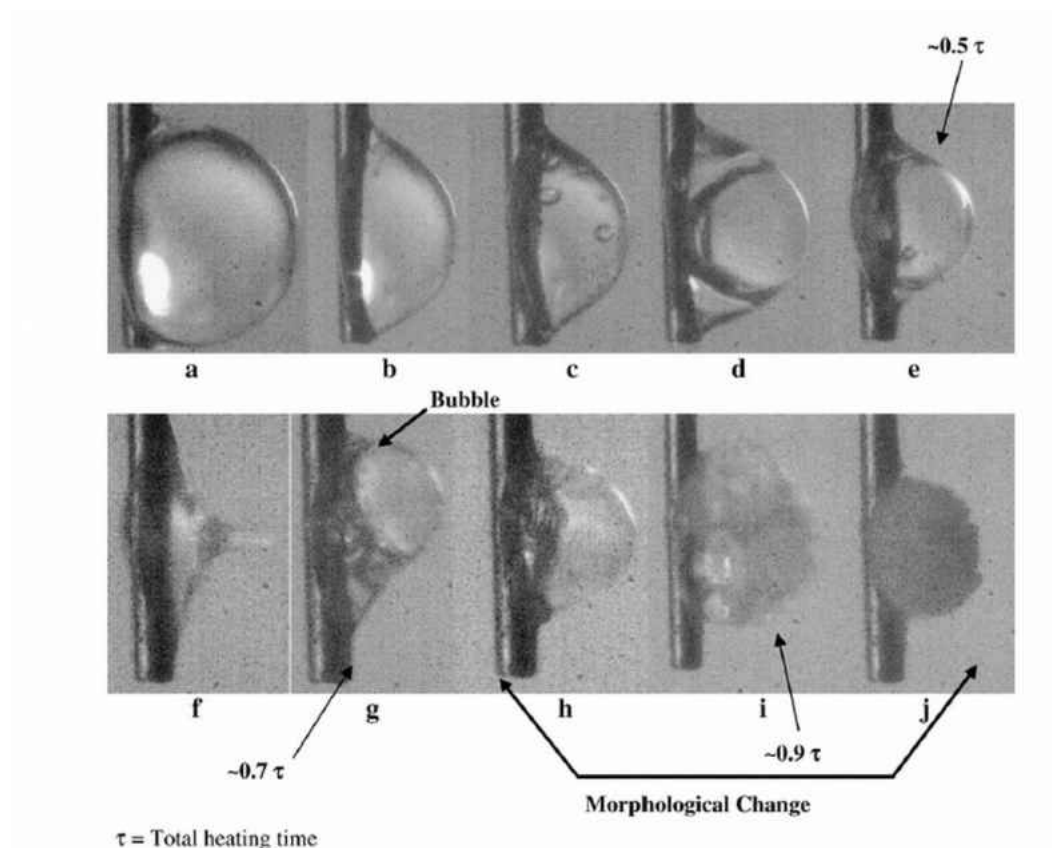
Figure 30: The high speed images (taken at 4000 fps) show the bubble formations occur after initial volumetric shrinkage for a droplet of medium concentration (0.23 M) precursor solution heated with high laser power (27 W).
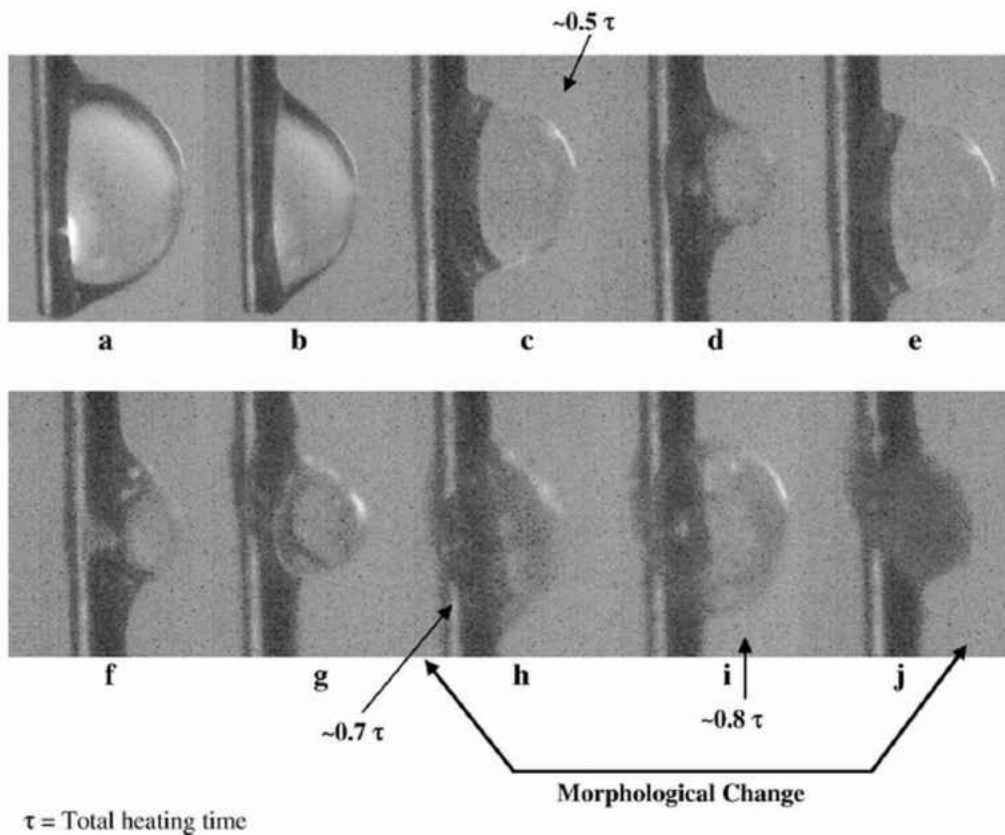
Figure 31: The high speed images (taken at 4000 fps) show the bubble formation occur after initial volumetric shrinkage for a droplet of medium concentration (0.23 M) precursor solution heated with medium laser power (21 W).

5.2.2.2.2 Medium laser power (21 W)

For medium laser power, the process is qualitatively equivalent to the high power results. Figure 31 shows different time snapshots of the heating process. The droplet under this condition took 1121 msec to get completely pyrolyzed. The initial surface evaporation with volumetric shrinkage occurred over 68% of the total heating time, reducing the droplet diameter by 75%. It can be noted that percentage of time taken for initial evaporation process is higher than the higher power case as described in previous section. As noted previously with medium concentration precursor, the initial surface evaporation process is unaffected by bubble

formations, signifying that shrinkage is due to solvent evaporation only which depends on the heating rate. So with lower laser power the percentage of time where solvent evaporation dominated increases. Morphological changes can be seen in Figure 31 (frames h–j).

However, the latter part of the heating process leads to severe droplet deformations. Compared to high power case, the rate of deformation is significantly lower.
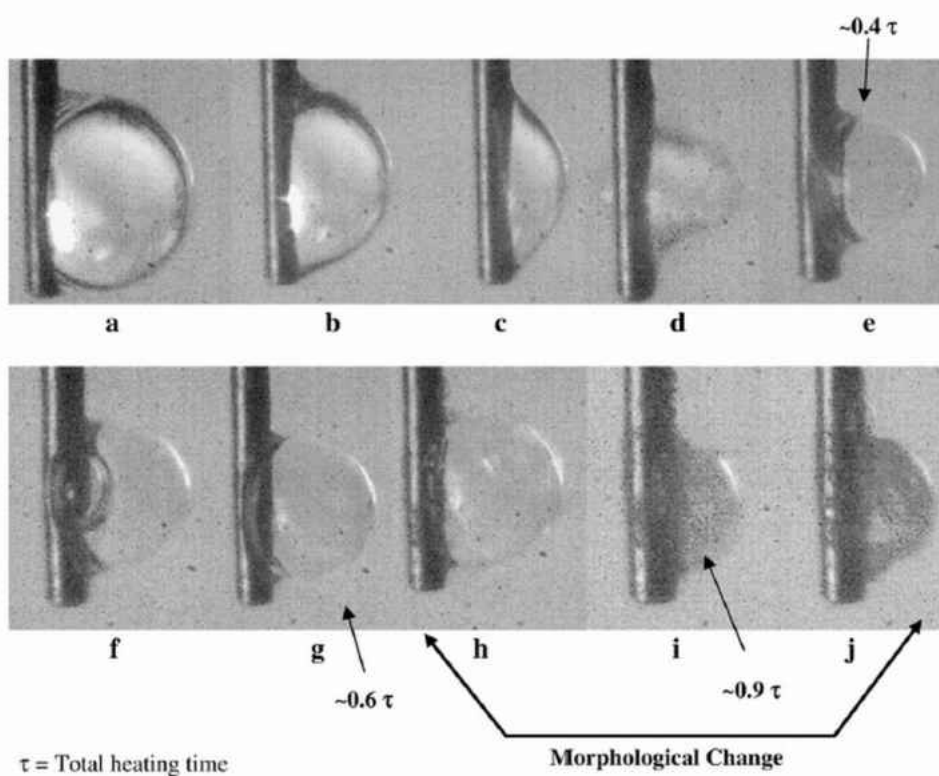
Figure 32: The high speed images (taken at 4000 fps) show the bubble formations occur after initial volumetric shrinkage for a droplet of medium concentration (0.23 M) precursor solution heated with low laser power (15 W).

5.2.2.2.3 Low laser power (15 W)

The most noticeable change in this case is that the bubble formation rate is much lower compared to previous cases. High speed images from different time instances also reveal similar

phenomena as observed in the previous sections (Figure 32). The total heating time was found to be 1315 msec, while the initial surface evaporation time duration was 73% of this time reducing the droplet size by 78%. The last 5% of the heating time is marked by the morphological changes to the residue. It is agreeable with the trend which was observed for the previous cases of higher laser power, where the percentage time for surface evaporation process increased with reduction of laser power. Morphological changes within the precipitates could be observed in Figure 32 (frames h–j).

For medium concentration precursor solution it was observed that during the initial phase of heating, when surface evaporation was predominant, the bubble formation rate is low. But the latter part of the heating process is dominated by droplet deformation. It is observed that the rate of deformation is higher than the case of high concentration precursor. This is a result of the reduction in precursor viscosity as described earlier. It is also noted that with reduction in power, the percentage of time consumed by the droplet for initial evaporation process increases, which is expected as the rate of evaporation is directly related to the intensity of laser power. It is also evident that total yield of the pyrolized precipitate after the completion of the heating process has reduced compared to the case of high concentration precursors. This is expected as medium concentration (0.23 M) has less amount of cerium nitrate as solute in the same amount of solvent compared to higher concentration (0.576 M).
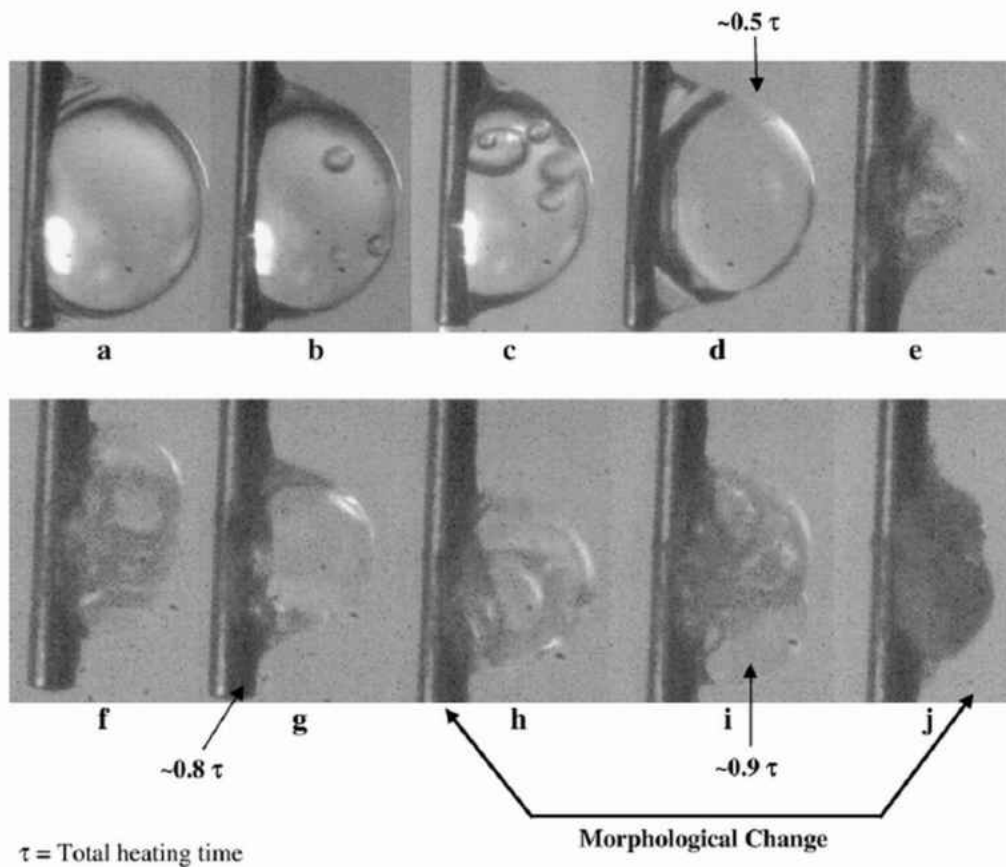
Figure 33: The high speed images (taken at 4000 fps) show the bubble formations occur after initial shrinkage for a droplet of low concentration (0.115 M) precursor solution heated with medium laser power (21 W).

5.2.2.3 Low concentration precursor (0.115 M)

5.2.2.3.1 High laser power (27 W)

For the lower concentration precursor, the initial vaporization phase is completely free of bubble formation. A noticeable difference observed is that the first few bubbles formed grow in size and violently explodes the droplet leaving a very small amount of the parent droplet attached with the needle. This can be attributed to the change of viscosity and the surface tension with reduction in solute mass fraction in the precursor. As a matter of fact for the lower concentration precursor, the viscosity at room temperature reduces by 22% compared to the viscosity of the higher

concentration (0.576 M) solution [Ouerfelli and Bouanz (1996)]. As explained earlier it is the viscosity that helps the precursor droplet to dampen deformations resulting in an increase of stability. The viscosity being reduced substantially in this case, the deformation of the droplet was high enough to detach most of the part of the precursor from the droplet leaving a tiny amount on the needle. As a result the precipitation phenomena could not be imaged very properly for this case.

5.2.2.3.2 Medium laser power (21 W)

In this case as well explosive boiling was observed as with the high laser power. But as the power of laser was lower than the previous case, bubble formation rate followed by the explosion phenomena with pressure pulse generation was less intense. This results in lower amount of fluid detachment from the needle. The initial evaporation process occurred over 83% of the total heating time (1291 msec) reducing the initial droplet diameter by 85%. The images from different stages of this heating process have been shown in Figure 33 which depicts the fact that during initial evaporation process, very few bubbles formation was observed. In this case, the laser power was lower than the previous case increasing the stability of the droplet against deformation. The last images in Figure 33 (frames h–j) show morphological changes within the precipitate.

5.2.2.3.3 Low laser power (15W)

The high speed video images in this case (Figure 34) exhibit that initial evaporation process is not affected by large number of explosive bubble formations. The time analysis of the process reveals that before precipitation is triggered, the initial evaporation time duration occupies 85%

of total heating time (1407 msec) reducing the droplet diameter by 87%. In comparison with higher heating rates, the relative timescale of the evaporation process with respect to the total heating time is higher. This is aligned with trend which was observed for the medium concentration.
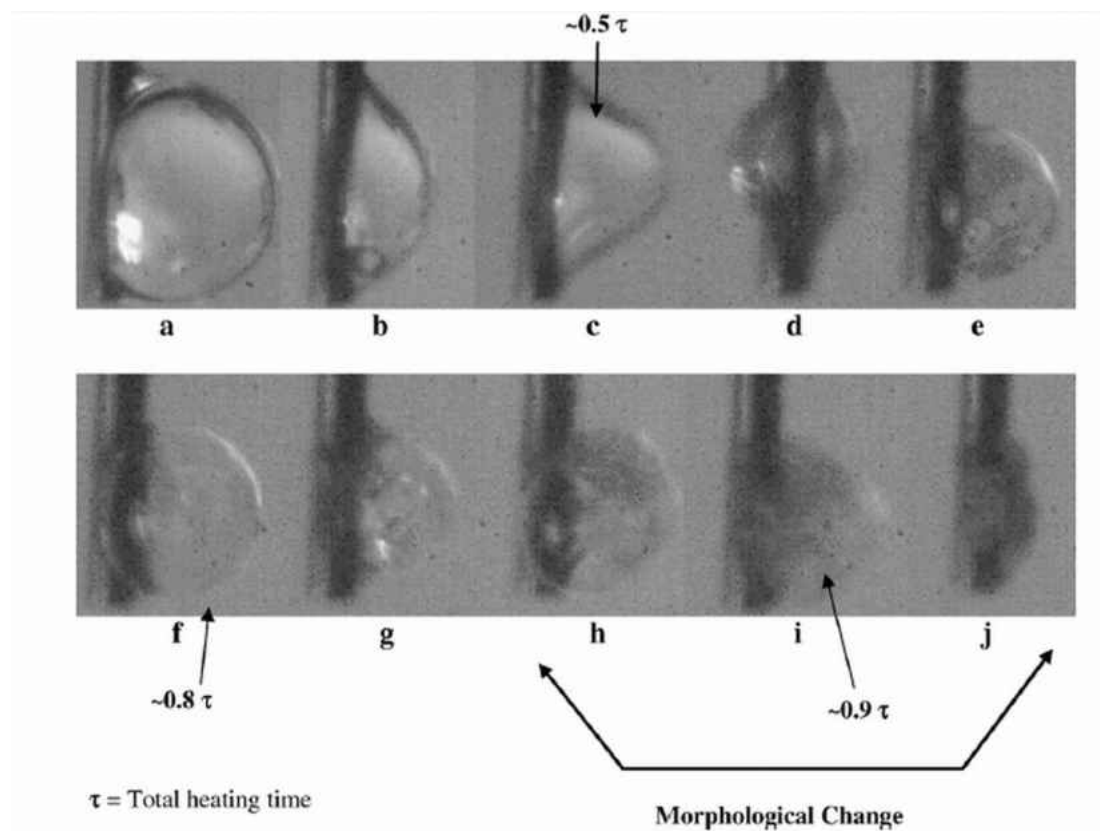
Figure 34: The high speed images (taken at 4000 fps) show the bubble formations occur after initial shrinkage for a droplet of low concentration (0.115 M) precursor solution heated with low laser power (15 W).

5.2.2.4 Summary of laser heating

In case of lower concentration the precursor droplets have less viscosity and surface tension. Due to this reason as explained earlier the instability increases and during the bubble explosion the droplets loose a substantial amount of precursor liquid. In the case of high laser power, this

phenomenon was so dominant that after few initial bubble explosions almost all the liquid precursor in the droplet got detached from the parent droplet. Study of the heating phenomena for different concentration of liquid precursor revealed that for higher concentration the bubbling phenomena was very rapid and it almost starts at the onset of heating, while in lower concentration cases, the initial surface evaporation process devoid of bubble formation for some period of time. Also the instability and deformation rate of the droplets increase with the decrease in solute concentration resulting in explosive breakup which causes substantial amount of fluid detachment from the parent droplet for low concentration cases. The reduction in diameter due to initial surface evaporation phase increases for lower concentration which is expected as lower concentration liquid precursor contains higher solvent (water) mass fraction. It was also found that during the last part of the heating process, the precipitate goes through a chemical change resulting in a transformation of initial gelatinous morphology into a solid one.

The whole study also reveals the fact that the droplet deformation during heating process is dependent on droplet size, heating rate and solute concentration. It was evident from the images that droplets tends to show more stability when the size reduces due to vaporization. The low laser power cases exhibited lower deformation rates. Also the viscosity of the precursor solution assists in stabilizing the droplet. That is why the higher concentration droplets had lower rate and intensity of size deformation.

It can be inferred from the results that the vaporization phase during the actual plasma spray processes are dominated by bubble formation and related instabilities within the droplet.

However, chances of these unwanted phenomena will be lower in case of higher concentration and smaller droplet size.
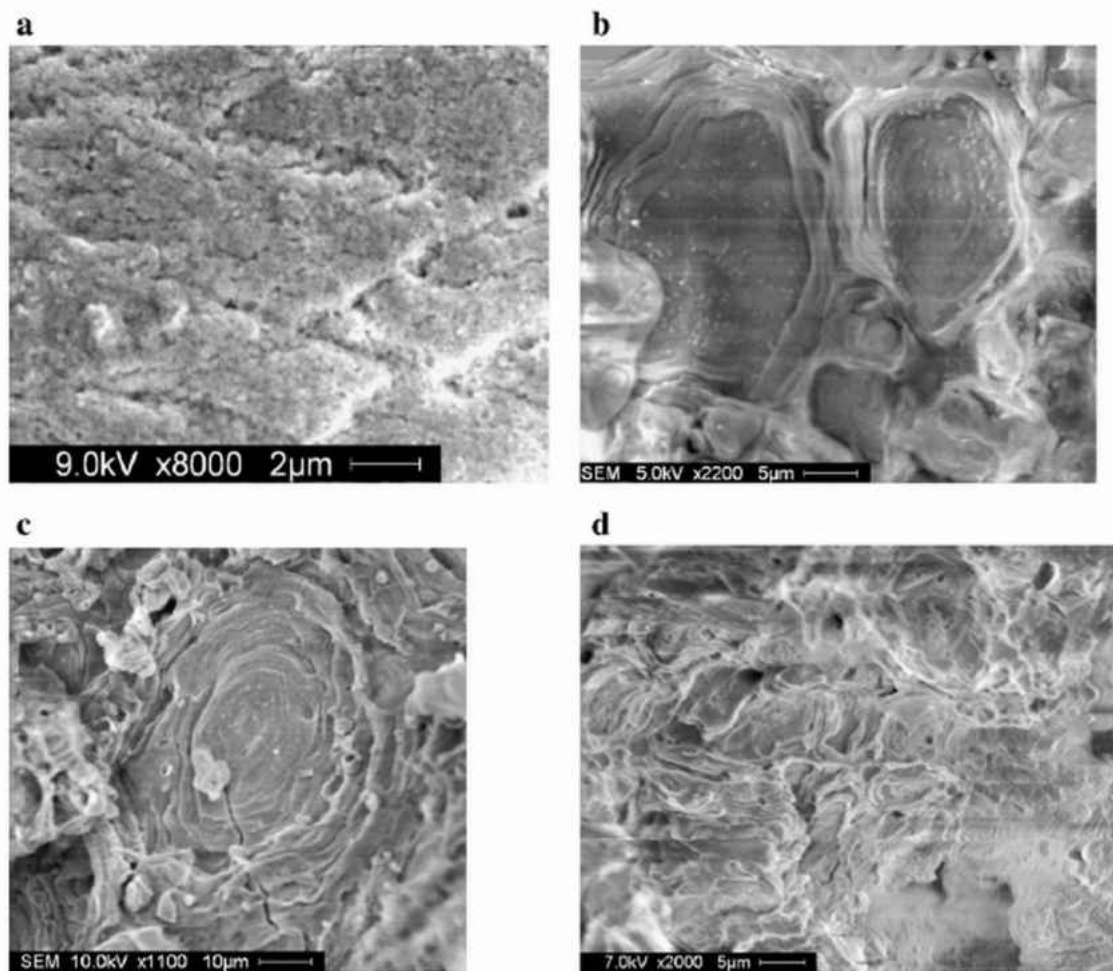
Figure 35: SEM images of the precipitates generated by different radiative heating rates from high concentration (0.5 M) cerium nitrate precursor: (a) 3W, (b) 15W, (c) 21W, and (d) 27 W

5.2.3 Ex-situ analysis

The second phase analysis is based on ex-situ characterization of the precipitates collected under different conditions [laser power and concentration] described earlier. Scanning electron microscopy images showed some distinct changes within the morphologies of final precipitates

acquired in different cases. These changes can mostly be attributed to the variation in heating rates and initial solute loadings.

For high concentration precursor, it can be noted that with increase in laser power level, the microstructure of the final precipitate exhibits flaky and porous features. However with low heating rate, the precipitate is dense. Figure 35a shows very dense microstructure of the precipitates for 0.5 M precursor solution heated with 3 W of laser power. However the same concentration solution under higher laser power results in very porous precipitates (Figure 35 b–d). For medium concentration (0.2 M) precursor solution it was seen that power variation does not have much effect on the precipitate microstructure. Figure 36 shows the SEM images of the precipitates from 0.2 M solution precursor at different power levels. Also it is interesting to note that for both high and medium concentration precursors, there are evidences of irregular circular patterns within the microstructures, which can be thought of as different nucleation wave-fronts.
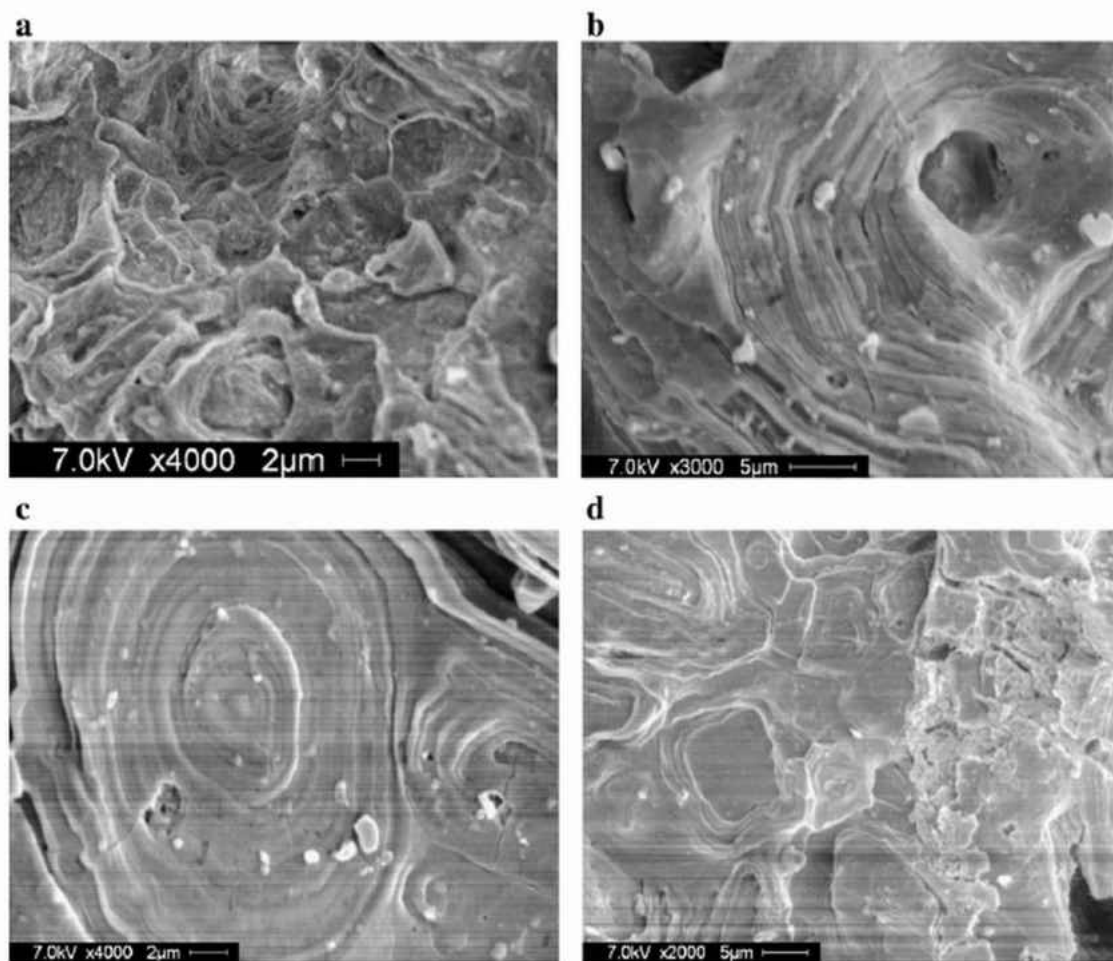
Figure 36: SEM images of the precipitates generated by different radiative heating rates from medium concentration (0.2 M) cerium nitrate precursor: (a) 3 W, (b) 15 W, (c) 21W, and (d) 27 W

In the current experimental procedure (or inside the plasma during SPPS process) the droplets face the inverse solidification of liquid melt. In usual solidification processes, like solidification of molten metals in moulds, the solidification front moves towards the center while the heat energy flows from the center to the periphery. But in the present case, both the solidification front and heat energy flow towards the center of the droplet from the periphery as shown in Figure 36. At first, the outer crust of the droplet solidifies and then the solidification front moves towards the core of the droplet. During the solidification/precipitation process and the

111

corresponding phase change, water vapor and gaseous oxides of nitrogen are formed. These gases move from center to the outer surface. The process of formation and liberation of these gases results in pores and micro voids. The higher concentration solution has less amount of solvent or water content. As a result, during the heating phase, less amount of vapor is released compared to the low concentration precursors. The precipitates from higher concentration (Figure 35) hence have lesser number of micro-voids compared to the lower concentration case (Figure 36). Now with the change in power level of the laser, the time required for solidification/precipitation also changes. For higher power of the laser, the outer surface solidifies/precipitates very quickly while the inner sections do not get adequate time to solidify and vent the vapor out before the outer layer solidifies. So, the vapor and the gas liberated from the precipitated droplet generate a porous path through the already solidified outer surface resulting in a porous micro-structure. In case of low heating rate, the outer layer takes a considerable amount of time to solidify and so the inner layers have enough time to vent most of the gas out while the outer layer is in semi-solid state. This results in less porous or comparatively dense microstructure. However for same laser power, with lower concentration solutions the amount of water to be vaporized is higher. So the required time for the outer layer for solidification is not enough for the inner layers to go through considerable amount of solidification. In this case the solidification and gas releasing phenomena in inner layers continue even after the complete solidification of the outer layer. This also makes the microstructure porous. These phenomena could be evidently seen in the high speed images as well. Figure 38 shows few high speed images of the heating process for higher concentration (0.5 M) solution. In

these images there are evidences of vapor formation in the inner layers, when the outer layer is already solidified.
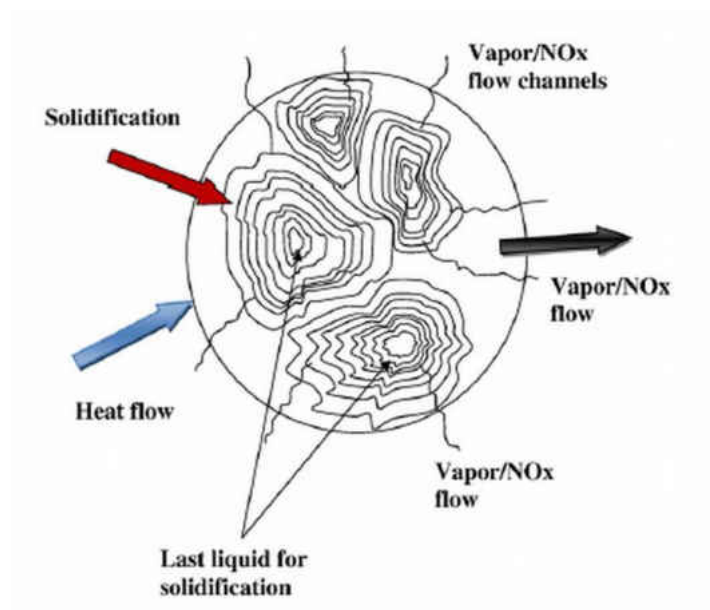
Figure 37: Solidification/precipitation pattern within the precursor droplet during irradiative heating.
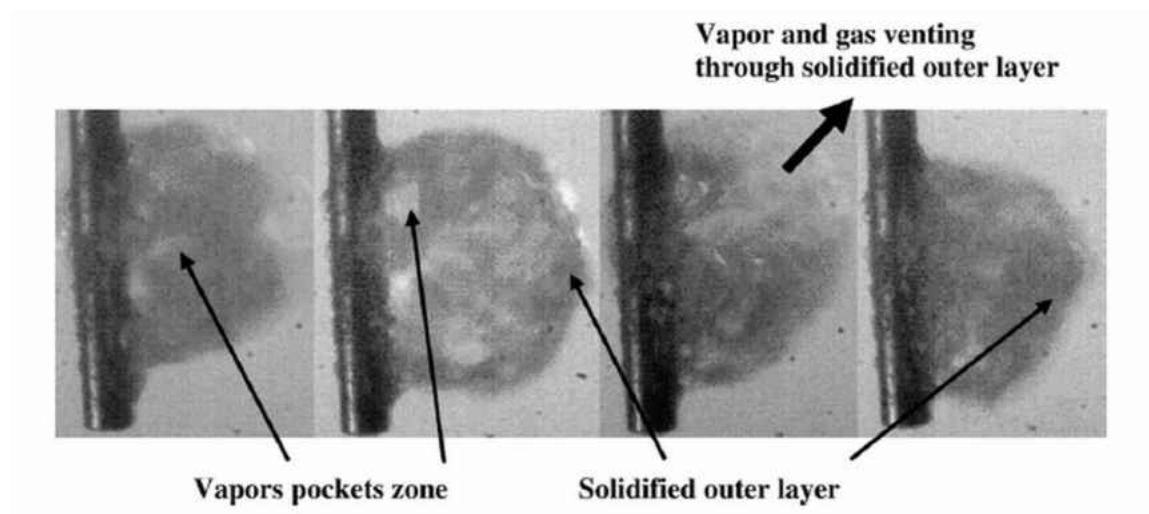
Figure 38: Evidences of gas venting out through solidified outer layer during heating process of higher concentration (0.576 M) solution with higher heating power (27 W).

The entire solidified/precipitated residue shows a similar kind of behavior i.e. some kind of layer formation, which can be seen as an irregular circular pattern. Only morphology and size of the pattern change with solute concentration. When liquid precursor droplet containing solute is heated, it does not solidify into one solid spherical particle. Besides, solidification starts at different location depending on the solute concentration. For higher solute concentration the nucleation sites will be higher in numbers. SEM images of higher concentration (0.5 M) hence show smaller size of ripple formations (Figure 35).

	0.1 M	0.2M	0.5M
Ce^{3+}	19	21	17.6
Ce^{4+}	81	79	82.3

Table 3: XPS result of the final precipitates (Percentage of Ce^{3+} and Ce^{4+} for different concentration of samples)

The chemical characterization analysis has also been done on different precipitates. The XPS shows the presence of Ce^{3+} and Ce^{4+} in all the precipitates resulted from heating with different concentration levels. Table 3 shows percentages of Ce^{3+} and Ce^{4+} in different cases. It is evident that Ce^{4+} is predominant in the final residues. The presence of Ce^{4+} is good for thermal barrier coating where the coating has also to be oxidation resistive in nature.

5.2.3.1 Summary of ex-situ analysis

In summary, it can be commented that the radiative heating of cerium nitrate droplets shows the intermediate stages dominated by bubble formation within the droplet. Intensity of the 'bubbling' phenomena decreases with reduction in the power and precursor concentration. The ex-situ analysis shows that with high concentration and lower power the final microstructure can be

dense and thick, whereas with higher powers or lower concentration the microstructure becomes porous and flaky. The presence of irregular patterns also indicates presence of different nucleation sites during solidification process.

5.2.4 Summary of pendant droplet heating experiments

In this work it has been demonstrated that radiative heating of precursor droplet can simulate the plasma environment in order to study the intermediate thermo-physical processes inside the precursor droplet. The high speed imaging of the process shows various thermo-chemical stages like volumetric shrinkage, bubble formation, explosive breakup of droplets, surface precipitation, outer crust formation, volumetric precipitation and morphological transformations of precipitates. These phenomena were also predicted by the different models of the thermo-physical phenomena during SPPS process. One important phenomenon observed during the heating process is formation and explosion of bubbles leading to droplet instability. For higher concentration droplet 'bubble phenomena' could be observed from the onset of heating. In case of lower concentration precursors, initial evaporation phase is free from bubble growth. The bubble formation can be attributed to formation of hotspots within the droplet during heating. The droplet instability primarily depends on the droplet size, heating rate and concentration of the solution. The combined effects of these parameters dictate the dynamics of the heating process. In cases like high heating rate with low concentration solution, the degree of instability becomes too high such that the droplet separates from the needle. In can be inferred that SPPS process with high heating rate will induce a high amount of deformation within the droplet if the solute concentration is high and the droplet is large in size. It is worth mentioning here that the amount of precipitate formed by heating the droplet al.so reduces with the concentration. It also

indicates that use of lower concentration solution in case of SPPS may result in insufficient coating thickness requiring more passes.

The ex-situ analysis also revealed some information about the process. In most of the cases, the micro-structure is exhibited irregular patterns, which is evidence of the presence of multiple nucleation sites. The number of nucleation centers increases with the increase of solute concentration and laser power. Also it was understood that as the outer surface precipitates first and the precipitation/solidification front moves inward during the heating process. This normally creates an outer crust while the inner layers are in semi-solid or liquid state. Further precipitation of the inner layers release vapor and gaseous oxides of nitrogen, which are liberated through the solidified outer layer resulting in micro-voids and porosity. In case of higher concentration solution with lower heating power, dense microstructure is produced.

The results in the laser heating experiment can be directly correlated to the SPPS process. It is expected that in actual plasma spray process, precursor solution of higher concentration will result in dense microstructure which is favorable for resistive coating. On the other hand, precursors of lower concentrations will result in porous microstructure favorable for TBC.

It can also be inferred from the results, that the smaller droplets show higher stability against deformation and hence have higher chances of reaching the substrate in a pyrolized state. However, larger droplets exhibit greater propensity towards breakup which can result in unpyrolized coating.

The XPS of different samples reveals the fact that the final form of ceria in the precipitates is in both higher and lower valance level. The presence of Ce^{4+} is dominant, which is good for oxidation resistive coating.

It is worth mentioning that the heating environment during the current work is different from actual solution precursor plasma spray process. The presence of vorticity, turbulence and pressure variation within the plasma field affect the in-flight droplet behavior. However, the heating rates of both the scenarios (plasma and laser) being similar, the droplets in plasma spray process are expected to undergo similar instability and phase transformation observed in the current case. The irradiative heating process can also be used for predicting the thermal behavior of the droplets during HVOF process. However, in that case the laser power needs to be tuned down to a lower value to match the heating rate of HVOF process which is substantially lower than that of SPPS.

5.3 Levitated droplet

The experimental work reported in this section uses high speed imaging and IR-thermography for in-situ optical diagnostics of a cerium nitrate droplet heated by a tunable CO_2 laser. The objective of this study is to determine the different thermo-physical stages and phase changes during the heating process. The current study is also aimed at understanding the effect of laser power on the vaporization process and the final precipitate morphology.

5.3.1 Experimental setup

Referring to Figure 1, the experimental set up included an ultrasonic levitator (Tec5 ultrasonic levitator, 100 kHz) to suspend the droplet. The suspended cerium nitrate droplet was heated by a

CO_2 laser irradiating at 10.6 µm with a beam diameter of 2 mm. The power of the laser can be tuned from 0 W (no heating) to 30 W (~10MW/m^2) using a controller coupled with a power supply. An IR camera was placed perpendicular to the laser beam to measure the temperature of the droplet. A high speed camera (Fastec TSHRMM, with maximum speed of 16000 frames per second) along with a zoom lens assembly (Navitar 6000) was used to capture the physical processes occurring within the droplet during laser irradiation. This camera was placed at an angle of 30° to the laser axis as shown in Figure 1. The vaporization process was recorded at 1000 fps, the maximum that could be achieved without loss of spatial resolution. The images from the high speed camera were used to determine the instantaneous diameter of the droplet. To facilitate fine adjustment of the relative position, the IR camera was placed on an X-Y stage while the levitator was attached to an X-Y-Z stage. The high speed camera was also positioned on a unidirectional stage (X-stage). The laser and the cameras were synchronized using an external delay generator as shown in Figure 1. A detailed description of the setup and the instruments are provided in Chapter 2. The uncertainties in temperature and diameter measurement have already been discussed in that chapter.

In this work, 0.576M cerium nitrate aqueous solution was used as the initial concentration. The solution was prepared by dissolving 99% pure Cerium Nitrate hexa-hydrate salt into deionized (DI) water with the help of a magnetic stirrer. The droplets were generated and deployed to the pressure node of the levitator by a micro needle. For every experiment, the initial diameter of the droplet was maintained at 500 µm (±10 µm). The droplet was heated with the laser at different power levels until phase transformations and chemical reactions were complete.

After the experiment, the IR and high speed images were analyzed to obtain the temperature and diameter data. The temperature data was obtained by defining a zone of interest around the surface of the droplet in each IR image, and the maximum, minimum, average and standard deviation of the temperature on the droplet surface were calculated. It is important to mention that the droplet sometimes oscillated from side to side with respect to the IR camera axis during experiment which resulted in some out-of-focus images. These out-of-focus images were not considered for further analysis. The high speed images with higher temporal resolution were used to calculate the diameter of the droplet using Motion Measure software. To calculate the instantaneous diameter, an edge around the droplet was defined. An equivalent diameter was calculated from the area under the curve (edge).

The samples were analyzed for their microstructural features using optical microscopy (magnification of 40X), Scanning Electron Microscopy (Zeiss ULTRA-55 FEG SEM) and Transmission Electron Microscopy (TEM FEI Tecnai F30) techniques. The TEM technique was especially useful in characterizing the microstrucutre, crystal structure, and composition of the films at high resolutions. For this characterization, the precipitates were collected on copper grids which were directly loaded into the specimen stage of the TEM. Bright-field and dark-field microscopy studies helped in identifying the microstructural features, selected area diffraction to identify the crystal structure features, and the energy dispersive spectroscopy (EDS) method to determine the compositions of the phases.

5.3.2 Results and discussion

The experiments and analyses have been broadly divided into two sub-sections. The first section describes the results for unheated condition to analyze the effect of acoustic streaming due to levitation on droplet vaporization. The next section describes the results for heated conditions (laser tuned at different power levels). Separate experiments with and without laser heating help in delineating the effects of acoustic streaming and laser heating.

5.3.2.1 No heating: Effect of acoustic streaming

Acoustic streaming in a levitator plays an important role on the droplet dynamics. Xie and Wei (2007), Yarin et al. (1998), Tian and Apfel (1989) analyzed the effect of acoustic streaming in ultrasonic levitator on the vaporization rate of a suspended droplet. They reported a change in the aspect ratio of the droplet under acoustic forces. Xie and Wei (2007) and Yarin et al. (1998) discussed how the horizontal diameter gets stretched compared to vertical diameter. They also showed that this horizontal stretching increases with increase in diameter and levitator pressure level. Both Yarin et al. (1998) and Tian and Apfel (1989) showed that the natural evaporation process gets affected when the droplet is suspended in acoustic field. However, their work confirmed that with a levitator setting of 100 kHz frequency and 154 dB amplitude (current experimental condition), acoustic streaming has negligible effect on global vaporization pattern for pure liquid droplets in a forced convection field.
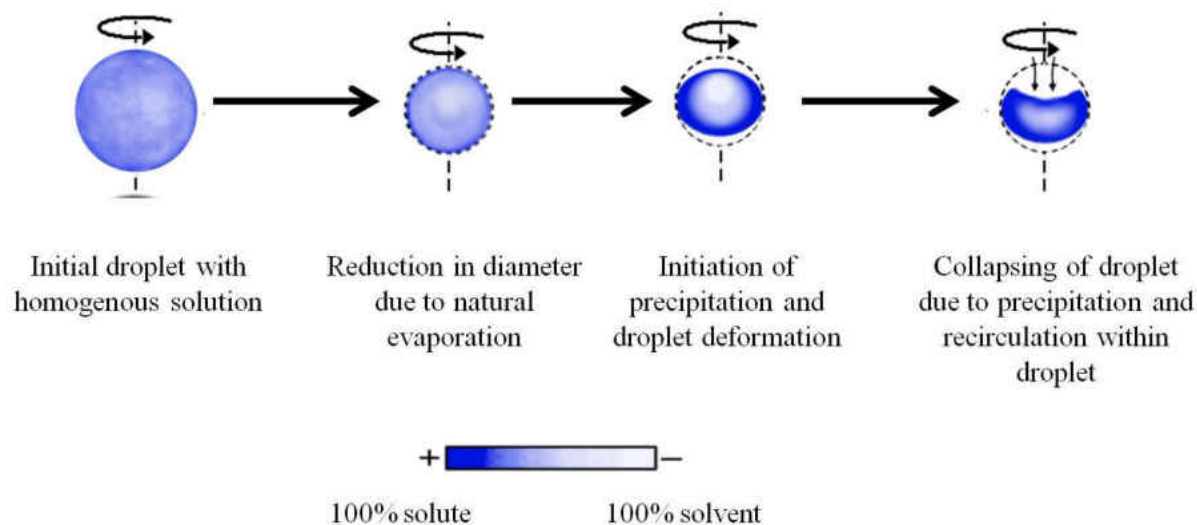
Figure 39: Schematic of evaporation process of levitated cerium nitrate droplet in the presence of acoustic streaming without external irradiation.

To identify the effect of acoustic levitation in the current experiment, vaporization dynamics of the cerium nitrate droplet was observed with a high speed camera in the absence of laser heating. Figure 39 shows a schematic of the thermo-physical phenomenon observed in the experiment due to acoustic streaming only. High speed images show that the droplet vaporizes and reduces in size, increasing the solute (cerium nitrate) concentration particularly near the surface. It is also evident from the high speed images that the droplet has a rotational motion about the vertical axis of the levitator. After some time, the top half of the droplet collapses transforming the droplet into a bowl-shaped structure. It was also noticed that the solvent portion of the droplet gets almost depleted due to evaporation before the droplet takes a bowl shape. In the absence of heating, the total time for this vaporization process was 25 minutes which is very high compared to the cases with heating (described in subsequent sections). Evidently, during evaporation without any external heating source, the temperature of the droplet did not increase. This also

suggests that evaporation in the absence of laser heating does not trigger any thermal decomposition of cerium nitrate to ceria (as will be seen in the heated cases). This phenomenon (Figure 39) can be explained by the experimental evidence and theoretical modeling developed in the previous chapter (Chapter 4).

Initially, when the droplet has higher liquid concentration, strong rotation about horizontal axis and very weak rotation about vertical axis can be observed	Later stage, when the droplet takes a bowl shape, rotation about both horizontal axes stops. Rotation about vertical axis becomes stronger
b) (i)	b) (ii)
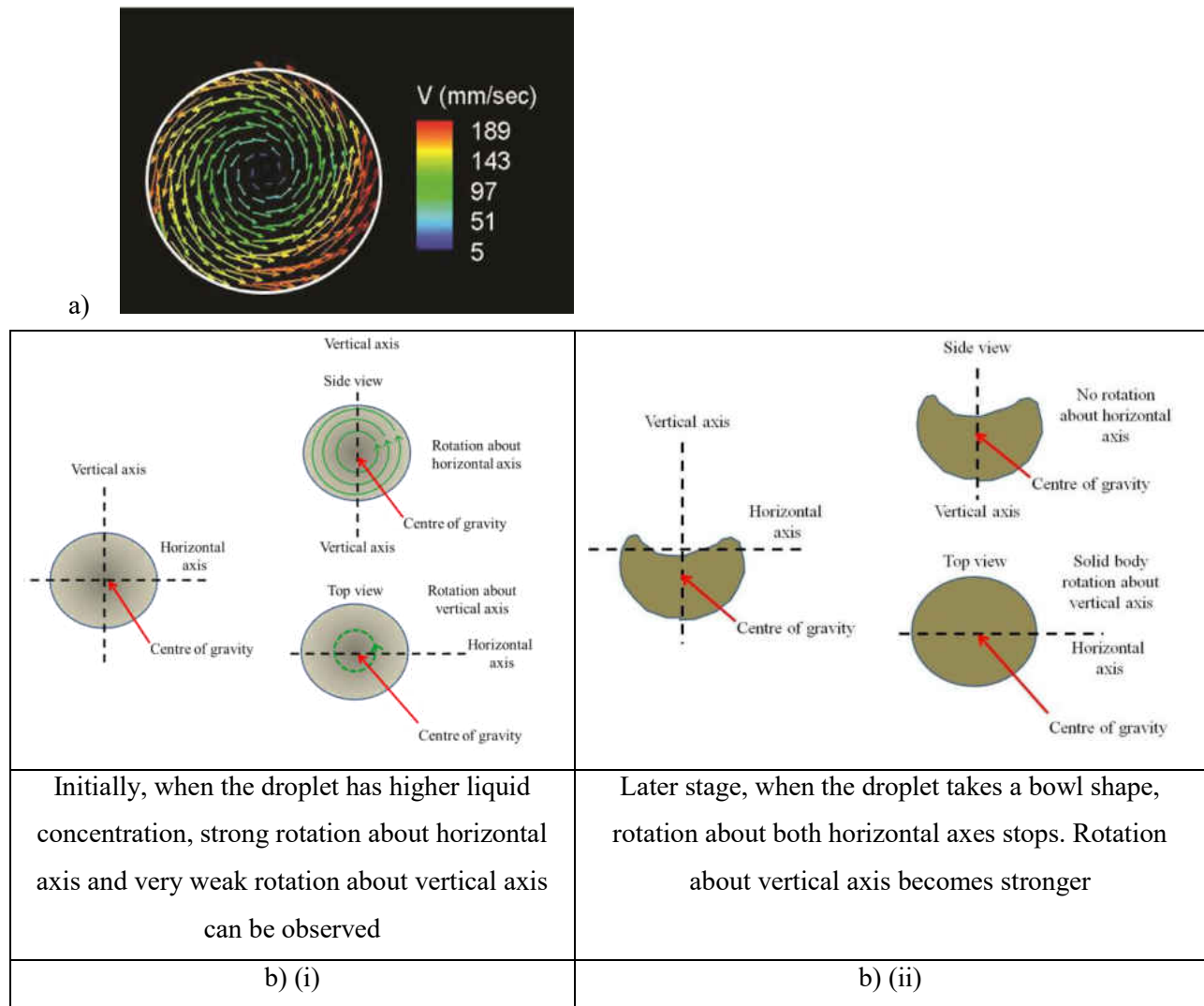
Figure 40: (a) Velocity vectors (mm/sec) for 700μm cerium nitrate droplet [Saha et al. (2012a)], (b) Schematic of rotation about two axes: (i) initial time instant, (ii) after bowl formation

As mentioned in the Chapter 3 (Section 3.2) levitated droplet under acoustic streaming shows two kind of motions: one about horizontal axis and other about a vertical axis. For pure liquid droplets rotation about horizontal axis is much stronger than rotation about vertical axis. The rotational speed is correlated with droplet size and viscosity as shown in Chapter 3 (section 3.3.5). Figure 40a shows a velocity vector on a vertical plane in a 700 μm levitated cerium nitrate droplet obtained by particle image velocimetry (PIV). This shows a stronger recirculation in the droplet. As detailed earlier, the natural evaporation process is dominated by vaporization of solvent (water in our case) resulting in an increase of local concentration of solute (cerium nitrate). Due to this recirculatory motion, precipitates get deposited at the bottom of the droplet as described for nanosilica in Chapter 4. This results in local precipitation of solute, cerium nitrate. This preferential accumulation of the solute at the lower half results in a bottom heavy structure with increased rigidity against deformation. Due to imbalance in force distribution, the upper section of the droplet containing the liquid solvent is, hence, prone to deformation due to acoustic force, allowing the top portion to cave in. Thus, the droplet attains the shape of a bowl. Note that in our experiments with pure water (no solute present), no bowl structure was observed. This affirms the fact that the presence of precipitated solute in the levitated droplet coupled with acoustic streaming led to a bowl-shaped structure formation.

It is also important to note that velocity vectors obtained from PIV did not capture the droplet rotation about the vertical axis. It is also evident from the high speed images and videos that the suspended droplet rotates about the levitator axis. The speed of rotation increases with time when the droplet turns into a semi-solid bowl. It is realized that this rotation is due to the asymmetric pressure field in the radial direction. After precipitation, the droplet can only undergo a solid

body rotation. However, the bowl-shaped structure does not allow the rotation about the horizontal axis because the gravitational force needs to be overcome. On the other hand, imbalance of acoustic pressure in the radial direction allows the droplet to rotate freely about the vertical levitator axis. The viscosity of the cerium nitrate solution was measured to be 20% higher than that of water. With increase in viscosity and subsequent precipitation, the recirculation (rotation) within the droplet about the horizontal axis is dissipated while the rotation of the droplet about the vertical axis is increased. These phenomena have been schematically shown in Figure 40b.

5.3.2.2 Experiments with laser heating

This section analyzes the results obtained with laser heating of the cerium nitrate droplet suspended in the acoustic levitator. Although many different laser powers were used, detailed discussion was limited only to those extreme cases which showed distinctly different phenomena.

5.3.2.2.1 The high laser power case (laser flux 1.8 MW/m^2)

The analysis of high speed and IR images showed that the droplet goes through at least four distinct stages during the heating process. These four stages are 'pure evaporation', 'evaporation with precipitation', 'chemical reaction with bubble formation' and 'porous precipitate'. The identification of these zones was done manually with the help of high speed images, temperature data and diameter plots. Stage 1: Pure evaporation starts with heating. Stage 2: Evaporation with precipitate formation is considered to be initiated when the diameter and temperature plots exhibit a change in slope and the high speed images show the formation of a bowl-shaped droplet

from a predominantly spherical one in stage 1. Stage 3: Chemical reaction with phase change to bubble formation is marked by the increase in droplet diameter, sharp change in the temperature slope and onset of bubble formation. Stage 4: Porous precipitate is formed when the bubbles stop forming and the droplet attains the form of a stable precipitate. A change in slope is not very apparent in cases of low laser power where other criteria such as temperature change or high speed images are given priority to delineate the different stages.
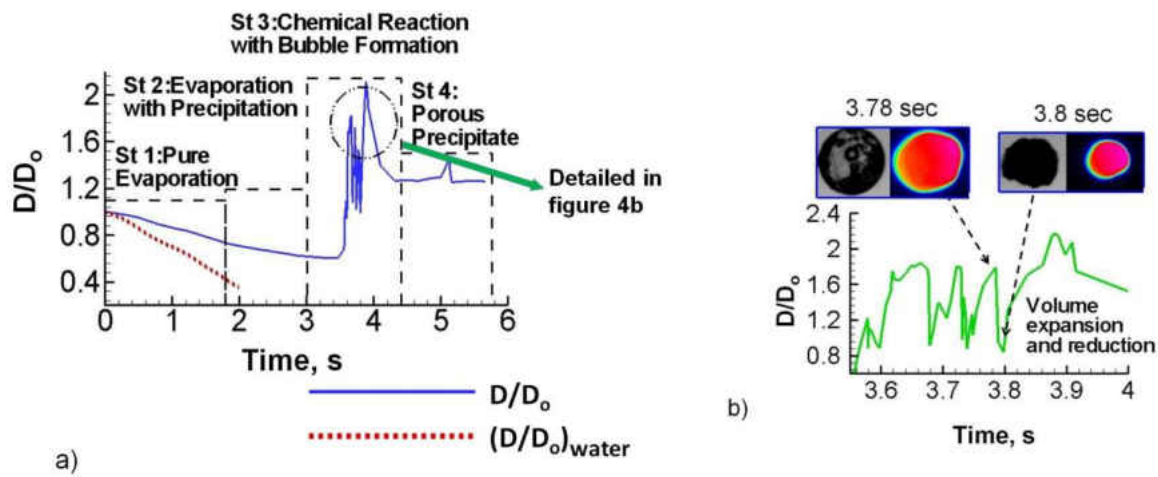
Figure 41: (a) Evolution of diameter with time at high laser power (1.8 MW/m^2) for cerium nitrate and water (b) Expanded view of phase 3: chemical reaction and bubble formation

Figure 41 shows the change in diameter for a laser flux of 1.8 MW/m^2. The total heating time for this laser power is 5.3sec. In the pure evaporation phase, the cerium nitrate droplet diameter reduces almost linearly with time reaching a value of 76% of the initial diameter. The maximum and average droplet temperatures profiles in Figure 42 exhibit a steady increase for the first 0.8 sec of the heating process and attain almost a steady value subsequently. The initial 0.8 sec of heating shows a large difference between maximum and average temperature of the droplet, which is also reflected as higher standard deviation of surface temperature. This difference in

maximum and average values of the temperature can be attributed to the directional nature of radiative heating used in the current experiment. The temperature front moves across the droplet surface and at the end of this phase at 1.8 sec, the surface temperature equilibrates out, marked by smaller differences in maximum and average temperature, resulting in lower standard deviation. This phase ends at a maximum temperature of 68°C. Simple convective evaporation is generally characterized by D^2 law which is attributed to the parabolic nature of diameter reduction curve with time. However, D^2 law assumes uniform surface temperature of the droplet of pure composition (no solute present). The current experiment satisfied none of these conditions. Also D^2 law is generally applied for convective heating, where the heat transfer is governed by a temperature difference (between droplet surface and ambient gas phase). On the other hand, the radiative heating in the current experiment uses a constant heat flux, which depends on laser intensity. Hence the results deviated from the D^2 law.
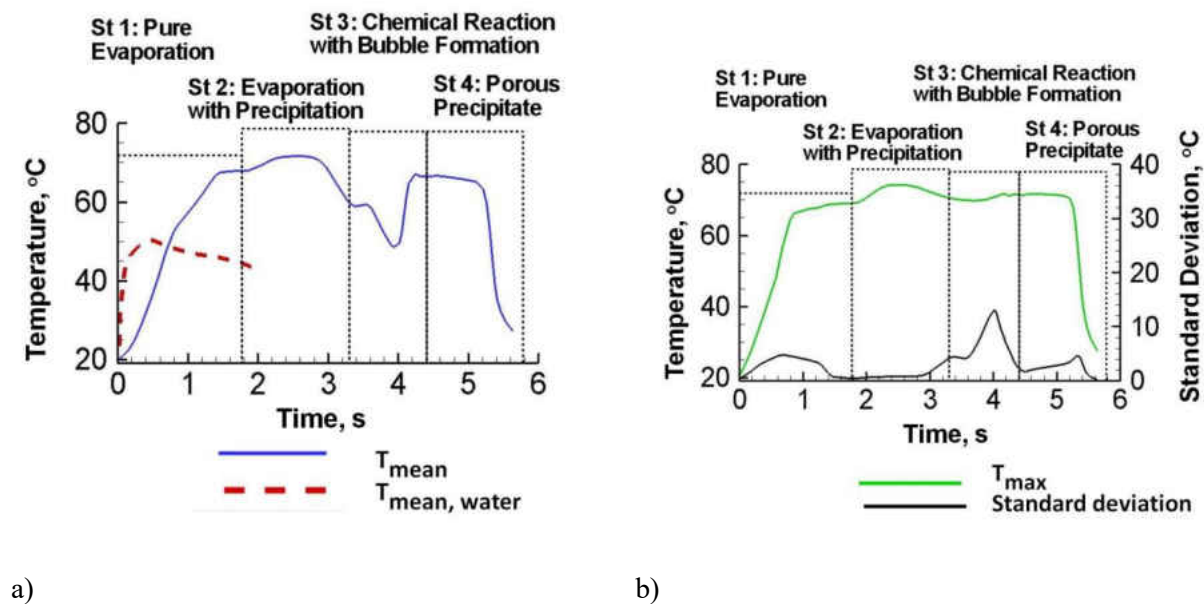
Figure 42: Temperature evolution with time: (a) Mean temperature for cerium nitrate and water and (b) Maximum temperature and standard deviation

The second stage of heating process is characterized by slower evaporation. The onset of this stage is marked by the triggering of surface precipitation of cerium nitrate. This stage is referred to as evaporation with surface precipitation. Precipitation reduces the droplet to a bowl-shape (Figures 39 and 43). The heating process during the pure evaporation phase resulted in a substantial amount of evaporation of water, increasing the solute concentration to super-saturation limit near the droplet surface. This triggers precipitation which engulfs regions of the droplet (especially near the surface) where local saturation concentration of the solute (cerium nitrate) is exceeded. The precipitate is believed to be a perforated solid matrix and not a continuous shell (with a trapped liquid core). The rate of evaporation is reduced in the presence of the solid precipitate and high solute concentration near the surface due to reduced vapor pressure as given by Raoult's law: $P_{sat-eff} = \chi_{solv}.P_{sat}$, where $P_{sat\text{-eff}}$ and P_{sat} are effective and actual vapor pressure of the solvent and χ_{solv} is mole fraction of solvent. An increase in the solute concentration reduces χ_{solv}, the mole fraction of the solvent (water). Thus the effective vapor pressure decreases and consequently, the vaporization rate is reduced. This is confirmed by the decrease in slope of the diameter reduction plot in this phase (Figure 41a). Slower evaporation rate (compared to pure evaporation) lowers latent heat and increases available sensible heat and thus the droplet temperature increases with time in Stage 2 and reaches a maximum of 75°C. The surface temperature of the droplet remains almost uniform with a lower standard deviation. This stage extends for 1.2 sec reducing the diameter to 60% of the initial value.

Next stage of heating involves phase transformation and is distinctly marked by bubble formation and droplet expansion. This stage is termed as chemical reaction and bubble formation. High speed images and video (not shown) show erratic bubbling and collapsing phenomena. This bubble formation is a marker of the initiation of thermal decomposition of cerium nitrate, which results in ceria and oxides of nitrogen. Nitrogen dioxide and oxygen created as byproducts of chemical reaction are manifested by the formation of bubbles. These bubbles result in sudden expansion of the droplet like a balloon, and are subsequently vented out through the pores. This process of ballooning and collapsing is repeated throughout Stage 3, showing rapid oscillations in droplet diameter (Figure 41b) for 0.4s, ranging from 70% to 200% of its original diameter. The IR images also show a non-uniform temperature distribution of droplet surface temperature due to the presence of vapor pockets. The sudden decrease in surface temperature clearly indicates the formation of ceria as the reaction is endothermic. Although the maximum droplet temperature remains around 70°C (Figure 42b), the average temperature decreases to a low value of 50°C (Figure 42a). The non-uniformity of droplet surface temperature during this phase is also marked by a standard deviation as high as 15°C. From the beginning of this phase to the peak in violent reaction for 1.1 second, the average temperature decreases. When the reaction is complete, the temperature rises again rapidly within 0.2s to nearly the mean value in the previous phase. This stage of chemical transformation has a lifetime of 1.4 sec resulting in the formation of transparent ceria from cerium nitrate.

$Ce(NO_3)_3 \rightarrow CeO_2 + NO_2 + \frac{1}{2} O_2$ - 208.8 J/mole of Cerium Nitrate   (5.1)
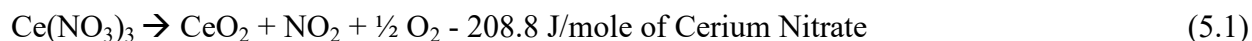
The final stage of heating, termed the porous precipitate, is quiescent in nature. This region does not exhibit significant change in diameter which signifies the completion of solvent evaporation and chemical transformation (cerium nitrate to cerium oxide). Droplet diameter does not change with time except for the formation of very small bubbles. The final diameter of the droplet is around 120% of its initial size due to its porous microstructure. The venting of gases (oxides of nitrogen) liberated during chemical transformation of cerium nitrate creates pores in the solid precipitate. This process of chemical transformation is so rapid that some of the gases might have been trapped as submerged bubbles within the precipitate. Both the mean and maximum temperature (Figure 42a and b) plots in this stage of heating show almost a constant trend until the laser was turned off. Subsequently, the temperature drops very sharply. Some portions of the droplet cool down faster than others (especially the pores) resulting in a high standard deviation of surface temperature (Figure 42b). A synopsis of the different stages undergone by the droplet subjected to high heat flux is provided in Figure 43 along with samples of high speed, IR images, maximum, average temperature along with the standard deviation during each stage.

A separate experiment was performed with pure water droplets without any solute being present. Figures 41 and 42 show the diameter and temperature plots for water droplet. Clearly the water droplet vaporizes much faster than the cerium nitrate droplet. As explained earlier, the presence of solute results in a decrease in vapor pressure of the solvent, which in turn reduces surface vaporization. Faster evaporation of pure water requires more latent heat reducing the available sensible heat for the temperature rise. This results in lower temperature rise in the case of pure water. Fourier Transform Infra-Red Spectroscopy (not shown here) has shown water and cerium nitrate solution have the same absorption characteristics at wavelength of 10.6 μm. This confirms

that the departure of diameter and temperature plots of cerium nitrate from those of pure water is purely due to different governing physics like precipitation and solute presence. Experiments reported here are repeatable, with the global features remaining the same with utmost 5% deviations in temperature and drop size.
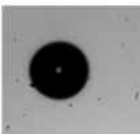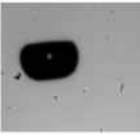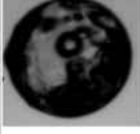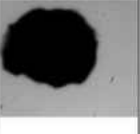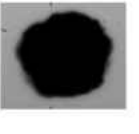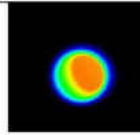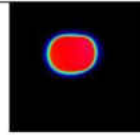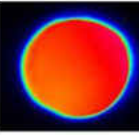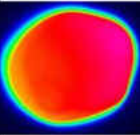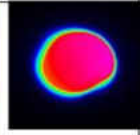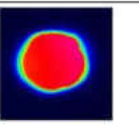
	Stage1: Pure Evap.	Stage2: Evap. With Precip.	Stage3: Chemical Reaction and Bubble Formation			Stage4: Porous Precip.
	1.53 s	2.54 s	3.65 s	3.78 s	3.8 s	5.25 s
High Speed Image						
IR images						
D/Do	0.8	0.7	1.7	1.8	0.8	1.2
Mean Temp, °C	68	72	54	49	52	66
Std dev, °C	0.4	0.8	5.3	7.9	6.2	2.1

Figure 43: Different phases of heating process for high flux (1.8 MW/m^2).

5.3.2.2.2 Microstructural characterization

Microstructural characterization revealed interesting morphologies of the precipitate as shown in Figure 44 and also helped in identifying the phases present unambiguously. Under the optical microscope, the precipitate looked optically translucent (Figure 44a). SEM results, at a higher magnification, showed the presence of a smooth layer which is partially optically clear (Figure 44b). TEM images (Figures 44c and d) provided the most useful information. Figure 44c clearly shows the presence of trapped gases in the form of bubbles inside the microstructure. These bubbles coexisted with the precipitate particles. The precipitate particles were found to be present both in crystalline and amorphous conditions. While there was no diffraction contrast in the amorphous particles, clear lattice fringes could be observed in the crystalline precipitates at higher resolutions.

It is possible that the precipitate has transformed into an amorphous phase due to rapid cooling. Once the laser power has been turned off, the particle, being small in size, cools very quickly. Rapid cooling of melts has been known to result in formation of amorphous (glassy) phases in several materials systems [Suryanarayana and Inoue (2010)]. In fact, it is much easier to form glassy phases in oxide systems. Therefore, it is not surprising that the precipitate has transformed into an amorphous phase. It could be easily inferred that the amorphous phase is responsible for the translucent nature of the precipitate.
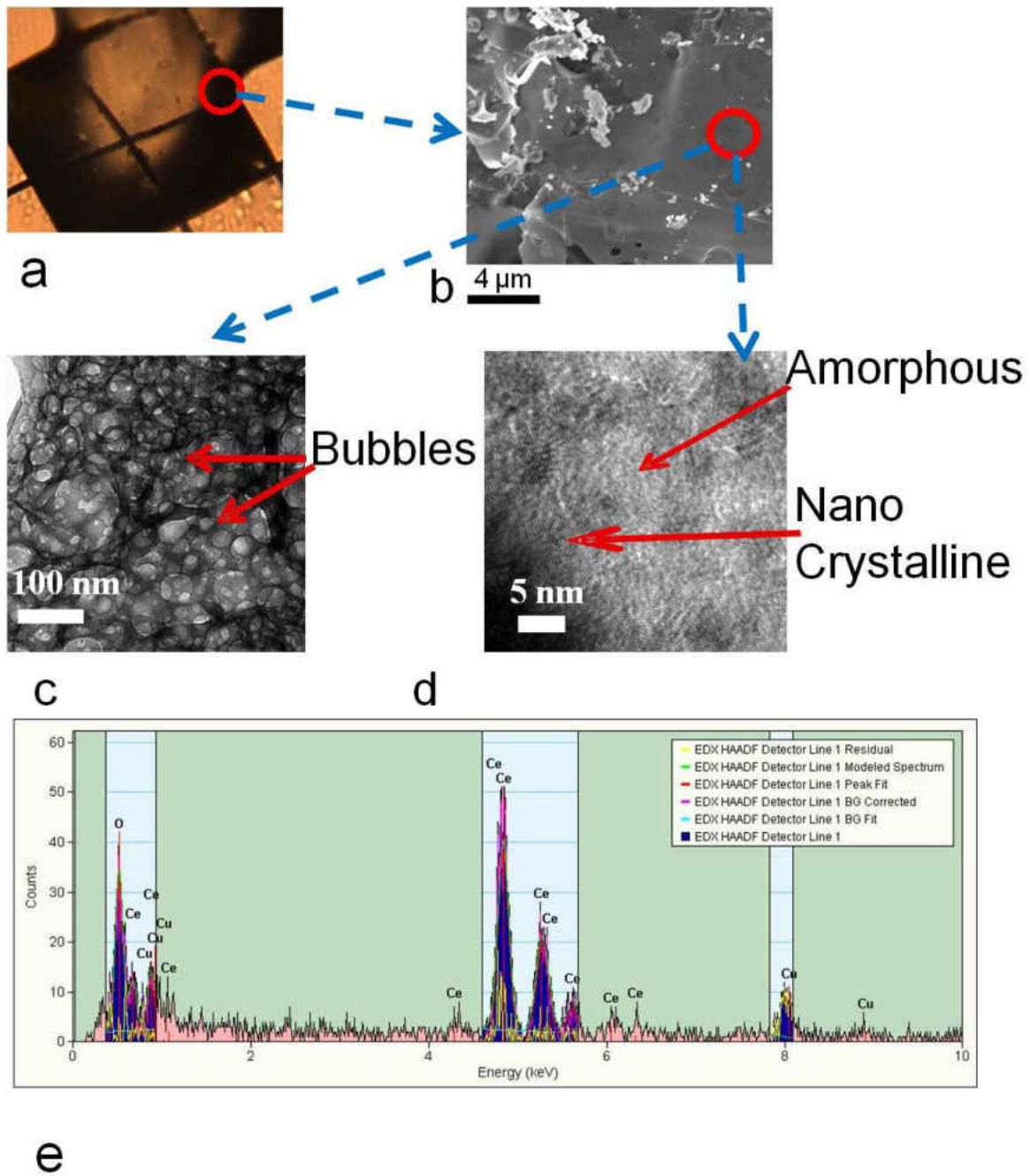
Figure 44: Final precipitate (a) Under optical microscope, (b) Scanning electron microscope, (c) and (d) Transmission electron microscope, e) EDX

Some of the precipitate particles have been observed to be crystalline in nature, as revealed by the presence of lattice fringes. The crystalline precipitates have a grain size of about 5-10 nm, confirming the formation of nanoparticles of ceria. From selected area diffraction patterns recorded from the crystalline precipitate particles, it could be shown that these particles have a face-centered cubic (FCC) structure with a lattice parameter of a = 0.5412 nm. By comparing this information with the standard diffraction patterns, it could be confirmed that the precipitate formed is CeO_2 [JCPDS Card #81-0792]. The crystalline precipitates might have formed due to crystallization of the amorphous phase.

EDX plots (Figure 44e) from the precipitate revealed that the two primary elements present in the precipitates are about 27% (73 wt.%) cerium and 73% (27 wt.%) oxygen. Since oxygen is a light element, the accuracy with which it could be analyzed is rather low. However, using the data from both selected area diffraction patterns and EDX, it could be concluded that the precipitate formed is CeO_2. Thus, it could be inferred that cerium nitrate has transformed into ceria.

5.3.2.2.3 The low laser power case (laser flux 0.45 MW/m^2)

All the four stages of the heating process described in the previous section are also observed in the case of low power with a heating flux of 0.45 MW/m^2. However, the total time of heating is much longer (23.2s) compared to the high laser power (flux 1.8 MW/m^2). Figures 45 and 46 show the diameter and temperature plots for the low power condition.

The pure evaporation stage is extended up to 8 sec with a sharp rise in temperature at the initial stage. The mean temperature reaches around 55°C and becomes almost constant (Figure 46a).

Figure 46b shows that the maximum temperature follows the same trend and saturates around 58°C. As in the case of high power heating, the initial stage of heating process shows a higher standard deviation of the droplet surface temperature (Figure 46b). As explained earlier, this can be attributed to the directional nature of the heating process. The diameter plot in Figure 45 shows a slower vaporization rate for the initial stage of 2.5 sec.
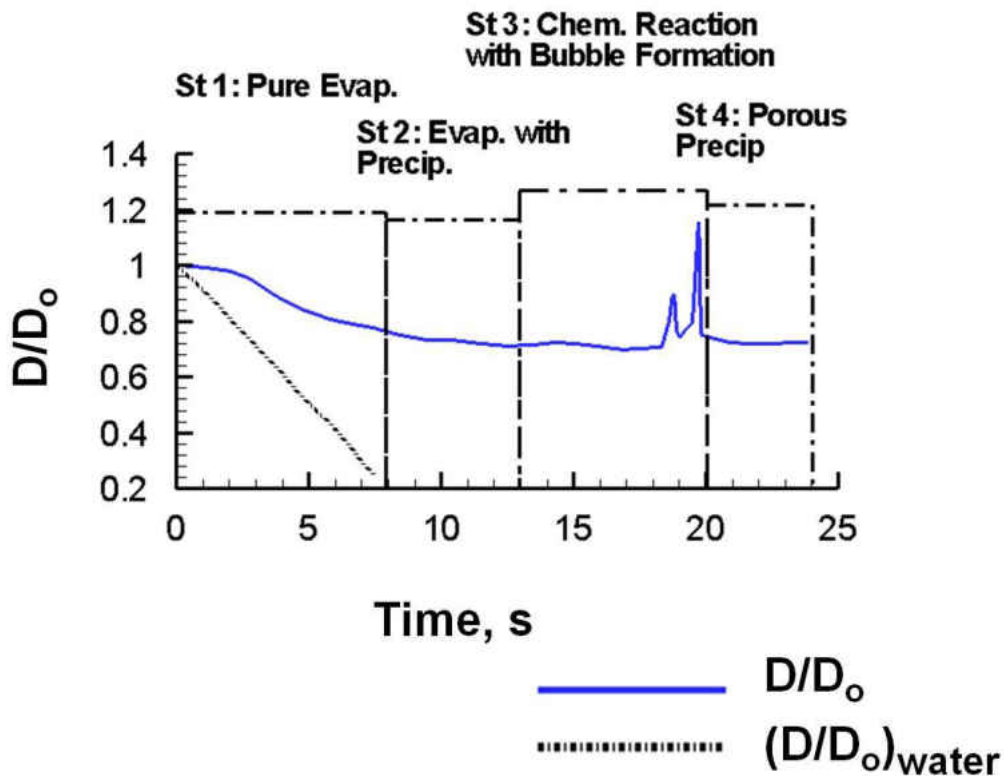
Figure 45: Diameter evolution for cerium nitrate and water for low flux (0.45 MW/m^2).

The second stage of heating 'evaporation with precipitation' is very similar in the case of high heating (laser flux 1.8 MW/m^2) with a slow vaporization rate and uniform surface temperature around the droplet. The slope change between the first and second stages is discernable as in high power.
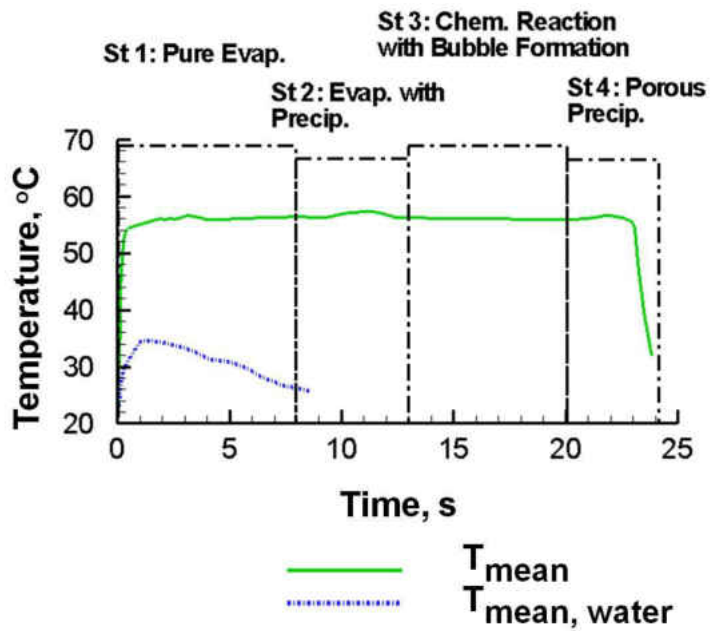
a)
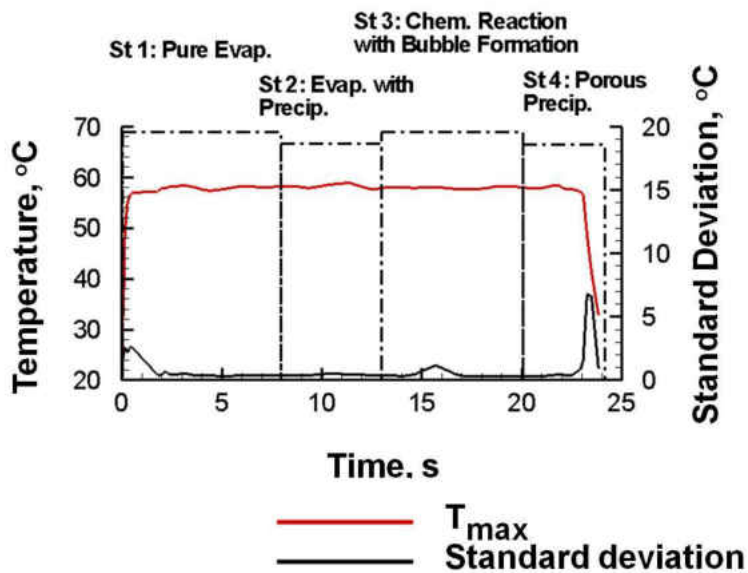
b)

Figure 46: Temperature evolution for low laser flux (a) T_{mean} for cerium nitrate and water, (b) T_{max} and standard deviation of temperature for cerium nitrate.

135

The third stage of 'chemical reaction and bubble formation' in the case of low laser flux of 0.45 MW/m^2 is not as erratic in nature as in the high flux (1.8 MW/m^2) case. The primary reason is that the amount of irradiative heat dumped into the droplet is low and hence the thermal decomposition of cerium nitrate is slow in progression. The droplet expands slightly as seen in the diameter plot of Figure 45 towards the end of this phase. The temperature remains constant around 55-57°C. At the end of this stage (after 20s) the droplet is completely transformed into a porous precipitate.
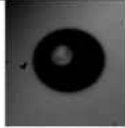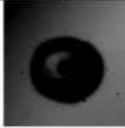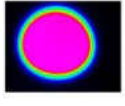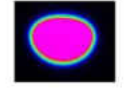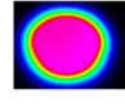
	Stage1: Pure Evap.	Stage2: Evap. With Precip.	Stage3: Chemical Reaction and Bubble Formation			Stage4: Porous Precip.
	5.15 s	11.5 s	18.5 s	19.0 s	19.8 s	22.0 s
High Speed Image						
IR images	60 °C	50 °C	40 °C		30 °C	20 °C
D/D$_o$	0.82	0.75	0.87	0.78	1.1	0.8
Mean Temp, °C	56.1	59.2	56.2	56.4	52	56.26
Std dev, °C	0.3	0.66	0.29	0.33	0.35	0.41

Figure 47: Different phases of heating process for low flux (0.45 MW/m^2)

As in the case of high laser power, the last stage of porous precipitate is quiescent and uneventful. Figure 47 shows the different stages for low power along with representative images, drop size and temperature in each phase.

The ex-situ analysis with the TEM showed similar results. TEM images showed that the final precipitate contained both nanocrystalline and amorphous structures. Also, the primary elements present in the microstructure were found to be cerium and oxygen, forming nanoceria.

A separate experiment was conducted with pure water which shows faster evaporation and lower temperature rise compared to cerium nitrate solution as shown in Figures 45 and 46. As described before this can be explained by Raoult's law.

5.3.2.2.4 Very high power laser power (laser flux 2.5 MW/m^2) case with explosive vaporization

To observe the effect of very high heating rate on the droplet evaporation process, a laser flux of 2.5 MW/m^2 was used. At 2.5 MW/m^2, the droplet undergoes an explosive heating process and detaches from the levitator anti-node. Figure 48 shows a series of high speed and IR-thermography images of the process. They show that the droplet surface temperature increases very rapidly to almost 95°C and subsequently the droplet explodes. The whole event has a timescale of the order of 1 sec. This kind of explosive nature of droplet evaporation has also been reported by Park and Armstrong (1989). According to their work, at high powered laser irradiation, some portion of the droplet may attain a temperature more than the superheat value. These hot-spots will serve as nucleation sites for bubble formation resulting in volumetric expansion and consequently explosion, leading to the disintegration of the droplet.

Formation of these hot spots does not occur when the laser power is below a certain level. This can be attributed to the thermal diffusion processes. Directional heating results in sharp temperature gradient through the droplet at the very initial stage of heating. Depending on the rate of thermal diffusion, it takes a finite amount of time for the temperature to equilibrate across the droplet. If the heating rate or laser power in current experiment is higher than the critical value, heat addition will dominate over the thermal diffusion rate resulting in a sharp temperature rise creating a hot spot. This induces localized bubble formation which breaks up the droplet. The experiment shows the critical laser flux to be 2.5 W/m^2.
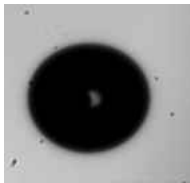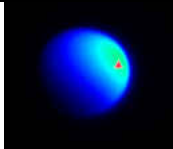
	Time = 0.5 sec	Time = 1.1 sec	Time = 1.2 sec
High Speed Images			
IR Images			No IR image was available at this instant

Figure 48: High speed and IR images for 2.5 MW/m^2 laser flux.

5.3.2.2.5 Intermediate laser powers

Other than the cases described in the previous sections, three intermediate flux (power) levels have also been used for experimentation: 0.98 MW/m^2, 1.3 MW/m^2 and 1.5 MW/m^2. Predictably, high speed and IR images indicate that the result for these cases fall between the two extreme cases marked by lowest (flux 0.45 MW/m^2) and higher laser power (flux 1.8 MW/m^2). Except in the case of the highest flux (previous section), all other cases show the evolution of all four stages of transformation from evaporation to ceria precipitate formation.

5.3.2.2.6 Final volume to initial volume of ceria

The TEM analysis of the final microstructure for both high and low power cases were found to contain bubbles. Thus, the final precipitates for all laser powers are porous in nature. The porosity occurs due to gases liberated during the chemical reaction. The calculation of the final volume with trapped gases as a fraction of the theoretical volume of ceria is done as follows. The mass of cerium nitrate contained in the droplet is calculated first, which yields a certain amount of cerium oxide, assuming complete reaction has taken place. Using Equation 5.1 the mass and volume of cerium oxide are then determined, assuming the density of amorphous and crystalline ceria to be the same. Since the concentration used was the same, this theoretical volume of ceria is the same for all the cases. The final volume of the precipitate including porosity was then determined using high speed images. A conservative analysis was performed to quantify the porosity of the final microstructure. Finally, the ratio of the final to theoretical volume of ceria is a measure of porosity and is plotted in Figure 49. The final volume ratio plot shows that the

porosity increases with laser power and so does the maximum droplet temperature. With an increase in heating power the chemical reaction time scale also decreases, i.e., the gases are released much faster. This increases the amount of trapped gases and therefore the porosity.
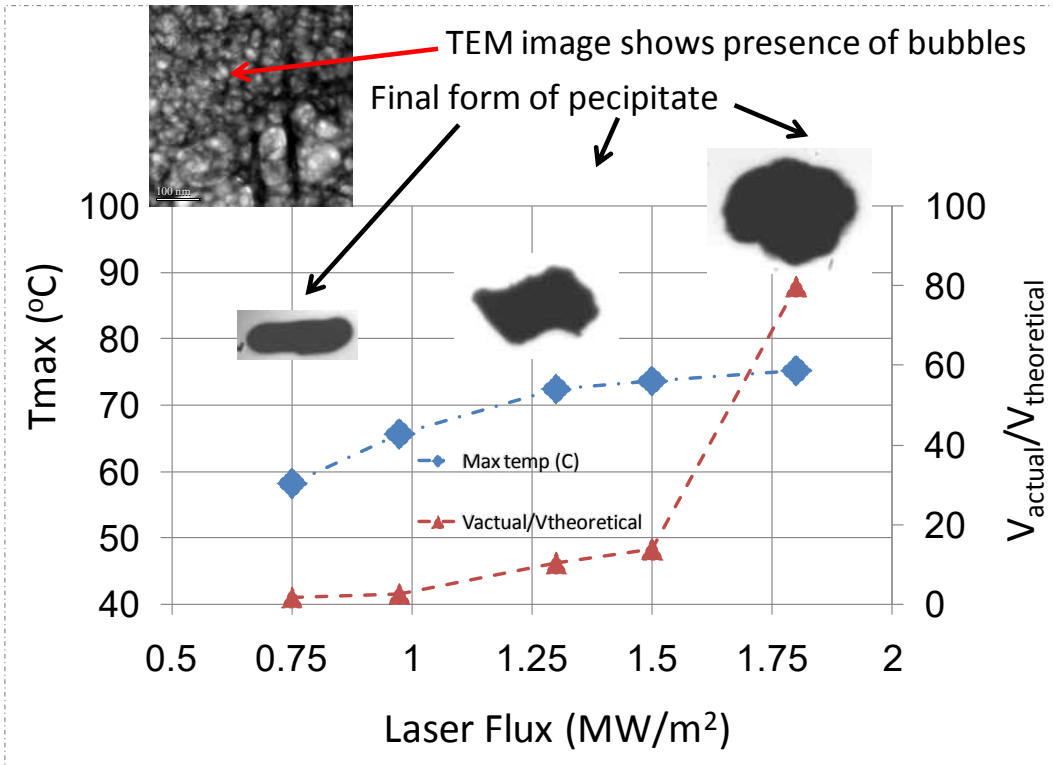
Figure 49: Ratio of actual and theoretical volume of final precipitate with maximum temperature for different laser power.

5.3.2.2.7 Time scale analysis

A comparison of time duration for different stages at different power levels is shown in Figure 50a. It clearly shows that the time for each stage decreases with an increase in power. For stages 1 and 2 which involve mostly vaporization of liquid solvent, the rate of vaporization increases with laser power reducing the time required for the first two stages. On the other hand, the chemical reaction and bubble formation stage needs heat for the completion of thermal

decomposition of cerium nitrate. Since the reaction is endothermic in nature, faster transformation is registered for higher heating, reducing the time involved in this stage.

Based on the above observation, a scaling analysis is developed to non-dimensionalize the time duration in each phase. A scaling parameter, t_s, has been defined to normalize the physical time to obtain non-dimensional time, τ. From the energy balance it can be written,

laser irradiation on the droplet = sensible heat + latent heat, i.e.,

$$I_0(\pi r^2) = mC_p \frac{dT}{dt} + \dot{m} h_{fg} \tag{5.2}$$

With $\dfrac{dT}{dt} \sim \dfrac{\Delta T}{t_s}$ and $\dot{m} \sim \dfrac{m}{t_s}$ Equation 5.2 may be rewritten as

$$I_0(\pi r^2) \sim \frac{4}{3}\rho\pi r^3 C_p \frac{\Delta T}{t_s} + \frac{\frac{4}{3}\rho\pi r^3}{t_s} h_{fg} \tag{5.3}$$

Finally, the time scale is given by

$$t_s = \left[\frac{\frac{4}{3}\rho r(C_p \Delta T + h_{fg})}{I_0}\right] \tag{5.4}$$

This simple analysis shows that with increasing laser power, the time scale decreases. During the experiment the maximum temperature was observed to be varying between 57°C and 75°C for different power levels. An average value of 66°C has been considered to calculate the change in temperature ΔT (= 66-20=46°C).

Using the time scale, t_s, to non-dimensionalize the time during each stage, all the points seem to collapse to yield a single non-dimensional time in each stage (4.0 in Stage 1; 1.75 in Stage 2; 3.5 in Stage 3) as shown in Figure 50b. Small deviations can be attributed to uncertainty in identifying the transition points between different phases.
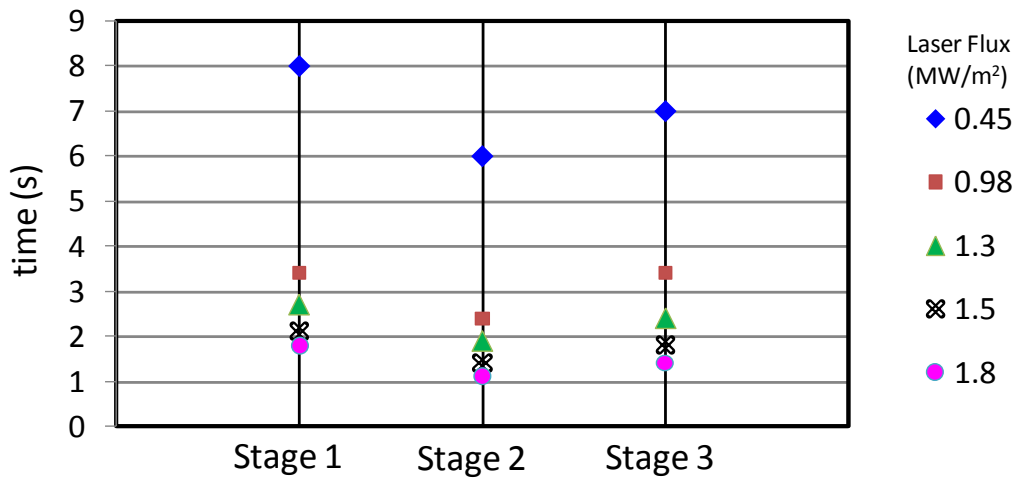
a)
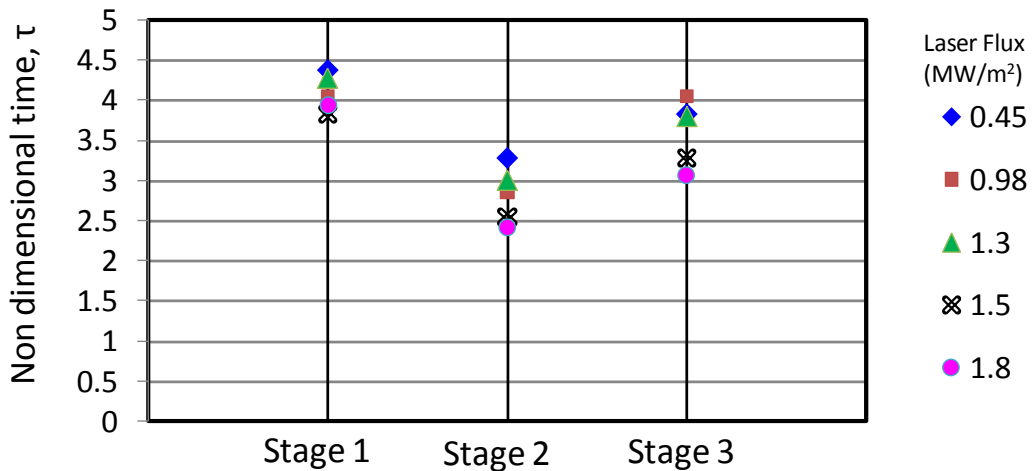
b)

Figure 50: (a) Absolute time and (b) Non dimensional time (τ) for different phases of heating at different laser power

As seen earlier, the initial stages of a droplet heating process are evaporation dominated. At these stages, the droplet shrinks and local precipitation starts. The droplet takes the shape of a bowl. This deformation of droplet is principally the result of solute transport within the droplet. This convective transport can be due to Marangoni convection [Hegseth et al. 1996] caused by a surface tension gradient as well as acoustic streaming due to resonant acoustic frequency. For the frequency and pressure level used in this study (f= 100 kHz; 154 dB), the velocity induced by acoustic streaming within the droplet is of the order of 200 mm/s (Chapter 3) whereas Marangoni velocity scale is of the order of 1 mm/sec. Thus, the acoustic streaming velocity is an order of magnitude higher than that due to Marangoni effects.

When the drop is heated radiatively, surface vaporization increases the solute concentration near the droplet surface symmetrically in the absence of acoustic streaming. However, acoustic streaming coupled with radiative heating leads to a higher probability of concentration increase along the surface in the lower half of the droplet. In addition, due to the pressure difference between the poles, the particles tend to rotate about an axis tilted from the horizontal. This asymmetry in the flow also tends to accumulate the particles near the bottom of the droplet preferentially. Although the droplet shows very weak rotation about the vertical initially, with increased rigidity in the bottom half, the upper section deforms and tends to cave inwards at the top due to the acoustic pressure difference, and the droplet slowly starts rotating faster about the

vertical axis. With time, the drop changes to a bowl structure from a predominantly spherical morphology as seen in the earlier sections.

5.3.2.2.9 Chemical pathway

The results obtained for various laser powers provide different thermo-physical and chemical pathways of the droplet in Figure 51. It describes the different processes observed during the heating cycle. It shows two major paths. If the power level is more than the critical value of 2.5MW/m^2, the droplet will experience rapid temperature rise and nucleate boiling resulting in explosion. This will detach the droplet from the levitator node. On the other hand, if the laser power is kept below the critical level, the droplet goes through four well-delineated stages as mentioned in previous section (5.3.2.2).
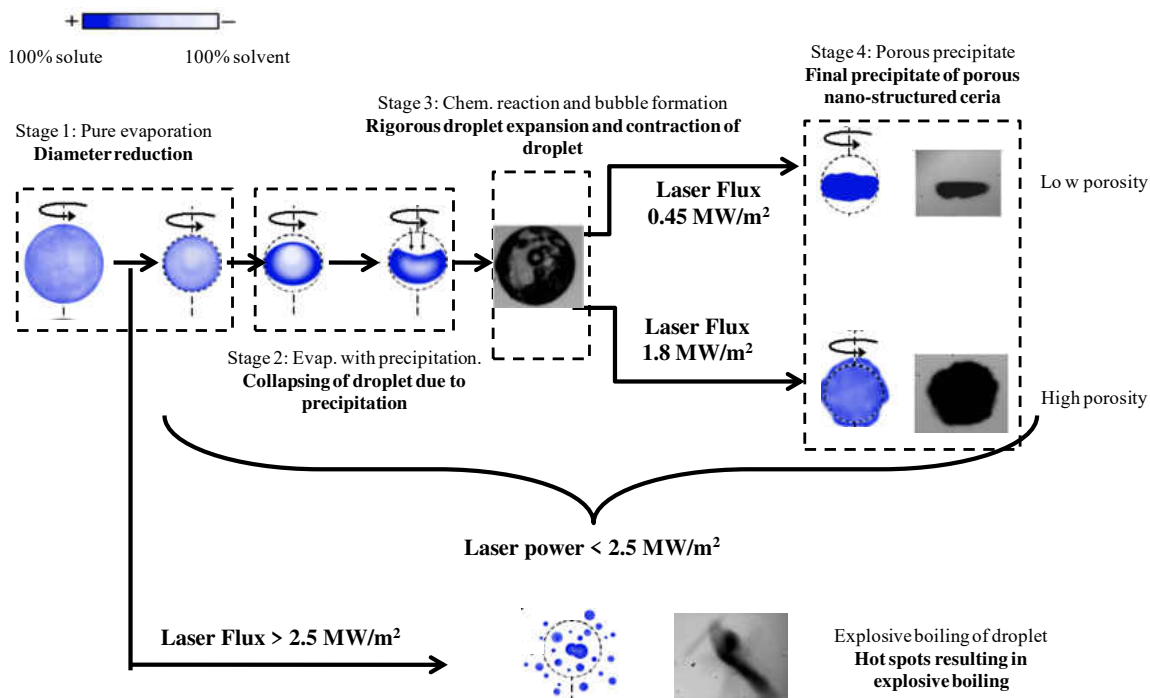
Figure 51: Thermo-physical and chemical pathways for a levitated droplet heated by a CO₂ laser in the presence of acoustic streaming.

5.3.3 Summary of levitated droplet experiments

This investigation shows decomposition of cerium nitrate into nanoceria particles at low temperatures when a droplet is levitated and radiatively heated by a CO_2 laser. Four distinct stages have been identified and the heat transfer process in each stage is discussed. High speed and IR imaging clearly show the distinction in the first two stages of pure vaporization and precipitate formation. The third volatile stage where the chemical reaction takes place within a second is the highlight of this work. This stage is marked by the formation of nanoceria and nitrogen oxides; the formation of gases causes expansion of the droplet and its release through the pores. This remarkable oscillatory behavior is captured for each of the laser power, albeit at different frequencies. Due to the chemical reaction, the final precipitate contains porous microstructure, as confirmed by the TEM images. The effect of laser power in distinguishing the stages was predictable and a time scale was established. The maximum temperature of the droplet increases with power, and the time scale for chemical reaction is lower, which explains the high porosity in the droplet at higher laser power.

Acoustic levitation has an effect on the droplet dynamics especially in the case of binary droplets (solute+solvent). Strong recirculation zone allows the accumulation of the precipitate at the bottom of the levitated droplet. Due to the pressure difference in the poles, the droplet is prone to deformation in the top half, resulting in a bowl-shaped structure. This effect was observed in the absence of laser heating confirming the hypothesis that acoustic streaming and not Marangoni convection is solely responsible for the bowl structure formation. Finally, a criterion has been proposed for possible chemical-thermal path for the droplet depending on the laser power. Very high laser power will disintegrate the droplet due to nucleate boiling. However, laser power

below a critical value will ensure chemical reaction and formation of porous microstructured nanoceria precipitate.

CHAPTER SIX: THERMALLY INDUCED INSTABILITY

6.1 Introduction

Interaction of fluid flow with an external acoustic field has been an important field of study for its wide range of applications in both micro and macro scales such as flame stability in combustion [Lieuwen (2001)], atomization and generation of liquid droplets [Qi et al. 2008], and ultrasonic levitation [Yarin et al. (1998), Xie et al. (2006), Saha et al. (2010a), (2012a), (2012b), Kumar et al. (2010)]. Results have been reported on the generation of droplets from the long range capillary waves using ultrasound [Qi et al. (2008), Lobdell (1968), Anilkumar et al. (1991), Lierke (2002)]. The physics of ultrasonic atomization of fuels in the presence of a surface tension gradient and temperature dependent properties is not treated in these studies, particularly for vaporizing droplets subject to significant external heating.

In this chapter, the thermal effects that lead to possible instability and break up are reported in acoustically levitated fuel droplets. Our observations clearly illustrate that under certain conditions, heated droplets are susceptible to two distinct modes of instability: a) short wavelength Kelvin-Helmholtz instability that pinches into satellite droplets at the equator but triggers no significant transient shape change, and b) long wavelength capillary wave instability that leads to significant variation in droplet aspect ratio and eventually to catastrophic breakup of the droplet. This unexpected finding that the temperature-dependent fuel properties and external heating rate may be exploited to provide insight into the relative strength of these two instabilities. Depending on the surface tension and viscosity gradients with temperature, either or both or no instabilities can occur in a droplet. Furthermore, the secondary atomization caused by

short range pinching at the droplet equator always precedes the capillary waves that trigger bulk breakup, if both instabilities were to occur. The criteria for the occurrence of such instabilities are provided. Without external heating, no instabilities are observed throughout the entire lifetime of the droplet. In this chapter, the first type of instability that can be observed at the droplet equator is discussed. The second type of instability of long wavelength will be discussed and explained in a subsequent section.

6.2 Experimental setup

A 100 kHz acoustic levitator with amplitude of 156 dB (SPL) was used to suspend the droplets. The droplets were generated at the levitator pressure node using a micro syringe. A CO_2 laser with a beam diameter of 4 mm, lasing at 10.6 μm has been used to heat the droplet. The heating event has been recorded simultaneously by a high speed camera whose images were processed to obtain instantaneous diameter, aspect ratio and shape changes, and an infra-red (IR) camera to obtain the surface temperature of the droplet. Both cameras use microscopic lenses to increase the spatial resolution. The high speed camera was operated at 3000-10000 fps, while the IR camera was operated at 100 fps. For further details please refer to the Chapter 2.

	T_S (°C)[#]	σ (mN/m)[\$]	dσ/dT (mN/m/K)[##]	μ (cP)[\$]	P_{sat}/P_{atm} [\$]	ρ_l (kg/m³)[\$\$]	h_{fg} (kJ/kg)[\$\$]
Kerosene	25 – 80	29.1 - 22.0	-0.117	1.82 - 0.85	4.33×10^{-3} - 4.38×10^{-2}	790	322.2
Ethanol	25 – 60	22.5 - 19.4	-0.088	1.36 - 1.02	2.28×10^{-1} - 6.15×10^{-1}	789	904
Diesel	25 – 80	31.6 - 23.9	-0.140	2.81 - 1.60	1.49×10^{-3} - 1.13×10^{-2}	760	588.7
Bio-diesel	25 – 90	31.7 - 23.0	-0.123	4.60 - 1.70	4.49×10^{-9} - 1.01×10^{-5}	787	254

[#]: initial and final temperature, [\$]: determined at initial and final temperature, [##]: averaged over the temperature range

observed during the experiment, [\$\$]: at initial temperature

Table 4: Temperature dependent property values for the fuels. T_s: surface temperature, σ: surface tension, μ: dynamic viscosity, P_{sat}: vapor pressure, ρ_l: liquid density, h_{fg}: latent heat
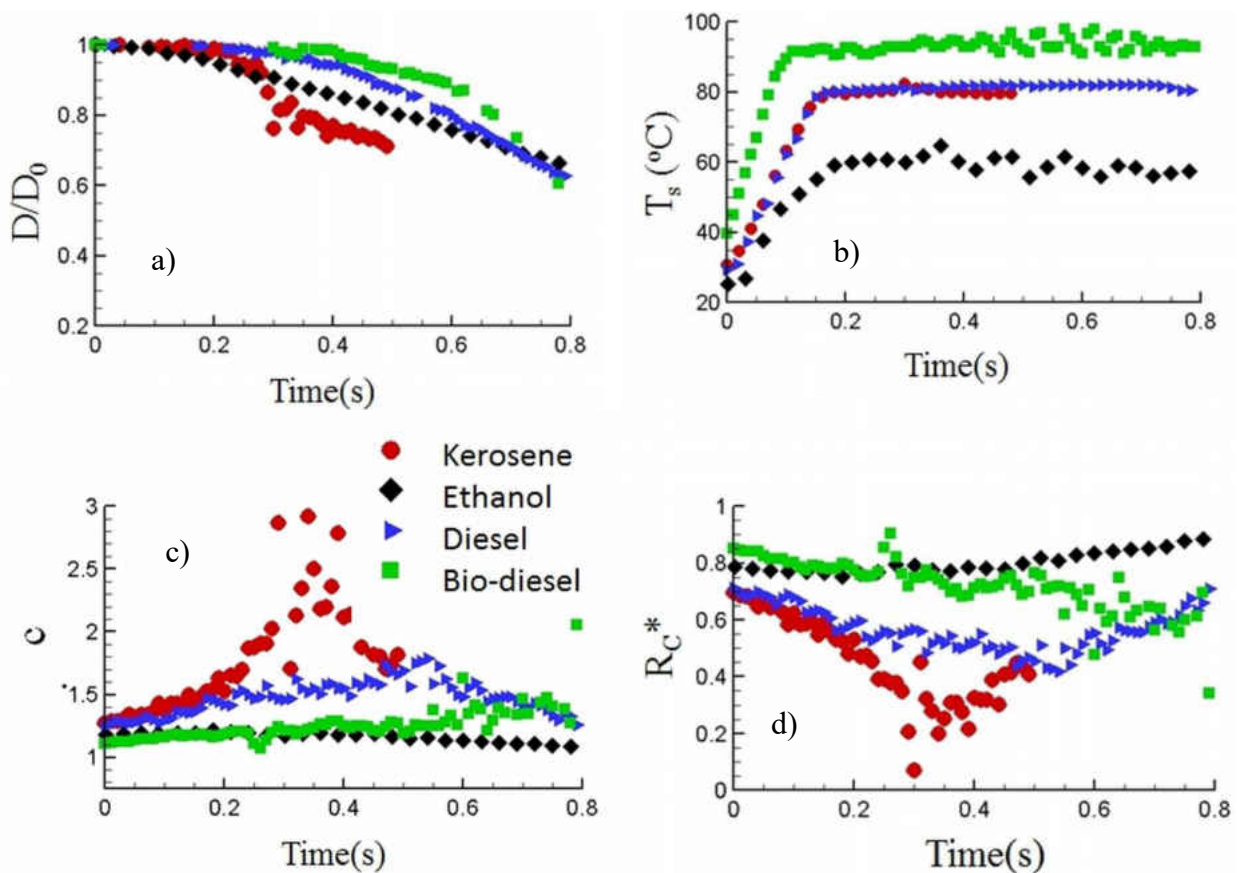
Figure 52: (a) Non-dimensional diameter (D/D$_0$), (b) Average surface temperature (T$_s$), c) Aspect ratio (c), (d) Non dimensional radius of curvature (R$_c$*=R$_c$/R) for different fuels, R is equivalent radius of the droplet

6.3 Results

Pure liquid droplets of four different fuels namely ethanol, diesel, kerosene, bio-diesel were levitated. The droplets had initial diameter of 500 +/- 10 μm and were irradiated with 1.25 MW/m^2 heat flux. The radiative heating causes a sharp regression in droplet diameter (Figure 52) for the initial 0.2s. The diameter reduction rate is fastest for ethanol, while kerosene, diesel and bio-diesel vaporize slowly. The ethanol vapor pressure is higher (Table 4) compared to the other three fuels, leading to a faster vaporization rate. The surface temperature of the droplet (Figure 52) is analogous to the wet-bulb temperature of a vaporizing droplet in a hot gas medium, and is low at the onset of heating; however as the vapor pressure of the liquid increases with temperature, the evaporation rate increases. Faster vaporization progressively requires higher amount of latent heat thereby reducing the available sensible heat responsible for temperature rise. Maximum temperature is reached at equilibrium, which depends on the heating rate, vapor pressure, latent heat and specific heat of the fuel. It is lowest (60°C) for ethanol and highest (95°C) for bio-diesel. Both kerosene and diesel exhibit maximum temperature of 80°C.

After 0.3-0.4s of heating, one can observe different types of instabilities arising in kerosene, diesel and bio-diesel droplets. These fuels start atomizing from the equator in the form of small droplets of sizes ~1-10 μm (Figure 53). This is a short wavelength instability that pinches tiny droplets at the equator. At the onset of this secondary atomization, the diameter reduction becomes a cumulative outcome of two events, i.e., evaporation and small scale atomization for all three fuels. Ethanol droplet, on the other hand, does not exhibit any atomization, hence the slower diameter reduction rate. Other events related to kerosene will be discussed in the next section (6.3.2).

150
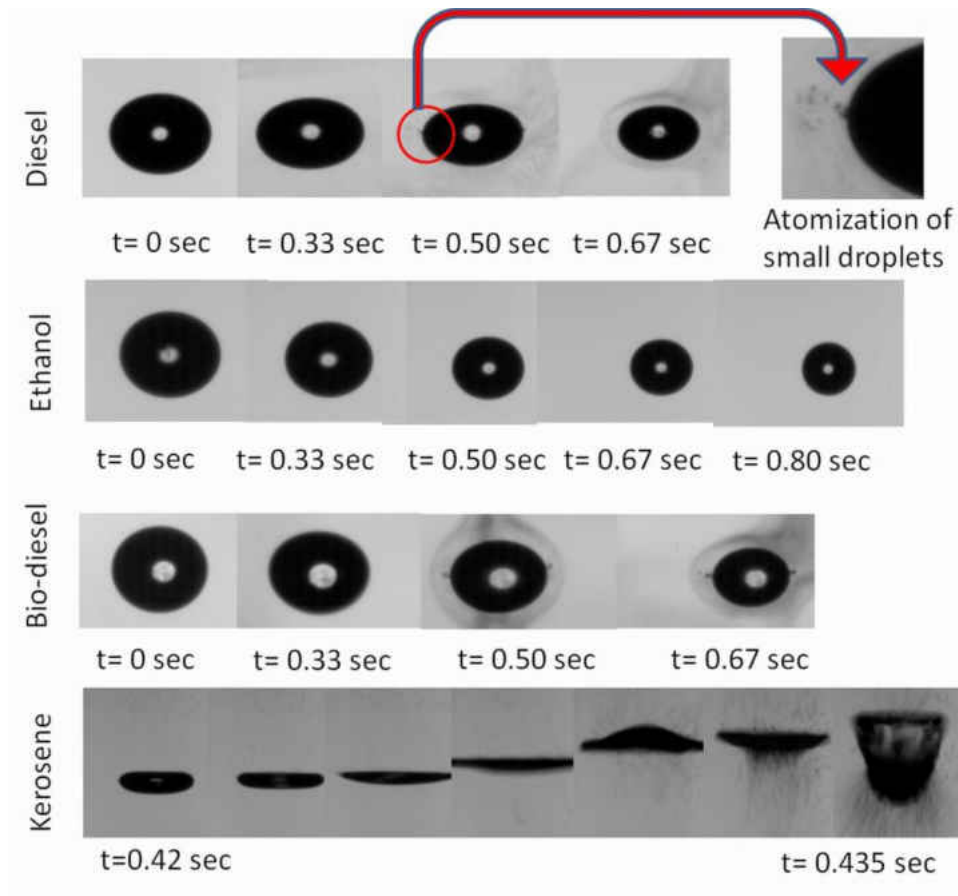
Figure 53: High speed images of atomization [diesel: atomization, biodiesel: atomization, Ethanol: no atomization] and stretching [kerosene: stretching] of droplets

6.3.1 KH instability

The classical Kelvin-Helmholtz (KH) type instability sets in when the relative motion between the levitated droplet and the surrounding air exceeds a critical value. This depends on the surface tension and density of the fluids [Chandrashekhar (1981)]:

$$u_{crit}^2 = [2(\rho_l + \rho_0)/\rho_l \rho_0]\sqrt{\sigma.(\rho_l - \rho_0).g} \qquad (6.1)$$

where ρ_l and ρ_0 are densities of liquid and air respectively, σ is surface tension, g is acceleration of gravity. The relative velocity can be approximated by the acoustic streaming velocity, u_{str}.

151

For KH-instability, $u_{str} > u_{crit}$ condition has to be satisfied. In general the KH instability is the imbalance between gravitational force and shearing force due to relative motion between two fluid layers. In a levitated droplet, this can be extended to the instability between shear force due to acoustic streaming velocity at the droplet surface and net downward or upward force acting on the droplet, which can be scaled as 'g' (gravitational acceleration). Although the net force may be different on the top and bottom sectors of the droplet, the critical condition always occurs near the equator, as it has the smallest radius of curvature (explained later) and at this point the shear force due to streaming velocity (which is parallel to droplet surface) and the net gravitational force will act against each other leading to maximum instability. The acoustic streaming velocity is expressed as,

$$u_{str} = P_0 \gamma_0 Ma / \rho_0 c_0 \tag{6.2}$$

where P_0 = atmospheric pressure; γ_0 = ratio of specific heats; ρ_0 =density of air stream around the droplet; c_0 =sonic velocity; Ma =acoustic Mach number. Mach number is directly related to the SPL (Sound Pressure Level) of the levitator (constant for the current experiment) by $SPL[dB] = 197 + 20\log(Ma)$. Note that the heated, vaporizing droplet will always be covered with a concentrated fuel vapor blanket. Moreover, the acoustic streaming around the droplet suppresses the natural diffusion process of this concentrated vapor blanket. It is necessary to include the effect of this vapor blanket around the droplet while calculating the streaming velocity. From classical vaporization theory [Sirignano (2010)], the mole fraction ($X_{l,s}$) and mass fraction ($Y_{l,s}$) of fuel vapor at the droplet surface can be calculated as

$$X_{l,s}(T_s) = \frac{P_{sat}(T_s)}{P_0}$$
(6.3)

and

$$Y_{f,s}(T_s) = \frac{X_{l,s}(T_s).W_l}{X_{l,s}(T_s).W_l + (1 - X_{l,s}(T_s)).W_{air}}$$
(6.4)

where P_{sat} is vapor pressure of the fuel, T_s is the average surface temperature of the droplet, W_l and W_{air} are molecular weights of the liquid and air respectively. The effective density of the vapor film around the droplet is

$$\rho_{0,eff}(T_s) = \left[\frac{Y_{f,s}(T_s)}{\rho_{l,vap}(T_s)} + \frac{1 - Y_{f,s}(T_s)}{\rho_{air}(T_s)} \right]^{-1}.$$
(6.5)

The streaming velocity can be redefined as

$$u_{str-eff} = \frac{P_0 \gamma_0 Ma}{\rho_{0,eff}(T_s) c_0}$$
(6.6)

which is a strong function of the vaporization characteristics of the different liquid fuels.

In general, the criterion for droplet atomization events is defined in terms of Weber number, which is the ratio of pressure force and capillary force. In acoustically levitated droplet, the Weber number, $We = 8 P_B / P_\sigma$, is defined as the ratio of Bernoulli's stress (pressure) and stress due to surface tension [Lierke et al. (2002)], where $P_B = 0.5 P_0 \gamma_0 Ma^2$. The stress due to surface

153

tension is given by $P_\sigma = 2\sigma/R$, where R is the droplet radius. Thus, $We = 2P_0\gamma_0 Ma^2 R/\sigma$; Using an effective Mach Number,

$$Ma_{eff} = u_{str\text{-}eff}/c_0 \tag{6.7}$$

$$We_{eff} = \frac{2P_0\gamma_0 Ma_{eff}^2 R}{\sigma} = \frac{2P_0\gamma_0 (u_{str\text{-}eff}/c_0)^2 R}{\sigma} \tag{6.8}$$

We_{eff} is transient for a vaporizing droplet due to temperature dependent properties and fuel type. Without external heating, the effective Weber number exhibits dependence only on the droplet diameter and slow transient variations.

For KH instability, the critical Weber number for atomization is

$$We_{crit} = 2P_0\gamma_0 (u_{crit}/c_0)^2 R/\sigma \tag{6.9}$$

 Since the small scale atomization only occurs at the droplet equator, it is more appropriate to use R_c (radius of curvature at the droplet equator) as the length scale to redefine We_{eff} and We_{crit}. The aspect ratio of the droplet changes dynamically as heating and vaporization progress with time (Figure 52). The shape of the droplet approximates to an ellipse, and its local radius of curvature at any point on the equator perimeter is $r_c = \dfrac{(b^2 \cos^2 t + a^2 \sin^2 t)^{3/2}}{a.b}$; a and b are the major and minor axes; c(=a/b) is the aspect ratio, and 't' is calculated by $\varphi(t) = \tan^{-1}(\dfrac{a}{b}\tan t)$. φ is the polar angle with the ellipse center as origin. For $\varphi = 0$ or $\pi/2$ at the equator, $R_c = b^2/a = b/c$. The criterion for atomization can be recast as $We_{eff} > We_{crit}$ where $We_{crit} = 2P_0\gamma_0 (u_{crit}/c_0)^2 R_c/\sigma$

and $We_{eff} = 2P_0\gamma_0(u_{str-eff}/c_0)^2 R_c/\sigma$. The liquid surface tension is a function of temperature and the droplet size exhibits a transient regression with heating. From these expressions it can be observed that $We_{crit} \sim \dfrac{u_{crit}^2}{\sigma}$ and $u_{crit}^2 \sim \sqrt{\sigma}$. Thus, one can see We_{crit} varies as $\sigma^{-1/2}$ while We_{eff} exhibits a σ^{-1} dependence. This implies that during the both We_{eff} and We_{crit} will progressively decay as the droplet surface temperature increases and the difference $(We_{crit} - We_{eff})$ can decrease until the atomization criterion is satisfied. Therefore, for liquid droplets, with similar surface tension gradients, the probability of KH instability increases for higher surface temperature.

Initially, We_{crit} is larger compared to We_{eff} for all fuels (Figure 54). For diesel and bio-diesel, high speed images corroborate the time at which We_{eff} converges to We_{crit} and atomization is triggered. Kerosene reaches this condition fastest (around 0.3 sec). In the absence of external heating, We_{crit} and We_{eff} would have exhibited a very slow change due to natural evaporation of the droplet. Thus, no atomization would be observed if there is no external heating. With heating, the vaporization pattern for each fuel droplet is different. The change in the temperature and diameter of a vaporizing droplet depends on the vapor pressure, latent heat and specific heat. The surface temperature and vapor pressure also dictate the change in vapor density around the droplet as explained earlier. Ethanol shows a low surface temperature, thereby reducing the possibility of KH instability.
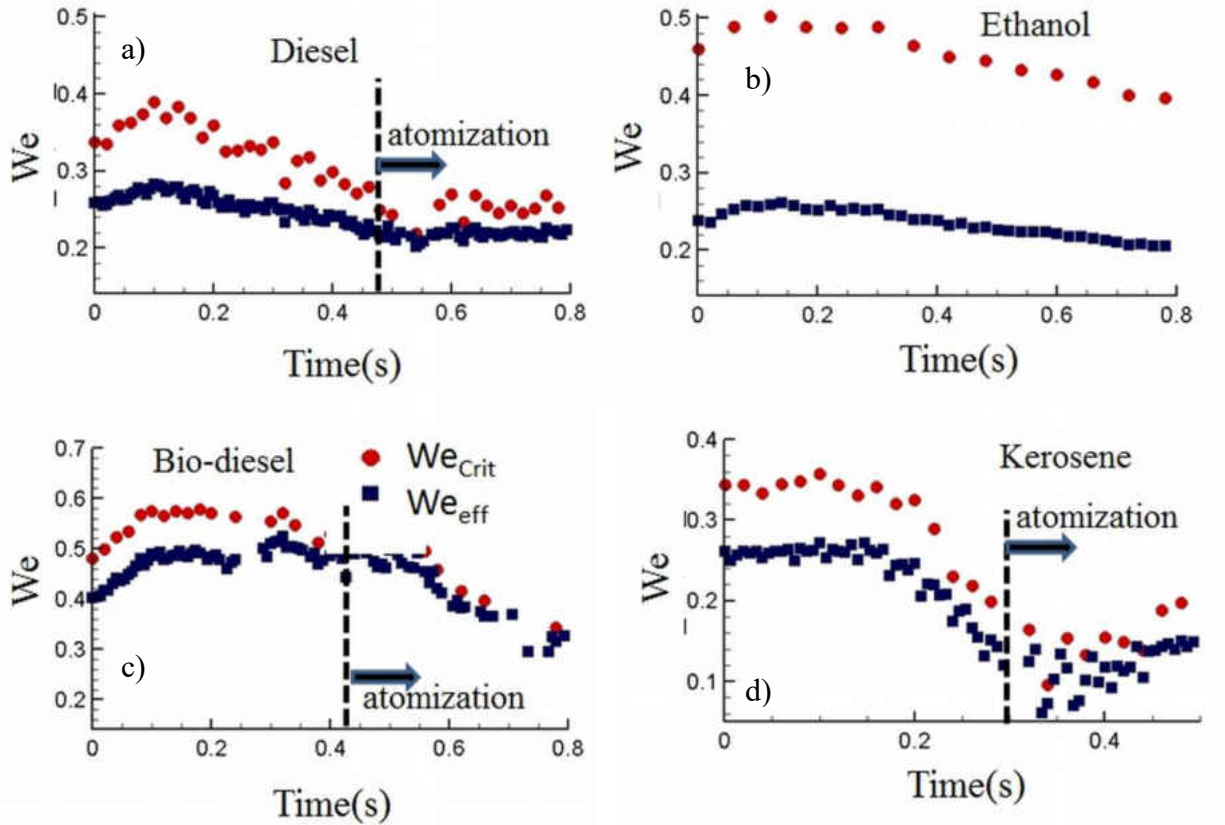
Figure 54: Critical Weber number (We$_{crit}$) and Effective Weber number (We$_{eff}$)

In general, all droplets deform into an ellipsoidal shape and the oblateness or the aspect ratio is higher for the atomizing droplets (Figure 53). The theory of levitation [Yarin et al. (1998), Lierke (2002)] suggests that the aspect ratio is dependent on levitator SPL, surface tension, density and droplet diameter. As mentioned earlier, the atomization occurs at the equator as it has minimum radius of curvature. For a given volume of droplet, the aspect ratio determines the radius of curvature at the equator. Parameters such as SPL and surface tension affect the aspect ratio and, in turn, affect the atomization. Increase in SPL and reduction in surface tension result in the augmentation of aspect ratio. However, both definitions of Weber numbers

$(We_{crit} = 2P_0\gamma_0(u_{crit}/c_0)^2 R_c/\sigma$ and $We_{eff} = 2P_0\gamma_0(u_{str-eff}/c_0)^2 R_c/\sigma)$ use the radius of curvature

as the length scale. So the change in SPL which alters the radius of curvature would have the same effect on both the Weber numbers and hence would not change the instability criterion. On the other hand, the surface tension has separate and distinct effects on We_{crit} and We_{eff}. Change in surface tension would not only affect the aspect ratio but would also influence the Weber numbers directly. The change in aspect ratio (or radius of curvature) would create similar changes on both the Weber numbers as mentioned earlier. However, We_{crit} and We_{eff} show $\sigma^{-1/2}$ and σ^{-1} dependence. Surface tension decreases with temperature, leading to a sharper rise in We_{crit} than We_{eff}. It is difficult to conduct experiments with liquid droplet under external heating to demonstrate the effects of surface tension on KH instability, as the droplet will vaporize and create a vapor blanket around it, changing the streaming velocity and thereby altering We_{eff}. However, for liquids like kerosene (Figure 52), vaporization is not significant for the initial 200 msec, so the effect of the vapor blanket on streaming velocity would not be significant. Similarly, diesel also does not vaporize in the same duration, resulting in a sharp increase in temperature (up to 80^oC), which reduces its surface tension. In the first 100 msec (Figure 54a), We_{crit} and We_{eff} increase by ~20% and ~10% respectively. The experiments were repeated a few times and were observed to be within 5-10 % of each other in terms of We_{crit} and We_{eff}, time of atomization and critical aspect ratio. Thus, the physics reported here is repeatable and sensitive only to the SPL of the levitator, properties of the fluid and the laser heating rate. However, the SPL of the levitator and the laser power level were maintained constant for all fluids for all experimental runs. The uncertainty in We_{crit} and We_{eff} due to jitter in laser power and variation in the initial droplet diameter and SPL level of the levitator is negligibly small.

6.3.2 Catastrophic breakup

In addition to KH induced atomization, kerosene experiences bulk deformation leading to bag type and capillary wave induced breakup. With progressive heating, the kerosene droplet initially gets stretched in the horizontal direction and subsequently morphs into a thin disk with a significant variation in aspect ratio and eventually undergoes breakup (Figure 53). It is to be noted that other fuels like biodiesel and diesel show shape changes but do not regress into a disk-shaped morphology. This clearly suggests that general criterion maybe established to ascertain the stability of droplet based on the external acoustic pressure field, internal recirculation due to acoustic streaming and the variation of temperature dependent properties like viscosity and surface tension.

As shown in Figure 55, the breakup process of a kerosene droplet occurs over 15 msec, and can be further subdivided into three stages. In Stage I, the levitated droplet deforms to a disk or pancake-shaped structure while displaying high amplitude oscillations in aspect ratio along with low damping and a high velocity gradient in the liquid phase. Subsequently in stage II, the droplet resembles a disc and blows up like a bag near the center. Stage III is marked by violent breakup of the bag along with capillary waves induced on the flattened surface of the deformed droplet. No atomization is observed in stage I, but it is marked by substantial distortion of the droplet which serves as a precursor to the eventual catastrophic breakup in stages II and III. Although this catastrophic break up begins to occur around 0.42 sec, this instability is triggered earlier when the temperature of the droplet increases due to radiative heating. All liquid droplets are subject to deformations under acoustic loading. However, only Kerosene and FC 43 (Figure 55) reach the critical deformation limit necessary for breakup.
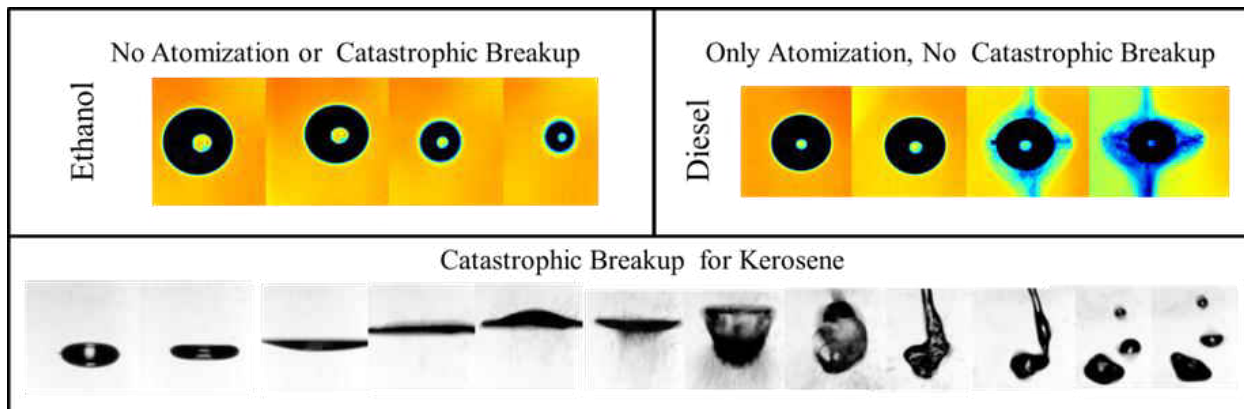
a)
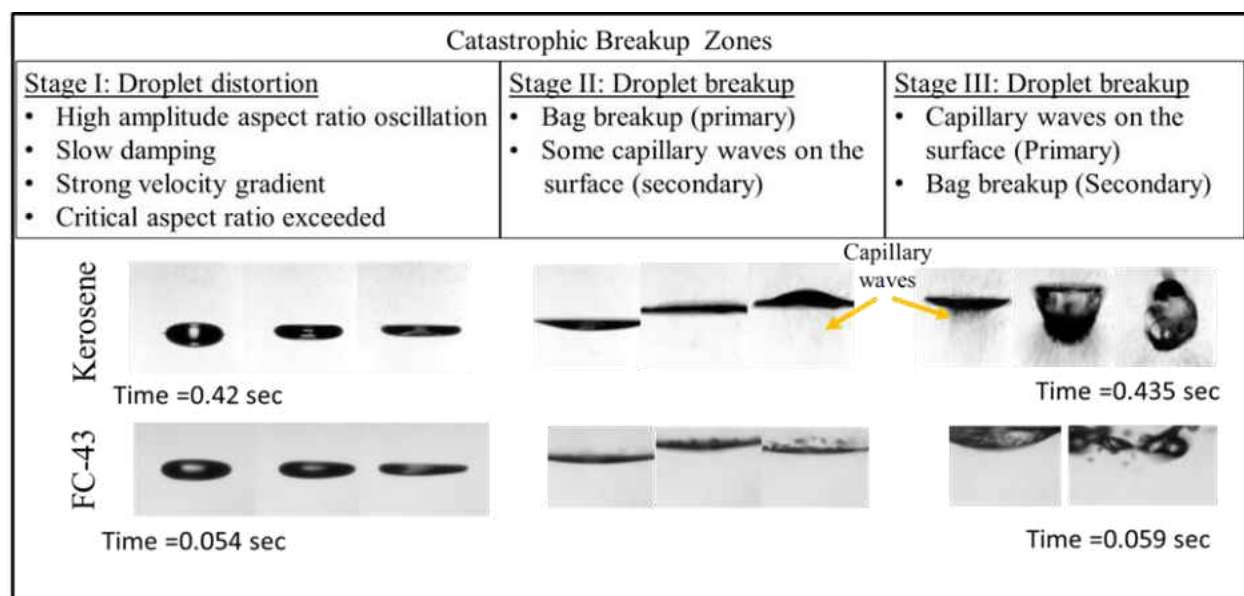
b)

Figure 55: **(a) Atomization and catastrophic breakup of different liquids. (The streaks are colorized during image processing to improve clarity. No dye has been added. The blue streaks show the daughter droplets (~10µm) resulting from atomization) (b) Catastrophic breakup of kerosene and FC 43 droplet**

6.3.2.1 Stage I (Droplet distortion stage)

A levitated droplet takes the shape of an ellipsoid (c>1) due to the non-uniformity of the

acoustic/Bernoulli pressure around the droplet [Saha et al. (2012b)]. The pressure force around

the droplet deforms it and the surface tension force tends to restore the spherical shape. The amount of oblateness or the tendency to deviate from the spherical shape (c=1), depends on the fluid properties such as, density and surface tension. Hence, the mean aspect ratio can be written as $\bar{c} = f(\rho, \sigma)$. For stability the balance in external acoustic pressure force and maximum surface tension force (at the equator) can be expressed as,

$$P_{pole} - P_{eq} = \sigma / R_c \tag{6.10}$$

where P_{pole}-P_{eq} is the difference between the Bernoulli pressure at the pole (P_{pole}) and at the equator
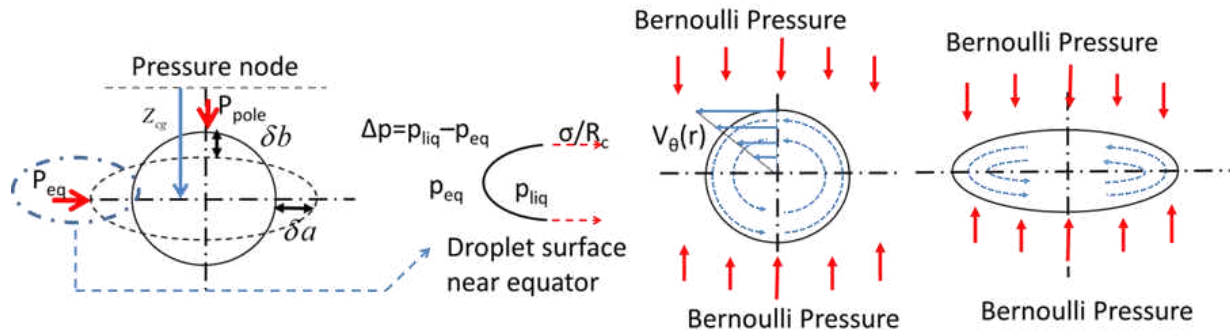
Figure 56: Bernoulli pressure and surface tension force around the levitated droplet

Bernoulli pressure outside the droplet (P_{eq}) and R_c is the radius of curvature at the equator as shown in Figure 56. (P_{pole}-P_{eq}) represents the appropriate scale for the external acoustic force that accounts for the local inhomogeneity of the pressure distribution due to shape change.

160

Small perturbations in the external pressure field around the droplet al.so oscillate which triggers an oscillation in the aspect ratio. In Chapter 3 and also in references [Saha et al. (2012a), (2012b)], it was shown that the velocity field in a levitated spherical droplet is tangential in nature, i.e., $v_r = 0$, and that $v_\theta = K \cdot r$, where K is a constant which depends on the droplet and levitator properties. With the departure from the spherical shape (aspect ratio, c>1), polar radius decreases, increasing the equatorial radius, which subsequently augments the fluid flow towards the equator resulting in the droplet getting stretched away from the center. Therefore, in a nutshell, Bernoulli pressure continues to deform a levitated droplet. However, in most cases, surface tension inhibits the Bernoulli pressure to continuously deform the droplet.

The radius if curvature at the equator is expressed as

$$R_c = \frac{b}{c} = \frac{3V}{4\pi a^2 c}$$

(6.11)

where V is volume of the droplet ($V = \frac{4}{3}\pi a^2 b$), a and b are polar and equatorial radii. So with increase in aspect ratio, R_c will decrease, which, in turn, will increase the surface tension pressure. Thus, the droplet shape continues to oscillate about a mean value. Fluid properties also play an important role in controlling the intensity of this oscillation. The fluid viscosity acts as a damping force on the velocity field. Higher viscosity reduces the flow towards the equator. Strong damping due to viscosity can, in essence, dissipate the high energy shape fluctuations (especially high amplitude modes of vibration) before it assumes catastrophic proportions.

161

For a small change in aspect ratio, δc, the change in critical radius can be calculated mathematically. For an ellipsoidal droplet, whose horizontal and vertical radii are a and b, with an aspect ratio c (=a/b), from Equation 6.11, one can write $b = \dfrac{3V}{4\pi a^2}$. We know, $c = \dfrac{b}{a}$. Thus one can write

$$c = \frac{a}{b} = \frac{4\pi}{3V} a^3 \Rightarrow a = \left(\frac{3Vc}{4\pi} \right)^{1/3} \tag{6.12}$$

$$\frac{da}{dc} = \left(\frac{3V}{4\pi} \right)^{1/3} \left[\frac{1}{3c^{2/3}} \right] = \frac{a}{3c} \tag{6.13}$$

$$\frac{db}{dc} = \left(\frac{3V}{4\pi} \right)^{1/3} \left[\frac{-2/3}{c^{5/3}} \right] = -\frac{2b}{3c} \tag{6.14}$$

Also one can show, using Equation 6.12

$$\frac{dR_c}{dc} = R_c \left[\frac{-2}{a} \left(\frac{a}{3c} \right) + \frac{-1}{c} \right]$$

Or, $\quad \dfrac{dR_c}{dc} = -\dfrac{5}{3} \dfrac{R_c}{c}$

Or, $\quad \delta R_c = -\dfrac{5}{3} \dfrac{R_c}{c} \delta c \tag{6.15}$

Thus for a small change in aspect ratio, δc, the change in critical radius can be written as

$\delta R_c = -\dfrac{5}{3}\dfrac{R_c}{c}\delta c$. The Bernoulli pressure or the acoustic pressure which also changes with change in aspect ratio, can be expressed as

$$P(r,z) = P_{max}\sin(k_z z).J_0(k_r r) \tag{6.16}$$

where, $P_{max} = P_0\gamma_0 Ma$ is constant in the current the experiment; P_0 is the atmospheric pressure, γ_0 is the specific heat ratio ; Ma is the acoustic Mach number and r and z are radial and axial coordinate measured from the pressure node and J_0 is Bessel function of zeroth order. Acoustic Mach number (Ma) directly depends on the SPL of acoustic levitator by the relationship, $SPL[dB] = 197 + 20\log(Ma)$. P_{max} represents the pressure intensity of the acoustic pressure. The droplet under gravity will be shifted downwards from the pressure node in order to balance the weight of the droplet [Lierke (2002), Saha et al. (2012b)]. Under stable levitation, the droplet center is shifted downwards from the pressure node by Z_{cg} (Figure 56). Consequently, the pressure distributions at the pole and equator are

$$P_{pole} = P_{max}\sin\left(k_z(z_{cg} - b)\right) \tag{6.17}$$

and

$$P_{eq} = P_{max}\sin\left(k_z z_{cg}\right)J_0(k_r a) \tag{6.18}$$

respectively.

Now using Equations 6.17 and 6.13,

$$\frac{dP_{pole}}{dc} = -\left[P_{max}k_z \cos\left(k_z(z_{cg} - b)\right)\right]\frac{(-2b)}{3c}$$

Or, $\delta P_{pole} = \left[P_{max}k_z \cos\left(k_z(z_{cg} - b)\right)\right]\frac{2b}{3c}\delta c$ (6.19)

Similarly, from Equation 6.18 and 6.14, one can also write

$$\frac{dP_{eq}}{dc} = -\left[P_{max}k_r \sin\left(k_z z_{cg}\right)J_1(k_r a)\right](\frac{a}{3c})$$

Or, $\delta P_{eq} = -\left[P_{max}k_r \sin\left(k_z z_{cg}\right)\right]\frac{a}{3c}\delta c$ (6.20)

A change in aspect ratio by δc will induce changes in Bernoulli pressure at the pole and equator

and are given by $\delta P_{pole} = \left[P_{max}k_z \cos\left(k_z(z_{cg} - b)\right)\right]\frac{2b}{3c}.\delta c$ and

$\delta P_{eq} = -\left[P_{max}k_r \sin\left(k_z z_{cg}\right)J_1(k_r a)\right]\frac{a}{3c}\delta c$.

Thus, an increase in aspect ratio, i.e., δc, will reduce the radius of curvature at the equator, (negative δR_c) and increase the Bernoulli pressure at the pole. This, in turn, will create a fluid flow from the pole to the equator, increasing the liquid pressure near the equator (P_{liq} in Figure 56). A positive δc will also decrease the Bernoulli pressure at the equator. Thus, a positive δc will result in an increase in Bernoulli's pressure ($P_{pole}-P_{eq}$). In other words, change in aspect ratio shifts the droplet from equilibrium condition through changes in geometry and pressure distribution around the droplet. The relative changes of R_c and external pressure distribution ($P_{pole}-P_{eq}$) along the droplet surface dictate the stability of the droplet. For a small positive δc,

the surface tension force increases and counteracts the increased Bernoulli pressure. Thus the droplet is normally restored to its original shape and exhibits some oscillation in aspect ratio about a mean value. In low surface tension fluids, higher deformation and oscillation of the droplet aspect ratio can be observed, although low surface tension does not always critically deform the droplet and lead it to catastrophic breakup. Normally, the shape oscillations are dissipated or damped quickly by viscosity. However, in cases where surface tension and viscosity are both low, the droplet can exhibit a propensity to approach the critical deformation limit due to high inhomogeneous Bernoulli pressure. It is important to note that the levitated droplet does not exhibit any shape oscillations in the unheated condition under the same acoustic loading. This implies when the droplet is heated, surface tension and viscosity decrease with temperature leading to potentially unstable situation.

Figure 52 shows that the temperature continues to rise for ~0.2sec before it reaches a steady state value. Increase in temperature triggers a decrease in surface tension thereby, disturbing the equilibrium. In order to regain stability, the droplet tries to reshape itself with a lower radius of curvature (R_c) at the equator.

6.3.2.2 Stability parameter

P_{pole} and P_{eq} are two extreme values of Bernoulli pressure acting on the levitated droplet. In a levitated droplet $\dfrac{\sigma}{R_c}$ represents the maximum surface tension pressure on the droplet- air interface as R_c represents the minimum radius of curvature on the droplet surface. So, one can define a parameter $\dfrac{(P_{pole} - P_{eq})R_c}{\sigma}$ as the ratio of the external acoustic pressure forces around the

droplet and the maximum surface tension force on the droplet surface. This quantity represents an index for equilibrium between the external acoustic pressure field and surface tension forces at the droplet equator. Initially when the droplet is in equilibrium, one can expect this parameter to be close to 1. With heating, surface tension decreases, resulting in an increase in aspect ratio, and also the force distribution. A small change in aspect ratio increases the $(P_{pole} - P_{eq})$ which in turn increases the aspect ratio and corresponding reduction R_c. If both of these changes are of the same order, the droplet retains its mean shape and does not undergo stretching or deformation. However, for kerosene (and FC 43) droplet, the change in pressure force $(P_{pole} - P_{eq})$ is stronger compared to the increase in surface tension force (σ/R_c) due to the reduction in R_c. As explained in previous section, depending on the relative changes in these parameters and the damping coefficient, either the droplet remains near equilibrium or it stretches. If the droplet stretches it

will imply $\dfrac{(P_{pole} - P_{eq})R_c}{\sigma} > 1$. If $\dfrac{(P_{pole} - P_{eq})R_c}{\sigma} \approx 1$ or initial value (<1), then the droplet will

retain its shape. However, $\dfrac{(P_{pole} - P_{eq})R_c}{\sigma} \gg 1$ implies a monotonic increase in the aspect ratio,

i.e., continuous stretching of the droplet.

6.3.2.3 Dependence of stability parameter on surface tension, droplet size and SPL

From the previous section, it is clear that for stretching, criterion $\dfrac{(P_{pole} - P_{eq})R_c}{\sigma} \gg 1$ needs to be

satisfied. Now to ascertain the effect of small change in aspect ratio, one can write,

$$\frac{\partial P_{pole}}{\partial c}\delta c - \frac{\partial P_{eq}}{\partial c}\delta c \gg \frac{\partial(\frac{\sigma}{R_c})}{\partial c}\delta c \tag{6.21}$$

Substituting P_{pole} and P_{eq} in Equation 6.21 one can show,

$$\frac{P_{max}R_c}{\sigma}\left[k_z \cos\left(k_z(z_{cg} - b)\right) + k_r \sin\left(k_z z_{cg}\right)J_0(k_r a)\right] \gg 1 \qquad (6.22)$$

Now, using $R_c = \dfrac{b}{c}$ one can rewrite,

$$\frac{P_{max}(\frac{b}{c})}{\sigma}\left[k_z \cos\left(k_z(z_{cg} - b)\right) + k_r \sin\left(k_z z_{cg}\right)J_0(k_r a)\right] \gg 1 \qquad (6.23)$$

From Equation 6.23, it can be seen that if surface tension of the liquid decreases or if the levitator SPL increases, or for a large droplet size, the left hand side of the equation increases making the droplet more susceptible to breakup. Equation 6.23 cannot be plotted without the experimental data for b/c. Since the analysis has not considered viscous damping at this time, and the experiments would automatically include effects of damping, Equation 6.23 is only a necessary condition for stretching but not a sufficient condition for breakup. It is possible that all four liquids studied here would satisfy the stretching criterion, but not necessarily deform uncontrollably due to viscous damping.

By analogy of the aerodynamic break up (see Appendix), one can define a modified Weber number as $We_{TAB} = \dfrac{(P_{pole} - P_{eq})R}{\sigma}$. Thus the stability parameter defined in this section can be written as, $We_{TAB}R_c^*$. It is important to mention here that the Weber number used here is based on the aerodynamic breakup modeled by using Taylor Analogy Breakup (TAB). This We_{TAB} is therefore different than Weber number (We_{eff}) used for KH instability [Basu et al. (2012)]

analysis. The latter is used for characterizing global force balance for the successful levitation and it is based on the RMS value of the acoustic pressure (RMS of pressure distribution around the droplet) acting around the droplet and does not account for the increasing inhomogeneity of the pressure distribution due to shape change, which is important for analyzing localized instability such as oscillation in aspect ratio.

Our observation has been that among the liquid droplets, only kerosene (and FC 43) undergoes significant distortion and eventual breakup. Therefore, the author considers the viscous damping effect next.
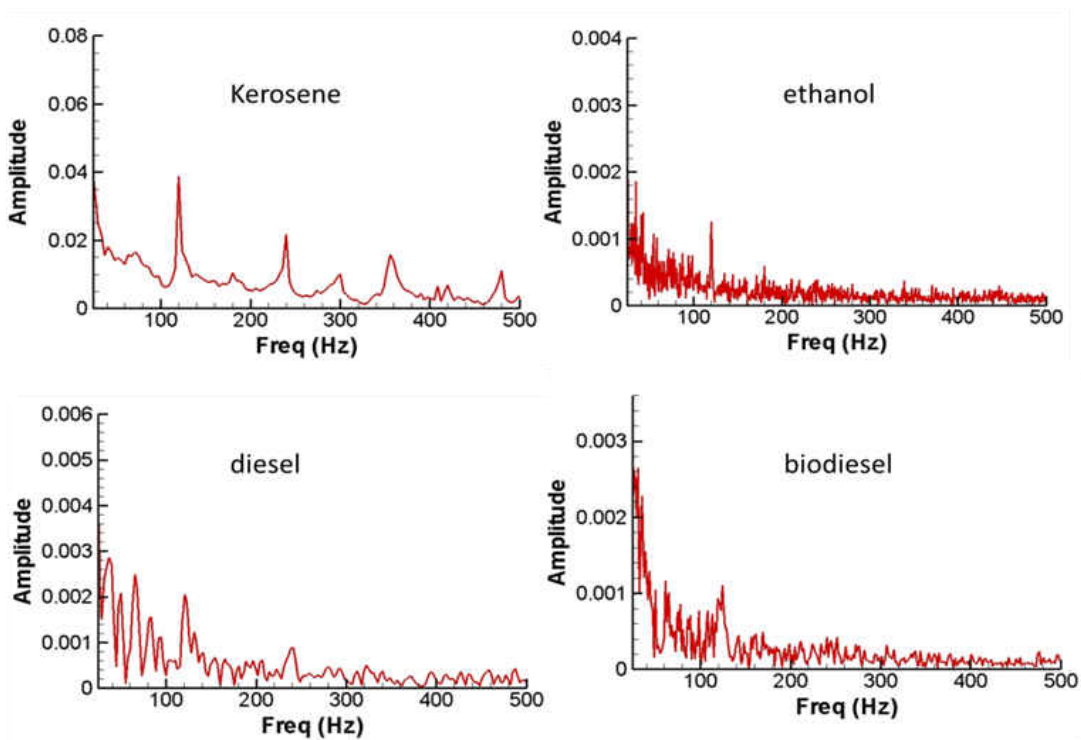
Figure 57: FFT of aspect ratio (c) four different liquids (a) Kerosene, (b) Ethanol, (c) Diesel and (d) Biodiesel

6.3.2.4 Viscous damping effect

In order to characterize the principal frequency modes of the change in aspect ratio observed for different liquids, Fast Fourier Transform (FFT) was performed for each droplet. FFT of the transient aspect ratio data for all droplets (Figure 57) shows the presence of a few harmonic modes at some specific frequencies of 125 Hz, 250 Hz, 300 Hz etc. Although the higher frequencies are absent in some fuels, 125 Hz seems to be the omnipresent frequency for all fuels. This frequency was confirmed for water-based solutions as well (not shown). The large amplitude in Figure 57 for kerosene also suggests that the oscillation is strongest for kerosene compared to other fuels.

The change in aspect ratio can be expressed as a series solution,

$$c(t) = \overline{c}(t) + \sum_i c_i'(t).\sin(2\pi f_i t) \tag{6.24}$$

Where $\overline{c}(t)$ denotes the bulk or mean (slow variation with time) variation in aspect ratio and $c_i'(t)$ denotes the change in aspect ratio due to different energy carrying capillary modes.

$\overline{c}(t)$ can be modeled by Taylor Analogy Breakup hypothesis [O'rourke and Amsden (1987)], as this stretching and increase in aspect ratio is predominantly caused by the significant time varying inhomogeneity in the acoustic pressure distribution i.e. the pressure difference between the pole and equator, which tries to deform the droplet while surface tension acts as a spring with a certain stiffness and tries to retain the spherical shape. The viscosity acts as a damping mechanism to attenuate the stretching of the droplet.

Using simplified formulation of TAB model (see Appendix), one can write the damping ratio for $\bar{c}(t)$ is

$$\zeta = \frac{C_d}{2\sqrt{C_k}} \sqrt{\frac{\mu^2}{\sigma \rho R}} = \frac{C_d}{2\sqrt{C_k}} Oh$$

(6.25)

where Oh is the Ohnesorge number. The damping time scale (for attenuation of the droplet deformation), can be expressed as, $\tau_d = \frac{2}{C_d}\frac{\rho R^2}{\mu_l}$, where C_k and C_d are proportionality constants in the TAB model and considered to be constant for different fuel droplets. The transient variation of the damping ratio (Oh/2) as illustrated in Figure 58a, shows that it is weakest for kerosene. The damping timescale (Figure 58b) is also found to be highest for kerosene, indicating slow attenuation of the droplet deformation due to external acoustic pressure. Figure 57 and 58 in summary show that not only kerosene exhibits the highest amplitude in aspect ratio oscillation but also it has a low damping ratio leading to a large damping timescale.
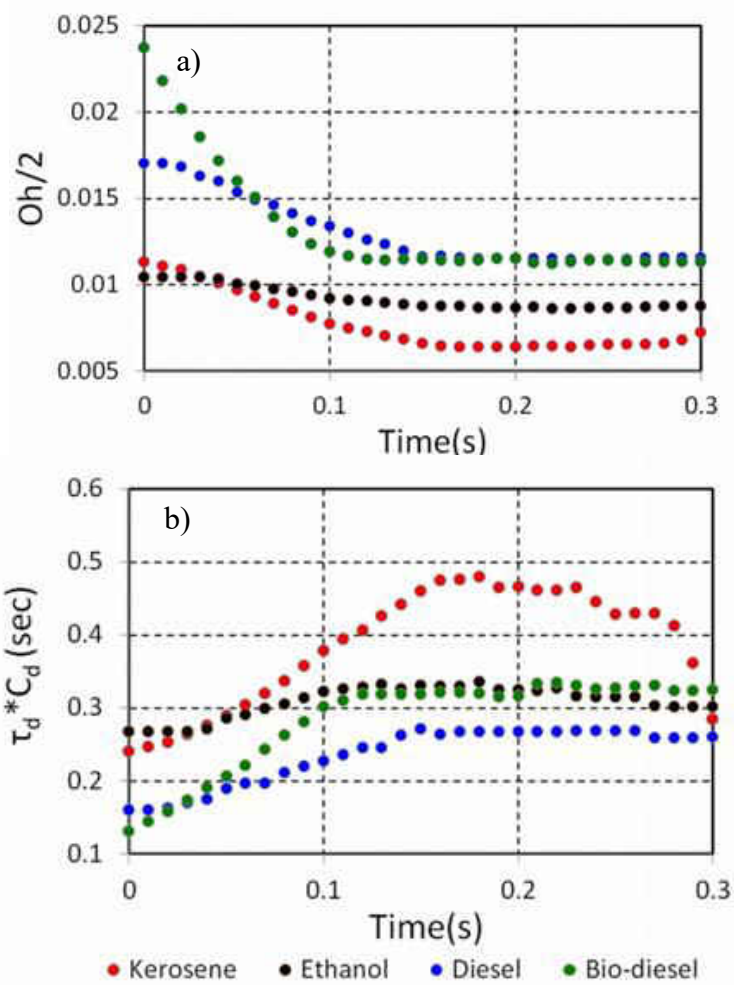
Figure 58: (a) Ohnesorge number ($Oh = \dfrac{2\sqrt{C_k}}{C_d}\zeta$ **) and (b) Damping timescale (** $\tau_d C_d$ **) of aspect ratio (** $\overline{c}$ **) oscillation as a function of time.**

The changes in $c_i'(t)$ is due to surface capillary waves on the droplets. Using theory of Capillary surface wave (See Appendix) it can be shown that the damping of the surface wave at all principal modes (fast varying energy containing capillary modes) (Figure 57) is high during

171

stage I of the droplet deformation process. The energy and the intensity of a damped capillary wave can be expressed as

$$\overline{I(t)} = \overline{I}_0 . e^{-2C_{damp}t}$$

(6.26)

where $\overline{I}$ is amplitude of the capillary waves [Landau and Lifshitz (1987)] (see Appendix). The damping coefficient $C_{damp} = 2\dfrac{\mu\omega^{4/3}}{\rho^{1/3}\sigma^{2/3}}$., where ω is the angular frequency of the oscillation of the droplet shape.

The quantity c' can be written as $c_i'(t) = c_0' . e^{-2C_{damp}t}$. From high speed images $c_i'(t)$ can be expressed as

$$c_i'(t_{n+1}) = c_i'(t_n) . e^{-2C_{damp}(t_{n+1}).(t_{n+1}-t_n)}$$

(6.27)

where n is the frame number of high speed images. Using C_{damp} and Equation 6.27 the instantaneous intensity ($c_i'(t)$) of oscillation for four fuels is calculated. It has been observed that the damping time scale for this capillary wave oscillation is in the order of 0.05 sec by which time the amplitude reduces by 90%. This oscillations (c') in aspect ratio in stage I is not very strong as the change takes place over 0.4 sec (Figure 55). On the other hand this oscillation (c') becomes important in Stage II and III when the pertinent timescale leading to breakup is of the order of 0.01 sec.

If ζ and C_{damp} for any fuel is very high, then the thermally induced oscillations in aspect ratio will dissipate faster even when $We_{TAB}R_c^* > 1.0$. In those cases, the droplet never approaches the critical deformation limit needed for bag type breakup. One may conclude that for the droplet to become critically unstable, two criteria must be satisfied together, 1) $We_{TAB}R_c^* > 1.0$ and 2) low ζ and C_{damp}. The first condition will initiate strong oscillation in aspect ratio and the latter will reduce the chances of damping that oscillation. Together these two conditions are necessary for droplet to oscillate beyond a critical limit and experience a catastrophic breakup.
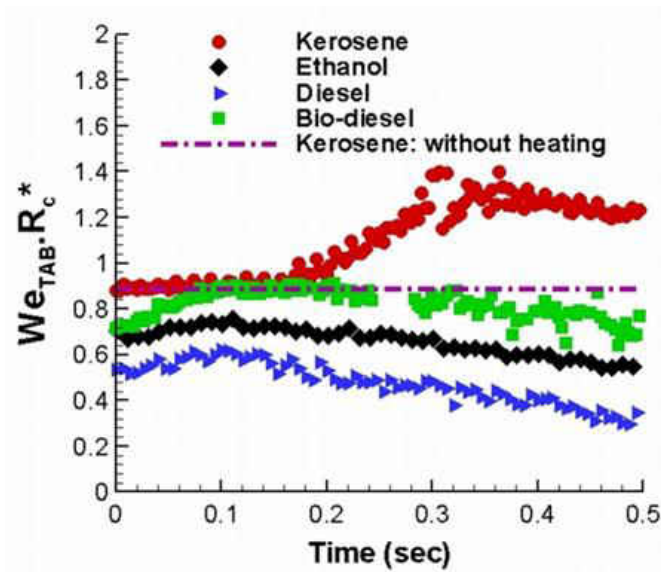
Figure 59: Stability parameter ($We_{TAB}R_c^*$) as a function of time

The data in Figure 59 represents the true experimental conditions that include oscillations and viscous damping. It shows that for diesel, ethanol and bio-diesel, the parameter $We_{TAB}R_c^*$ initially increases only marginally with time and then decreases due to viscous damping. With increase in temperature, the droplet stretches and increases $We_{TAB}R_c^*$, but due to corresponding increase in

surface tension force and due to viscous damping, the droplet shape returns to equilibrium. On the other hand for kerosene, the droplet stretches beyond a controllable limit with little resistance due to low viscous damping, hence, the parameter $We_{TAB}R_c^*$ increases monotonically and obtains a value of 1.4 which is much higher than 1.0. In a separate experiment the author has observed that FC43 also displays uncontrollable stretching and bulk breakup like kerosene. Further calculation shows for FC43 the initial value of $We_{TAB}R_c^*$ is 0.92 while at the point of catastrophic breakup the value is 1.33. In absence of heating the kerosene droplet maintains its equilibrium shape since the criteria $We_{TAB}R_c^* > 1.0$ is not satisfied.

6.3.2.5 Stages II and III

After the droplet stretches beyond the critical value in the stage I, it morphs into a disk/membrane shaped structure. The Bernoulli pressure acting on this membrane tries to stretch it along the levitator axis or axis leading to the formation of a bag type structure. In stage III this sudden expansion in the perpendicular direction inflates the disk shaped liquid film and eventually disintegrates. One more important phenomenon the author observes is that during the stretching and bag type break up process, the surface of the disk shaped liquid film shows small capillary waves. The tip of these small capillary waves which are moving around the droplet surface, disintegrates to form small droplets. For kerosene, the viscous damping is weak and also the damping time scale for these oscillations due to capillary wave is on the order of 0.1sec, while the total duration of stage II and II are 0.02 sec. Hence the amplitude of these oscillations grows and tip of these wave fronts detach to form very tiny droplets. This phenomenon of

breaking of capillary wave to generate tiny droplets is clearly visible in the vicinity of droplet surface during the bag type break up.

6.4 Summary

In summary, this analysis shows that the observed secondary atomization in levitated fuel droplets is due to thermal effects. Since the density of fuels tested are close to each other, properties such as vapor pressure, latent heat and specific heat govern the vaporization rate and temperature history, which affect the surface tension gradient and gas phase density, ultimately dictating the onset of KH instability. High surface temperatures achieved in diesel, bio-diesel and kerosene favor small scale atomization through KH instability. High surface temperatures achieved in diesel, bio-diesel and kerosene favor small scale secondary atomization. The temperatures for fuels having high vapor pressure and high latent heat remain rather low and these droplets tend to be more stable like ethanol due to lower surface tension gradient.

In addition to the small scale atomization through KH instability, a second type of instability occurs in kerosene (also in FC 43) droplet due to a decrease in surface tension and viscosity with temperature. The change in surface tension causes the droplet to flatten due to increased Bernoulli pressure at the poles resulting in an increase in aspect ratio. The imbalance in pressure force and surface tension force near the equator creates shape oscillation. If the viscous damping of this oscillation is not strong enough, the droplet goes through unbounded stretching morphing into a disk-like object, followed by a bag type catastrophic breakup. Analysis shows there are two important parameters which dictates inception of this instability. A parameter $We_{TAB}R_c^*$ represents relative strength of Bernoulli pressure to surface tension, where the former is

responsible for stretching the droplet and the latter acts as stiffness of the droplet. Other important parameter is viscous damping or damping ratio, which is a function Ohnesorge number, Oh. A criterion for catastrophic breakup of droplet is obtained as $We_{TAB}R_c^* > 1.0$ and a low damping ratio as represented by Ohnesorge number. In a containerless levitated droplet, KH instability always precedes this second type of instability. These instabilities arise due to external heating and temperature dependent properties of the liquid fuels, and cannot occur due to natural drying alone.

CHAPTER SEVEN: MODELLING OF SOLUTION PRECURSOR PLASMA SPRAY PROCESS

7.1 Introduction

Production of high value powders and coatings is a large industrial enterprise worth multibillion dollars in U.S. economy. Production of functional materials has been achieved by different processes including spray drying [Masters (1985)], combustion and plasma processing [Pawlowski (1995)]. Among the different processing techniques, plasma and high velocity oxy-fuel (HVOF) techniques [Pawlowski (1995)] have been successfully employed for production of protective coatings on hardware components such as thermal barrier coatings on gas turbine blades, among other numerous examples. In both of these techniques, micrometer sized powder of the coating material is typically heated in a plasma or HVOF jet and deposited in partially or fully molten state onto a substrate forming a coating with thickness ranging from 100 μm to several millimeters [Pawlowski (1995)]. An alternate route to this process to manufacture coating with layers structured at the sub-micrometer scale and even in some cases at the nanometer scale is the injection of liquid spray composed of droplets containing dissolved salts of the materials (precursor) to be deposited [Padture et al. (2001), (2002), Jordan et al. (2004), Bhatia et al. (2002), Ozturk and Cetegen (2005a), Ravi et al. (2006), Oberste-Berghaus et al. (2005)]. In this case, droplets injected into thermal plasma (Solution Precursor Plasma Spray or SPPS) or HVOF environment vaporize resulting in an increase in the concentration of the salt solutes followed by heterogeneous or homogeneous nucleation of solid intermediates along with chemical transformations and melting before getting deposited on a substrate. One example of a precursor system that is used in the fields of catalysis, superionic conductors, solid oxide fuel

177

cells, polishing media and even nanobiology is nanoceria. In such precursors, the process engineering and operating parameters determine the physical characteristics of the final product. However, the design of a manufacturing process using thermal spray intrinsically depends on the heat and mass transfer and the physico-chemical processes that occur at the droplet scale. Thus careful optimization of the in-situ processing of liquid droplets in a high temperature environment critically determines not only the chemical make-up of the coatings but also its microstructural characteristics. Depending on the heating rate of droplets and the nature of precipitation during heat-up and evaporation phases, different particle morphologies are obtained including solid particles, hollow shells, and fragmented shells as shown in Figure 60a–c. Small droplets with high solute diffusivity exhibit a propensity to precipitate volumetrically to form solid particles as shown in Figure 60a. Rapid vaporization combined with low solute diffusivity and large droplet sizes can lead to significant increase of solute concentration near the droplet surface resulting in surface precipitation to form a crust around the liquid core of the droplet. The crust/shell may have varied levels of porosity. Shells having low porosity usually rupture due to internal pressurization to form shell fragments (path b-I). Shells that are completely impervious rupture and secondary atomization of trapped liquid core may be observed (path b-III). For shells with high level of porosity, internal pressure rise is counterbalanced by the vapor venting through the pores and results in hollow shells (path b-II). For particular precursors, elastic inflation and subsequent collapse and rupture of the shell can be observed (path c). The particle morphology obtained from droplets is sensitive to the solute chemistry, mass diffusivity, solute solubility, droplet size, thermal history (slow vaporization in spray drying versus injection into 10,000 K high velocity plasma jet), injection type and injection velocity.

The fluctuating and turbulent nature of the plasma flow makes it very difficult to perform experimental analysis of the thermo-physical processes inside the droplets injected into plasma. Though some optical methods are available to measure the temperature and velocity field of the plasma, analysis of droplet level transport is still limited to qualitative experimentation like extractive sampling and ex-situ characterization by SEM, XPS, FTIR and RAMAN. All of these experimental methods do not analyze the in-flight thermal processes within the droplet. Judged in this light modeling is the only way on a short term basis to study the phenomena at hand.
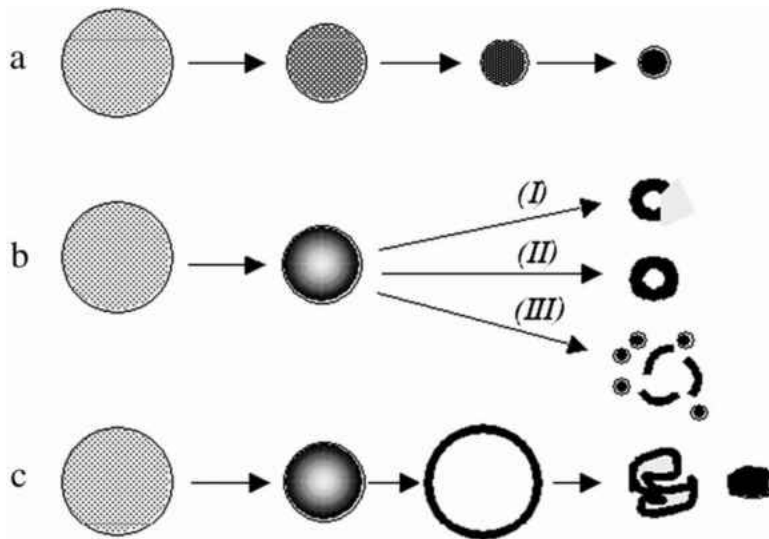
Figure 60: Different routes for droplet for vaporization and solid precipitations: (a) Uniform concentration leading to solid particles by volume precipitation. (b) Super-saturation near the surface: (I) Low permeable shell leading to fragmented shell formation. (II) High permeable shell leading to unfragmented shell formation. (III) Impermeable shell leading to droplet internal heating, pressurization and droplet breakup, secondary atomization. (c) Elastic shell formation causing inflation and deflation by solid consolidation

Modeling of the process of vaporization in a convective high temperature field of dc arc plasma or oxy-fuels has been described by Ozturk and Cetegen (2004), (2005b), (2006). Castillo and Munz (2007) provided detailed modeling of droplets injected in a low temperature RF plasma. A collective analysis of the various stages in the SPPS process is portrayed in the work of Basu and

Cetegen (2008b). SPPS nanoceria coating on martensitic steel is chosen as the precursor system to be investigated in this work. Corrosion resistance is considered to be one of the most important material properties for many engineering applications. The corrosion resistance of stainless steel can be improved by producing extrinsically or intrinsically a protective coating by either surface modifications or pretreatments. It is also hypothesized that the presence of cerium oxide in the coating acts as nucleation sites for Cr_2O_3 formation which assists in the prevention of material degradation.

In the chapter, a complete modeling effort has been detailed to study the intermediate in-flight thermo-physical processes within the droplet injected into a plasma field for cerium nitrate precursors. Complete analysis of the variation of droplet level transport as a function of initial droplet diameter and injection type was performed. The work particularly emphasizes on the relationship among the final droplet states (hence the likely morphology of the expected coating) with process parameters, droplet size and injection methodology.

7.2 Droplet transport processes in a plasma jet

The injection of precursor within the plasma flow can be achieved by two routes namely as liquid stream or droplets. Here the second type of injection is assumed [i.e. droplet]. The droplets injected into the plasma jet undergo four distinct thermo-physical transitions. They are namely aerodynamic breakup, rapid vaporization and precipitation, internal pressurization with shell rupture and rapid heating of volumetrically precipitated solid particles.

7.2.1 Aerodynamic breakup

Droplets injected are immediately entrained by the high velocity plasma field. The drag force between the droplet and the plasma creates shear deformations in the droplets. Basu et al. (2008b) showed that depending on the droplet size and surface tension, shear instability dissociates the droplet into smaller droplets. Basu et al. (2008b) have also shown that the time involved with this phenomenon is of the order of microseconds. The controlling and determining parameters for this process are droplet size, relative velocity between the droplet and the plasma field and surface tension of the precursor. This aerodynamic breakup is very favorable to obtain a highly dense durable coating on the substrates [Basu et al. (2008b)].

7.2.2 Rapid vaporization and precipitation

In the second stage, the child droplets from the aerodynamic breakup undergo rapid vaporization in the high temperature plasma field. For most precursors, it is observed that mass diffusivity of the solute in the solvent is a very slow process. Vaporization of solvent therefore non-uniformly increases the relative concentration of solute with the highest concentration registered at the droplet surface. Whenever the surface concentration of the solute reaches a preset super-saturation limit it precipitates engulfing all the regions of the droplet where equilibrium concentration is exceeded. This process has been described as homogeneous precipitation hypothesis by Messing et al. (1993). The precipitate morphologies (surface precipitation versus volume precipitation) are dependent on droplet size and mass transportation processes. Though homogeneous nucleation hypothesis governs the precipitate thickness, it is very hard to predict the porosity of the same.

In spray pyrolysis literature, evidences of shell (precipitate) formation have been found, though they are at much lower heating rate compared to the plasma. Zhang et al. (1990), Jain et al. (1997), Che et al. (1998) and Linn and Gentry (2003) have shown that with different solute properties and droplet sizes, different shell structures and morphologies are possible. Their works with different aqueous solutions like sodium acetate, calcium acetate detailed phenomena like droplet shrinkage, precipitations, crust formation and subsequent fracture. The morphologies of the crust were dependent on the solution. Subsequently rigorous experimental works [Jordan et al. (2004), Bhatia et al. (2002), Padture et al. (2002)] and [Zhang et al. (1990), Jain et al. (1997), Che et al. (1998) and Linn and Gentry (2003)] have shown that similar morphologies exist in the SPPS process as well. Figure 61 shows that in SPPS process, solid particles and fragmented shells are omnipresent.

7.2.3 Internal pressurization with shell rupture

The third transition encountered by the precipitated droplet is the heating and internal pressurization. For a surface precipitated droplet, the liquid inside the solid crust gets heated by the plasma forming a vapor zone. The vapor formed increases the internal pressure inside the shell. This pressure development depends on the porosity of the shell. For low porosity shells, the internal vapor pressure rises and becomes higher than the shell rigidity causing it to rupture. The internally trapped liquid core contained within the shell undergoes secondary atomization following shell fracture to form daughter droplets. The daughter droplets formed undergo a similar cycle of heating and vaporization, followed by precipitation and subsequent internal pressurization with shell rupture. This cyclic process creates progressively smaller diameter daughter droplets till one reaches a state where the droplet is small enough to undergo volumetric

precipitation to form a solid particle with no liquid core. It should be however noted that high

porosity shells (>30% porosity) vent out the vapor formed to relieve the internal pressure rise

and hence do not undergo rupture to form daughter droplets. These droplets mostly arrive at the

substrate in un-pyrolized form with a hot liquid core.
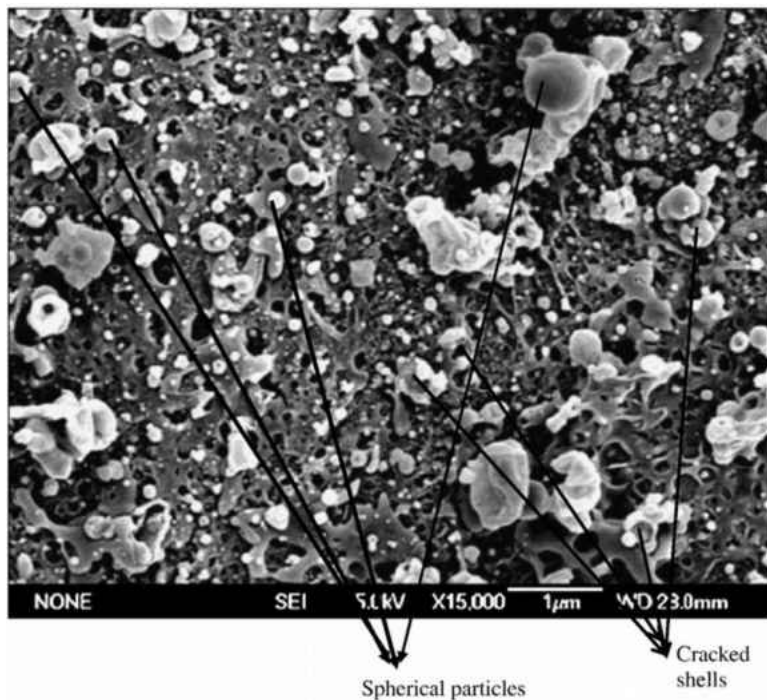
Figure 61: SEM analysis of the deposition after single pass in the plasma. The precursor solutions used in this SPPS process are aqueous (water as solvent) salts containing zirconium and yttrium. The precursors are mixed according to the final composition of 7 wt.% yttria-stabilized zirconia (7YSZ). The coating these single scan correspond to is reasonably dense (88%) and hard (1023 Hv). Same morphology has been observed in single pass for dense Al_2O_3–40 wt.% 7YSZ coatings, TiO_2 coatings and in 7YSZ coatings for porous TBCs. Cracked shells as well as molten solid mass are visible.

7.2.4 Rapid heating of volumetrically precipitated solid particle

The fourth stage is the heating phase of the volumetrically precipitated solid particles by the

plasma. The solid particle depending on the location where it forms in the plasma jet undergoes

rapid heating and temperature rise due to the absence of evaporation. All the four regimes the

droplet encounters are shown in Figure 62. Modeling approaches for each of the regimes are described in the next section.
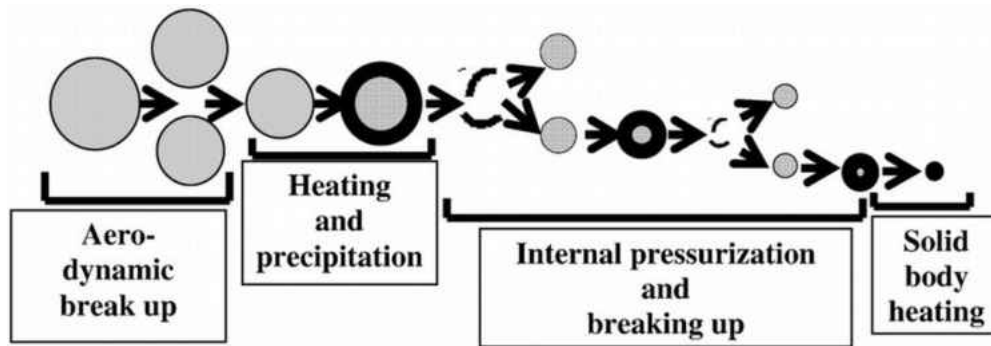
Figure 62: Four thermo-physical stages of the droplet.

7.2.5 Initial stages of aerodynamic breakup

Aerodynamic breakup is the first physical transformation a droplet undergoes as soon as it is injected into the plasma. The precursor droplets can be injected transversely or axially into the plasma, although transverse injection is the most common way of injecting droplets and particulates into a DC-arc plasma. The injected droplets experience high velocity convective flow field which causes aerodynamic shear on the droplet surface. The flow induced shear gives rise to a variety of instabilities depending on the droplet size and thermo-physical properties leading to deformation and breakup. The factors influencing the droplet breakup are the relative velocity between the droplet and surrounding flow, damping forces due to viscosity and surface tension. Other effects like surface evaporation are usually considered to be negligible at the timescale of the droplet breakup process. The relevant non-dimensional parameters to enunciate the relative importance of the inertia and surface tension is the Weber number defined as, $We = (\rho_p \Delta u^2 d)/\sigma$, where ρ_p, Δu, d and σ are the density (specific mass) of the plasma, the relative

velocity between the droplet and the plasma flow, the diameter of the droplet and the surface tension of the liquid respectively. Values of Weber number greater than unity suggest that inertia forces are much more dominant than the surface tension and hence the droplets are prone to deformation and breakup. Weber number is hence considered the key parameter responsible for the breakup process. For all practical purposes, a Weber number of about 14 [Watanabe and Ebihara (2003)] can be chosen as the critical value below which the droplets may deform but do not undergo breakup. It is to be noted that the time duration of the breakup process decreases with increase in droplet size due to the increase in Weber number. The viscous damping force acts as a counter measure to the deforming aerodynamic force (due to high relative velocity between droplet and plasma) and prevents the droplet from breakup. The nondimensional parameter detailing the effect of viscosity is Ohnesorge number, which is defined as

$Oh = \dfrac{\mu_p}{\sqrt{\rho_p \sigma d}}$, where μ_p, ρ_p, d, σ are the viscosity of the plasma flow, density of the plasma

flow, the diameter of the droplet and the surface tension of the liquid respectively. However for all practical purposes, the effect of viscosity is considered negligible compared to the effect of Weber number. The aerodynamic breakup process has been elaborately studied by Basu et al. (2008b) using the Taylor Analogy Breakup (TAB) model. This model works well with lower Weber number (<100), which is relevant to our study. It assumes that the droplets behave analogous to an oscillating spring mass system with the external loading simulated by the aerodynamic drag, restoring forces being the surface tension and the viscous damping forces. But for higher injection velocity and higher Weber number (N100), the droplet breakup physics starts drifting from the solution predicted by TAB model. At that point, the wave model can be used

for analyzing the droplet shear instability. Detailed discussions of the TAB model can be found under Ref. [Basu et al. (2008b)].

7.2.6 Droplet heating, vaporization and internal precipitation

The aerodynamic breakup of droplets occurs within a timescale of a few microseconds and produces droplets of stable size which do not undergo further shear breakup in the plasma. The daughter droplets now undergo severe heating and vaporization in the high temperature plasma leading to increase in concentration of solute near the droplet surface. At a critical value of solute concentration, precipitation occurs resulting in the formation of a porous shell around the liquid core. The precipitation leading to shell formation is assumed to be instantaneous based on the super-saturation concentration value of solute based on the data in the literature [Messing et al. (1993)]. This part of the analysis is extended from our earlier model [Basu et al. (2008b)] that provides mathematical solution for the heat and mass transport within the droplet. The coupling with the surrounding hot gases is described by a one dimensional (i.e. in the radial direction) coupling of heat and mass transfer fluxes from the plasma flow field. The measured temperature and velocity fields are utilized in these computations. The droplet trajectory is obtained from integration of droplet momentum equation with the external flow field of the plasma. As detailed in the references [Messing et al. (1993), Zhang et al. 1990, Jain et al. (1997), Yuen and Chen (1976), Abramzon and Sirignano (1989)], these models are capable of predicting the solute concentration and temperature distributions within the droplet and the corresponding precipitation zones (based on supersaturation levels). The instantaneous position and size of the individual droplets are also calculated within the plasma field. This current work however did not consider the effect of neighboring droplets limiting the analysis to dilute spray situation.

186

The droplets are assumed to be composed of cerium nitrate (solute) dissolved in liquid water (solvent) with a prescribed initial cerium nitrate mass fraction. Droplet motion in the hot convective gas environment is governed by the droplet momentum equation given by,

$$\frac{\partial U}{\partial t} = \frac{3C_D}{8r_s}\frac{\rho_\infty}{\rho_L}|U_\infty - U|(U_\infty - U) \tag{7.1}$$

$$\frac{\partial V}{\partial t} = -\frac{3C_D}{8r_s}\frac{\rho_\infty}{\rho_L}V^2. \tag{7.2}$$

where U and V are the droplet velocities in axial and transverse directions, C_D is the drag coefficient due to the relative motion between the droplet and the surrounding hot gases with U∞ being the free stream flow velocity. The change in the droplet radius is given by,

$$\frac{\partial r_s}{\partial t} = -\frac{\dot{m}}{4\pi\rho_L r_s^2} \tag{7.3}$$

where $\dot{m}$ is the rate of mass vaporization, ρ_L is the liquid specific mass. These equations are supplemented by the Clausius–Clapeyron equation and Raoult's Law to determine the mass vaporization rate, surface temperature and surface vapor concentration. The surface temperature and mass vaporization rate are then used as boundary conditions in the solution of the conservation of energy and species equations in the liquid phase. For small droplets less than 100 μm, the surface tension forces maintain the droplets in spherical shape.

Non-dimensional unsteady conservation of energy and solute species equations inside the droplet are written in the spherical polar (r, θ) coordinates as [Ozturk and Cetegen (2004), (2005b), (2006)],

$$\bar{r}_s^2 \frac{\partial \bar{T}}{\partial \tau} + \left(0.5 Pe_L \bar{V}_r \bar{r}_s - 0.5 \frac{dr_s}{d\tau} \eta\right) \frac{\partial \bar{T}}{\partial \eta} + 0.5 Pe_L \frac{\bar{V}_\theta \bar{r}_s}{\eta} \frac{\partial \bar{T}}{\partial \theta} =$$
$$\frac{1}{\eta^2} \frac{\partial}{\partial \eta}\left(\eta^2 \frac{\partial \bar{T}}{\partial \eta}\right) + \frac{1}{\eta^2 \sin\theta} \frac{\partial}{\partial \theta}\left(\sin\theta \frac{\partial \bar{T}}{\partial \theta}\right)$$

(7.4)

$$Le_L \bar{r}_s^2 \frac{\partial \bar{\chi}_i}{\partial \tau} + \left(0.5 Pe_L Le_L \bar{V}_r \bar{r}_s - 0.5 Le_L \frac{dr_s}{d\tau} \eta\right) \frac{\partial \bar{\chi}_i}{\partial \eta} + 0.5 Pe_L Le_L \frac{\bar{V}_\theta \bar{r}_s}{\eta} \frac{\partial \bar{\chi}_i}{\partial \theta} =$$
$$\frac{1}{\eta^2} \frac{\partial}{\partial \eta}\left(\eta^2 \frac{\partial \bar{\chi}_i}{\partial \eta}\right) + \frac{1}{\eta^2 \sin\theta} \frac{\partial}{\partial \theta}\left(\sin\theta \frac{\partial \bar{\chi}_i}{\partial \theta}\right)$$

(7.5)

where following dimensionless quantities are employed $\bar{r}_s = r/r_o$, $\tau = \alpha_L t / r_o^2$, $\eta = r/r_s$, $\bar{T} = (T - T_o)/T_o$, and $\bar{\chi} = (\chi - \chi_o)/\chi_o$ with r_0 is the initial radius, α_L is the liquid thermal diffusivity, t is time, r_s is the droplet surface radius, T is temperature with T_0 being the initial value and correspondingly χ being the solute mass fraction with χ_0 being its initial value. $\bar{V}_r$ and $\bar{V}_\theta$ are the radial and angular components of the velocity within the droplet taken as the spherical Hill's vortex with its circulation determined from the surface shear [Ozturk and Cetegen (2005b)]. $Pe_L = (r_s \Delta U)/\alpha_L$ is the liquid Peclet number and $Le_L = D_s/\alpha_L$ is the liquid Lewis number. The initial and boundary conditions within the droplet can be written as,

$$\left\{\begin{matrix} \bar{T} \\ \bar{\chi} \end{matrix}\right\}(\tau = 0) = 0, \ \frac{\partial}{\partial \eta}\left\{\begin{matrix} \bar{T} \\ \bar{\chi} \end{matrix}\right\}\bigg|_{\eta=0} = 0, \ \frac{\partial}{\partial \theta}\left\{\begin{matrix} \bar{T} \\ \bar{\chi} \end{matrix}\right\}\bigg|_{\theta=0,\pi} = 0$$

$$\frac{\partial}{\partial \eta}\left\{\begin{matrix} \bar{T} \\ \bar{\chi} \end{matrix}\right\}\bigg|_{\eta=1} = \begin{cases} \int_0^\pi \frac{\partial \bar{T}}{\partial \eta} \sin\theta d\theta = \frac{Q_L}{2\pi r_s k_L T_o} \\ \int_0^\pi \frac{\partial \bar{\chi}}{\partial \eta} \sin\theta d\theta = \frac{\dot{m}\bar{\chi} - \dot{m}_i}{2\pi r_s \rho_L D_{i,s} \chi_{z,o}} \end{cases}$$

(7.6)

where $\dot{Q}_L$ is the heat flux to the droplet, k_L is the liquid conductivity, ρ_l is liquid density, D_s is the mass diffusivity of solute in solvent. Further details of this model can be found in references [Ozturk and Cetegen (2004), (2005b), (2006), Basu and Cetegen (2007)].

7.2.7 Internal pressurization and droplet breaking-up

Subsequent to shell formation, for spherically symmetric assumption, further heating of the particle containing a liquid core is modeled as follows. The particle motion through the hot plasma is still governed by Equations 7.1 and 7.2 except that the particle size is now fixed to the outer diameter of the precipitate shell. The Nusselt number for the porous and nonporous shells is obtained as described by Basu and Cetegen (2007). The model for the particle interior is divided into three zones: solid shell, vapor annulus, and liquid core. In each region, the energy equation is of the same form as Equation 7.4 without the 'O' dependence (spherically symmetric) and a moving interface between the liquid core and the vapor film. The enthalpy carried by the vapor escaping through the pores is accounted for in the model as detailed by Basu and Cetegen (2007). Depending on the type of shell formed, they found that one may or may not have any venting effect through the pores in the shell. However, for the general case of a shell of porosity ε, with the ideal gas law assumption Basu et al. (2008b) showed

$$\frac{dp_v}{dt} = \frac{RT_v}{V_v}\left[4\pi r_l^2 \rho_v \left|\frac{dr_l}{dt}\right| - 4\pi r_l^2 \rho_l \frac{dr_l}{dt} - \rho_v A_{pore} V_{pore} \right] \tag{7.7}$$

where V_{pore} is the velocity of the gas venting through the pores of the shell estimated from Karman–Cozeny equation while A_{pore} is the total area of the pores. ρ_v and ρ_l denote the densities of the vapor and liquid phase while r_l is the radius of the liquid core. Equation 7.7 gives Basu et

189

al.'s (2008b) expression for internal pressure rise as a function of shell porosity, the vapor velocity escaping through the pores and the rate at which the liquid front is receding towards the droplet center. Internal pressurization of the shell due to vaporization of the trapped liquid can lead to shell rupture or inflation depending on the shell type that forms during precipitation. They showed that this depended on the solute and solvent characteristics and the thermo-physical conditions under which the precipitation occurs. The simplest shell fracture criterion is the failure stress of the shell material.

In this approach, the fracture criterion becomes

$$p_v = \frac{2\delta\sigma}{r_s} \tag{7.8}$$

where σ represents the failure stress of the shell material and δ is the shell thickness. Depending on the morphology of the crust, the trapped liquid inside it will atomize to give birth to two or more new daughter droplets. These new droplets will go through the same process of heating up, shrinking and internal precipitation. All the equations described previously in this section (Equations 7.1–7.7) are applicable for modeling the transport of the daughter droplets.

7.2.8 Solid particle heating

Processes described in Sections 2.6 and 2.7 occur in cyclic fashion till the daughter droplet size becomes small enough that it undergoes volumetric precipitation in the plasma. The volumetrically precipitated droplet subsequently undergoes rapid heating. The rate of heating is considered to be governed by a lumped capacitance model with the temperature difference

between the particle and the high temperature plasma playing a significant role. The energy balance equation for a solid particle is written as,

$$m_{pt} C_{pt} \frac{dT_{pt}}{dt} = h A_{pt} (T_{\infty} - T_{pt})$$ (7.9)

where m_{pt}, C_{pt} and T_{pt} are the mass, specific heat and temperature of the solid particle and T_{∞} is the local plasma temperature. The coefficient for convection heat transfer (h) can be found from Nusselt number (Nu), which can be calculated from the Ranz–Marshall correlation given by [Ranz and Marshall (1952)]

$$Nu = \frac{h d_{pt}}{k_{\infty}} = 2.0 + 0.6 \, \mathrm{Re}^{1/2} \, \mathrm{Pr}^{1/3}$$ (7.10)

where Re, Pr, d_{pt} and k_{∞} are the Reynolds number based on relative velocity between the particle and plasma field, Prandtl number, diameter of the particle and thermal conductivity of the plasma respectively. The motion of the particle in the hot convective gas environment is still governed by Equations 7.1 and 7.2. Equations 7.1, 7.2 and 7.9 are solved simultaneously by Range–Kutta method yielding the instantaneous location and the temperature of the particle. Depending on the precipitated droplet size and injection pattern, the solid particle may or may not reach the substrate before melting. The melting point for ceria is taken as 2300 K [Viswanathan et al. (2007)].

Properties of cerium nitrate solution [precursor properties] [Castillo and Munz (2007)]	
Density [kg/m^3]	ρ = 847.94443 + 1.2919255*Temperature – 0.0026644444*Temperature^2
Specific heat [J/kg/K]	C_p = 7453.3509 – 19.151393*Temperature + 0.027465156*Temperature^2
Thermal conductivity [W/m/K]	K=–0.35088198 + 0.0050174555*Temperature – 6.058655*10^{-6} *Temperature^2
Viscosity [Pa s]	μ=exp(−67.638222 + 4425.7586 /Temperature + 8.0352064*ln(Temperature))
Binary diffusivity of cerium nitrate in water [m^2/s]	10^{-9}
Saturation mass fraction of solute	0.74
Super-saturation mass fraction of solute	0.99
Properties for ceria [solid phase]	
Specific heat [J/kg/K] For Temperature b850 K	For Temperature < 850 K C_p = 1.1 + 8.32*Temperature + 0.5*10^{-4} *Temperature^{-2} For 850 K < Temperature < 1400 K C_p = 3.6 + 29.43*Temperature + 0.95*10^{-4} *Temperature^{-2} For Temperature > 1400 K C_p = 8.1 + 33.29*Temperature + 1.3*10^{-4} *Temperature^{-2}
Density [kg/m3]	7650 m^3/kg
Melting point	2400 K

Table 5: Thermo-physical properties [the initial mass fraction for cerium nitrate in the precursor solution was 0.05] (The property values of plasma and vapor phase have been cited in references [Ozturk and Cetegen (2004), (2005a), (2005b), (2006) and Semenov and Cetegen (2001)]

7.3 Results

The plasma field used in the model is similar to a high velocity and high temperature turbulent Ar–H$_2$ jet issuing out of an 8 mm nozzle. The temperature and velocity of the gases at the nozzle exit plane was found to be 9000 K and 600 m/s respectively. Semenov and Cetegen (2001) used a combination of Laser Doppler Anemometry, high speed imaging and emission spectroscopy to measure the temperature and velocity of the entire plasma flow. The experimental values reported by them were curve fitted and supplied as user defined functions to the current model.

In the following sections, the results from the proposed model for cerium nitrate precursor, with initial solute mass fraction of 0.05 are described. Both axial and transverse injections of the droplets into the plasma were considered. For both the cases, the substrate is stationed at a distance of 12 cm from the nozzle exit plane. For axial injection, the injection port is located at a distance of 8 mm downstream of the nozzle tip. In case of transverse injection, the injection port is located at a radial distance of 12 mm away from the plasma jet axis and at an axial distance of 8 mm downstream of the nozzle tip. The injection velocity for the droplets was 12 m/s. Initial temperature of the droplets at the injection port was 300 K. Thermo-physical properties of the liquid precursor are detailed in Table 5. Plasma and vapor phase properties are taken from Refs. [Ozturk and Cetegen (2004), (2005b), (2006), Semenov and Cetegen (2001)].

The phenomenon of aerodynamic breakup has been studied in details by Basu et al. (2008b). Their results predicted that for an injection velocity of 12 m/s, axially injected droplets of size less than 50 μm do not exhibit any aerodynamic breakup. However if the surface tension of the solvent is reduced (addition of alcohol to water) significantly then droplets of 50 μm in diameter disintegrate into smaller droplets of varying sizes ranging from 5–30 μm. It is hence agreed generally that droplets smaller than 50 μm do not experience aerodynamic breakup under normal circumstances. As the current model deals with droplets less than 30 μm in diameter, the phenomena of aerodynamic breakup is not important for both types of injection schemes. Once the droplet is exposed to the plasma field, it starts shrinking in size due to rapid vaporization of the solvent resulting in an increase in solute concentration near the surface. When the surface concentration reaches the super-saturation limit, precipitation is triggered to form a crust around a liquid core where the solute concentration is still below the equilibrium concentration. The

super-saturation limit and equilibrium concentration for cerium nitrate are 0.99 and 0.74, respectively. Further heating vaporizes the trapped liquid inside the crust increasing the internal vapor pressure buildup. Depending on the crust porosity, when the pressure force exceeds the yield stress of the shell, it ruptures, forcing the trapped liquid core to undergo secondary atomization to form several small droplets. The new daughter droplets undergo through the same heating and vaporization processes in the plasma, which lead to a similar cycle of precipitation, crust formation, shell fracture and secondary atomization to form even smaller droplets. This cycle continues until the daughter droplet becomes so small that it undergoes volumetric precipitation of the solute to form a solid particle. It is evident that the diameter of the daughter droplets decreases with increase in number of daughter droplets produced by shell rupture. Smaller daughter droplets are more favorable for good microstructure as they easily get pyrolized by the plasma. Padture et al. (2001) and Jordan et al. (2004) showed that a good quality ceramic coating produced by SPPS process (for TBC) should have (1) micron sized splats, (2) grain sizes less than 30 nm, (3) through thickness, stress-relieving vertical cracks ,(4) nanometer and micrometer porosity levels and (5) semi pyrolized deposits. Dense coatings however require fully pyrolized deposits [Jordan et al. (2004)]. The larger daughter droplets on the contrary can be un-pyrolized resulting in unwanted coating quality, which includes horizontal cracks, presence of voids, non-uniform vertical cracks etc. Though it is possible that the number of droplets, produced from the liquid core as a result of shell rupture, may be more than two, we considered the minimum possible number (2) to do a conservative analysis. It is to be noted that our conservative estimate also results in largest daughter droplet size. As explained before, smaller droplets always result in better coating (nanometer sized grains, evenly spaced vertical

crack, semi to fully pyrolized deposit) but it is the larger droplets that contribute towards faulty coating microstructure and hence needs to be analyzed thoroughly. It is in this light that the estimate of "two daughter droplets per shell fracture" provides an opportunity to study "worst case scenario for resulting coating quality".

7.3.1 Axial injection

In this section results related to the axial injection of the droplets in plasma are explained. Three initial droplet diameters of 20, 10 and 5 μm have been considered for this study. Initial solute mass fraction is 0.05 for all cases.
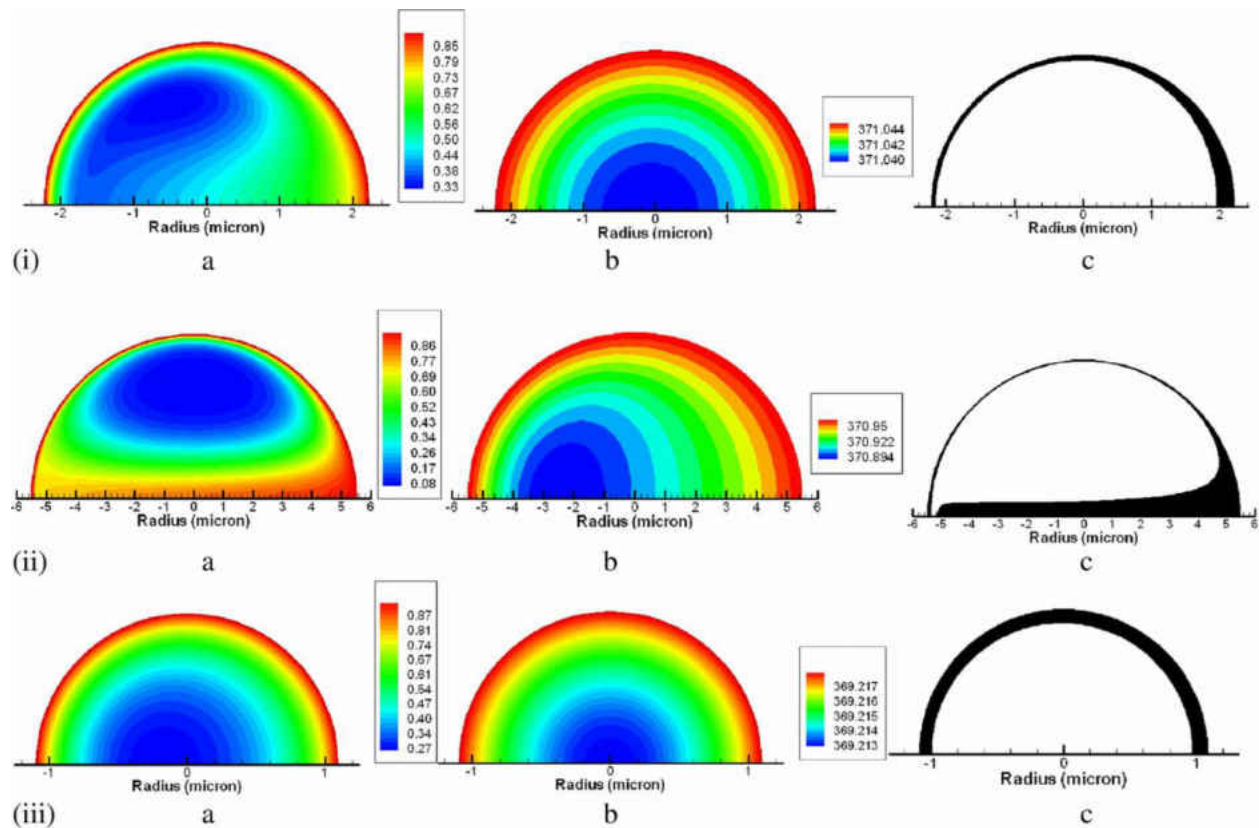
Figure 63: Concentration and temperature distribution within different sized axially injected droplets. (i): 10 μm droplet after 787 μs. (ii): 20 μm droplet after 1300 μs. (iii): 5 μm droplet after 393 μs. a: Concentration distribution b: Temperature distribution. c: Shell formation.

In this study, it is important to visualize the solute concentration and temperature distributions inside the droplet as it traverses the plasma flow. Axially injected 10 μm droplet shrinks in size to a diameter of 4.3 μm due to rapid surface vaporization before precipitation is triggered. The entire time span of the first vaporization and precipitation process is 787 μs. Prior to precipitation, the solute concentration distribution exhibits the presence of sharp concentration gradient within the droplet as shown in Figure 63(i)a. The temperature profile on the contrary exhibits a very uniform profile as shown in Figure 63(i)b. This is because high Peclet number resulting from low mass diffusivity of cerium nitrate in water makes the iso-concentration lines coincide with the streamlines of the recirculating flow within the droplets whereas the high thermal diffusivity equilibrates out the temperature gradient within a very small time interval. Figure 63(i)c shows the precipitated zones of the droplet. It is seen that the precipitated zone engulfs all the regions of the droplet where equilibrium concentration is exceeded. The precipitated crust has a finite thickness and subsequently undergoes internal pressurization and consequent shell fracture. The timescale of the shell fracture process as shown by Basu et al. (2008b) is of the order of 3–5 μs for low porosity crusts (0–20%). The final microstructural evidence of ceria coatings show that the crust formed is likely to be moderately impervious [Viswanathan et al. (2007)] and is likely to fracture in microseconds. Our conservative estimation predicts there will be two equally sized new droplets of diameter 3.14 μm formed as result of shell fracture. The initial concentration and temperature distribution of each daughter droplet is assumed to be equal to the mean concentration and mean temperature of entrapped liquid inside the solid crust just prior to shell fracture. The initial solute mass fraction of the

daughter droplets was calculated to be 0.54 after first precipitation and increased progressively after every subsequent stage. The dynamics of the daughter droplets subsequent to shell fracture is hard to predict. However it is anticipated that one of the two possible scenarios may happen. Due to the uncertainty in the direction of the force generated by shell rupture, the daughter droplet may follow the same axial path as the parent droplet (first case) or the droplet may follow an angular trajectory with respect to the parent (second case). Though there is directional ambiguity regarding the trajectory of the daughter droplets, the principle of momentum conservation is still valid. One of the aims of this work was to realize the magnitude of change expected in the final morphology of the droplet depending on the trajectory it follows subsequent to each individual shell fracture. In this study, it was approximated that 60° is the maximum inclination that an axially injected droplet can have during its flight with respect to the plasma axis. For any other inclination angle between 0 and 60°, the final droplet morphology should fall within the limits specified by the 0° (axial) and 60° cases (considering two droplets of same mass and velocity generated from a droplet which was traveling axially it is very likely for the daughter droplets to follow the path between 0 and 60° with the plasma axis). So our alternate angular path has been approximated by 60° inclination with the plasma axis.

7.3.1.2 20 μm droplet

For 20 μm droplet the primary (first) surface precipitation occurs after 1300 μs. At this stage the droplet shrinks to a diameter of 10.8 μm. The iso-concentration lines shown in Figure 63(ii)a depict the presence of recirculation resulting from low mass diffusivity of cerium nitrate within water. Due to the high degrees of internal circulation in the droplet, the core region of the droplet contains high solute concentration. The abundance of solute in the droplet core ultimately

197

triggers precipitation to form a shell around the droplet that is internally connected at the core with solution present in the torus i.e. in two physically separated regions. The temperature contours in Figure 63(ii)b exhibits the presence of higher temperature gradient towards the forward stagnation point though the overall temperature difference throughout the droplet is less than 0.1 K. The portion of the droplet having concentration higher than equilibrium solubility forms a crust engulfing the liquid core inside it as illustrated in Figure 63(ii)c. The nature of the crust with a bridge near the core as interconnect suggest that each of the two separated liquid cores will produce at least two new droplets of diameter 7.94μmeach after shell rupture. Once again, the timescale of shell rupture for these low porosity shells is of the order of microseconds making the process almost instantaneous after precipitation.
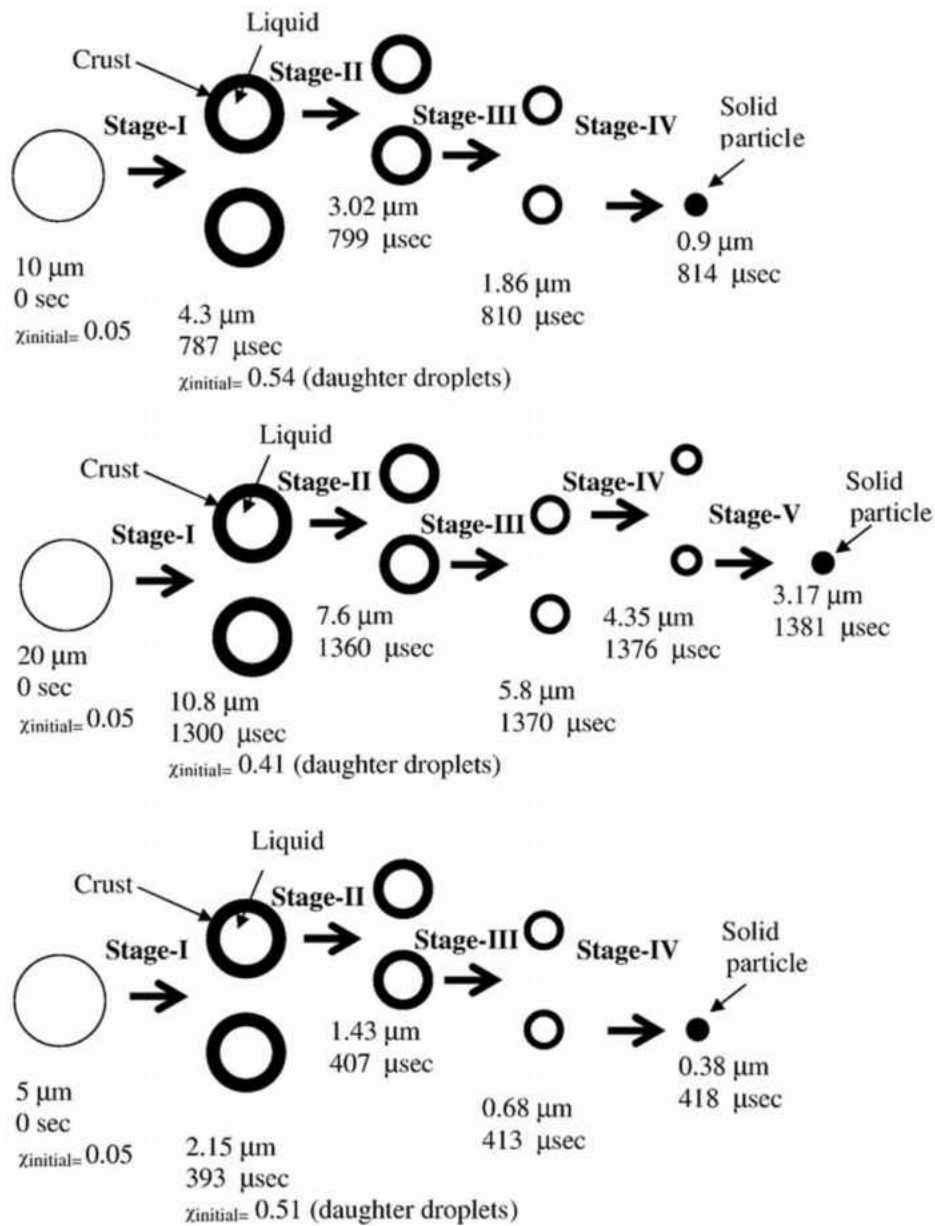
Figure 64: The interim stages for the different sized axially injected droplets (time for all stages is calculated from the instant of injection) (a) 10 μm, (b) 20 μm, (c) 5 μm.

7.3.1.3 5 μm droplet

The 5 μm droplet precipitates much faster than the 10 and 20 μm droplets. The primary precipitation occurs after 400 μs. The concentration distribution shown in Figure 63(iii)a depicts

199

that mass diffusion is much more dominant than advection as the droplet is very small in diameter. As compared to the larger droplets, the concentration levels increase more uniformly within the droplet. The temperature contour shown in Figure 63(iii)b also shows no variation and negligible gradient within the droplet. The precipitated droplet is shown in Figure 63(iii)c which depicts a concentric shell of moderate thickness.

7.3.1.4 Interim precipitation stages (Droplets with initial diameters from 5 to 10 μm)

After the interim precipitation as shown in Figure 63(i), the 10 μm droplet undergoes series of secondary atomization stages before it eventually precipitates volumetrically resulting in the formation of solid particle. These in-flight intermediate stages are depicted in the Figure 64a. It should be noted in Figure 64a that the droplet size decreases from 10 μm to 0.9 μm before it precipitates volumetrically. The daughter droplets formed after secondary atomization processes of 20 μm initial diameter droplets go through similar cycles explained earlier before it encounters volumetric precipitation to form a solid particle of diameter 3.17 μm. Figure 64b illustrates the interim inflight stages of a 20 μm droplet. It can be noted that all the interim stages are of very short duration. The 5 μm droplet following primary precipitation (Figure 63(i)c) ruptures to form two daughter droplets with diameter of 1.59 μm each. The daughter droplets go through couple of secondary precipitations before forming a solid particle of 0.38 μm after volumetric precipitation. The interim stages, shown in Figure 64c, depict the low time scale involved in the processing of small sized droplets injected axially into the plasma.

The notable observation is that in all cases, the parent droplet undergoes 4 to 5 surface precipitation cycles before precipitating volumetrically into a solid particle. Figure 64 also shows

that the time scale involved in the entire process increases with increase in size of the initial droplet. This is expected as larger droplets having larger amount of solvent content need longer time vaporization time.
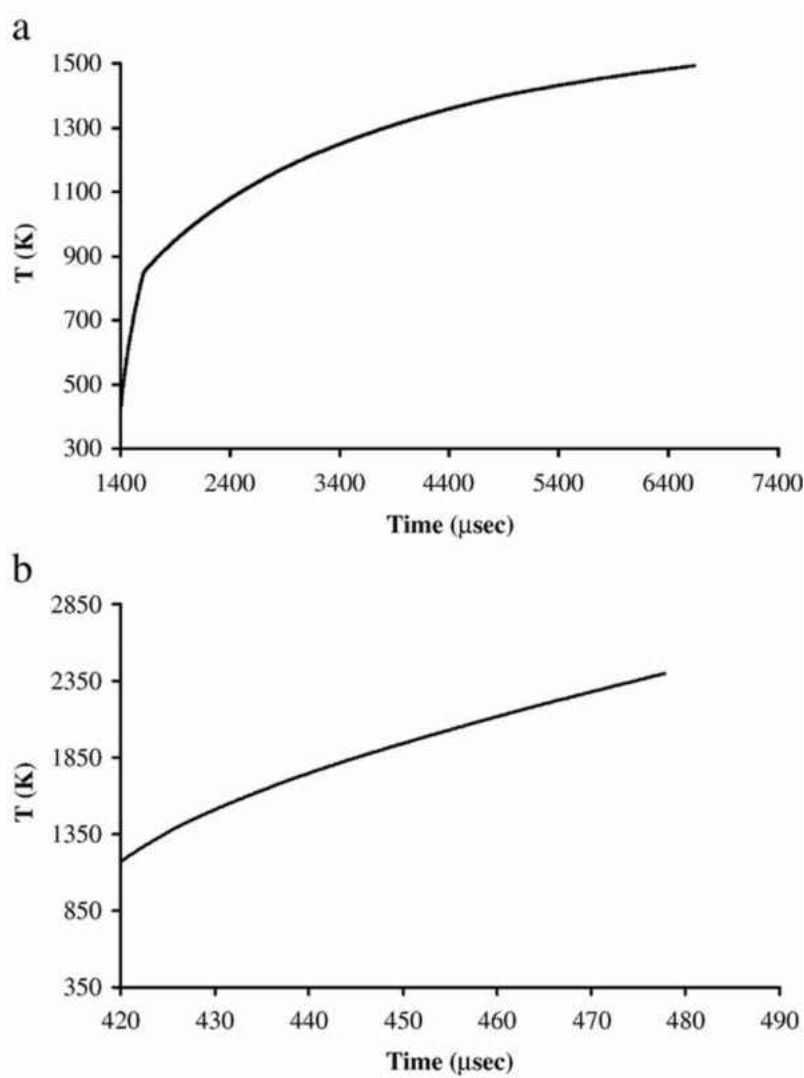
Figure 65: Transient thermal history for solid particle formed from axially injected droplets. (a) 20 μm, (b) 5 μm (time for all stages is calculated from the instant of injection).

7.3.1.5 Pyrolization stages

The 0.9 μm solid particles resulted from volumetric precipitation of 10 μm droplets as shown in Figure 64a subsequently undergo heating in plasma to become almost pyrolized at a temperature of 2110 K before reaching the substrate plate. In case of 20 μm initial diameter droplet, the precipitated solid particle (1.59 μm) undergoes rapid heating and record temperature rise up to around 1500 K as shown in Figure 65a. Hence these droplets get deposited on the substrate in partially pyrolized form.

The 0.38 μm particle resulting from volumetric precipitation of 5 μm droplet is heated by the plasma and is completely pyrolized before reaching the substrate. The transient temperature response of the particle is illustrated in Figure 65b.

7.3.1.6 Effect of inclined trajectory

As mentioned earlier the current study also looked into the secondary atomization and precipitation stages of the droplet following an inclined trajectory after primary precipitation. But the results show that there is negligible change in the final morphology of the droplet even with a 60° inclination. Figure 66 shows one to one comparison of the interim stages of the two droplets following axial and angular trajectories. The stages are almost identical which is expected as the timescale involved for secondary precipitation (interim) stages are small compared to the primary precipitation process. It is therefore inferred that the angle of the trajectory does not have any significant effect on the final microstructure. The same kind of result has been observed for other droplet sizes as well. So, the remainder of the results is reported for daughter droplets having same trajectory as the parents.
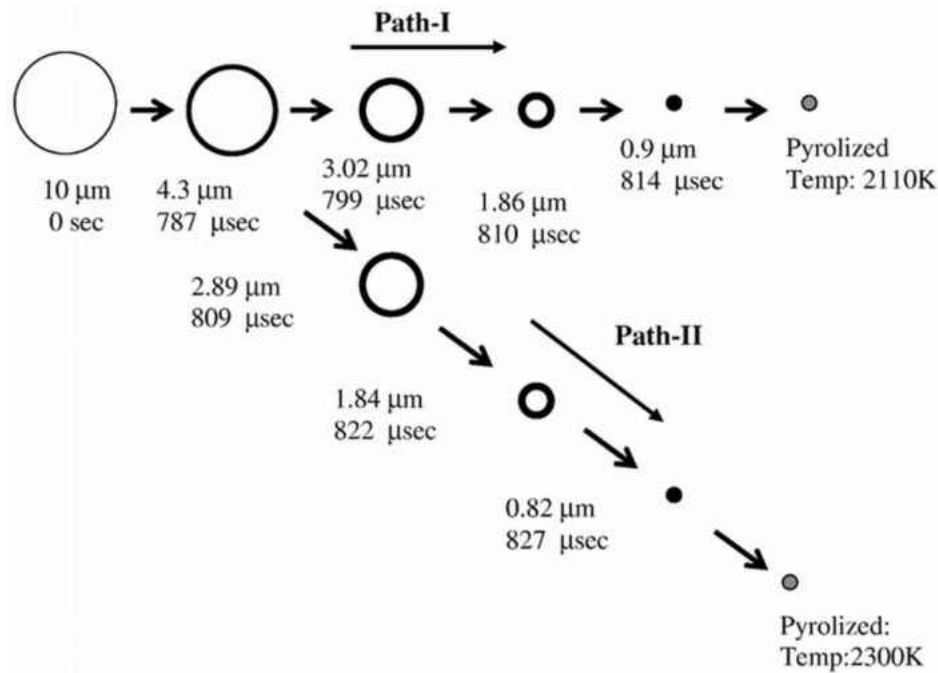
Figure 66: Comparative analysis of trajectory for axially injected 10 µm droplet: Path I: traversing in an axial trajectory after primary (first) precipitation. Path II: traversing in an inclined trajectory after primary (first) precipitation (time for all stages is calculated from the instant of injection).

7.3.1.7 Summary of axial injection

The comparative study of the axially injected droplets shows that droplets with smaller initial diameters are better pyrolized in the plasma before deposition on the substrate. It also can be inferred that for same sized droplets, the trajectory does not have much effect on the final microstructure. Figure 66 shows that for 10 µm axially injected droplet, the final morphology is almost similar for both axial and angular trajectories.

7.3.2 Transverse injection

In this section results related to the transverse injection of the droplets in plasma are explained. Once again initial droplet diameters of 20, 10 and 5 µm have been considered for this study.

Transverse mode involves injection of the droplet in the outer shear layer of the plasma instead of the hotter core as in the axial mode. The injected droplet hence at first encounters a low temperature and low velocity plasma environment. Depending on the speed of injection and initial size, the momentum of the droplet helps it to penetrate the outer layer and approach the high temperature core of the plasma. The larger droplets by virtue of the higher inertia, penetrates the outer shear layer more effectively than the smaller droplets with lower inertia.
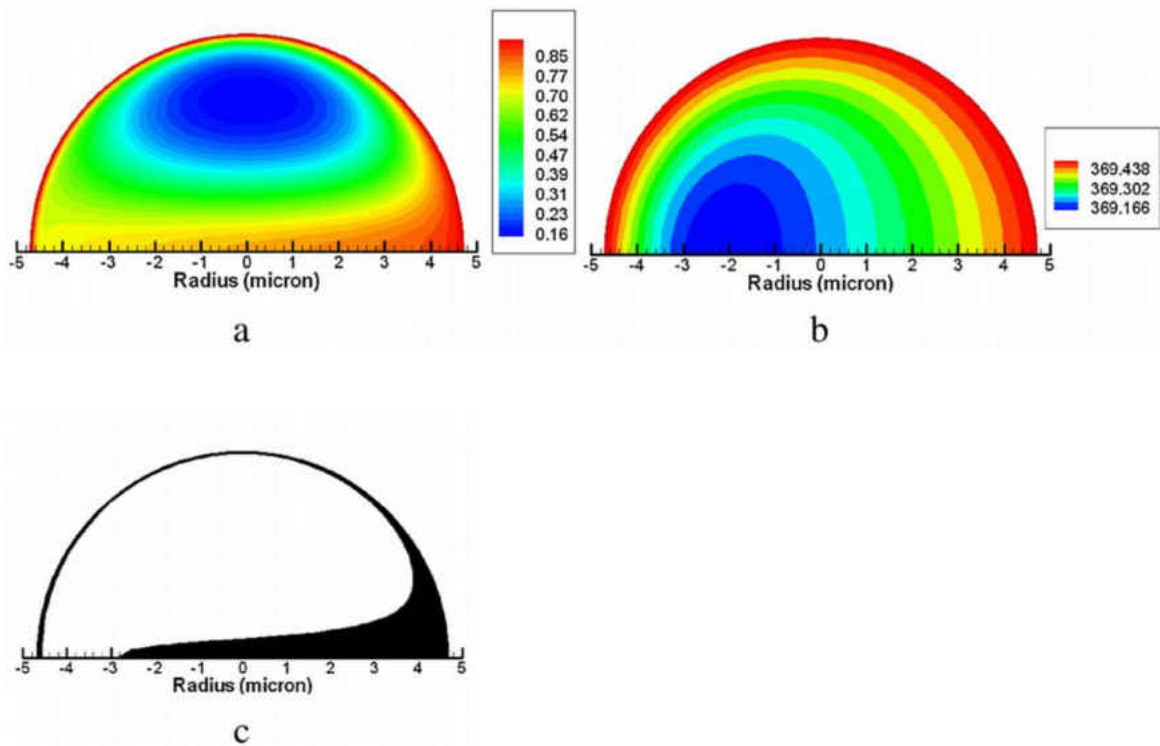
Figure 67: Transversely injected 20 μm droplet after 1544 μs. (a) Concentration distribution, (b) Temperature distribution, (c) Shell formation.

20 μm droplets injected into the plasma flow are entrained as they penetrate through the shear layer. The vaporization of the solvent causes rise in surface concentration of solute leading to primary surface precipitation. The 20 μm initial diameter droplet shrinks to a size of 9.19 μm

prior to precipitation. The iso-concentration lines coinciding with the streamlines, as shown in Figure 67a depicts highly convective mass transfer within the droplet due to the very low mass diffusivity. The temperature contour shown in Figure 67b depicts a very uniform profile. The results are similar to axial injection. The formation of thin crust interconnected at the core is shown in Figure 67c. The interconnect divides the liquid core into two zones along the diameter. The crust following internal pressurization ruptures to produce four daughter droplets of diameter of 9.19 µm each.
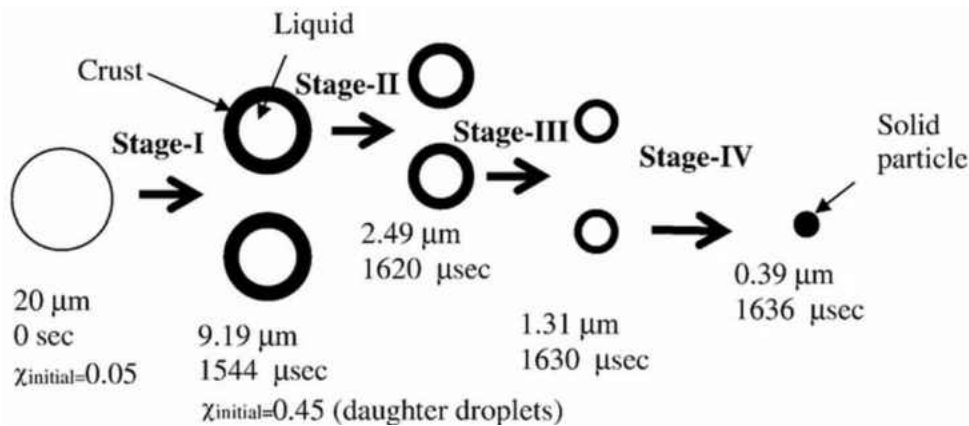
Figure 68: The interim stages for the 20 µm transversely injected droplet which follows 60° inclined path after first precipitation (time for all stages is calculated from the instant of injection)

In case of transverse injection, the droplet starts with a pure radial velocity. So, it is very unlikely that the daughter droplets will have only axial component of velocity after shell fracture. The droplets will always have a radial velocity component which will make them to traverse in an inclined path. So, in the transverse injection pattern, the trajectory of the droplets inclined at 60° and 45° angles with respect to the plasma axis are considered to study the variations of possible microstructures.

The daughter droplets that follow the 60° inclined trajectory go through the cyclic processes of secondary surface precipitations and corresponding shell ruptures. After couple of secondary precipitations however, the droplet becomes so small that volumetric precipitation occurs to form a solid particle of diameter of 0.39 μm. The intermediate stages are exhibited in Figure 68. The solid particle then undergoes rapid heating and it reaches the substrate plate unpyrolized. Figure 69 shows the transient thermal response of the solid particles. One key observation is that the solid particle is first heated at a very rapid rate to attain a temperature as high as 2050 K (Figure 69) before undergoing decay to reach a temperature of 1600 K near the substrate. This is because the plasma exhibits a decaying temperature profile with increase in axial distance from the nozzle tip. Initially the particle encounters the relatively high temperature plasma zone to get heated up but after some distance downstream, the local plasma temperature becomes lower than the particle temperature. The particle hence starts loosing heat and eventually cools down to a comparatively lower temperature before reaching the substrate plate.
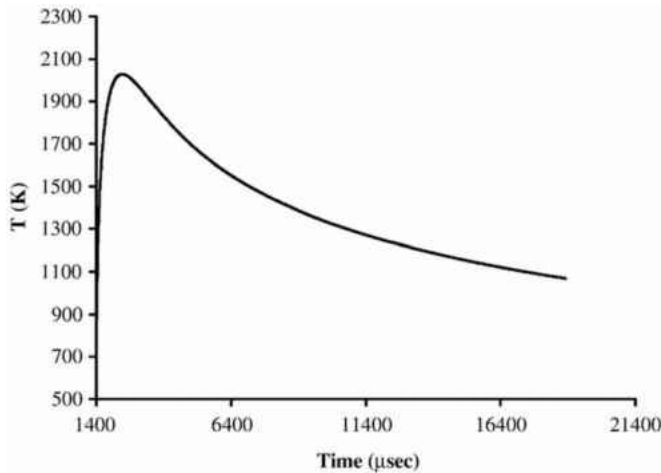
Figure 69: Transient thermal history for solid particle formed from transversely injected 20 μm droplet (time for all stages is calculated from the instant of injection)

206

For the droplets that follow a trajectory having 45° inclination, the secondary surface precipitations occur almost at the same rate as the 60° inclination. This is expected as the time involved with these interim stages are always very small and the deviation in trajectories before the onset of volumetric precipitation is negligible. It is also found to be true for other droplet sizes for transverse injection. So, in the following sections only the daughter droplets whose trajectories are 60° inclined with plasma axis have been reported.
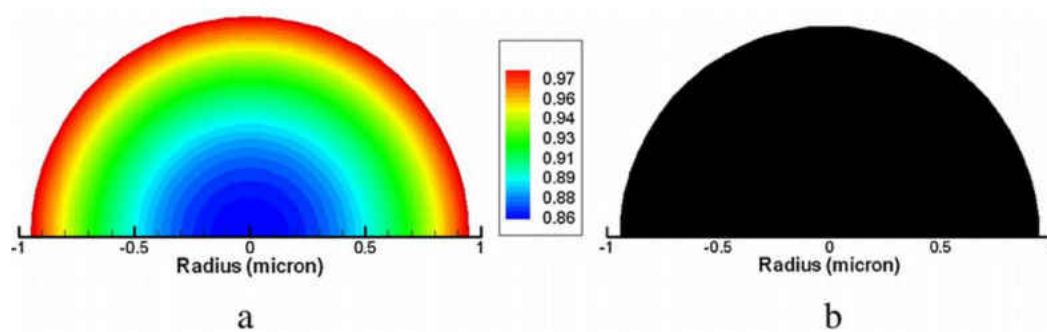
Figure 70: Transversely injected 5 µm droplet after 1294 µs: (a) Concentration distribution, (b) Volumetric precipitation

7.3.2.2 10 µm droplet

The 10 µm droplets yield very unsatisfactory coating quality. They go through a series of surface and volumetric precipitation to form a solid particle. But as the inertia for these small droplets are very low, they cannot penetrate the outer shear layer of the plasma to reach the high temperature core. So the solid particle formed from the 10-µm parent droplet reaches the substrate completely un-pyrolized at a very low temperature. Furthermore, the primary surface precipitation leads to drastic reduction in size, which further reduces the inertia making it impossible for the droplet to penetrate the outer shear layer of the plasma.

7.3.2.3 5 μm droplet

The 5 μm droplets also yield poor coatings, like the 10 μm droplets. The droplet due to low momentum cannot penetrate the outer shear layer of the plasma and stays in the periphery. However the comparatively colder outer shear allows the droplets to have extended residence time in the plasma. Combination of small size and relatively colder surrounding allows mass diffusion to be the dominant mechanism compared to advection. The droplet velocity is identical to the low velocity plasma field. This weakens the internal circulation of liquid, resulting in concentric iso-concentration lines as shown in Figure 70a. Slow and low vaporization rate assist in diffusion dominated transport enabling volumetric precipitation to occur as shown in Figure 70b. The solid particle hence formed cannot reach the inner hot core of plasma and remain un-pyrolized.

7.3.2.4 Summary of transverse injection

In short for transversely injected droplets, size plays a very important role. The comparative analysis shows that if the droplets are small, like 5 or 10 μm they would not be able to penetrate the outer shear layer. They always will remain in the low temperature zone of the plasma and consequently will reach the substrate un-pyrolized. The larger droplets like 20 μm penetrate the plasma more effectively and have better chances to get pyrolized.

7.4 Summary

The model described above along with the results depicts the complete thermo-physical behavior of the injected droplets along with the probable microstructures in the SPPS process using cerium nitrate precursor. The quality and property of the microstructure depends on the injection

type and droplet size. It can be seen that for axial injection, smaller initial diameter droplets are favorable to get pyrolized. In the axial mode, the droplets are injected right at the high temperature plasma core. Hence they readily undergo through the maximum possible heating rate helping the vaporization process. The smaller droplets undergo volume precipitation faster than the larger droplets in axial injection. Droplets like 5 or 10 μm get pyrolized completely before reaching the substrate plate, while the 20 μm droplets remain partially pyrolized. For transverse injection, the droplets are injected at the outer shear layer of the plasma, where the temperature and velocity are low. To get the maximum heating effect, the droplets need to penetrate that outer layer and reach the high temperature core of the plasma. The smaller droplets like 5 μm and 10 μm cannot penetrate the shear layer as they do not have the required inertia. They always remain in the outer low temperature zone. On the other hand the larger droplets, like 20 μm have enough inertia to penetrate the outer layer and reach closer to the high temperature core. So, they are favorable for pyrolization. However the results show that 20 μm droplet do not reach the substrate fully pyrolized. After reaching a high temperature they eventually cools down to some lower temperature value. Another important finding from the results presented is that the daughter droplet trajectory does not have much effect on the final microstructure. It was observed that by changing the angle of the trajectory for axially injected droplets insignificant changes occur in the final morphology. This is also true for the case of the transversely injected droplets. So in summary the final microstructure depends on the size of the droplet not on whether they follow an axial route or an inclined one after primary precipitation. The modeling encompasses the complete thermo-physical phenomena behind the SPPS processes. These results can be used in designing process variables to have better control over

the final microstructure. However there are several uncertainties within the process, which need to be validated experimentally.

CHAPTER EIGHT: SCALING ANALYSIS: EQUIVALENCE OF CONVECTIVE AND RADIATIVE HEATING OF LEVITATED DROPLET

8.1 Introduction

Evaporation of pure liquid droplet has been extensively studied in the last few decades. In a hot gas stream, it has widespread applications in gas turbines, thermal sprays and spray drying of food, ceramics and pharmaceutical products. Although the spray processes include droplet-droplet interactions and their effect on heat and mass transfer, the study of single droplet evaporation aids in the understanding of fundamental physics by visualization of breakup, precipitation, agglomeration kinetics and structure formation. Owing to the difficulties in conducting droplet level investigation in an actual spray, the spray models are mostly developed and validated by single pendant droplet experiment.

Acoustic levitation is an alternative method to study micron-sized droplets without wall effects, which eliminates chemical and thermal contamination with surfaces. Acoustic levitator has been successfully used in material processing, crystal growth, pure and multicomponent droplet evaporation and protein synthesis [Xie et al. (2002), (2006), Yarin et al. (1999), Saha et al. (2010a)]. Experiments with droplet evaporation could be done only at very low air flow rate and temperature so that the droplet can remain levitated [Yarin et al. (1999), Saha et al. (2010a)]. Alternatively, moderate to low laser heating of a levitated drop has been shown to be an effective way of droplet vaporization. This method allows us to understand the vaporization and agglomeration characteristics of new fluids, e.g. biofuel [Saha et al. (2010a), Basu et al. (2012)], nanosuspensions [Kumar et al. (2010), Saha et al. (2012a), (2012b)] and precursors [Saha et al.

(2009b), (2010b)] economically without having to fabricate complicated optically accessible pre-mixers or combustion chambers.

Despite the advances made in droplet vaporization in a levitator using laser flux or by gas phase in convective environment, the two methods of heating have not been compared quantitatively so far, mainly due to the difficulties encountered in conducting experiments for the same size droplet under equivalent conditions, and the lack of robustness of analytical techniques and the disparity in timescales that may exist between the two systems. We address four important issues pertaining to this problem. First, using scaling analysis and simplified droplet energy transport model (transient and steady state regimes), we will show that the droplet wet bulb temperature and the time required to attain that temperature can be calculated analytically for both radiative and convective heating. Second, the normalized temperature data using the theoretical wet bulb temperature will be matched with the experimental data from the literature for both radiative and convective heating. Third, the normalized transient profiles from different sets of experiments will be shown to follow a single profile irrespective of the mode of heating. Fourth, the scaling analysis will be further extended to develop a connection between gas phase temperature in convective heating and effective laser flux in radiative heating for different fluids. A droplet in a convective environment vaporizes under the driving influence of temperature difference between the droplet surface and the gas field. In order to mimic similar conditions in the laser heating system in a levitator, the laser flux will be tuned to match the temperature difference. In addition, different fluids show a wide variation in absorption of laser irradiation. The equivalence (established through theoretical analysis) between the two modes of heat transfer will be

validated by matching the experimental data for 125 μm and 1000 μm droplets from radiation experiments with the convective counterpart.

Theoretical models have been developed for droplet and spray evaporation [Sirignano (2010), Law (1982)]. This involves solving the liquid phase transport equations and gas phase equations to calculate the heat and mass transfer. The effect of non-equilibrium modelling of droplet laden flows was also studied using Langmuir-Knudsen formulations [Miller (1998)]. Experimental studies of droplet evaporation have been largely restricted to dropsize over 1 mm [Miller (1998), Yuen and Chen (1976), Daif et al. (1998)] in different fluids. A deviation from this norm is the series of articles published using optical techniques to measure evaporation characteristics of 100 μm droplets [Maqua et al. (2008), Castanet et al. (2002), (2005)].

Theoretical and experimental work in levitators [Yarin et al. (1998), (1998); Saha et al. (2010a), (2012b), (2012a), (2012b), Kumar et al. (2010), Basu et al. (2012)] have paved the way for conducting fundamental research in levitated functional droplet evaporation either due to natural drying or external heating. The shape and deformation of the droplet and its displacement from the pressure node may be used to calculate the acoustic streaming and the average distribution of Sherwood and Nusselt number around the droplet [Yarin et al. (1999)]. For comparable evaporation characteristics found in convective heating, levitated droplets can be irradiated with lasers[4-8]. Laser heating of liquid droplets has also been studied by many authors albeit in non-levitator environment both experimentally and numerically [Park and Armstrong (1989), Dombrovsky and Sazhin (2003), Basu and Cetegen (2008a)].
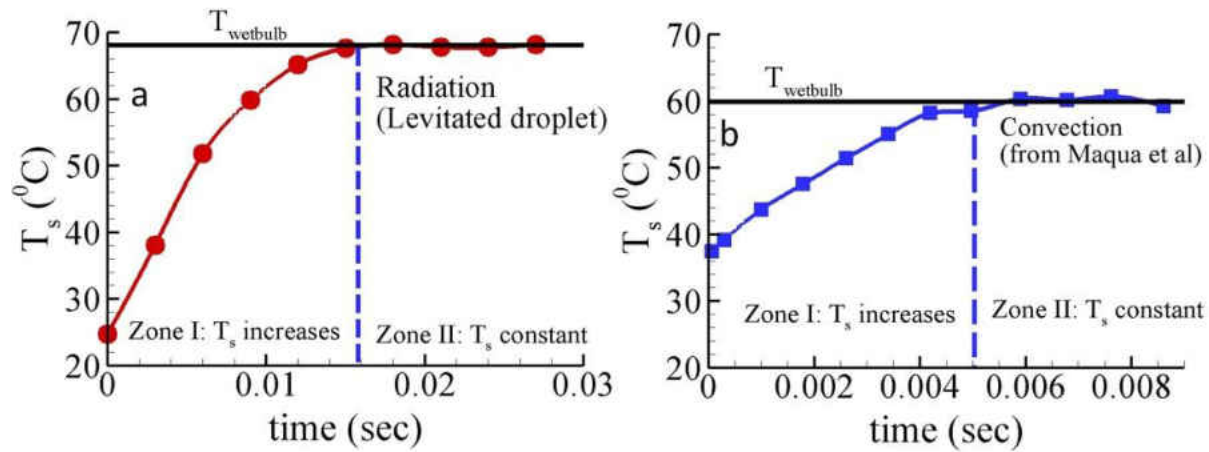
Figure 71: Temperature rise during heating of ethanol droplet: (a) Radiation (0.65 MW/m^2 laser flux with 125 µm droplet) using IR camera, (b) Convection (Gas temperature 837°C with 105 µm droplet) from Maqua et al. (2008)

8.2 Analysis and results

An evaporating droplet undergoing external heating (radiation or convection) exhibits two distinct regimes: the initial transient phase during which the bulk temperature increases and the steady state phase during which the temperature is constant (wet bulb temperature). The timescale and temperature scale associated with the external heating of a droplet is determined by both these phases. In the transient phase (Zone I in Figure 71), the droplet temperature history is usually characterized by a balance between the energy supplied by the external heating source and the sensible enthalpy requirement for droplet temperature rise. Even though evaporation is present, it is not significant during this regime. However, the temperature increase implies a sharp upsurge of saturation vapor pressure which leads to increased evaporation rate. This shifts the balance and the droplet now exhibits a steady state temperature (wet bulb limit) with all the input energy from the external heating source being utilized for vaporization (Zone II in Figure 71). The two regime lifecycle of a droplet is governed by thermo-physical properties such as latent heat, thermal conductivity, saturation vapor pressure, mass diffusivity, Reynolds number

214

of the flow field as well as the external heating conditions like laser flux (pure radiative heating) or the temperature of the surrounding gas phase (pure convective heating). The temperature scale and timescale are only relevant in the transient phase of the droplet (Zone I) though the steady state phase (Zone II) provides a limiting condition that enables us to uniquely ascertain the values of these scales. Similar methodology can be applied to both radiative and convective heating to establish the time and temperature scales. Using the same scales, one can also show the equivalence of radiative and convective heating.

8.2.1 Radiation

The heat balance equation for a droplet under monochromatic radiation can be written as [Park and Armstrong (1989), Dombrovsky and Sazhin (2003), Basu and Cetegen (2008a)]

$$I_{eff}.A_s = \frac{4}{3}\pi R^3 \rho_l C_p \frac{dT_s}{dt} + Q_{loss} + \dot{m}h_{fg} \qquad (8.1)$$

I_{eff} is the effective laser flux that is absorbed by the droplet (including effects of scattering losses and variation of absorption coefficients among various liquids), A_s is the surface area of the droplet exposed to the laser flux, R is instantaneous droplet radius, ρ_l is liquid density, C_p is specific heat of the liquid, h_{fg} is the latent heat of the droplet, $\dot{m}$ is the vaporization rate, T_s is the surface temperature. Q_{loss} represents the heat loss to the surrounding, and is modeled as $Q_{loss} = 4\pi R^2.h_{loss}.(T_s - T_0)$ where h_{loss} is the convective heat transfer coefficient and T_0 is the ambient temperature and initial droplet temperature.

Neglecting vaporization until equilibrium (Zone II), the energy transport equation becomes,

$$I_{eff}.A_s = \frac{4}{3}\pi R^3 \rho_l C_p \frac{dT_s}{dt} + 4\pi R^2.h_{loss}.(T_s - T_0)$$ (8.2)

Since the droplet is asymmetrically heated from one side, the surface area irradiated is $A_s = 2\pi R^2$. It should be noted that for low to moderate laser flux, the asymmetric heating does not deviate significantly from the spherically symmetric heating [Park and Armstrong (1989)]. Although there is non-uniformity in the laser power and absorption coefficient along the droplet surface, Park and Armstrong (1989) analytically showed for low to medium heating, the droplet temperature becomes more or less uniform. In our experiments, we do not observe any catastrophic breakup of droplets; hence, the effect of non-uniformity in absorption coefficient is not significant. IR images from the current experiments also display uniform temperature profile across the droplet surface. The heat loss can be calculated using the heat transfer analysis of a vaporizing droplet under acoustic levitation. Yarin et al. (1999) showed that the Nusselt number (and Sherwood number) depends on acoustic streaming or acoustic intensity. The heat transfer coefficient is $h_{loss} = Nu_{str}k_{air}/2R$. Equation (8.2) can be written as

$$\frac{dT_s}{dt} = \frac{3I_{eff}}{2R\rho_l C_p} - (\frac{3Nu_{str}k_{air}}{2R^2\rho_l C_p}).(T_s - T_0)$$ (8.3)

Assuming constant fluid properties and constant droplet diameter (till equilibrium or Zone II) and $T_s(t=0) = T_0$, Equation 8.3 can be solved and the closed form solution is given by

$$T_s(t) = T_0 + \frac{C_{2-rad}}{C_{1-rad}}\left[1 - \exp(-C_{1-rad}t)\right]$$ (8.4)

where $C_{1-rad} = \dfrac{3Nu_{str}k_{air}}{2R^2\rho_l C_p}$ and $C_{2-rad} = \dfrac{3I_{eff}}{2R\rho_l C_p}$. To estimate the wet bulb temperature of the

droplet in Zone II, it is assumed that the latent heat dominates sensible heat and the total heat

flux is spent in vaporizing the droplet and heat loss to the surrounding. Thus, at equilibrium,

$$I_{eff}.(2\pi R^2) = 4\pi R^2.(\frac{Nu_{str}k_{air}}{2R}).(T_s - T_0) + \dot{m}h_{fg} \tag{8.5}$$

The vaporization rate, for a single droplet is estimated [Sirignano (2010)] to be

$\dot{m} = 2\pi\rho_g D_{i\infty}R.\overline{Sh}\ln(1+B_M)$. Here, Spalding mass transfer number, $B_M = \dfrac{\chi_{g,s} - \chi_{g,\infty}}{1 - \chi_{g,s}}$ depends on

vapor mass fraction on the droplet surface $\chi_{g,s}$ and vapor mass fraction far away from the droplet

surface, $\chi_{g,\infty}$. The vapor mass fraction of the liquid on the droplet surface can be calculated by

Raoult's law [Sirignano (2010)]. We used the incompressible limit of Sherwood number

specified for small droplet [Yarin et al. (1998)]. The average Sherwood number $\overline{Sh}$ is given by

$\overline{Sh} = 1.89B/\sqrt{\omega D_{i\infty}}$, where ω is the angular frequency of the levitator and $D_{i\infty}$ is the mass

diffusion coefficient of the liquid vapor into air and B is the velocity scale which depends on the

levitator sound pressure level (SPL) and frequency [Yarin et al. (1998)].

Equation 8.4 is used to calculate the temperature (T_s) at small steps until it converges [99% rule]

and satisfies the equilibrium condition given in Equation 8.5. We denote this equilibrium

temperature as T_{f-rad}, which is the desired temperature scale for radiation. To calculate the

equilibrium time scale (t_{s-rad}) required by the droplet to reach T_{f-rad}, a modified form of Equation

8.3 (including a correction based on energy spent for vaporization) is used to obtain the expression:

$$t_{s-rad} = -\frac{1}{C_{1-rad}} \ln\left[1 - \frac{C_{1-rad}}{C_{2-rad}}(T_{f-rad} - T_0)\right] \qquad (8.6)$$

To validate the theory and the scaling argument presented above, a set of experiments has been conducted with different liquids and different laser intensities. The experimental setup used an acoustic levitator (100kHz, 156dB) to suspend the droplet which was irradiated at different intensities by a CO_2 laser (10.6 μm wavelength, maximum heat flux of 10MW/m^2). A high speed CCD camera along with an IR camera was used for simultaneous imaging. High speed images, captured at 3000 to 5000 fps, were used for calculating droplet diameter reduction rate. IR images, captured at 100-300 fps were used for measuring surface temperature of the droplet. The uncertainties in diameter and temperature measurements were 4μm and 0.5^{o}C respectively. Further details of the experimental setup are provided in Chapter 2. The effective laser flux or I$_{eff}$ is less than the actual laser power due to different factors: a) absorption coefficient, b) scattering loss, c) divergence of laser beam. However, except for absorption coefficient, the other factors generally depend on radiation wavelength and geometry of the droplet. With the consideration that the levitated droplets are perfectly spherical in shape, we can assume that these effects are uniform for all liquids when heated with the same monochromatic source. Thus, efficiency, η, is defined as $I_{eff} = \eta.I_0$. This efficiency term includes the cumulative effect of all the losses. In the current levitation setup, η will change only with absorption coefficient of fluids. To obtain the laser efficiency, we performed a calibration experiment using a water droplet at different laser

fluxes, and determined the efficiency to be 22%. The laser flux efficiency can also change due to small oscillations observed in levitated droplet. The oscillations are generally of the order of 50μm. This results in 1-2% change in droplet location, and we ignored this minor inhomogeneity.

The efficiency η mentioned here is based on heat flux, not on laser power. The laser used for this experiment has a 2mm beam diameter with the maximum power output of 30W. This results in a maximum laser flux of around 10MW/m^2. Based on efficiency, η=22%, the maximum effective laser flux for a water droplet is 2.2MW/m^2. However, the corresponding laser power on the droplet depends on droplet size. For a 500μm water droplet, this maximum laser power absorbed by the droplet is 0.43W which is approximately 1.5% of the maximum laser power, 30W.

Figure 72 shows an increase of surface temperature with time for ethanol droplets. The 125 μm droplet with effective laser flux (I_{eff}) of 0.65MW/m^2 undergoes a rapid temperature rise compared to the 500 μm droplet with I_{eff} of 0.25 MW/m^2 [Figure 72 a and b]. The former required around 0.02 sec to attain the wet bulb temperature of 68°C while the latter reached a wetbulb temperature of 62°C in 0.2 sec. The figures also show the theoretical temperature rise (using Equation 8.4) and the theoretical wetbulb temperature, $T_{f\text{-rad}}$, using equation 8.5. The intersection of these two curves denotes the equilibrium time scale, $t_{s\text{-rad}}$. The theoretical analysis shows the correct order of magnitude of the timescale and almost exact wetbulb temperature ($T_{f\text{-rad}}$) when compared to the experimental data. The normalized temperature T* ($T^* = (T_s - T_0)/(T_{f-rad} - T_0)$) vs t* ($t^* = t/t_{s-rad}$) for the two drop sizes show excellent agreement with the experimental data.
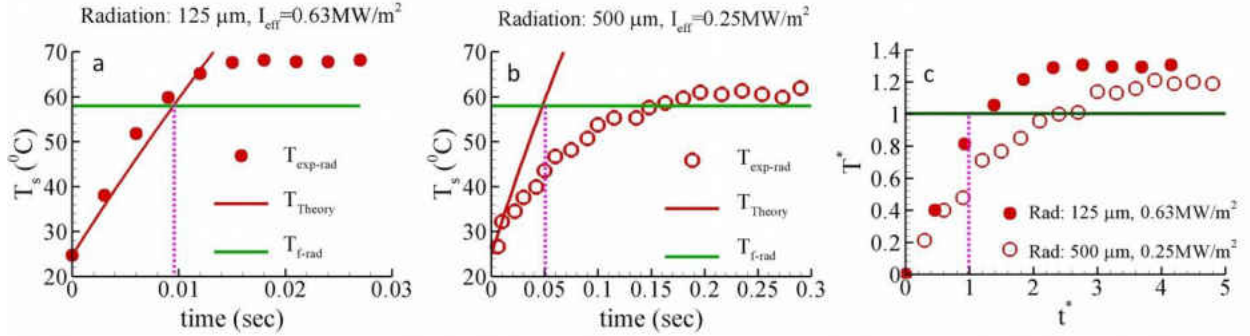
Figure 72: Ethanol: $T_s(^0C)$ vs time (sec): (a) 125 μm droplet, I_{eff} = 0.25MW/m^2, (b) 500 μm, I_{eff}=0.63MW/m^2, (c) T* vs t* for these two cases

8.2.2 Convection

Next, in order to obtain a timescale for convective heating and establish equivalence with radiative heating, we invoke some of the theoretical framework developed in the literature for a convectively vaporizing droplet and spray [Sirignano (2010), Law (1982)]. For droplet with small diffusion time scale, one can ignore the thermal gradient within the droplet [Biot Number < 0.1]. Following the previous analysis, it can be concluded that the vaporization rate at the initial stages [Zone I in Figure 71] is negligible. Hence the heat balance equation becomes

$$h_c.4\pi R^2.(T_\infty - T_s) = \frac{4}{3}\pi R^3 \rho_l C_p \frac{dT_s}{dt} \tag{8.7}$$

T_∞ is the ambient hot gas temperature. The heat transfer coefficient h_c is calculated as $h_c = Nu^* k_{air} / 2R$. We assume Lewis number to be equal to 1. Nusselt or Sherwood number for a vaporizing droplet is calculated using Sirignano's model [Sirignano (2010)]. The Nusselt and the Sherwood number are both functions of droplet Reynolds number and on the Spalding heat and mass transfer numbers when surface blowing effect is included. For the current analysis, the Reynolds number has been considered to be 10. This is a good assumption because our analysis

220

focuses on the initial period of heating when the relative velocity between the gas and the droplet is highest.

Equation (8.7) is solved to yield

$$T_s(t) = T_0 + \frac{C_{2-rad}}{C_{1-rad}} \left[1 - \exp(-C_{1-rad}t) \right] \tag{8.8}$$

where, $C_{1-conv} = \left(\frac{3Nu^* k_{air}}{R^2 \rho_l C_p} \right)$ and $C_{2-conv} = \left(\frac{3Nu^* k_{air}}{R^2 \rho_l C_p} \right).(T_\infty - T_0)$. The equilibrium temperature of a droplet in a convective field can be calculated using Sirignano's model [Sirignano (2010)] of isolated droplet. Under this assumption, at equilibrium temperature, the droplet should satisfy the equation [Sirignano (2010)]:

$$\chi_{g,s} = \frac{C_{p,air}(T_\infty - T_{f-conv})}{h_{fg} + C_{p,air}(T_\infty - T_{f-conv})} \tag{8.9}$$

where $C_{p,air}$ is the specific heat of air and $\chi_{g,s}$ is the mass fraction of vapor phase on droplet surface, which can be calculated based on Sirignano's model [Sirignano (2010)]. An iterative process has been used to determine the equilibrium temperature of the droplet, T_{f-conv}. The equilibrium time scale to reach this temperature has been calculated by using a modified form of equation 8.8 similar to the radiation counterpart,

$$t_{s-conv} = -\frac{1}{C_{1-conv}} \ln \left[1 - \frac{C_{1-conv}}{C_{2-conv}} (T_{f-conv} - T_0) \right] \tag{8.10}$$
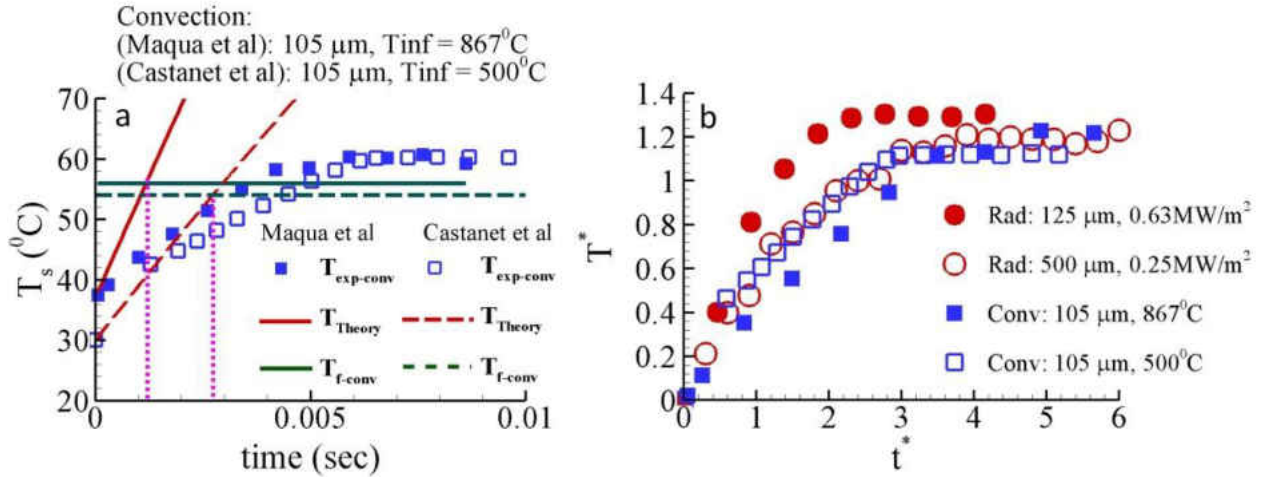
Figure 73: (a) Ethanol T_s (^{o}C) vs time (sec): 105 micron droplet Castanet et al. (2002) and Maqua et al. (2008), (b) Normalized data (T^* vs t^*) for both radiative and convective experiments

The proposed scaling analysis for convective heating of droplets was validated against the experimental data of References [Maqua et al. (2008), Castanet et al. (2002)] for ethanol droplet evaporation in hot air using a monodisperse droplet stream. For the purpose of analysis, we considered a constant gas phase temperature of 500°C in experiments [Castanet et al. (2002)]. We also validated against [Maqua et al. (2008)] in a flame environment where the gas phase temperature was as high as 867°C. These data are shown in Figure 73a. Figure 73 also contains the theoretical profile for temperature rise (Equation 8.8) and theoretical wet bulb temperature, $T_{f\text{-}conv}$ (Equation 8.9). The intersection of these two curves yields the equilibrium time scale ($t_{s\text{-}conv}$). There is excellent agreement with the experimental data with respect to the equilibrium temperature and the equilibrium timescale. There is excellent agreement with the experimental data with respect to the equilibrium temperature and the equilibrium timescale. The normalized profiles (T^* vs. t^*, where for radiative: $T^* = (T_s - T_0)/(T_{f\text{-}rad} - T_0)$ and $t^* = t/t_{s\text{-}rad}$ and for convective $T^* = (T_s - T_0)/(T_{f\text{-}conv} - T_0)$ and $t^* = t/t_{s\text{-}conv}$) also show excellent unification of the

222

two entirely different sets of data (Figure 73b) for both radiative and convective heating, for different droplet sizes, gas phase temperature and laser flux.

8.2.3 Equivalent I_{eff}

The scaling analysis not only shows that the data from the two modes of heating can be unified, but also provides the required laser flux (I_{eff}) to simulate a certain convective condition. Using Equation 8.9, the wetbulb temperature scale (T_{f-conv}) for a certain size of the droplet of a fluid can be calculated at a given ($T_{inf} - T_0$). Now, using equation 5 for the same droplet diameter, one can estimate required I_{eff} for irradiated droplet to reach the same wetbulb temperature scale (T_{f-rad}). Figures 74 a and c show the variation of equivalent I_{eff} with ($T_{inf} - T_0$) for 1mm water droplet and 105 μm ethanol droplet. Five experimental convective conditions for water and two for ethanol have been reported [Miller (1998), Yuen and Chen (1976), Maqua et al. (2008), Castanet et al. (2002)]. The wetbulb temperatures for convection and radiation experiments (Figures 74 b and d) compare favorably using equivalent I_{eff}. The minimum practical ethanol dropsize that could be levitated was 125 μm in the radiation experiment that could be compared with the 105 μm drop [Castanet et al. (2002)] in the convection experiment.
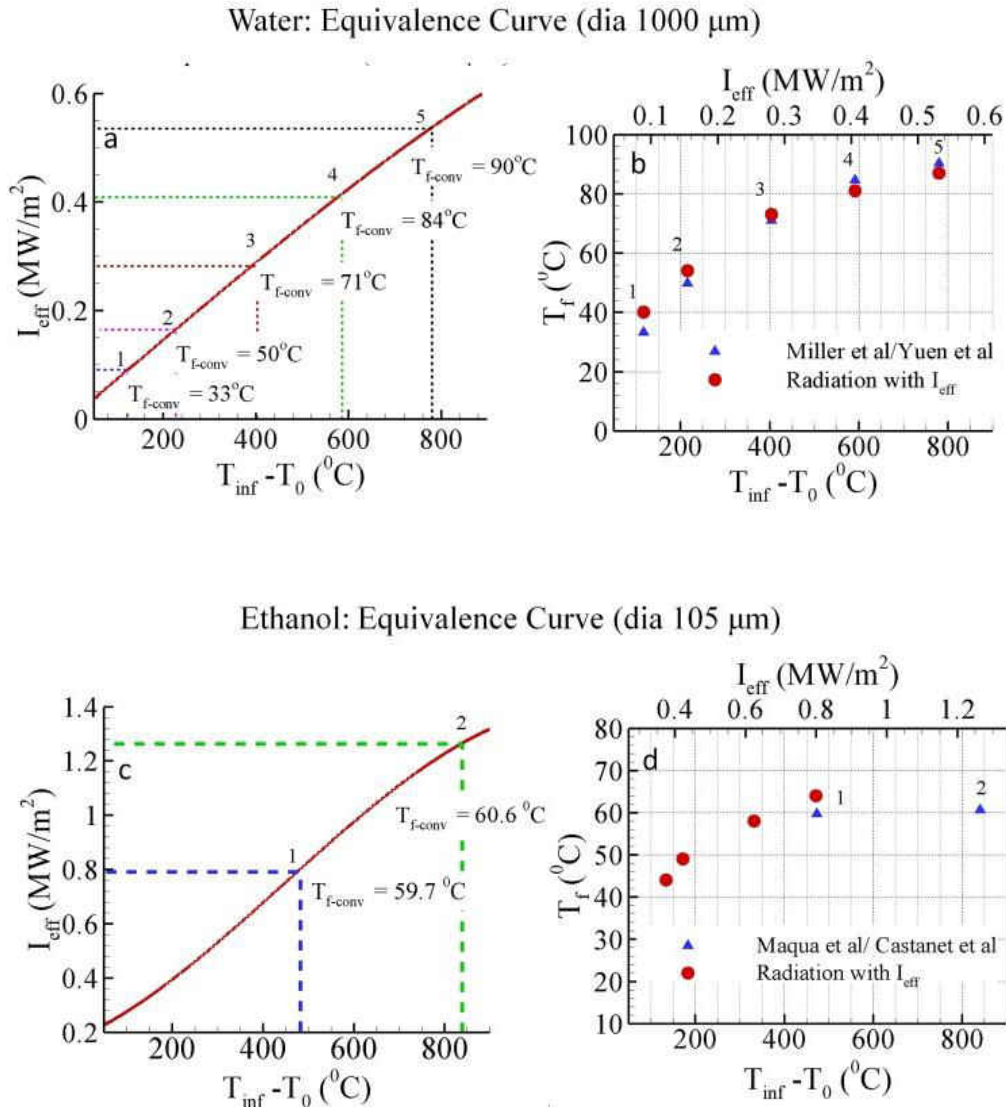
Figure 74: Equivalent laser flux corresponding to different gas phase temperatures [(a) Water (1000μm) and (c) Ethanol (105μm)], Wet bulb temperature achieved in experiments using certain gas phase temperature and equivalent laser flux [(b) Water (1000μm) and (d) Ethanol (105μm)][Convection data are taken from Yuen and Chen (1976), Miller et al. (1998), Maqua et al. (2008) and Castanet (2002)]

Similar equivalence curves for other fuels like, Diesel and Kerosene have been generated as shown in Figure 75. However, at this stage the convection experiment data for these liquids are not available, which will be done in future.
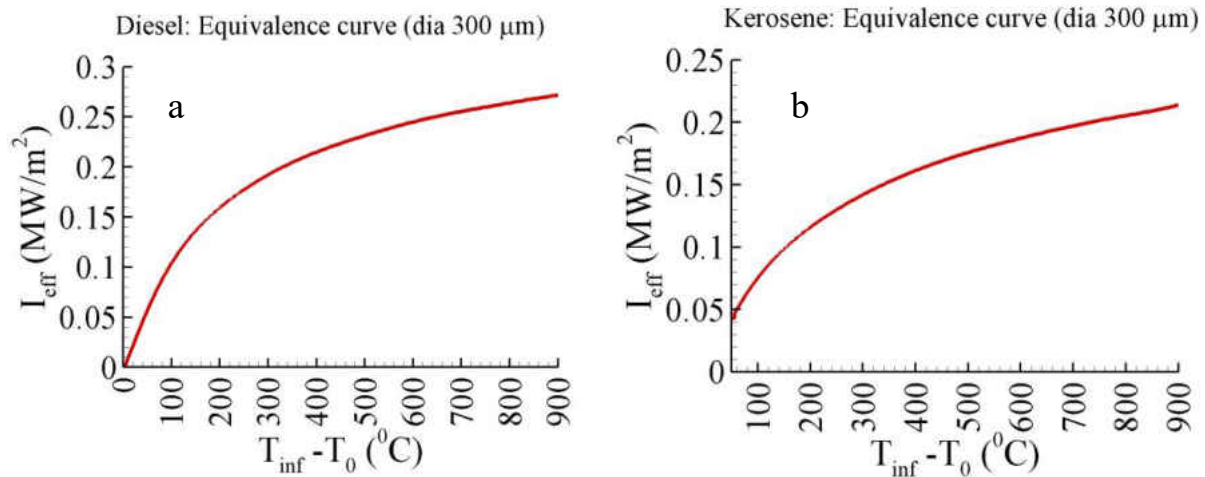
Figure 75: Equivalent laser flux corresponding to different gas phase temperatures [(a) Diesel (300μm) and (b) kerosene (300μm)]

8.3 Summary

Time and temperature scales are developed in this letter, which can be applied to both convective heating and radiative heating of liquid droplets. The transient temperature profiles normalized by these scales show a single unified profile irrespective of the heating mode, liquid properties and external heating conditions. A much needed connection between a single stream of convectively heated droplet and irradiated levitated droplets has been established to obtain the wet bulb temperature. A theoretical framework has also been provided to match the laser flux to obtain the wet bulb temperature in an equivalent convective environment at a given gas phase temperature.

CHAPTER NINE: CONCLUSION

Thermo-physical changes in vaporizing functional droplets have been studied in this dissertation with a focus on phase transformation and morphology evolution. An acoustic levitator has been utilized here to study droplets ranging from 125 to 1000µm in diameter without the effects of solid surface. Most of the previous studies report the vaporization characteristics on pendant droplets suspended from a needle or crosswire. Optical techniques such as high speed imaging, infrared (IR) thermography and particle image velocimetry have been used to delineate different stages of evaporation of droplets containing nanosuspensions or precursor solution.

The flow structure inside levitated droplet has been mapped qualitatively using high exposure streak imaging and quantitatively using Particle Imaging Velocimetry. The flow inside the droplet was found to be dominated by a single cell vortex around droplet center. High frequency of single axis levitator along with small droplet sizes results in unavoidable misalignment in levitator axis, resulting in rotation of the droplet around a horizontal axis. This rotation becomes weaker with increase in viscosity and droplet diameter. It was also observed that levitated droplets show a second rotational motion about vertical axis of the levitator as well. In a vaporizing droplet with suspension or precursor solution, the rotation about the horizontal axis is observed to be stronger initially, however with time as the solvent vaporizes and the solid content of the droplet increases (which also means increase in viscosity), the rotation about the vertical axis becomes stronger.

Droplets with nanosuspensions were also studied. Two distinct stages of evaporation were observed. The first stage is characterized by faster evaporation of the solvent and the second stage is dominated by perikinetic or orthokinetic agglomeration of nanoparticles leading to structure formation. For high-concentration systems (concentration > 0.1 %), Brownian motion of particles (perikinetics) dominates the aggregation compared with shear driven motion (orthokinetics). Simultaneous high speed and infrared thermography show that the vaporization in the first stage of heating results in a linear change in droplet diameter. However, owing to decrease in effective vapor pressure, the rate of vaporization reduces with increase in nanofluid concentration. In the second stage, the droplets undergo morphological changes. Initially the top half of the droplet collapses forming a bowl shaped structure. Upon further heating at high concentration, the bowl structure morphs into a ring shaped structure. It is shown that due to internal flow the particles travel to the lower half of the droplet and agglomerate resulting in a concentration (density) gradient across two halves of the droplet. This leads to a force imbalance between two halves of the bottom heavy droplet. Eventually when the difference in force, which is a function of density gradient, crosses a critical value, the top half of the droplet collapses and a bowl is formed. In addition to predicting the critical density gradient and corresponding location of chord along which top half collapses, the analysis also showed the time scale of this force imbalance is of the same order as perikinetic time scale for nanosilica suspensions.

Study of droplets with cerium nitrate precursor solution shows four stages of evaporation. Initial stage of rapid evaporation is followed by a slower evaporation stage as the solute precipitates around the droplet surface. According to Raoult's Law, these precipitates around droplet surface results in a decrease of effective vapor pressure leading to slower vaporization rate. Once the

liquid content significantly decreases, the droplet undergoes a chemical transformation where cerium nitrate decomposes into ceria releasing nitrogen oxides. High speed images show expansion and contraction of the droplet as the gaseous products vent out through the precipitates. Once the chemical transformation is complete, the final precipitate undergoes a benign stage of heating. Ex-situ analysis shows porous micron structures created by gaseous products and the porosity increases with increase in heating rate. TEM also confirmed the presence of nanoceria in crystalline form.

Droplet stability in a levitator is an important aspect in the study of droplet drying. It is shown that the liquid properties such as viscosity and surface tension not only affect the flow field within the droplet but also determine the droplet shape and stability under levitation. When the levitated droplets are heated externally, the surface tension and viscosity decrease. This may induce two types of instabilities in a droplet, which otherwise would be stable at room temperature. If the acoustic Weber number is higher than critical Weber number based on critical velocity, the velocity gradient across liquid and gas phase in the droplet surface triggers Kelvin-Helmholtz type instability leading to the generation of micron-size satellite droplets from the equator. If the surface tension reduces significantly, the droplet starts deforming under inhomogeneous acoustic force. Viscosity can induce a damping effect to resist this deformation. If the viscous damping is not strong enough, the droplet morphs into a disk, which eventually undergoes a catastrophic breakup.

A computational model has been developed to understand the effect of droplet size and injection type on pyrolization of cerium nitrate precursor droplet in a plasma field. The model also

considers crust formation around the surface due to precipitation and resulting breakup due to an increase in internal pressure. Analysis shows that for transverse injection, larger droplets show a better probability of pyrolization. Smaller droplets with lower momentum are not capable of penetrating the outer shear layer to reach high temperature plasma core. While larger droplets reach closer to the high temperature core and thus vaporizes and pyrolizes better. On the other hand, for axial injection, droplets are injected in the core of the plasma. Smaller droplet here vaporizes faster and also shows higher capability for pyrolization.

To bridge the gap between the convection in actual spray experiments and radiative heating in a levitated experiments used in this study, a time and temperature scale have been proposed. This scaling analysis not only shows similarity of the convection and radiation data, but also allows the calculation of required laser flux for levitator experiments that is equivalent to the gas temperature in a spray system. One can use this scale to design separate effects experiments using a levitated droplet to understand the droplet evaporation dynamics in actual spray systems.

9.1 Future work

This work deals with one nanosuspension and one precursor solution in a levitated environment to study the droplet evaporation and precipitation dynamics. To carry forward the information or the knowledge gained in this dissertation, the future work is proposed.

- The effects of viscosity, surface tension and particle size can be studied for nanosuspensions. This work used 10nm nanosilica as nanosuspension to show the effect of viscosity and particle size on agglomeration and structure formation. However, it is

expected that larger particle size or nanosuspensions with significantly higher viscosity and concentration of nanoparticles will result in some different structure formation.

- Effect of acoustic standing wave on agglomeration has been shown in this work for a single levitated droplet. One can extend this idea in actual spray to see the effect of acoustic wave on drying of liquid droplets. One advantage of the levitator is that the droplet is stationary compared to the acoustic wave. In an actual spray, the dynamics of droplet and acoustic field interaction is more complicated. Thus, the spatial acoustic impedance in the droplet path may be mapped while drying in a spray system.

APPENDIX: DISCUSSION ON TAB MODEL AND CAPILLARY WAVE THOERY

Analogy to TAB model

The Taylor Analogy Breakup [TAB] model is frequently used for the analysis of a droplet deforming under an aerodynamic loading. The TAB model can be modified and recast for a levitated droplet under acoustic loading [O'Rourke & Amsden (1987).]. The governing equation assumes the form

$$F - k(\delta a) - d(\frac{d(\delta a)}{dt}) = m\frac{d^2(\delta a)}{dt^2} \tag{A.1}$$

δa is increase in equatorial radius, k is stiffness $(\frac{k}{m} = C_k \frac{\sigma}{\rho R^3})$, d is damping factor/coefficient$(\frac{d}{m} = C_d \frac{\mu}{\rho R^3})$. In aerodynamic breakup, the force, F depends on relative velocity, while in current situation of droplet under Bernoulli (acoustic) pressure, force F can be written as, $F = (P_{pole} - P_{eq})A_{eff}$. The effective area, A_{eff} can be estimated as $A_{eff} \approx \pi R^2$. Thus

$\frac{F}{m} = C_F \frac{(P_{pole} - P_{eq})}{\rho R} = C_F We_{TAB}(\frac{\sigma}{\rho R^2})$. In the case of the acoustic levitator, the driving force for breakup is inhomogeneity in external Bernoulli (acoustic) pressure, thus the modified Weber number can be written as, $We_{TAB} = \frac{(P_{pole} - P_{eq})\sigma}{R}$.

Capillary surface wave

A surface wave on a liquid with energy E will dissipate the energy due to internal friction or viscosity. The dissipation rate, $\dot{E}$ can be expressed as, $\dot{E} = -\frac{1}{2}\mu\int\left(\frac{\partial u_i}{\partial x_k} + \frac{\partial u_k}{\partial x_i}\right)^2 dV$, where μ is dynamic viscosity and u_i and u_j are velocities in x_i and x_j direction.

Now, for capillary wave, $\phi = Ae^{kz}\cos(kx - \omega t)$ the dissipation rate of mean energy can be written as, $\bar{\dot{E}} = -8\mu k^4\int\bar{\phi}^2 dV$. Mean energy for a small oscillatory motion can be assumed to have the same potential and kinetic energy. Therefore, mean energy is written as $\bar{E} = \rho\int\overline{v^2}dV = \rho\int\overline{\left(\frac{\partial\phi}{\partial x_i}\right)^2}dV = 2\rho k^2\int\bar{\phi}^2 dV$. From wave theory, the damping coefficient (C_{damp}) is $\overline{E(t)} = \bar{E}_0.e^{-2C_{damp}t}$, where $\bar{E}_0$ is the initial energy. Then one can write $C_{damp} = \left|\bar{\dot{E}}\right|/2\bar{E}$ or $C_{damp} = 2\frac{\mu}{\rho}k^2$. For capillary wave, $\omega^2 = \frac{\sigma k^3}{\rho}$. Thus, $C_{damp} = 2\frac{\mu\omega^{4/3}}{\rho^{1/3}\sigma^{2/3}}$ [Landau and Lifshitz (1987)]. As energy and amplitude are analogous, one can also write, $\overline{I(t)} = \bar{I}_0.e^{-2C_{damp}t}$.

233

LIST OF REFERENCES

Abe Y, Yamamoto Y, Hyuga D, Aoki K, Fujiwara A (2007) Interfacial stability and internal flow of a levitated droplet, Microgravity Science and Technology, 19, pp 33–34

Abramzon B and Sazhin S S (2005), Droplet vaporization model in the presence of thermal radiation, International Journal of Heat and Mass Transfer, 48, pp 1868

Abramzon B and Sirignano W A (1989), Droplet vaporization model for spray combustion calculations, International Journal of Heat and Mass Transfer, 12, pp. 1605–1648

Agarwal A, Mckechnie T and Seal S (2003), Net shape nanostructured aluminum oxide structures fabricated by plasma spray forming, Journal of Thermal Spray Technology, 12, pp 350-359.

Al-Zaitone B A and Tropea C (2011), Evaporation of pure liquid droplets: Comparison of droplet evaporation in an acoustic field versus glass-filament, Chemical Engineering Science, 66, pp 3914-3921

Anilkumar A V, Lee C P and Wang T G (1993), Stability of an acoustically levitated and flattened drop: An experimental study, Physics of Fluids, 5, pp 2763-2774

Barmatz M and Collas P (1985), Acoustic Radiation Potential on a Sphere in Plane, Cylindrical, and Spherical Standing Wave Fields, Journal of Acoustic Society of America, 77, pp 928-945

Basu S and Cetegen B M (2007), Modeling of thermo-physical processes in liquid ceramic precursor droplets injected into a plasma jet, International Journal of Heat and Mass Transfer, 50, pp 3278-3290

Basu S and Cetegen B M (2008a), Modeling of thermophysical processes in liquid ceramic Precursor droplets heated by monochromatic irradiation, Journal of Heat Transfer, 130, pp 071501-1--8

Basu S, Jordan E H and Cetegen B M (2008b), Fluid Mechanics and heat transfer of liquid precursor droplets injected into high temperature plasmas, Journal of Thermal Spray Engineering, 17, pp 60-72

Basu S, Saha A and Kumar R (2012), Thermally Induced Secondary Atomization of Droplet in an Acoustic Field, Applied Physics Letters, 100, pp 054101-1--4

Bhatia T, Ozturk A, Xie L, Jordan E, Cetegen B M, Gell M, Ma X and Padture N (2002), Mechanisms of Ceramic Coating Deposition in Solution-Precursor Plasma Spray, Journal of Materials Research, 17, pp. 2363–2372

Borra J P (2006), Nucleation and aerosol processing in atmospheric pressure electrical discharges: powders production, coatings and filtration, Journal of Physics D, 39, pp. R19

Botros P, Law C K, and Sirignano W A (1980), A droplet combustion in a reactive environment, Combustion Science and Technology, 21, pp 123–30

Brandt E H (2001), Acoustic physics suspended by sound, Nature, 413, pp 474-475.

Bremer L G, Walstra P and Vilet T V (1995), Estimations of the aggregation time of various colloidal systems, Colloids Surfaces A: Physico. chem. Eng. Aspects, 99, pp 121-127

Bremson M A (1968), Infrared radiation: a handbook for applications, Plenum Press, NY

Brinley E, Babu K S and Seal S (2007), The solution precursor plasma spray processing of nanomaterials, Journal of the Minerals, Metals and Materials Society, 59, pp 54-59

Castanet G, Lavieille P, Lemoine F , Lebouche M, Atthasit A, Biscos Y and Lavergne G (2002), Energetic budget on an evaporating monodisperse droplet stream using combined optical methods Evaluation of the convective heat transfer, International Journal of Heat and Mass Transfer, 45, pp 5053-5067

Castanet G, Lebouche´ M and Lemoine F (2005), Heat and mass transfer of combusting monodisperse droplets in a linear stream, International Journal of Heat and Mass Transfer, 48, pp 3261-3275

Castillo and R.J. Munz (2007), Transient heat, mass and momentum transfer of an evaporating stationary droplet containing dissolved cerium nitrate in a rf thermal argon-oxygen plasma under reduced pressure, International Journal of Heat and Mass Transfer, 50, pp 240-256

Chandrashekhar S (1981), Hydrodynamic and Hydromagnetic Stability, Dover Publications

Che S, Sakurai O, Shinozaki K, and Mizutani N (1998), Particle structure control through intraparticle reactions by spray pyrolysis, Journal of Aerosol Science, 29, pp 271-278

Chen K, Chang B Z, Ju M, Zhang X H and Gu H (2006), Comparative study of photodynamic therapy vs. CO_2 laser vaporization in treatment of condylomata acuminata, a randomized clinical trial, British Journal of Dermatology, 156, pp 516-520

Chen X D, Lin S X O (2004), Changes in milk droplet diameter during drying under constant drying conditions investigated using the glass-filament method. Transactions of I Chem E, Part C, Food and Bioproducts Processing, 82, pp 213–218

Chow J. C. F. (1964) Attenuation of Acoustic Waves in Dilute Emulsions and Suspensions, Journal of Acoustic Society of America, 36, pp 2395-2401

Cohen J and Anderson T (1996), Experimental investigation of near-blowout instabilities in a lean premixed combustor, Proceedings of 34th AIAA Aerospace Sciences Meeting and Exhibit no: 96-0819

Cohen M D, Flagan R C and Seinfeld J H (1987), Studies of concentrated electrolyte solutions using the electrodynamic balance. 3. Solute nucleation, Journal of Physical Chemistry 91 (1987), pp 4583-4590

Daif A, Bouaziz M, Chesneau X and Cherif A A (1998), Comparison of multicomponent fuel droplet vaporization experiments in forced convection with the Sirignano model, Experimental Thermal and Fluid Science, 18, pp 282-290

Danilov S D and Mironov M A (1992), Breakup of a droplet in a high-intensity sound field, Journal of Acoustic Society of America, 92, pp 2747-2755

Deegan R D, Bakajin O, Dupont T F, Huber G, Nagel S R and Witten T A (1997), Capillary Flow as the Cause of Ring Stains from Dried Liquids, Nature, 389, pp 827-829

Deegan R D, Bakajin O, Dupont T F, Huber G, Nagel S R and Witten TA (2000), Contact line deposits in an evaporating drop, Physical Review E, 62, pp 756-765

Deprédurand V, Castanet G and Lemoine F (2010), Heat and mass transfer in evaporating droplets in interaction: Influence of the fuel, International Journal of Heat and Mass Transfer, 53, pp 17-18

Dhiman R, McDonald A G and Chandra S (2007), Predicting splat morphology in a thermal spray process, Surface and Coating Technology, 201, pp 7789 –7801.

Dombrovsky L and Sazhin S (2003), Absorption of thermal radiation in a semi-transparent spherical droplet: a simplified model, International Journal of Heat and Fluid Flow, 24, pp 919-927

Elidrissi B, Addou M, Regragui M, Monty C, Bougrine A and Kachouane A (2000), Structural and optical properties of CeO_2 thin films prepared by spray pyrolysis, Thin Solid Films, **379**, pp 23-27.

Fernandez-Pello A C and Law C K (1982a), A Theory for the Free-Convective Burning of a Condensed Fuel Particle, Combustion and Flame, 44, pp 97–112

Fernandez-Pello A C and Law C K (1982b), On the Mixed-Convective Flame Structure in the Stagnation Point of a Fuel Particle, in Proceedings of the Nineteenth Symposium (International) on Combustion, pp 1037–1044. The Combustion Institute: Pittsburgh, PA

Hasegawa K, Abe Y, Kaneko A and Aoki K (2009), PIV measurement of internal and external flow of an acoustically levitated droplet, Proceedings of ITP: Interdisciplinary Transport Phenomena VI: Fluid, Thermal, Biological, Materials and Space Sciences, October 4-9 (2009), Volterra, Italy

Hegseth J J, Rashidnia N and Cha A (1996), Natural convection in droplet evaporation, Physical Review E, 54, pp 1640-1644

Incropera F P, DeWitt D P, Bergman T L and Lavine A S (2007), Fundamentals of heat and mass transfer (6th Edition), John Wiley and Sons, New Jersey

Jain S, Skamser D J and Kodas T T (1997), Morphology of single–component particles produced by spray pyrolysis, Aerosol Science and Technology, 27 (1997), pp 575-590.

Joint Commission on Powder Diffraction Standards (JCPDS) card # 81-0792.

Jordan E H, Xie L, Ma X, Gell M, Padture N P, Cetegen B M, Ozturk A, Roth J, Xiao T D and Bryant P E (2004), Superior thermal barrier coatings using solution precursor plasma spray, Journal of Thermal Spray Technology, 13, pp. 57-65

Kang K H, Lee S J, Lee C M and Kang S (2004), Quantitative visualization of flow inside an evaporating droplet using the ray tracing method, Measurement Science and Technology, 15, pp 1104-1112

King L V (1934), On the Acoustic Radiation Pressure on Spheres, Proceedings of Royal Society, London A, 147, pp 212-240.

Kumar R, Tijerino E, Saha A and Basu S (2010), Structural Morphology of Acoustically Levitated and Heated Nanosilica Droplet, Applied Physics Letters, 97, pp 123106-1--3

Lage P L C and Rangel R H (1993), Studies of concentrated electrolyte solutions using the electrodynamic balance. 1. Water activities for single-electrolyte solutions, Journal of Thermophysical Heat Transfer, 7, pp. 502

Landau L. D. & Lifshitz E. M. (1987) Fluid Mechanics, Butterworth-Heinemann

Law C K (1973), A simplified theoretical model for the vapor-phase Combustion of metal particles, Combust. Sci. Technol. 7, pp 197–212

Law C K (1976a), Multicomponent Droplet Vaporization with Rapid Internal Mixing, Combustion and Flame, 26, pp 219–33

Law C K (1976b), Unsteady Droplet Combustion With Droplet Heating, Combustion and Flame, 26, pp 17–22.

Law C K (1977), A Model for the Combustion of Oil/Water Emulsion Droplets, Combustion Science and Technology, 17, pp 29–38.

Law C K (1982), Recent advances in droplet vaporization and combustion, Progress in Energy and Combustion Science, 8, pp 171-201

Leong K H (1987), Morphological control of particles generated from the evaporation of solution droplets: Experiment, Journal of Aerosol Science, 18, pp. 525-552

Lierke E G (2002), Deformation and displacement of liquid drops in an optimized acoustic standing wave levitator, Acta Acoustica United with Acoustica, 88, pp 206-217

Lierke E G and Holitzner L (2008), Perspectives of an acoustic-electrostatic/ electrodynamic hybrid levitator for small fluid and solid samples, Measurements in Science Technology, 19, pp 115803-1--16

Lieuwen T (2001), Theoretical investigation of unsteady flow interactions with a premixed planar flame, Journal of Fluid Mech. 435 (2001), pp 289-303

Lin J C and Gentry J W (2003), Spray Drying Drop Morphology: Experimental Study, Aerosol Sci. Technol., 37, pp 15-32

Lobdell D D (1968), Particle size-amplitude reactions for the ultrasonic atomizer, Journal of Acoustic Society of America, 43, pp 229-231

Maidanik G (1957), Acoustical radiation pressure due to incident plane progressive waves on spherical objects, Journal of Acoustic Society of America, 29, pp 738-742

Maqua C, Castanet G, Grisch F, Lemoine F, Kristyadi T and Sazhin S S (2008), Monodisperse droplet heating and evaporation: Experimental study and modeling, International Journal of Heat and Mass Transfer, 51, pp 3932-3945

Maskell W C and Steele B H C (1986), Solid state potentiometric oxygen gas sensors, Journal of Applied Electrochemistry, **16**, pp 475-489

Mason S G (1977), Orthokinetic phenomena in disperse systems, Journal of Colloids and Interface Science, 58, pp 275–285

Masters K (1985), Spray Drying Handbook (4th Edition.), Wiley, New York

McDonald A G, Chandra S and Moreau C (2008), Photographing impact of plasma-sprayed particles on rough substrates, Journal of Material. Science, 43, pp 4631-4643

McDonald A G, Moreau C and Chandra S (2010), Use of thermal emission signals to characterize the impact of fully and partially molten plasma-sprayed zirconia particles on glass surfaces, Surface and Coatings Technology, 204, pp 2323 – 2330

Messing G L, Zhang S C and Jayanthi G V (1993), Ceramic Powder Synthesis by Spray Pyrolysis, Journal of American Ceramic Society, 76, pp 2707-2726

Milanova D and Kumar R (2005), Role of ions in pool boiling heat transfer of pure and silica nanofluids, Applied Physics Letters, 87, pp 27233107-1--3

Milanova D and Kumar R (2008), Heat Transfer Behavior of Silica Nanoparticles in Pool Boiling Experiment, Journal of Heat Transfer, 130, pp 042401-1--6

Miller R S, Harstad K and Bellan (1998), Evaluation of Equilibrium and Non-Equilibrium Evaporation Models for Many-Droplet Gas-Liquid Flow Simulations, International Journal of Multiphase Flow 24, pp 1025-1055

Minor G, Oshkai P and Djilali N (2007), Optical distortion correction for liquid droplet visualization using the ray tracing method: further considerations, Meas. Sci. Technol., 18, pp L23–L28

Oberste-Berghaus J, Bouaricha S, Legoux J G and Moreau C (2005), Proceedings of the ITSC 2005, Advances in Technology and Application, ASM International, May 2–4, Basel, Switzerland, pp 512.

Omrane A, Santesson S, Aldéna M and Nilsson S (2004), Laser techniques in acoustically levitated micro droplets, Lab on a Chip, **4,** pp 287-291.

O'Rourke P J and Amsden A A (1987), The TAB Method for Numerical Calculation of Spray Droplet Breakup, SAE Technical , no. 872089

Ouerfelli N and Bouanz M (1996), A shear viscosity study of cerium (III) nitrate in concentrated aqueous solutions at different temperatures, Journal of Physics: Condensed Matter, 8, pp 2673-2774

Oxtoby D W (1992), Homogeneous nucleation: theory and experiment, Journal of Physics: Condensed Matter, 4, pp 7627-7650

Ozturk A and Cetegen B M (2004), Modeling of plasma assisted formation of ytrria stabilized zirconia from liquid precursors, Materials Science and Engineering A, 384, pp 331-351

Ozturk A and Cetegen B M (2005a), Experiments on ceramic formation from liquid precursor spray axially injected into an oxy-acetylene flame, Acta Materialia, 53, pp 5203–5211

Ozturk A and Cetegen B M (2005b), Modeling of axially and transversely injected precursor droplets into a plasma environment, International Journal of Heat and Mass Transfer, 48, pp 4367-4383

Ozturk, A and Cetegen B M (2006), Modeling of axial injection of ceramic precursor droplets into an oxy-acetylene flame environment, Material Science and Engineering A, 422, pp 163-175

Padture N P, Schlichting K W, Bhatia T, Ozturk A, Cetegen B M, Jordan E H and Gell M (2001), Towards Durable Thermal Barrier Coatings with Novel Microstructures Deposited by Solution-Precursor Plasma Spray, Acta Materialia, 49, pp. 2251–2257

Padture N P, Gell M and Jordan E H (2002), Thermal Barrier Coatings for Gas-Turbine Engine Applications, Science, 296, pp 280-284.

Palermo J A (1968), Crystallization, Industrial and Engineering Chemistry Research, 60, p. 65.

Park B and Armstrong R L (1989), Laser droplet heating: fast and slow heating regimes, Applied Optics, **28,** pp. 3671-3680.

Park J and Moon J (2006), Control of Colloidal Particle Deposit Patterns within Picoliter Droplets Ejected by Ink-Jet Printing, Langmuir **22**, pp 3506-3513

Patil S, Kuiry S C, Seal S and Vanfleet R (2002), Synthesis of Nanocrystalline Ceria Particles for High Temperature Oxidation Resistant Coating, Journal of Nanoparticle Research, **4**, pp 433–438.

Pawlowski L (1995), The Science and Engineering of Thermal Spray Coatings (first ed.), John Wiley & Sons, Chichester, England

Pershin V, Lufitha M, Chandra S and Mostaghimi J (2003), Effect of Substrate Temperature on AdhesionStrength of Plasma-Sprayed Nickel Coatings, Journal of Thermal Spray Technology, 12, pp 370-371

Prasad A, Adrian R, Landreth C, Offutt P (1992), Effect of resolution on the speed and accuracy of particle image velocimetry interrogation, Experiments in Fluids, 13, pp 105–116

Qi A, Yeo L Y & Friends J R (2008), Interfacial destabilization and atomization driven by surface acoustic waves, Physics of Fluids, 20, pp 074103

Raffel M, Willert C and Kompenhans J (1998), Particle image velocimetry: a practical guide. Verlag, Berlin

Ranz W E and Marshall J R (1952), Evaporation from drops 1. Chemical Engineering Progress 48, pp 141–146.

Ravi B G, Sampath S, Gambino R, Parise J B and Devi P S (2006), Plasma spray synthesis from precursors: Progress, issues, and considerations, Journal of Thermal Spray Technology, 15, pp 701-707.

Rednikov A Y, Zhao H, Sadhal S S and Trinh EH (2006), Steady streaming around a spherical drop displaced from the velocity antinode in an acoustic levitation field, Quarterly Journal of Mechanics and Applied Mathematics, 59, pp 377–397

Saha A, Seal S, Cetegen B, Jordan E, Ozturk A and Basu S (2009a), Thermo-physical processes in cerium nitrate precursor droplets injected into high temperature plasma, Surface and Coatings Technology, 203, pp 2081-2091

Saha A, Singh V, Seal S and Basu S (2009b), Vaporization and precipitation characteristics of cerium nitrate precursor droplets heated by monochromatic irradiation, Surface and Coatings Technology 203, pp 2102-2115

Saha A, Basu S, Suryanarayana C and Kumar R (2010b), Experimental analysis of thermo-physical processes in acoustically levitated heated droplets, International Journal of Heat and Mass Transfer, 53, pp 5663-5674

Saha A, Basu S and Kumar R (2010a), Infrared thermography and numerical study of vaporization characteristics of pure and blended bio-fuel droplets, International Journal of Heat and Mass Transfer, 53, pp 3862–3873

Saha A, Basu S and Kumar R (2012a), Particle image velocimetry and infrared thermography in a levitated droplet with nanosilica suspensions, Experiments in Fluids, 52, pp 795-807

Saha A, Basu S and Kumar R (2012b), Effect of acoustic-streaming-induced flow on vaporizing nanofluid droplet, Journal of Fluid Mechanics, 692, 207-219

Saha A, Basu S and Kumar R (2012c), Scaling analysis: Equivalence of Convective and Radiative Heating of Levitated droplet, Applied Physics Letters, 100, pp 204104-1--5

Sampath S, Jiang X Y, Matejicek J, Leger A C and Vardelle A (1999), Substrate temperature effects on splat formation, microstructure development and properties of plasma sprayed

coatings Part I: Case study for partially stabilized zirconia, Materials Science and Engineering A, 272, pp 181–188

Santiago J G, Wereley S T, Meinhart C D, Beebe D J, Adrian R J (1998), A particle image velocimetry system for microfluidics, Experiments in Fluids, 25, pp 316–319

Sazhin S S, Sazhina E M and Heikal M R (2000), Modelling of the gas to fuel droplets radiative exchange. Fuel, 79, pp 1843–1852

Sazhin S S, Abdelghaffar W A, Sazhina E M, Mikhalovsky S V, Meikle S T and Bai C (2004), Radiative heating of semi-transparent diesel fuel droplets, Journal of Heat Transfer, 126, pp. 105.

Sazhin S S (2006), Advanced models of fuel droplet heating and evaporation. Progress in Energy and Combustion Sciences, 32, pp 162–214

Scarano F and Riethmuller M L (1999), Iterative multigrid approach in PIV image processing with discrete window offset, Experiments in Fluids, 26, pp 513–523

Seal S, Roy S K, Bose S K and Kuiry S C (2000), Ceria-Based High-Temperature Coatings for Oxidation Prevention, Journal of Materials Science, 52, pp 1-8.

Semenov S Y and Cetegen B M (2001), Spectroscopic temperature measurements in DC-arc plasma jets utilized in thermal spray processing of materials, Journal of Thermal Spray Technology, 10, pp 326-336

Sirignano WA (1999) Fluid dynamics and transport of droplets and sprays, (1st Edition) Cambridge University Press, Cambridge

Sirignano WA (2010) Fluid dynamics and transport of droplets and sprays, (2nd Edition) Cambridge University Press, Cambridge

Steele B C H (1984), Mass transport in materials incorporated in electrochemical energy conversion systems, Solid State Ionics, 12, pp 391-406

Suryanarayana C and Inoue A (2010), Bulk Metallic Glasses, CRC Press, Boca Raton, FL

Tarnuzzer R W, Colon J, Patil S and Seal S (2005), Vacancy Engineered Ceria Nanostructures for Protection from Radiation-Induced Cellular Damage, Nano Letters 5, pp 2573-2577

Tian Y and Apfel R (1996), A novel multiple drop levitator for the study of drop arrays, Journal of Aerosol Science, 27, pp. 721-737.

Tok A I Y, Boey F Y C, Dong Z and Sun X L (2007), Hydrothermal synthesis of CeO_2 nano-particles, Journal of Material Processing Technology, 190, pp 217-222.

Trinh E H and Wang T G (1982), Large-amplitude free and driven drop-shape oscillations: experimental observations, Journal of Fluid Mechanics, 122, pp 316-338

Tschope A., Schaadt D., Birringer R and Ying J Y (1997), Catalytic properties of nanostructured metal oxides synthesized by inert gas condensation, Nanostructured Materials, **9,** pp 423-432

Tye L and El-Masry N A (1994), Electrical characteristics of epitaxial CeO2 on Si(111), Applied Physics Letters, 65, pp 3081-3083

Vassallo P, Kumar R and D'Amico S W (2004), Pool boiling heat transfer experiments in silicawater nano-fluids, International Journal of Heat and Mass Transfer, 47, pp 407-411

Viswanathan V, Filmalter R, Patil S, Deshpande S and Seal S (2007), High-Temperature Oxidation Behavior of Solution Precursor Plasma Sprayed Nanoceria Coating on Martensitic Steels, Journal of the American Ceramic Society, 90, pp 870-877

Watanabe T and Ebihara K (2003), Numerical Simulation of Coalescence and Break-up of Rising Droplets, Computers and Fluids, 32, pp 823-823

Wolfe W I, Zissis G J (1978), The infrared handbook. Office of Naval Research, Department of Navy, Washington DC

Xie W J, Cao C D, Lu Y J and Wei B (2002), Levitation of iridium and liquid mercury by ultrasound, Physical Review Letters, 89, pp 104304-1--4

Xie W J, Cao C D, Lu Y J, Hong Z Y and Wei B (2006), Acoustic method for levitation of small living animals, Applied Physics Letters, 89, pp 214102-1--3

Xie W J and Wei B (2007), Sound field inside acoustically levitated spherical drop, Applied Physics Letters, **90,** pp 204104-1--3.

Yan Z L, Xie W J and Wei B (2011), Vortex flow in acoustically levitated drops, Physics Letters A, 375, pp 3306-3309

Yarin A L, Keller J, Pfaffenlehner M, Ryssel E and Tropea C (1997) Flowfield characteristics of an aerodynamic acoustic levitator, Physics of Fluids, 9, pp 3300–3314

Yarin A L, Pfaffenlehner M and Tropea C (1998), On the acoustic levitation of droplets, Journal of Fluid Mechanics, 356, pp 65-91

Yarin A L, Brenn G, Kastner O, Rensink D and Tropea C (1999), Evaporation of Acoustically Levitated Droplets, Journal of Fluid Mechanics, 399, pp 151-204

Yarin A L, Brenn G, Kastner O, Tropea C (2002), Drying of acoustically levitated droplets of liquid–solid suspensions: evaporation and crust formation, Physics of Fluids, 14, pp 2289–2298

Yuen M C and Chen L W (1976), On Drag of Evaporating Droplets, Combustion Science and Technology, 14 (1976), pp 147-154

Zhang S C, Messing G L and Borden M (1990), Synthesis of solid, spherical zirconia particles by spray pyrolysis, Journal. American Ceramic Society, 73, pp 61-67

Zhang S H, Yoon J H, Li M X, Cho T Y, Joo Y K and Cho J Y (2010), Influence of CO_2 laser heat treatment on surface properties, electrochemical and tribological performance of HVOF sprayed WC–24%Cr3C2–6%Ni coating, Materials Chemistry and Physics, 119, pp 458-464

Zhao H, Sadhal S S and Trinh E H (2006), Internal circulation in a drop in an acoustic field, Journal of Acoustic Society of America. 106, pp. 3289-3295